An Investigation into Red Emitting Phosphors for Display and Lightings

A thesis submitted for the degree of Doctor of Philosophy

Name : Mohd Fathullah bin Ghazli

Student number : 1123131

Supervisor : Professor Jack Silver

Abstract

An Investigation into Red Emitting Phosphors for Display and Lightings

Two very different classes of red phosphors were evaluated in this thesis; sulfide based phosphors ($CaS:Eu^{2+}$) and phosphors based on the formulae:- $LiEu_{1-x}M_x(MoO_4)_{2-y}(WO_4)_y$, [$M=Al^{3+}$, Y^{3+} and Gd^{3+}]. $CaS:Eu^{2+}$ was coated with Al_2O_3 using atomic layer deposition technique and placed into a humidity chamber at high temperature and high humidity for a period of time. The emission spectra were measured and evaluated against uncoated $CaS:Eu^{2+}$. The results from the humidity tests revealed that Al_2O_3 coated $CaS:Eu^{2+}$ increased the life span of the phosphor and therefore can be the potential use for the purpose of application at moderate humidity and temperature. For the phosphors based on $LiEu_{1-x}M_x(MoO_4)_{2-y}(WO_4)$, all the findings reported herein showed that, depending upon the types of cations introduced to the host lattices, incorporation of M at some point offered very much the same or better luminous efficacy when compared to the parent compound with 100 mol% of Eu^{3+}. This work also attempted to examine the correlative relationship between the crystal structures and the luminous efficacies although some attempts were unsuccessful. The findings discovered within this research are beneficial for solid state lighting industries where the cost of using rare earth metals has become significant and recycling is difficult.

Table of Contents

List of Figures

List of Tables

Abbreviations

CIE	- Commission internationale de l'éclairage
CCT	- Colour Correlated Temperature (K)
CRI	- Colour Rendering Index
SEM	- Scanning Electron Microscope
LED	- Light Emitting Diode
Pc-LED	- Phosphor Converted White Light Emitting Diode
PL	-Photoluminescence
lm	- Lumens
lm/W	- Lumens per Watt
LE	- Luminous Efficacy (lm/W)
pc-WLED	- Phosphor converted white light emitting diodes
QE	- Quantum Efficiency (%)
XRPD	- X-Ray Powder Diffraction

Acknowledgements

This work was carried out in the Wolfson Centre for Materials Processing, Institute of Materials & Manufacturing, Brunel University between December 2011 to November 2015. I owe my appreciation to all individuals below who have made this thesis materialized as a result of whom my learning adventure has become one that I will value forever.

My deepest gratitude goes to my inspiring supervisor, Professor Jack Silver whose I have been incredibly fortunate to have worked with. He guided me to explore on my own and constantly helped me to recover whenever I lost momentum. His remarkable support helped and motivated me overcome many obstacles right up until I completed this thesis. I really hope for one day, I will develop to be as great as him in supervising my future students as what he has done to me. The late Professor Robert Withnall, from the Wolfson Centre, assisted me with great guidance on the early parts of my experimental works and also for the help with a paper published during this work.

I am also thankful to the members of the Wolfson Centre, Brunel University whom I interacted with during my graduate studies and leisure times. You are the best team I ever worked with. In particular I would like to acknowledge Dr. Lesley Hanna whose was always helpful whenever in need. My big appreciation is also dedicated to Professor Chris Frampton and Dr. George Fern for the assistance and advice given to me in learning crystallography. My deep gratitude also goes to Dr. Terry Ireland, Dr. Paul Marsh and Mr. Abdul Ghani, for their valuable assistance. Also to all PhD students in Wolfson Centre who always cheered me up when I was in tough times.

Special thanks to the ETC staff for their technical supports during my period of studies particularly to Dr. Lorna Anguilano, Dr. Nita Verma and Dr. Ashley Howkins for their assistance during the research was taking place.

Many friends helped me remained positive and motivated through these exciting years in United Kingdom. Their supports and cares helped me a lot in overcoming obstacles and to stay in focused on my studies and family. I greatly

value the friendship and I deeply appreciate their belief in me. To mention a few, special thanks to Abdul Hadi (and Azura), Amirah Sahar, Wan Toren (and Che Rosmawati), Shazrul (and Amizan), Mila Bohmann (and Habib) who were always there when in need.

Most importantly, I would like to express my heart-felt gratitude to my lovely wife Nurul Hayati Yusup for the persistent patience and love given through this journey. Becoming a wonderful mom to three small kids and also a loving wife, a professional chef and the best companion to me is surely not an easy task to accomplish day to day. To my three kids; Adam, Nuha and Hannan, I believe sooner or later you will learn how hard your dad had to work through to get to this level and I hope this can be your inspirational story when you have all grown up.

My sincere thanks to my parent and in law, Siti Maliah Saidin, Ghazali Saleh, Hj Yusup Ahmad and Shatirah Yub for the firm support and pray while we are thousand kilometres away from you. Also thank you to all my siblings and in laws for your support.

Finally, I would like to show my appreciation for the financial support given to me by the Ministry of Higher Education of Malaysia and Universiti Malaysia Perlis. My sincere thank you also goes to ESPRC, Brunel University for partly supporting the research during the last 6 months of the project.

Chapter 1

Introduction

1.1 The Importance of Artificial Lightings

The contribution of artificial light in our daily lives passes the vast majority of humankind by without them realising its importance. According to The Royal Commission on Environmental Pollution [1], a massive transformation of artificial lighting took place in the United Kingdom during the last 200 years. In these modern times, many people are not aware of the huge contribution of artificial lighting in their lives, compared to earlier times when the moon and stars were the key light sources during the night time. Artificial lighting is used in all areas of modern life: on the streets, in automobiles and other moving platforms, in buildings (domestic, office and commercial), as well as airports and stations with it now essential for human beings in running their day-to-day lives. Currently the search is on in the modern era for bright and efficient lighting to save both time and energy in the developed world (and reduce carbon dioxide emissions) and export the technology to the third world countries which are still living with difficulties in power distribution and insufficient artificial lighting [2].

1.2 Electromagnetic Spectrum

Visible light is a type of electromagnetic radiation composing of waves as well as energy related to magnetic fields. The electromagnetic spectrum covers all radiation types including infra-red, visible light, ultra violet light, radio waves, gamma rays, and X-rays. The wavelength that is related to electromagnetic radiation is called the electromagnetic spectrum [3, 4]. In this thesis the main area of interest will only be in the region of 250 nm to 750 nm wavelengths.

1.3 Photopic Eye Response

The human eye is an important organ that evolved to aid in the perception of light within the wavelength of 390 nm to 750 nm. Reflection of light from an object enters into the eye through the pupil, and is focused by the cornea and formed into images on the eye's retina. The retina is the section of the human eye that is light-sensitive due to the presence of rod cells and cone receptors. The retina also contains ganglion cells and nerve fibers that send out image signals to the brain [5]. There are three different regimes of vision as shown in Figure 1.1. Photopic vision as seen from the figure happens to be active when a human is seeing in a high level of luminance (> 3 cd/m^2) such as during daylight. This vision actually comes from the cones that mediate vision and is very sensitive to colours. In contrast, scotopic vision is associated with rods cells on the retina that only perform their job at a low luminance level (0.003 cd/m^2). However, any vision that comes from this regime is insensitive to colours and therefore can only recognize certain amounts of greyness in a subject [6]. The eye's interaction with the electromagnetic spectrum is not uniform throughout all wavelengths. Human eyes are really sensitive in responding to green light as compared to any other colours. This is due to the photopic eye sensitivity function (see Figure 1.2) where the highest level of sensitivity comes in the green spectral range at a wavelength of 555 nm.

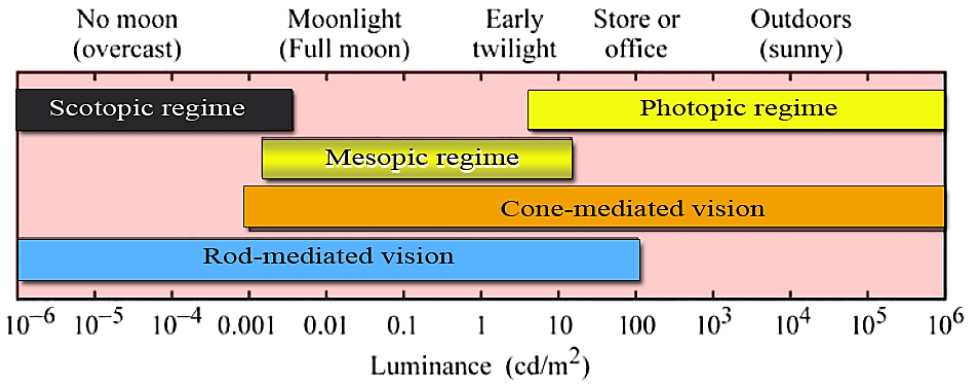

Figure 1.1: Ranges of vision and receptor regimes [6]

1.3.1 Measuring Visible Light

In order to produce artificial light that aims to have all the qualities of the natural sunlight that humans evolved in, a system is needed to quantify light in terms of its

brightness and the colour tones so it can meet the purposes of its applications. A number of ways to measure light have been established and these are discussed in the following sub topics.

1.3.1.1 Colour Rendering Index (CRI)

The CRI is an index that measures the quality of colours of specific subjects illuminated by a light source that conforms to the ones from the same subjects as illuminated using a reference source. The reference source for illumination is a black body radiator, for test sources that have correlated colour temperature (CCT) of < 5000 K, or daylight source for test sources with CCT of > 5000 K. CRI is dimensionless and rated on a scale from 0 to 100 (where the value of 100 represents the fact that all colour samples illuminated by a tested light source should show up to hold the equivalent colour to the same samples as illuminated by a reference source) [7].

1.3.1.2 Luminous Efficacy

Luminous Efficacy of optical radiation as defined by Schubert [6] is the conversion efficiency from optical power to luminous flux and measured in lumens per watt (lm/W). It is defined as:

$$LE = \frac{\Phi_{lum}}{P} = 683\,\frac{\text{lm}}{\text{W}} \times \frac{\left[\int_{\lambda} V(\lambda)\,P(\lambda)d\lambda\right]}{\left[\int_{\lambda} P(\lambda)d\lambda\right]} \qquad \textbf{Eq 1.1}$$

Φ_{lum} is the luminous flux
$V(\lambda)$ is the eye sensitivity function per unit wavelength
$P(\lambda)$ is the light power emitted per unit wavelength

The theoretically attainable maximum value, assuming for a complete conversion of energy (100% conversion) at the most sensitive monochromatic wavelength perceived by the human eye (555 nm), would be 683 lm/W. However, the luminous efficacy is inversely proportional to the CRI, and considering the fact that a large CRI covers a broad

spectral distribution across the visible wavelengths this can result in the luminous efficacy falling to a value lower than 683 lm/W. For that reason, both parameters need to be carefully selected in considering the requirements of specific lighting applications [7].

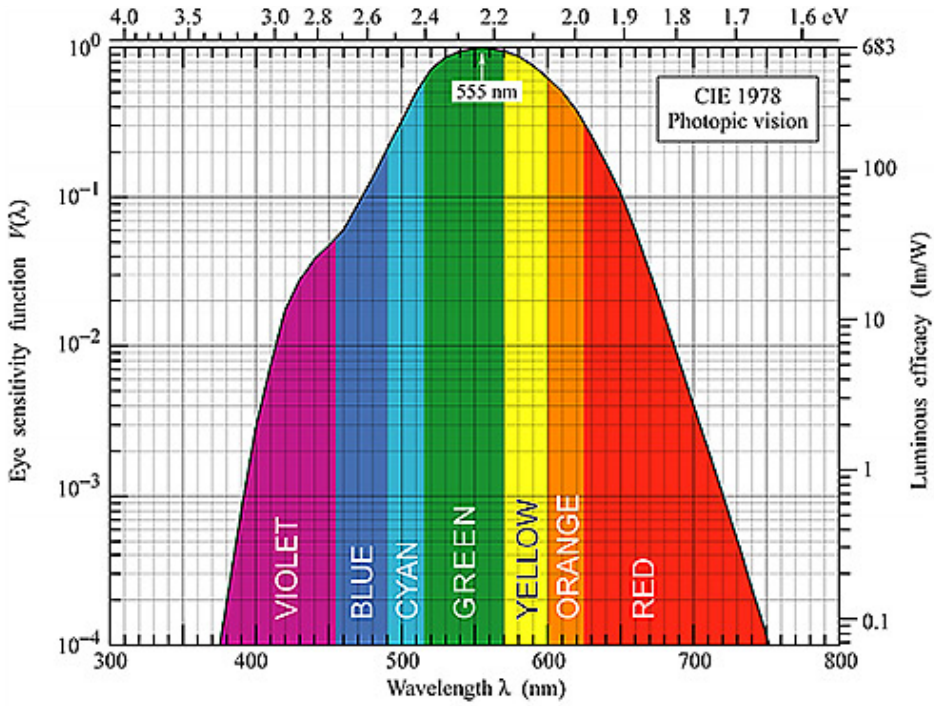

Figure 1.2: Eye sensitivity function measured in luminous efficacy (lumens per watt of optical power) [6]

1.3.1.3 Light Efficiency

The terms luminous efficiency and efficacy of a light source has sometimes been misused by some people. The meaning of luminous efficacy has been explained in 1.3.1.2 whereas the term efficiency is different depending on the contexts.

Quantum efficiency is a term that encompasses both the internal and external quantum efficiency and these are generally related to the ratio of the photons emitted over electrons injected. In terms of the photoluminescent concept, it means the ratio of photons emitted over photons excited. There is no unit to quantify quantum efficiency so normally it is expressed in percentage (%) or in decimal points. However, the term **luminous efficiency** is commonly used by the lighting community and is referred to as *the luminous efficacy of the light source* as it is a luminous flux (lm) of the light source over the

electrical input power (measured in W), meaning the unit is also in lm/W. Although the units are the same, unless a certain light source has a perfect electrical-to-optical power conversion, the luminous efficiency will never be equivalent to the luminous efficacy of photoluminescence [6].

1.3.1.4 CIE Coordinates

Colour sensations can differ from one person to another and are subjective according to each individual's perception. For that reason, since 1931 the International Commission on Illumination has made a standard measurement in identifying colours by establishing a chromaticity diagram (CIE) as a means of specifying colour coordinates based on human eye sensitivity (see Figure 1.3). The chromaticity values are calculated based on three main reference colours (called tristimulus) that can mix to provide visual sensation XYZ values [6]:

$$x = \frac{X}{X + Y + Z} \qquad \textbf{Eq 1.2}$$

$$y = \frac{Y}{X + Y + Z} \qquad \textbf{Eq 1.3}$$

x and *y* are chromaticity coordinates

X,Y and Z are tristimulus of three primary red, green and blue respectively

From the equations, because *z* equals to 1-*x*-*y*, the calculations for z coordinates are unnecessary as the two points in this colour space are enough to represent all three colour coordinates as seen in Figure 1.3.

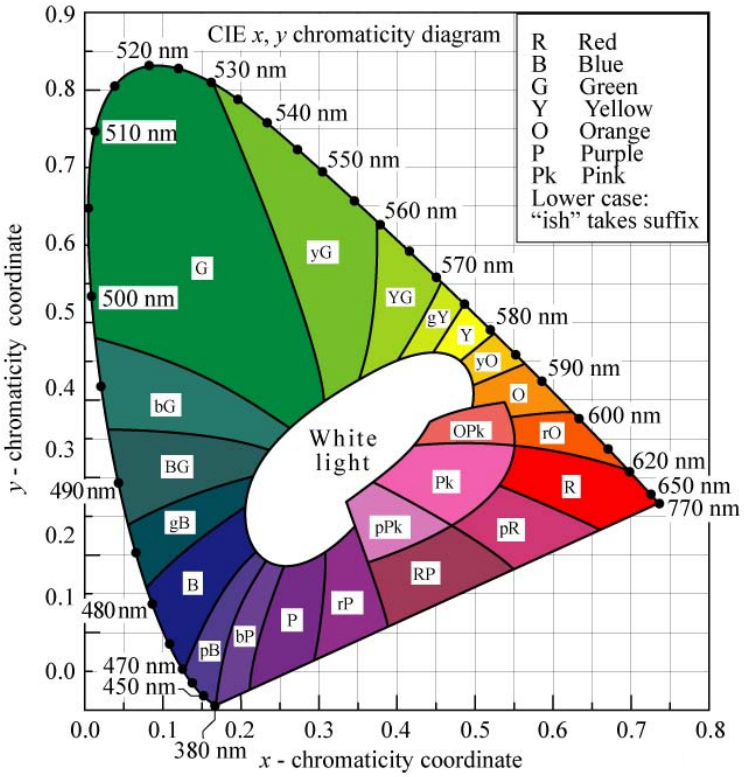

Figure 1.3: CIE 1931 chromaticity diagram as presented by E. Fred Schubert [6]

1.4 Luminescence

Luminescence is the name given to the process of emitting electromagnetic radiation in the visible region through a process other than thermal radiation [8]. There are a number of different types of luminescence and among them are photoluminescence, chemiluminescence (the energy of a chemical reaction), electroluminescence (electrical energy) and many more. The term luminescence originally comes from the Latin word *lumen* which refers to light. The term at the beginning was introduced as *luminescenz* by Eilhard Wiedemann in 1888 which he referred to as all lighting not caused by high temperature (which is supposed to be incandescence) [9].

It is of interest to learn briefly the history of luminescence which is related to the area of research reported in this thesis. The earliest mentioning of luminescence was found in the Chinese book called *Shih Ching* written between 1500-1000 B.C [9] which mentioned about the luminescence that came from glow worms and fireflies. The subject of luminescence was also mentioned in an old Indian Sanskrit book called the "*Vedas"* which mentioned *khadoyta,* referring to glow worms in the Sanskrit. An appropriate

definition of luminescence came about during the time of Aristotle (384-322 B.C) where he explained about the concept of non-incandescent light, referring to it as "certain bodies that although do not anticipate with nature of fire (such as a candle or fire wood) yet can still produce light". The Japanese were the first civilization that created and applied phosphors in the 10th Century where they used phosphorescent paints made from seashells [9].

Now follows a list of the most important developments in phosphors in the past 500 years [9-11];

- Year 1602 - Vincenzo Cascariolo reported about a persistent luminescent Bolognian phosphor (now believed to have been $BaSO_4$) which he found after heating ground stones [9][10].
- Year 1677 - Henning Brandt – Discovered "phosphor" referring to the element phosphorus that can produce glowing vapour when exposed to the moist air [10, 11].
- Year 1819 – Edward D. Clarke reported about fluorite crystals which produced a deep sapphire blue colour when seen under reflected light and an intense emerald green colour when viewed by the transmission of light. However no further explanation was made in the report [10].
- Year 1833 – Sir David Brewster described the red fluorescence of a chlorophyll solution which he believed was due to light scattering phenomena [10].
- Year 1852 – An important year in the history of photoluminescence; Sir George Gabriel Stokes identified through detailed studies that the dispersed light from his experiments always had longer wavelengths than the original light (the term are now referred to as Stoke's Law). One of the interesting findings was he proved that if a quinine solution is placed under UV light then blue light is emitted, but it is not emitted from the solution if the latter is irradiated within the visible spectrum[9, 10].
- Year 1862 - Victor Pierre authored papers on solutions of single fluorescent substances [10].

- Year 1866 – ZnS which was going to be a very important host for phosphor was recognized and developed by Theodor Sidot [11].
- Year 1888 – Eilhard Wiedemann classified phosphors into different categories based on types of excitation and introduced types of excitations amongst phosphors [11].

Over the past 100 years, research on phosphors started to become more systematic and some important years are highlighted below;

- Year 1928 – A systematic study on phosphors was first reported [9].
- Year 1936 – Kalman Tihanyi, a Hungarian engineer invented and patented a concept of flat-panel display system [12, 13].
- Year 1938 – Oxide lattice phosphors were introduced [9].
- Year 1942 – A fluorescent Calcium Halo phosphate lighting devices were found after a search by trial and error through hundreds of compounds [9].
- Year 1964 – Phophor's investigation were researched for colour televisions (TVs) [9].
- Year 1987 – Ching W. Tang and Steven Van Slyke reported the very first organic light-emitting diode (OLED) device [14].
- Year 1988 – Liquid Crystal Display panel was launched [12].
- Year 1992 – Commercial phosphor-based plasma TVs were launched by Fujitsu [9].
- Year 1996 – White GaIn/GaN LEDs using phosphor converters were first reported by Bando *et* al and further analysed by Nakamura and Fasol in the following year [6, 15].

Over the past 60 years, research on phosphors has increased rapidly due to the advancements needed in technology and of solid state physics and spectroscopy. In addition, the use of phosphors in phosphor-converted white light emitting diodes (pc-WLEDs) has grown rapidly and become an improved solution to replace previous inefficient lighting devices as seen in Figure 1.4. The demand for such lighting is expected

to grow considerably due to its ability to emit light with high efficiency and longer life as well as being free from any toxic elements [15].

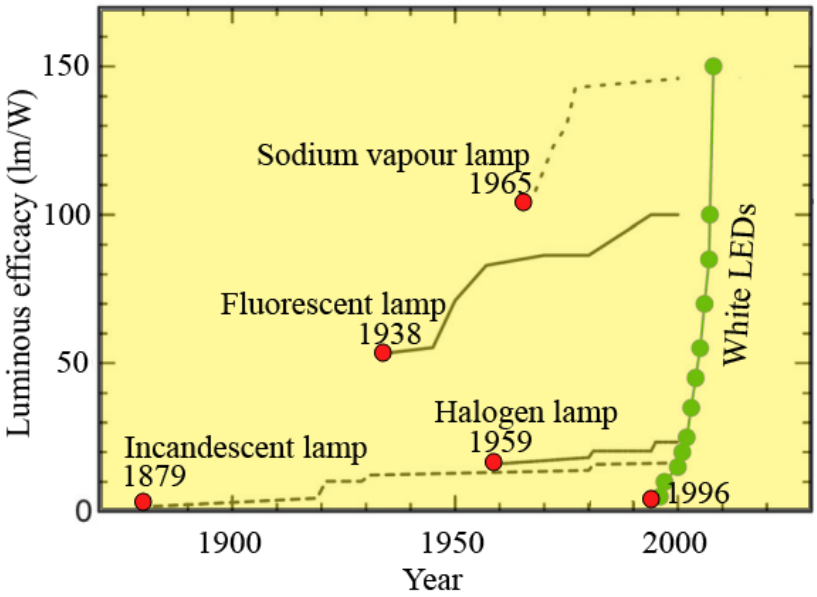

Figure 1.4: Life cycles of lighting devices with the rate of improvement in luminous efficacies starting in 1879 until the introduction of white LEDs [16].

1.5 Lanthanides

The term lanthanide originated from the Greek word *lanthaneien* which means "lying hidden". Lanthanides are a group of 15 elements in the periodic table that are very important in manifesting luminescence properties of materials. Lanthanide ions have remarkable luminescent characteristics because of their distinctive 4f orbitals. Unlike the electronic configurations of the other elements seen in the main periodic table, the half-filled 4f shells of the lanthanides is due to the energy of the shell being lower than that of the 5d shell. This consequently results in the electron beginning to fill the 4f shell instead of the 5d shells [17]. The transitions between the ground and excited states in the f orbitals of the lanthanide elements, is the process responsible for their luminescent properties in the M^{3+}.

1.5.1 Photoluminescent Phosphors

The phosphor materials reported in this thesis all exhibit the phenomena of photoluminescence. A photoluminescent phosphor is a material that has photoluminescent properties. Phosphors are generally found in a solid state form; they are inorganic materials consisting of a host lattice, in many cases doped with a tiny amount of impurities (cations) called activators (commonly rare earth element cations). The amount of activators is very small primarily because at greater quantities the effectiveness of the luminescence emitted decreases. In most cases the host is needed to absorb the photon from the exciting light source and the activators help to emit light at specified wavelengths [18].

Photoluminescence is excited by electromagnetic (normally ultraviolet) radiation and as a result it, raises electrons in the activator cations to an excited state as shown in Figure 1.5. The exciting energy is absorbed by the activator and promotes the electron in ground state (A) of the activator to jump to the excited (A*) state as shown in Figure 1.6 (left) [19]. After that, the excited state electron returns to its lower energy state via two ways; (1) light emission and (2) vibrational emission in the form of heat loss as seen in Figure 1.6 (right).

The energy can also be absorbed either by the host lattice or its co-activator (if any) and then transferred to the activator as visualized in Figure 1.6 (right). It can also be seen from the diagram that the exciting energy E_1 is larger than the emission energy E_2 which is in line with Stokes Law [8]. It is possible in some situations where $E_1 > E_2$, which is known as anti-Stokes law, to get emission by an upconversion.

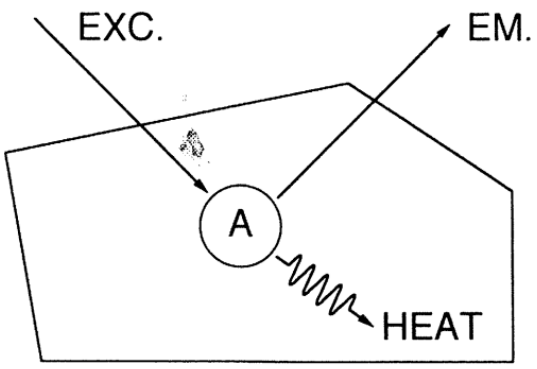

Figure 1.5: A luminescent ion A in a host lattice. EXC: Excitation, EM: Emission and HEAT: nonradiative return in form of heat loss [20].

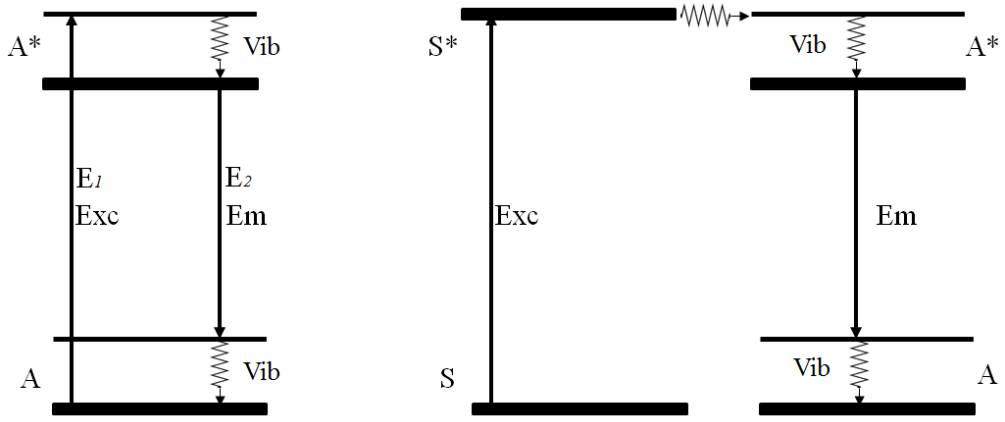

Figure 1.6: Schematic illustraition of luminescent process on phosphor as described by Feldmann et, al [19]

1.5.2 The Use of Activators in Phosphors

Activators are defined as any addition of atoms to a host lattice or any subtraction of atoms from host lattice which increase luminescence [9]. The addition or subtraction of atoms causes lattice defects due to rearrangements of the crystal stoichiometry of the lattice which sometimes can cause the luminescence to rise. Activators can be employed by either adding the atoms before precipitation takes place (co-precipitation) or by introducing the activators on a dry phosphor lattice before a firing process takes place.

The time taken by activators when they get excited until they revert to ground state is known as life time (See Table 1.1). Each activator has its own lifetime and the typical life times of common activators are listed in Table 1.1 below [9]:

Table 1.1: Life times of activators

Activators	Life Time (Seconds)	Electronic Transitions
Mn^{2+}	$\sim 10^{-2}$	(3d→3d)
Cu^{+}	$\sim 10^{-3}$ -10^{-4}	(4s→3d)
Ag^{+}	$\sim 10^{-6}$ -10^{-5}	(5s→4d)
Eu^{3+}	$\sim 10^{-4}$ -10^{-2}	(4f→4f)
Tb^{3+}	$\sim 10^{-4}$ -10^{-2}	(4f→4f)
Ce^{3+}	$\sim 3 \times 10^{-7}$	(5d→4f)
Eu^{2+}	$\sim 8 \times 10^{-7}$	(5d→4f)

1.5.3 Europium as Activators

Based on this work being related to the red element of lighting, europium (II), (Eu^{2+}) and europium (III), (Eu^{3+}) have become the main cations of interest as they can be activators that yield red emissions in the right host lattices for lighting applications. Europium is a rare earth element that can exist both in divalent and trivalent states as both ions possess different emission characteristics. The spectrum of Eu^{2+} is broad due to the allowed 5d-4f transitions when excited [21] and varies from the ultraviolet to red region depending on the type of host lattice in it. Although some phosphors used for red emission in pc-WLEDs have Eu^{2+} cations as activators there have been suggestions to use Eu^{3+} in certain lattices [22]. Electric dipole transitions with the same parity are forbidden, therefore the 4f - 4f transition between the trivalent lanthanide ions is not allowed as outlined by Laporte's rule. However, in the event that the ions are doped in an appropriate host and influenced by a non-centrosymmetric environment, the state of opposite parity with 4f wave functions arises. This activity relaxes the parity selection rule, therefore making the 4f - 4f transitions become partially allowed [23].

Eu^{3+} contains five narrow emission bands as presented by the Dieke Diagram in Figure 1.7 associated with the $^5D_0 \rightarrow {}^7F_i$ transitions (i = 0, 1, 2, 3 and 4) [9, 24]. The 4f orbital in Eu^{3+} is strongly shielded so it has very little interaction with the host lattice compared to d and p orbitals. As a consequence, the 4f orbitals are not available for chemical bonding with the host though they are sensitive to the symmetry of the bonding [25]. Therefore the luminescence should not change its shape but its intensity might be relatively affected if the symmetry of the bonding changes.

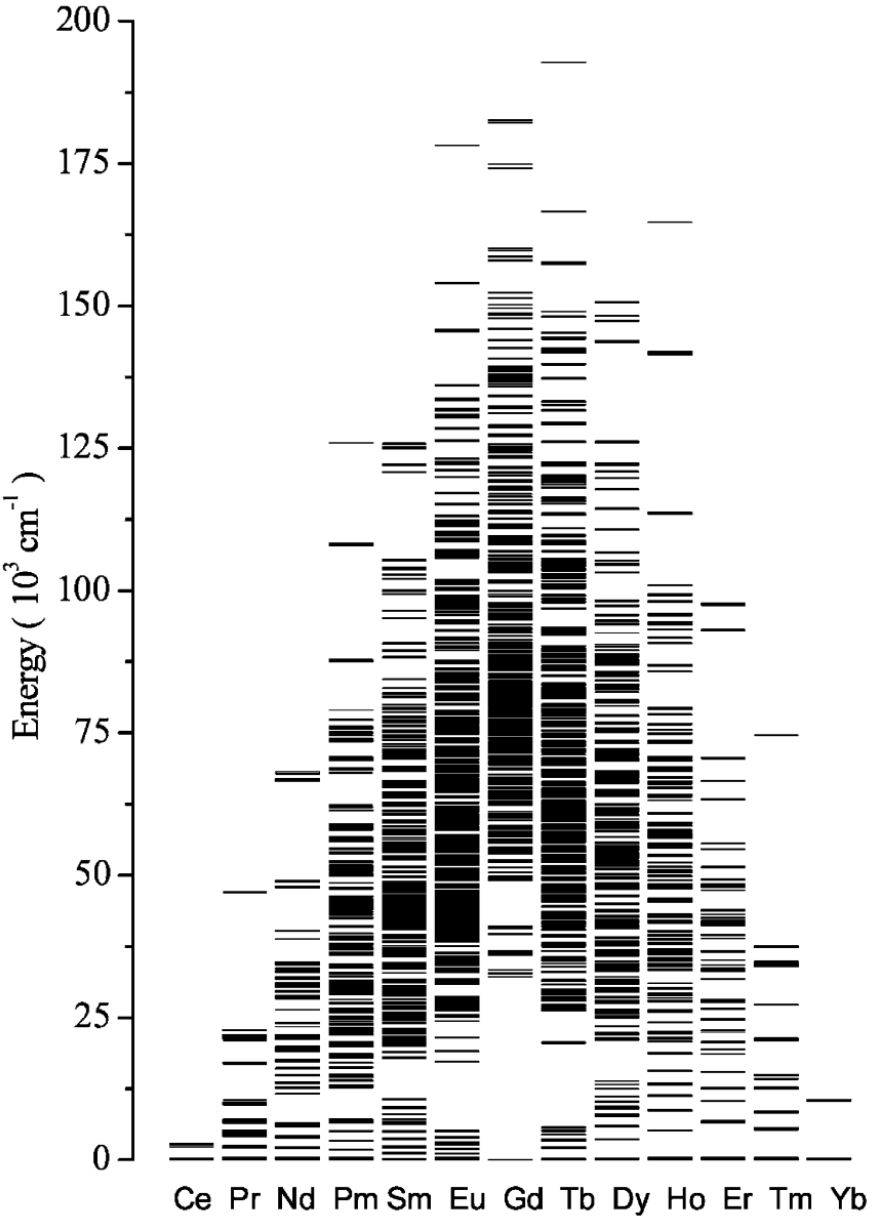

Figure 1.7: Energy level diagram for trivalent lanthanide ions as visualized by P.S Peijzel *et. al* [26]

1.6 Quenching

In certain circumstances the emission from the activators may also be reduced. This can happen due to a number of factors such as a rise in temperature (known as thermal quenching) or a change in the stoichiometric amount of activator (or sensitizer) within the host lattice (known as concentration quenching). The concepts of both quenching effects are discussed below.

1.6.1 Thermal Quenching

Some phosphors are operated in LEDs at high temperature (as high as 200°C) and because of that it is very important for a phosphor to sustain its performance at this level of temperature. Luminescence degradation of a phosphor due to rising temperature is called thermal quenching in which the excited energy is transferred to phonons and the relaxation happens in vibrations mode (lattice vibrations). Such phonon relaxation is also known as a leakage process which in return reduces the efficiency of the light emitted from the phosphor [26].

1.6.2 Concentration quenching

The amount of rare earth activators incorporated on host lattices does have a constraint and a further increase on its concentration (until it exceeds a certain limit) can easily lead to an increase in the non-radiative losses instead of an increase in the emission intensity. Two factors that cause concentration quenching are lattice defects and inappropriate distance between each activator [8]. There is a migration of energy between the activator ions during the cross-relaxation process. If the excited ions are in a close distance with each other they can easily transfer their excited energy to the neighbouring ions instead of returning to the ground state and emit radiations. In this case the excitation energy that transfers away from the active ion loses its excited energy to non-activators and therefore the mechanism quenches the emission [27].

1.7 Existing Technologies

The application of phosphors in displays and general lighting is gaining wide public acceptance. Pc-WLEDs have now become important lighting devices not only for general lighting but also on back-lighting of LED TVs, mobile phones as well as on automotive headlights. The industry now is maturing and the direction of LED lighting is now going towards slimmer, more compact integrated systems that come with optimised performance [28]. In terms of pc-WLEDs to date, $Y_3Al_5O_{12}:Ce^{3+}$ ($YAG:Ce^{3+}$) is the most common yellow phosphor to combine with other phosphors in pc-WLEDs and produces better luminous efficacy than the traditional inefficient lamps [29]. However, there are some

issues that need further investigation such as the colour rendering problems in the pc-WLEDs as well as the expensive cost of manufacturing due to using rare earth metals in phosphors.

1.8 Research Aim of the work reported in this Thesis

The aim of the work documented in this thesis was to study some red phosphors that may have potential for use in white light emitting LEDs. Two different approaches to such red phosphors were considered; the first was to look at known red emitting phosphors and consider the possibilities of using them; the second was to look at some new phosphor systems to asses their merits for such applications. The aims were:-

(1) To assess the effect of relative humidity and temperature on the loss of colour conversion performance of the $CaS:Eu^{2+}$ and $SrS:Eu^{2+}$ phosphors. These two phosphors are very sensitive to humidity and require protection from the environment if they are going to be useful. Thus their photoluminescence (PL) will be monitored as a function of ageing in order to find the effectivenes of coating materials applied on the phosphor.

(2) To synthesise a number of new phosphors based on existing phosphors by reducing their rare earth metal content to lower their prices whilst maximising their efficiencies.

1.9 Content of the Rest of this Thesis

Chapters 2 and 3 provide details of the experimental techniques used and also more detailed background to the phosphors studied in the thesis.

Chapters 4 to 7 set out and discuss the findings of this work, whereas Chapter 8 gives an overall summary of the conclusions and suggests areas for future work.

1.10 References

1. The Royal Commission on Environmental Pollution (2009) Artificial Light in the Environment.

2. Jane Brox (2011) Artificial light: How man-made brightness has changed the way we live and see forever. http://ind.pn/OyBPb1. Accessed August 14 2015.

3. Electromagnetic radiation. (n.d) American Heritage® Dictionary of the English Language, Fifth Edition. (2011). http://www.thefreedictionary.com/electromagnetic+radiation. Accessed August 14 2015.

4. Electromagnetic spectrum. (n.d) American Heritage® Dictionary of the English Language, Fifth Edition. (2011). http://www.thefreedictionary.com/electromagnetic+spectrum. Accessed August 14 2015.

5. Goldstein E (2009) Sensation and Perception. *Wadsworth Cengage Learning*,

6. E. Fred Schubert (2006) Light Emitting Diodes. *Cambridge University Press, New York.*

7. Pust P, Weiler V, Hecht C, Tücks A, Wochnik AS, Henß A, Wiechert D, Scheu C, Schmidt PJ, Schnick W (2014) Narrow-band red-emitting $Sr[LiAl_3N_4]: Eu^{2+}$ as a next-generation LED-phosphor material, *Nature materials*, *13*(9), 891-896.

8. Stone R, Silver J (September 2011) An investigation into novel red emitting phosphors and their applications. Dissertation, Brunel University.

9. Saltoun KY (2013) An investigation of the synthesis and properties of nano crystalline $Y_2O_3:Eu^{3+}$ (prepared using micelle-based precursors). Dissertation, Brunel University.

10. Valeur B, Berberan-Santos MN (2011) A brief history of fluorescence and phosphorescence before the emergence of quantum theory. *Journal of Chemical Education*, *88*(6), 731-738.

11. Smet PF, Moreels I, Hens Z, Poelman D (2010) Luminescence in sulfides: A rich history and a bright future. *Materials*, *3*(4), 2834-2883.

12. Francis N (2013) Selecting Video Monitors For The Home: Features Of The Best Video Monitor. *Speedy Publishing LLC*.

13. Betters E (2014) Farewell plasma TV: The moments that defined flatscreen. http://www.pocket-lint.com/ 131549-farewell-plasma-tv-the-moments-that-defined-flatscreen. Accessed 10/08 2015.

14. Tang CW, VanSlyke SA (1987) Organic electroluminescent diodes. *Applied physics letters*, 51(12), 913-915.

15. George NC, Denault KA, Seshadri R (2013) Phosphors for Solid-State White Lighting. *Annual Review of Materials Research*, *43*, 481-501.

16. Narukawa Y, Ichikawa M, Sanga D, Sano M, Mukai T (2010) White light emitting diodes with super-high luminous efficacy. *Journal of physics D: Applied physics*, *43*(35), 354002.

17. Larsen D Lanthanides: Properties and Reactions. Creative Commons Attribution. http://chemwiki.ucdavis.edu/Inorganic_Chemistry/Descriptive_Chemistry/ The_ Lanthanides%3A_Properties_and_Reactions. Accessed August 19 2015.

18. Ronda CR (2007) Luminescence: From Theory to Applications. John Wiley & Sons.

19. Feldmann C, Jüstel T, Ronda CR, Schmidt PJ (2003) Inorganic Luminescent Materials: 100 Years of Research and Application. *Advanced Functional Materials*, *13*(7), 511-516.

20. Blasse G, Grabmaier B (1994) Luminescent materials. *Springer-Verlag Berlin*.

21. Yen WM, Yamamoto H (2006) Fundamentals of Phosphors. *CRC press*.

22. Jüstel T (2007) Luminescent Materials for Phosphor–Converted LEDs: *Luminescence: From Theory to Applications*, 179-190.

23. Singh A, Singh S, Rai S (2014) Role of Li ion in the luminescence enhancement of lanthanide ions: favorable modifications in host matrices. *RSC advances*, 4(51), 27039-27061.

24. Parchur A, Ningthoujam R (2012) Behaviour of electric and magnetic dipole transitions of Eu^3 , $_5D^0 \rightarrow {}_7F^0$ and Eu–O charge transfer band in Li co-doped YPO_4: Eu^3. *RSC Advances*, 2(29), 10859-10868.

25. Jia D (2006) Enhancement of Long-Persistence by Ce Co-Doping in CaS: Eu2 , Tm3 Red Phosphor. *Journal of The Electrochemical Society*, 153(11), H198-H201.

26. Peijzel, P. S., Meijerink, A., Wegh, R. T., Reid, M. F., & Burdick, G. W. (2005). A complete 4fn energy level diagram for all trivalent lanthanide ions. *Journal of solid state chemistry*, 178(2), 448-453.

27. Šakirzanovas S (2011). Novel $Sm^{2+/3+}$ Phosphors as Luminescence Converter for Near UV Radiation. Dissertation, *Vilniaus Universitetas*.

28. Timothy A. Schuler (24 April, 2015) Technology: New Materials In Solid-State Lighting.. Accessed 21 September 2015.

29. Yuhua W, Ge Z, Shuangyu X, Qian W, Yanyan L, Quansheng W, Chuang W, Xicheng W, Xin D, Wanying G (2015) Recent development in rare earth doped phosphors for white light emitting diodes. *Journal of Rare Earths*, *33*(1), 1-12.

Chapter 2
Experimental Techniques

The quality of a phosphor is assessed mainly from its spectral properties. These include its luminous efficacy, its excitation / emission spectra and sometimes the ability of the phosphor to emit at elevated temperatures. Additionally, there are two other significant properties that need to be examined which are the particle sizes as well as the crystalline structure of the powder.

This chapter highlights all the equipment used in the characterisation of phosphors synthesised in our laboratories. The equipment used is listed below:-

1. Bentham Phosphor Quantum Efficiency (QE) System
2. Bentham Integrating Sphere with M300 Monochromator
3. X-ray powder diffraction (XRPD)
4. Scanning electron microscopy (SEM).
5. Attenuated Total Reflectance - Fourier Transform Infrared Spectroscopy (ATR-FTIR).
6. Speed mixer (to aid synthesis, not for characterization)

All the equipment listed above is briefly introduced over the following pages along with their operating principles and how they were deployed within this work.

2.1 Bentham Phosphor Quantum Efficiency (QE) System

The Bentham Phosphor Quantum Efficiency System (see Figure 2.1) consists of a set of devices designed for calculating the actual quantum efficiency and luminous efficacy of phosphor powder samples applied in commercial applications [1]. This instrument system can measure up to six samples at one time using a motorised carousel. It also has the ability to collect spectra at different temperatures up to 200˚C, making it useful for analysing thermal quenching of phosphors. In addition, it can provide information on the CIE colour coordinates of the emitted spectra in (*x, y*) coordinates with reference to the CIE chromaticity diagram. This instrument system includes:

a) IL75E xenon light source which is a reflector based on 75W xenon lamp to excite the phosphor.
b) Bentham 605 model power supply, used with stabilized light sources and calibration standard sources.
c) TMC3000 monochromator which has a 300 mm focal length that allows light to be measured from the minimum of a 300 nm wavelength connected through a USB 2.0 interface. The emission and excitation spectra are measured directly by this monochromator.
d) BenWin+ Version 4.1.0.10 software application for the system configuration and data acquisition.

In order to acquire a spectrum, a reflective powder (Ba_2SO_4) was used prior to the phosphor measurements. Ba_2SO_4 was used as a starting reference due to its ability to fully reflect any visible light targeted at it, thus allowing the accurate calculation of the luminous efficacy of light emitted from the phosphor samples. The surface of phosphor samples must be compacted and adjusted to all be level at the same height in order to get comparable results between different phosphors. In order to obtain the luminous efficacy value, the difference between the integration area of emitted light arising from the reference material and the phosphor measured will be calculated using a spread sheet supplied by the manufacturer. Due to the non-uniformity of phosphor powder and the way it is positioned under the exciting light, all luminous efficacies reported in this thesis are subject to errors of 10%.

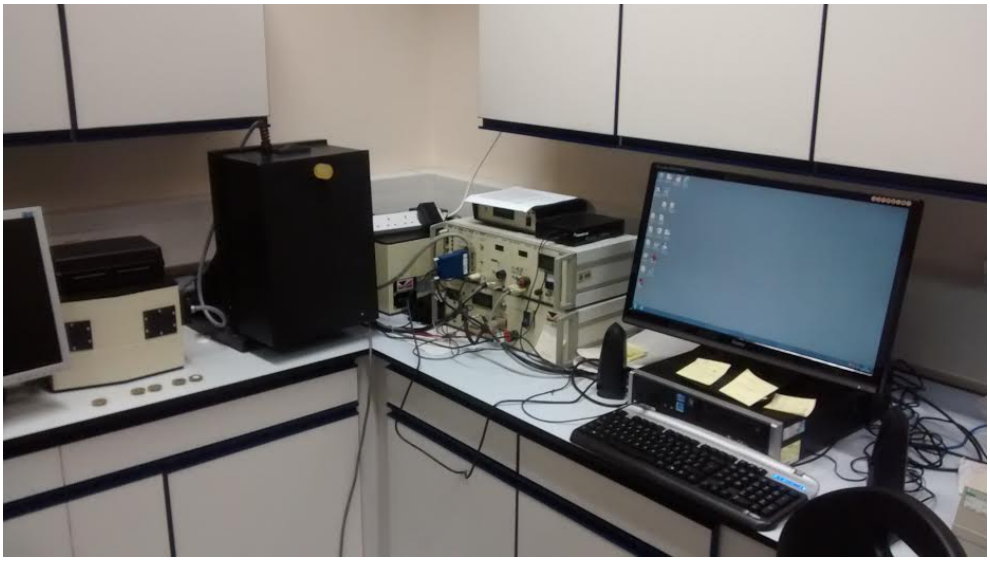

Figure 2.1: Bentham Phosphor Quantum Efficiency (QE) System

2.2 Bentham Integrating Sphere with M300 Monochromator

Although the Bentham Phosphor Quantum Efficiency (QE) System as discussed in 2.1 is an excellent quantitative system for measuring spectra, it is however unable to provide detailed visualization of the excitation and emission spectral bands. Therefore, another set of spectrometer devices were required in order to observe the spectral shape in detail. This second spectrometer was the M300 Bentham integrating sphere (see Figure 2.2). Similarly to the Bentham Phosphor Quantum Efficiency (QE) System, the Bentham M300 monochromator uses a xenon lamp as the light source to excite the phosphor. This system can provide spectra over a wide range from 250 nm to 800 nm wavelength and furthermore its step size (as small as 0.1 nm) can be controlled. This system is supported by a built-in stepping motor that can change the excitation or emission wavelength as desired (controlled by a computer using the "BenWin+" software application).

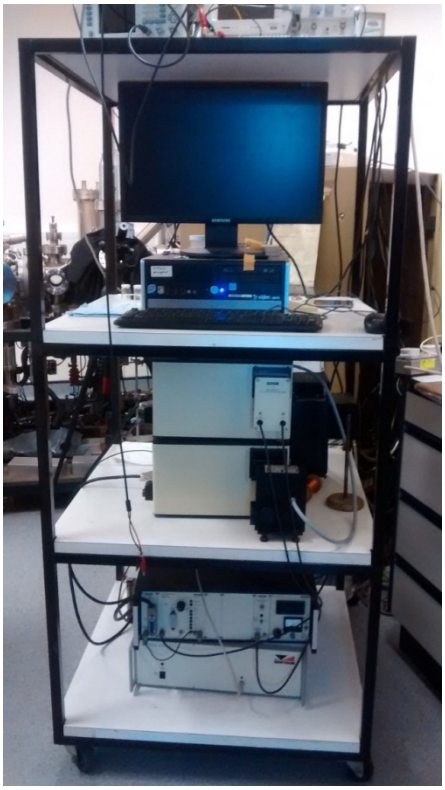

Figure 2.2: Bentham Integrating Sphere with M300 Monochromator

These instruments are very important in determining the true shapes of spectra emitted and excited from the phosphor. Although it does not have the ability to quantify the luminous efficacy and quantum efficiency of the spectra it produces, it is however

suitable for the detailed identification of any band-broadening of the spectra as well as quantifying shifts of the band position.

2.3 X-ray powder diffraction

X-ray powder diffraction (XRPD) is the most important method used to elucidate the actual crystal structure of a material. X-rays are created every time electrically charged particles, that have a certain level of kinetic energy, are instantly decelerated through impact. Generally, radiation is generated in a tube (x-ray tube) by applying an electric field between two metal based electrodes. Applying high voltage over the electrodes instantly draws out electrons that strike a point on the anode (target) with extremely high velocity, generating heat and a small percentage of X-rays. These X-rays are then used to investigate the crystal structure of materials, where in accordance with Bragg's law; several conditions need to be fulfilled in the event that diffraction is to take place [2]. Figure 2.3 illustrates the concept of Bragg's law which can be derived when parallel X-ray beams coincide and have their incident angles equal to the reflecting angles. In this situation, Beam 1 strikes the top surface of atom z and reflects at an angle θ, while Beam 2 hits atom B in the second layer also reflecting at the same angle (θ).

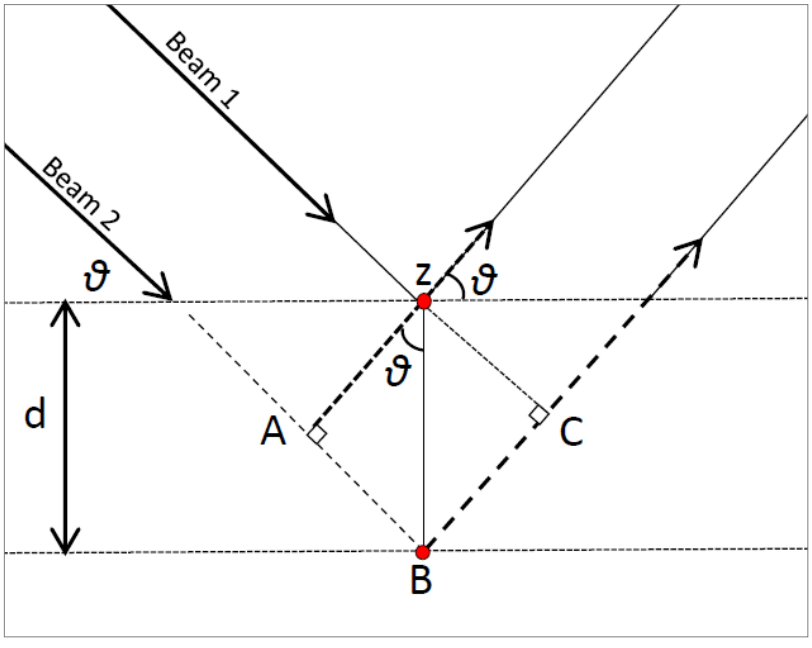

Figure 2.3: The concept of Bragg's law

From the image, it can be seen that the distance travelled by Beam 2 is longer than Beam 1 by (AB + BC) distance. This extra distance is expressed as an integral of the wavelength (nλ), therefore:

$$n\lambda = AB + BC \quad \textbf{Eq 2.1}$$

Since AB = BC, Eq 2.1 also can be expressed as:

$$n\lambda = 2AB \quad \textbf{Eq 2.2}$$

Using trigonometry, it is possible to relate the distance AB with the angle θ by equating the distance AB as equivalent to **d sine θ** as expressed by this modified Bragg's Law expression [2, 3];

$$n\lambda = 2\mathrm{d}\sin\theta \quad \textbf{Eq 2.3}$$

λ is the wavelength (m),
n is an integral / integer,
d is the lattice spacing (m),
θ is the angle of incidence (˚).

An X-ray diffractometer is used to record the positions of the diffracted x-rays. The instrument consists of an X-ray tube as the source of X-rays, a sample stage, and a detector to read the reflected beam. The X-ray beam is aimed at the sample at an angle of θ, while the detector located on the opposite side scans the intensity of the X-ray at 2 times the incident angle (2θ). The incident angle θ is gradually raised as the detector maintaining an angle of 2θ collects the diffracted signals and converts them to a unique pattern as shown in Figure 2.4.

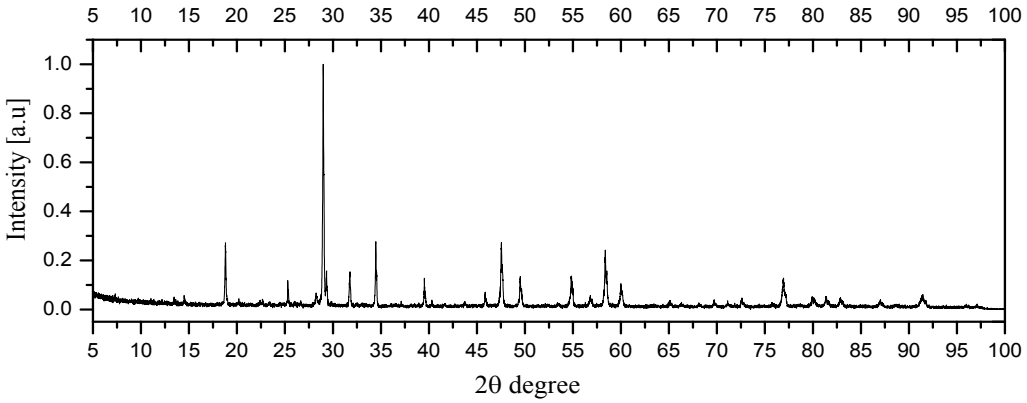

Figure 2.4: Example of XRPD diffracted pattern of $LiEu(WO_4)_2$ powder sample (normalized to 1)

The XRPD instrument employed in our lab is the Bruker Advance D8 which is fitted with a copper tube and a LynxEye detector (See Figure 2.5). To acquire an XRPD result, powder samples are placed and packed on the top of a cylindrical plastic holder which is then loaded into the instrument. Each powder sample is measured for 0.5 hours with rotational movement in an effort to minimize any preferential orientation which may arise from self-ordered crystals manifested in the powder measurement. Some data was recorded over longer timeframes (3 hours), with the purpose being to decrease the background noise and to have a very distinct pattern in comparison to the shorter measurement.

Figure 2.5: Bruker Advance D8 with copper tube and LynxEye detector used for XRPD analyses

There are three software packages used in characterizing the crystal structure of phosphors [4]:

I) DIFFRAC.SUITE MEASUREMENT CENTER is a software program that commands x-ray diffraction processes, measures and acquires_X-ray powder diffraction data as well as displaying all the information of the state of the Bruker Advance D8.

II) DIFFRAC.SUITE EVA is a software program used to identify the phases of the powder patterns acquired by the Bruker Advance D8. The phase identification process is performed by matching measured XRPD patterns against a database of published and verified patterns. This software is really helpful in giving an idea of the most likely phase(s) expected in a specific material. EVA also offers special features to convert x-ray diffraction data, measured in *. raw format, to a variety of preferable plotting formats (such as *.uxd); and additionally it facilitates their export and the matching data to an image format.

III) DIFFRAC.SUITE TOPAS is a computer based analytical software used to further analyse crystal structures. TOPAS helps users to fit a theoretical pattern to a measured pattern. It is also used to quantify multi-phase mixtures, estimate crystallite sizes, strain produced in the lattices, and the occupancy factors of various atoms. Its profile fitting analysis is based on the information obtained from DIFFRAC.SUITE EVA software in the form of a specific file (in *.cif format) which is matched against an online database called the Inorganic Crystal Structure Database (ICSD) [5].

A software program is needed in order to visualize structural models of synthesized compounds reported in this thesis. Visualization for Electronic and Structural Analysis (VESTA) software was used in visualization purpose as reported herein and it was obtained free of charged from its developer [6].

2.4 Scanning Electron Microscope

The human eye can capture objects with a dimension of approximately 0.1 mm at the optimum viewing distance of 25 cm. Human vision can be improved using optical microscopy, to view objects near to 2000 Å in dimension, elevating the importance of

microscopy in scientific research. In the 1980s, the use of electron microscopy started to progress due to the discovery that electrons can be deflected by a magnetic field. This finding has contributed to a new era of scientific research by enabling researchers to view particles at a higher magnification using a high-energy electron beam, thus replacing the conventional light source [7].

The scanning electron microscope (SEM) uses a targeted beam of high-energy electrons which produce a number of signals as it strikes the surface particles of its target. The signals which are created through interactions between the electron and the surface particles can reveal essential visual information related to the sample. This information includes the texture of the crystal surfaces, the particle/crystal shapes (also known as morphologys) and the orientation of material particles. SEM nowadays can also help researchers by providing information on the chemical composition of the targeted sample.

The SEM used, shown in Figure 2.6, is a Zeiss Supra 35VP with high-vacuum and variable operating pressure capabilities. To analyse the sample materials, a powder sample was dusted on the surface of double-sided carbon tape which was attached to an aluminium stub. The sample together with the carbon tape and aluminium stub were coated with gold to ensure the surface of the powder sample was electrically conductive to prevent the build-up of electrons on the sample surface, while allowing the charge dissipation along the carbon tape and stub. Only six samples can be placed at one time in the SEM chamber. Particle images can be seen once the correct magnification level, appropriate brightness and contrasts as well as other settings have been established. In the instance that electrons build up over a nonconductive surface area on the particles, the charge accumulated can result in divergence of the electron beam and could consequently affect the visual information received, necessitating the need to recoat the sample.

Figure 2.6: Zeiss Supra 35VP

2.5 ATR-FTIR Infrared Spectroscopy

Figure 2.7: Shimadzu Fourier Transform Infrared Spectrophotometer FTIR -8400S

Attenuated Total Reflectance – Fourier Transform Infrared Spectroscopy (ATR-FTIR) as seen in Figure 2.7 is a type of spectroscopy that relates to the spectrum collected in the infrared region of the electromagnetic spectrum and is dependent upon absorption spectroscopy. The output of the IR spectroscopy is a spectrum of infrared light transmittance (or it can also be in absorbance values) on the vertical axis versus frequency or wavenumber on the horizontal axis (in cm^{-1} units). An instrument that employs this technique is a Fourier transform infrared (FTIR) spectrometer with the FTIR used in this research being the Shimadzu Fourier Transform Infrared Spectrophotometer FTIR-8400S. $SrS:Eu^{2+}$ and $CaS:Eu^{2+}$ phosphors after ageing (which will be discussed further in Chapter 4) were measured to ascertain, if any formations of calcium carbonate ($CaCO_3$) or strontium carbonate ($SrCO_3$), due to reactions with atmospheric water and carbon dioxide, took place during the phosphors exposure to the atmosphere. The output from the FTIR represents the absorption or transmission of the infrared from the molecules, creating a distinctive molecular identity [8].

2.6 Speed mixer

The use of a speed mixer has not been mentioned in most literature articles on making phosphor powder through solid state reactions. The popular means of preparing phosphor powder via solid state reaction is straightforward and usually involves mixing all corresponding starting materials in stoichiometric ratios. The mixtures are subsequently ground using mortar and pestle until the materials are uniformly distributed. In the preparations section described in the following chapter a DAC 150 FVZ-K speed mixer (see Figure 2.8) was used to prepare phosphor samples. This mixer ensured that the powder materials synthesised through solid state reaction were completely uniformly distributed.

In this preparation, 5g of the starting materials, which had been mixed, were transferred into a special plastic container for the speed-mixing process. The container was then placed in the speed mixer and set to rotate at 2700 - 3000 rpm for 50 s before undergoing a subsequent firing process.

Figure 2.8: DAC 150 FVZ-K speed mixer

In the following Chapters, the outputs from the instrumentation mentioned in this Chapter will be presented and discussed. Furthermore, where appropriate, the errors on the measurements will be included to allow their accuracy to be assessed.

2.7 References

1. Bentham Instruments Ltd (16 July, 2014) Phosphor Quantum Efficiency (QE). http://www.bentham.co.uk/PhosQE.htm 1 August 2014.

2. B. D. Cullity (1978) Elements of X-RAY DIFFRACTION. *Addison-Wesley Series in Metallurgy & Materials*, University of Michigan.

3. Christopher Hammond (18 Feb 2010 (digitized)) The Basics of Crystallography and Diffraction. *Oxford University Press*, University of Michigan.

4. Bruker Corporation (2015) X-ray Diffraction DIFFRAC.SUITE™ Software package. https://www.bruker.com/products/x-ray-diffraction-and-elemental-analysis/x-ray-diffraction/xrd-software/overview.html 2015.

5. Royal Society Chemistry (2015) Inorganic Crystal Structure Database (ICSD). http://icsd.cds.rsc.org/search/basic.xhtml 2012-2015.

6. K. Momma and F. Izumi (2011) VESTA 3 for three-dimensional visualization of crystal, volumetric and morphology data, *Journal of Applied Crystallography*, 44, 1272-1276.

7. Weilie Zhou, Robert Apkarian, Zhong Lin Wang, David Joy (2007) Fundamental of Scanning Electron Microscopy (SEM). In: Anonymous Scanning Microscopy of Nanotechnology: Techniques and Applications, 1st edition edn. *Springer*, , pp 1-40.

8. A. Lungu, M. Lungu, A.Neculae, R. Giugiulan (2014) Nanoparticle Characterization Using Nanoparticle Tracking Analysis. In: Anonymous Nanoparticles' Promises and Risks, *Springer International Publishing,* , pp 245-268.

Chapter 3

Synthesis and Background of the Phosphors Studied in this Thesis

3.1 Introduction

This chapter introduces the need for red emitting phosphors for improving the current generation of white light emitting LEDs. Firstly the current demands and situations of LEDs will be explained before discussing a few approaches of how to generate white light using LEDs and colour converting phosphors. This will be followed by evaluating the problems with both the current LEDs in achieving the desired properties and also the cost and nature of the phosphors used. Finally, the background behind the red emitting phosphors studied in this thesis will be presented along with the synthetic methods to produce the phosphors.

3.2 Critical Supplies of Rare Earth Elements (REEs)

Within the last few years it has been apparent to both the Governments of the USA and the European Common Market countries that the rare earth elements (REEs) were becoming a critical resource. The concern is related to China's dominance in controlling 96 per cent of the total global supply of REEs. This situation puts the Chinese authorities in a powerful position to monopolize the market which could lead to price spikes, shortage of supplies, and trade manipulations which may affect many economic sectors. Due to this, the UK Government launched a report entitled 'Lanthanide Resources and Alternatives' to confirm the fact that REE shortages are predicted to happen in a few years [1]. China recently reported it had revised, with new complicated tariffs, the exporting of REEs (due to a new policy claiming to restrict illegal REE mining that affects the environment as well as to support their local industries), which in turn resulted in fierce price spikes worldwide [2]. The newly drafted policy has caused distress and anxiety to global REE industries

especially in European countries which have already been relying solely on Chinese supplies.

This continuing economic squeeze has led to an increased pressure on a plethora of industries and many academic research groups as well as government directives to undertake research to find the best ways to minimize the dependence on REEs in all associated industries, particularly in the displays and lighting sectors. Two of the many feasible approaches that can be considered are:-

(1) Ensuring the life span of present REE based phosphors that may be sensitive to the environment can be prolonged so the demands to replace them can be minimized. For that reason surface coating is probably a good way of protecting those phosphors which are known to be sensitive to humidity in warm environments. If this coating approach can offer good results it may become both a useful method of preserving the existing phosphor and at the same time offset some of the enormous demands on REEs.

(2) An alternative approach is to substitute REEs used as activators in phosphors with any other cheaper cations (could also be non-activating cations). If this approach was successful, it would be possible for manufacturers to reduce the cost of importing REEs and therefore reduce the dependency on them.

The outcome of these approaches, provided that the yield and the efficiency of the newly substituted materials is acceptable to specific displays or lighting applications, would mean that the new phosphor based lighting devices would not only be produced with less cost but could also be friendlier to the environment. This preceding point is important as REE mining in China has been extremely unfriendly to the environmentcentnt

3.3 White Light from LEDs

The increased awareness of over-consuming energy and the subsequent consequences continue to pile pressure on an already constrained world energy infrastructure [3, 4]. Conventional incandescent and fluorescent lamps rely on gases or heat discharging processes which are associated with large energy losses due to a number of factors including the need to generate high temperatures during an operation [3]. This trend has led to new on-going research in generating light emission from the p-n junction of light emitting diodes (LEDs) that originated in the 1950s. LEDs are devices that can efficiently

convert electrical energy to light. The emergence of bright-blue LEDs started in the 1990s, after the discovery made by Nakamura, and became a turning point in the utilisation of solid-state lighting products in numerous applications. Phosphors have been frequently used as a means of generating white light by downconverting UV or blue light emitted from an LED to longer wavelengths (to the desired colours depending on applications) or even broader wavelengths such as white light. The application of white light emitting diodes (WLEDs) is increasing all around the world and appears to be overtaking previous generations of lighting devices such as incandescent, halogen and xenon lighting [5]. The impact of research works on WLEDs has been recognized globally as the Nobel Prize in Physics 2014 was awarded to Isamu Akasaki, Hiroshi Amano and Shuji Nakamura for their contributions on highly efficient blue light-emitting diodes [6, 7].

3.4 RGB and Phosphor Converted LEDs

The interest in WLEDs has grown in accordance with expectations over the last 15 years. As European directives have phased out incandescent light bulbs in favour of fluorescent and other forms of more efficient lighting, the future domestic market for WLED lighting has become huge. Phosphor Converted -White Light Emitting Diodes (pc-WLEDs) are now regarded as cost-effective and are commonly used in commercial lighting and display applications. They can display a colour point which is dependent on the type, thickness, and packaging of the phosphor layer.

There are two common approaches in generating white light using LEDs. These approaches are selected depending on the purpose and application of the lighting due to the fact that there is a trade-off between the colour rendering index (CRI) and luminous efficacy as discussed in Chapter 1.

The first approach combines blue, green and red LEDs in one package. The drawback of this approach is that the different colour LEDs age differently so the white emitted white light can take on a hue depending on the ageing LEDs. Combining three coloured LEDs can provide good luminous efficacy because there is no quantum deficit as no phosphors are used to down convert the LED emissions. However, there are some serious drawbacks in this approach when RGB LEDs emit a poor quality Colour Rendering Index (CRI) as a result of their narrow emission wavelength ranges as illustrated in Figure

3.1. LEDs manufactured from this method offer flexibility but require complicated setups to satisfy sufficient levels of red, green, and blue light that have to be appropriately maintained as a result of several factors such as the current applied, temperature, as well as operating period [8].

The second approach employs one or more colour converting phosphors with either a blue or a UV emitting LED. There are a number of different approaches to achieve white light by this method as outlined by J. Silver and R. Withnall e*t. al* [9] and these are discussed further below:

1) pc-WLED that consists of two colour conversion phosphors
2) pc-WLED that consists of a blue LED and one colour conversion phosphor
3) UV LED with three colour conversion phosphors.

In method one, green and red emitting phosphors are used because of their capability to produce wide emission ranges, hence the CRI is greater than the RGB method. There is however a quantum deficit association due to the colour conversion from the blue light to green and red through two different phosphors. Method two is achieved by having pc-WLEDs comprised of a blue LED and one yellow-emitting phosphor. This technique involves only one phosphor that can cover a broad wavelength range within the orange-yellow area. However, its emission does not cover the complete region of red and blue, therefore the maximum CRI achievable is 80%. Despite the CRI being lower than that attained by a combination of two phosphors (red and green), its luminous efficacy is better than method one considering that the quantum deficit is less as energy loss in converting light here involves only one phosphor. As a result pc-WLEDs having a single phosphor do not possess the highest CRIs and as such have not become a sustainable popular choice as a substitute for conventional fluorescent lights in producing general white light. However, they have ongoing niche applications, e.g. for automotive industries. Finally, method three makes white LEDs by combining three phosphors (red, blue and green) to convert UV light from the LED. The presence of three different colour points of phosphors leads to a very good CRI but in return it also loses its luminous efficacy (in fact the worst luminous efficacy out of the all approaches) due to the combined quantum deficit effect on using the three phosphors.

From the approaches mentioned above, all of the methods are related to this work (although method two does not use red phosphor but red element is needed to enhance the CRI) and their results will be discussed in the next chapters.

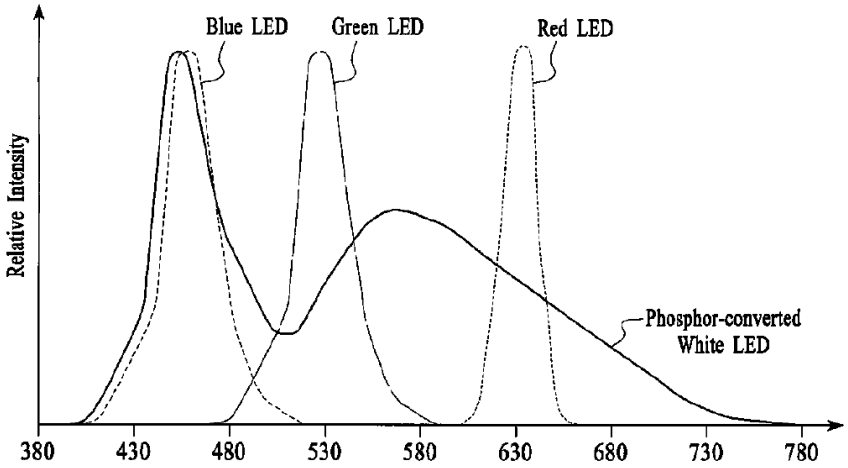

Figure 3.1: Comparison of colour gamut between RGB LED and PC-LED [10]

Pc-WLEDs are now a major force in the market and as the colour converting phosphors improve they are expected to dominate the domestic lighting market, replacing the older fluorescent and halogen lamps. They also provide a few other additional advantages over the traditional types of lighting in addition to their high power efficiency and luminous efficacy attributes. These are their long working life spans and the need for little maintenance other than end of life replacement. The latter is much longer than the other traditional light sources. As LEDs are point light sources this attribute can also make them preferable in areas where focussed light is required. In addition, they have zero mercury content as opposed to fluorescent lamps [11] so they are more environmentally friendly and their efficiency increases dramatically within a very short time span [12]. Until now, despite pc-WLEDs being popular in the commercial and niche markets of the lighting industry, they have struggled in the domestic market. This is due to a number of factors but it is principally cost. The cheapest LEDs are based on a blue emitting LED and a single yellow emitting phosphor therefore if an efficient and cheaper red phosphor could be included to improve the CRI it would be a force in the domestic market.

3.5 Red Phosphors for use in PC-WLED

As discussed in section 3.4, phosphors (such as yellow and green) can be excellent candidates to be employed as colour converters for LEDs however, the serious issue with

these phosphors is their restricted output in the red spectral range which limits the pc-WLEDs performance to cool white light application with correlated colour temperature ranged between 4000 to 8000 K, and poor CRI value less than 75 [9, 13]. Consequently there is a growing need to determine whether pc-WLEDs can become suitable lighting devices in line with the sensitivity of the human eyes and of course with more desirable luminous efficacy in the red spectral region. To facilitate the red element in pc-WLEDs, the use of adding red emitting phosphors to the yellow and/or green phosphors appears to be the right solution to improve the spectral emission and change from cool to warm white light. The role of the red emitting phosphor in providing better CRI inside a pc-WLED is illustrated in Figure 3.2. The type of red phosphor to be used depends on the spectral peak position and also the width of the colour point emitted from the selected phosphors [13]. Currently there are limited numbers of red-emitting phosphor materials that happen to be suitable for pc-WLED applications. Despite the contribution of these materials in facilitating a red colour point for the pc-WLEDs they also have several weaknesses which require further attention.

Examples of the materials which have weaknesses are $SrS:Eu^{2+}$ and $CaS:Eu^{2+}$ as they are both sensitive to degradation in humid environments (their accelerated ageing studies will be discussed in Chapter 4) and have poor thermal characteristics (their emission falls off badly as the temperature increases). Thus the introduction of metal sulfide based host lattice phosphors as red emitters are only an option in remote screens to overcome the temperature problems and as mentioned there are still chemical stability questions when exposed to moisture as they decompose to carbonates or sulphate lattices that do not exhibit the desired original luminescence [14]. Further examples are metal nitride and metal oxy-nitride based red emitting phosphors which are expensive and difficult to make as they require very high temperatures and are often non-stoichiometric leading to poor reproducibility.

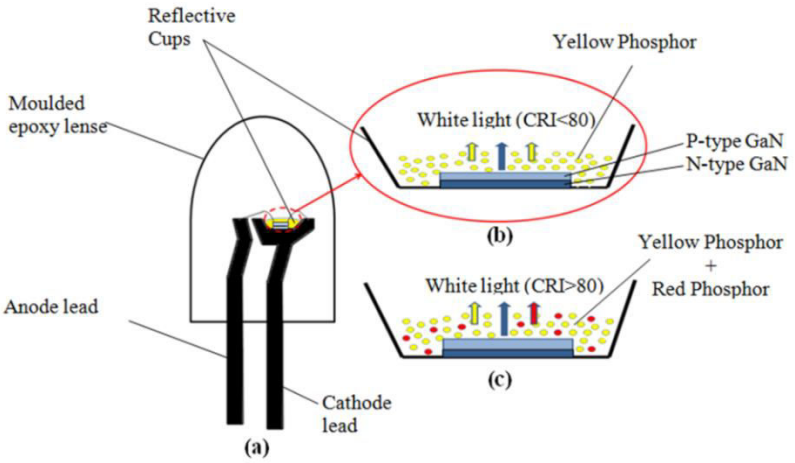

Figure 3.2: Schematic structure of (a) UV LED and (b) YAG:Ce yellow phosphor in the reflective cup that covers the LED chips (c) YAG:Ce phosphor with presence of red phosphor.

There are other red phosphors presently in the market for other applications such as Eu^{3+} doped Y_2O_3 or $Y_2O_2S:Eu^{3+}$ but these types of phosphors are also chemically unstable as well as their lifetimes and efficiencies not being satisfactory [15]. Therefore, further research for a stable, cost-efficient, inorganic, rare earth based red phosphor with high absorption in the near-UV/blue spectral region has become essential. To date, all the colour converting phosphors contain rare earth element (REE) activators. This is a major problem as the REEs are expensive and the supplies are governed by trading policies. Using less rare earth elements is thought to be a useful approach for reducing the costs of the phosphors, but this requires new efficient phosphors to be developed. Possible alternative red emitting phosphor solutions that have been suggested are now discussed below, but they are rich in Eu^{3+} and need to be modified.

3.6 Tungstate $(WO_4)_2^{-2}$ and molybdates $(MoO_4)_2^{-2}$ Based Phosphors

The prospect of tungstate / molybdate phosphors was first recognized in 1903 by Hammer with systematic research on its luminescent properties investigated 55 years later by Harrison and Hummel [16]. Since then the interest on these two materials has rapidly increased especially from the 2000s until now. The two classes of phosphor materials have excellent attributes in several areas including optical fibres and scintillators due to their interesting luminescent properties [17]. Tungstates and molybdates with europium (III) activators for example are claimed to be chemically stable and are viewed as excellent host lattices that come with broad absorption in the UV region and they emit very well in the

red region [18] enabling them to fulfil the demand for high-quality red phosphors for LEDs. [17, 19-59] However, no research had been done on the efficacy measurements up to the time of our work [47].

3.6.1 Crystal Structure of $LiEu(WO_4)_2$

The crystal structure of $LiEu(WO_4)_2$ has long been debated since the 1970s until now. Initially P. Klevtsov and R. Klevtsova [60] described the structure as a polymorphic between the tetragonal ($I4_1/a$) to the monoclinic (P2/c). The description was based on samples prepared via solid state reaction. However, in 2007, Chiu [61] prepared the materials again through a solid state reaction and suggested that the actual crystal structure was triclinic with space group $P\bar{1}$. This claim was rejected by K. Hwang, *et. al* [47] in 2009 and J. Postema, *et. al* (2011) [55] when they produced the materials via sol-gel method and solid state reactions respectively. Both described the crystal structure of the material as tetragonal with space group $I4_1/a$. The x-ray diffraction pattern published by Postema is shown in Figure 3.3 and the data is detailed out in Table 3.1. This ambiguous crystal information has also been discussed by J. R. de Moraes *et. al* [62] who also decided to choose the tetragonal structure (scheelite structure) type $I4_1/a$.

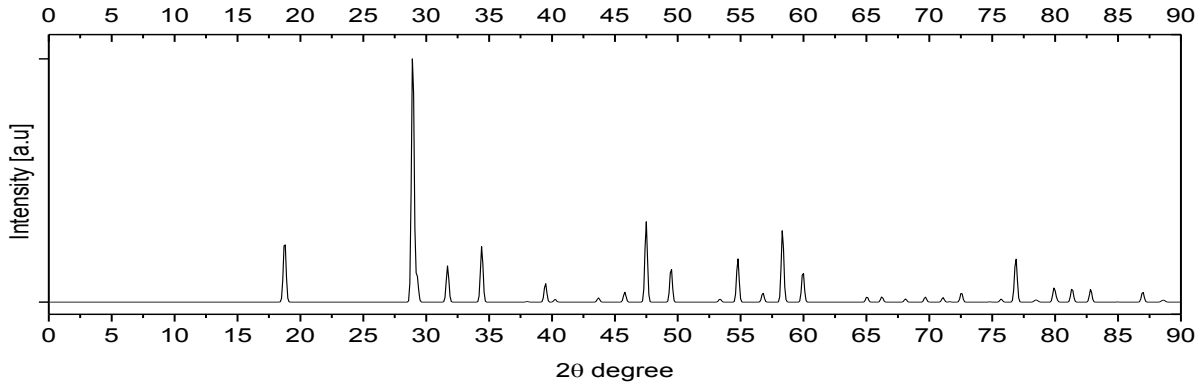

Figure 3.3: XRPD pattern of $LiEu(WO_4)_2$ as described by Postema et al[55] (ICSD collection code 261832) .

Table 3.1: Refined crystallographic data of $LiEu(WO_4)_2$ as outlined by Postema [55]

Type	Tetragonal	*x*	0.7476(8)
Space group	$I4_1/a$	*y*	0.5937(9)
a (Å)	5.21198(6)	*z*	0.0374(4)
c (Å)	11.2886(1)		Bond Distances (Å)
Li/Ln[b] (4*a*)	(0,1/4,1/8)	W-O	1.849(4) × 4
W (4*b*)	(1/2,3/4,1/8)	Li/Eu-O	2.397(4) × 4
O (16*f*)	(x,y,z)		2.423(4) × 4

Postema in the same report explained that the Li^+ and Eu^{3+} cations in scheelite are surrounded by eight O^{2-} ions. Therefore, the oxygen ions surround Li/Eu in eight coordination and W^{6+} in tetrahedral coordination. The XRPD powder data published by Postema in the ICSD was used as a reference in the next chapters and the modelled structure of this compound is shown in Figure 3.4. Although the crystal structure of $LiEu(WO_4)_2$ has been addressed by a number of reports including Postema, none of them came from the single crystal analysis.

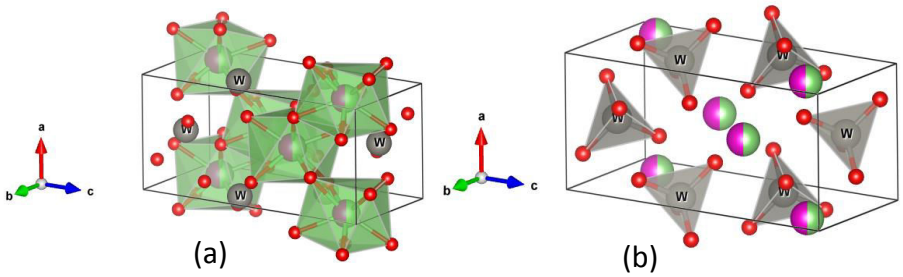

Figure 3.4: Scheelite modelled structures of $LiEu(WO_4)_2$ as viewed by Postema [55] that show (a) eight oxygen ions surrounding Eu/Li cations and (b) the tetrahedral shape of isolated $(WO_4)^{2-}$ in a lattice.

3.6.2 Crystal Structure of $LiEu(MoO_4)_2$

Double molybdates $ALn(MoO_4)2$ (A = alkali metal ions; Ln = trivalent rare earth ions), are known to possess excellent thermal stability and also to be stable to moisture which makes them good candidates to become excellent red phosphors [15]. Similar to the double tungstate structure, $LiEu(MoO_4)_2$ has also been reported to have tetragonal structure with space group $I4_1/a$ [17, 27, 52, 59, 63-66]. From this structure, Li^+ and Eu^{3+} are both eight-coordinated sites whereas Mo^{6+} occupies on four-coordinated sites. The specific crystallographic data of $LiEu(MoO_4)_2$ was found twice: once by Chiu [61] claiming it to be triclinic $P\bar{1}$ (which was rejected for the same reason as explained in section 3.6.1) and the second latter structure came from a single crystal analysis made by Schwung [67] as can be

seen in Table 3.2. However, Schwung did not provide details on the bond distances of the refined lattice nor published in the ICSD database for further reference.

Table 3.2: Crystallographic data of $LiEu(MoO_4)_2$ as refined by Schwung [67]

Type	Tetragonal
Space group	$I4_1/a$
a (Å)	5.2031(7)
c (Å)	11.343(7)
R	1.76%
$F_o>3\sigma$	176
Refines total	327

3.6.3 Crystal Structure of $LiEu(MoO_4)(WO_4)$

There are only a small number of articles that can be found discussing on combining both W^{6+} and Mo^{6+} in the same host with Eu^{3+} activators. Previous studies on europium doped tungsto-molybdate reported that the structure is similar to europium doped molybdate or tungstate (tetragonal structure with space group $I4_1/a$) [52, 68, 69].

3.7 Crystal Structure of $Li[Y/Gd/Al](MoO_4)_{2-y}(WO_4)_y$

3.7.1 Crystal Structure of $LiY(MoO_4)_{(2-y)}(WO_4)_y$

As explained above it is already known that the crystal structure of $LiEu(WO_4)_2$ is confirmed to be tetragonal with space group $I4_1/a$. On the other hand, if Eu^{3+} is gradually replaced by Y^{3+} ions then the structure of the materials is believed to have changed. There were a number of studies reporting the crystal structure of $LiY(WO_4)_2$. J.S. Kim *et. al.* [70] in 2006 performed an XRPD refinement on the compound they made and they reported that the structure of $LiY(WO_4)_2$ made from a ceramic process is tetragonal with space group P2 with all lattice parameters and related bond lengths provided in the article (see Table 3.3). The claim was supported by Glorieux [52] five years later who found that the material belongs to the same crystal structure. However, slightly different results were obtained in the same year by Postema *et. al* [55] who reported that although the crystal structure is monoclinic its space group is P2/n (with an *n* glide transition) as seen in Table 3.4, leading them to reject the possibility that the structure was just P2. This compound was made through a solid state reaction process and calcined at 800˚C for 19 hours.

Meanwhile the crystal structure of $LiY(MoO_4)_2$ has also been described by Kolitsch, [71] in a single crystal analysis of the sample, to be tetragonal $I4_1/a$ as shown in Table 3.5. Although this scheelite structured phosphor is reported excellent, the biggest concern is its high concentration of Eu^{3+} that makes the phosphor so expensive. In a program of work initiated over the last five years in Wolfson Centre's laboratories, the possibility of reducing the amount of Eu^{3+} cations has been worked out by replacing it with less expensive non-activating cations, the first reported was using Y^{3+} [47].

The work reported herein again will be on the effect of substituting Eu^{3+} with trivalent cations. To begin with, the work started with Y^{3+} as it is chemically identical to Eu^{3+}. Furthermore, the ionic radius of Y^{3+} for the eight coordination numbers of Y^{3+} is 1.019 Å which is slightly smaller than the size of Eu^{3+}1.066 Å. Therefore, it is expected that Y^{3+} can easily replace Eu^{3+} ions and simply settle down in the scheelite crystal lattice. There were some interesting works on the use of Y^{3+} in scheelite structured phosphor by previous researchers. The study on the effect of Y^{3+} to replace Eu^{3+} was first carried out by Zaushitsyn *et, al* [25] in 2005 and the phosphor samples with formula $LiY_{1-x}Eu_x(MoO_4)_2$ (x = 0.0005, 0.001, 0.01, 0.05, 0.1, 0.5, 1) were prepared through a conventional ceramic route process with them finding that $LiY_{0.5}Eu_{0.5}(MoO_4)_2$ offered the highest luminescence intensity. The result of their work appeared to be reaffirmed by the findings of a study conducted 4 years later by Xie An et. al,[68] who analysed $LiEu_{1-x}Y_x(WO_4)_{0.5}(MoO_4)_{1.5}$ where x=0 to 0.8 and it was discovered that the highest relative intensity can be spotted when the amount of Y^{3+} reaches 0.5 mol %, meaning that the strongest emission peak occurs when 50 percent of the initial concentration of Eu^{3+} had been replaced with Y^{3+}. However, there seemed to be a discrepancy on the explanation of why $(WO_4)^{-2}$ and $(MoO_4)^{-2}$ were set at a 1:3 ratio. On further investigation into the references we could not find any concrete evidence showing this ratio can provide the best luminescence intensity among other ratios [61]. In 2012, Xianju *et, al.* [72] analyzed the presence effect of both Eu^{3+} and Y^{3+} on the luminescence emission of $LiY_{1-x}Eu_x(MoO_4)_2$. However, they only set Eu^{3+} to be from 0.01 to 0.1 which was therefore unable to provide any evidence on its effects to the whole series from x=0 until x=1. Apart from the results obtained to answer the effect on the luminescent intensity of the spectra emitted by the phosphor there was no description of the luminous efficacy in their work.

Table 3.3: Refined crystallographic data of $LiY(WO_4)_2$ as outlined by Kim [70].

		Atom	x	y	z	Occupancy
Material	$LiY(WO_4)_2$	Li(1)	0.00(-)	0.3754(0)	0.00(-)	0.61(5)
Type	Monoclinic	Li(2)	0.50(-)	0.8667(12),	0.50(-)	0.375(5)
Space group	P2	Y(1)	0.00(-)	0.7898(0)	0.50(-)	0.50(-)
a (Å)	9.9815(5)	Y(2)	0.7262(12)	0.3929(65)	0.00(-)	0.50(-)
b (Å)	5.7913(3)	W(1)	0.2406(12)	0.2737(67)	0.4938(25)	1.00(-)
c (Å)	5:0058(2)	W(2)	0.7262(12)	0.9098(65)	-0.0044(21)	1.00(-)
β (˚)	94.2158(2)	O(1)	0.1416(8)	0.1457(67)	0.7930(20)	1.00(-)
R_{wp} (%)	8.65	O(2)	0.1533(10)	0.9552(64)	0.3040(20)	1.00(-)
R_p (%)	6.35	O(3)	0.8891(10)	0.4448(59)	0.6516(24)	1.00(-)
		O(4)	0.1366(11)	0.7055(65)	0.8581(30)	1.00(-)
		O(5)	0.6534(11)	0.1766(62)	0.7939(24)	1.00(-)
		O(6)	0.6267(8)	0.9895(64)	0.2646(19)	1.00(-)
		O(7)	0.6504(10)	0.4617(65)	0.3563(2)	1.00(-)
		O(8)	0.6161(13)	0.7036(59)	0.8330(2)	1.00(-)
Bond Distances (Å)						
Li1-O1	2.25(3) × 2	Y1-O1	2.84(2) × 2	W1-O1	2.00(3)	
Li1-O3	2.034(12) × 2	Y1-O2	2.11(2) × 2	W1-O2	2.23(5)	
Li1-O4	2.48(3) × 2	Y1-O3	2.43(4) × 2	W1-O3	1.75(3)	
Li1-O5	2.72(5) × 2	Y1-O4	2.225(17) × 2	W1-O5	1.93(2)	
Li1-O6	1.93(3) × 2	Y2-O5	2.28(3) × 2	W1-O6	2.38(4)	
Li1-O7	2.90(7) × 2	Y2-O6	2.93(4) × 2	W1-O7	1.68(4)	
Li1-O8	2.17(4) × 2	Y2-O7	2.279(16) × 2	W2-O1	2.12(4)	
		Y2-O8	2.33(4) × 2	W2-O2	2.009(17)	
				W2-O4	1.91(4)	
				W2-O5	1.96(4)	
				W2-O6	1.790(20)	
				W2-O8	1.78(4)	

Table 3.4: Refined crystallographic data of $LiY(WO_4)_2$ as described by Postema [55]

Type	Monoclinic	W (4*g*)	*(x,y,z)*	O3 (4*g*)	*(x,y,z)*	Bond Distances (Å)	
Space group	P2/n	*x*	0.0171(1)	*x*	0.1185(8)	W–O1	1.840(7)
a (Å)	9.9932(1)	*y*	0.1824(1)	*y*	0.084(1)	W–O2	1.798(8)
b (Å)	5.79743(7)	*z*	0.2522(1)	*z*	0.960(2)	W–O3	1.924(8)
c (Å)	5.00639 (7)	O1 (4*g*)	*(x,y,z)*	O4 (4*g*)	*(x,y,z)*		2.268(8)
β (deg)	94.1992(8)	*x*	0.1136(8)	*x*	0.10245(8)	W–O4	1.995(7)
Li (2f)	(1/4,y,3/4)	*y*	0.620(1)	*y*	0.892(1)		2.120(7)
y	0.230(5)	*z*	0.889(1)	*z*	0.457(2)	Li – O1	2.75(2) × 2
Ln (2e)	(1/4,y,1/4)	O2 (4*g*)	*(x,y,z)*	R wp (%)	7.47	Li – O2	2.16(1) × 2
y	0.6978(3)	*x*	0.1384(8)	R p (%)	5.61	Li – O3	1.94(1) × 2
		y	0.084(1)	X^2	2.08	Li – O4	2.80(2) × 2
		z	0.408(1)			Y – O1	2.231(8) × 2
						Y – O2	2.328(8) × 2
						Y – O3	2.928(8) × 2
						Y – O4	2.178(7) × 2

Table 3.5: Refined crystallographic data (single crystal) of $LiY(MoO_4)_2$ as described by Kolitsch [71]

Type	Tetragonal			Bond Distances (Å)	
Space group	P2/n			(Y,Li) - O × 4	2.3901(16)
a (Å)	5.148(1),			- O × 4	2.4023(17)
b (Å)	5.148(1)			(Y,Li) – O	2.396
c (Å)	11.173(2)			(Mo - O) × 4	1.7788(16)
Volume ($Å^3$)	296.11(10)				
Crystal dimensions (mm)	0.08 × 0.08 × 0.08				
Displacement parameters	***x***	***y***	***z***		
(Y,Li)	0.0	0.25	0.625		
Mo	0.5	0.75	0.625		
O	0.2535(3)	0.5949(3)	0.53935(15)		

3.7.2 Crystal Structure of $LiGd(MoO_4)_{2-y}(WO_4)_y$

The next focus is to look on the effect of swapping Eu^{3+} with Gd^{3+} in the lattice. This will be another interesting work to be studied as the Gd^{3+} element is of similar size to Eu^{3+}. (Europium with eight coordination number in $LiEu(WO_4)_2$ has ionic radius 1.066 Å, whereas atomic radius for Gd^{3+} with the same coordination number is slightly smaller (1.053 Å). From our literature research, we have found 2 literatures related to the photoluminescence properties of this phosphor and its correlation between the Eu^{3+} and Gd^{3+} in $LiEu_{1-x}Gd_x(MoO_4)_{2-y}(WO_4)_y$. Yi *et. al,* [73] in 2010 studied the photoluminescence effect associated with the increasing function of Eu^{3+} in the $LiGd_{1-x}(MoO_4)_2:Eu_x$ phosphors. They discovered that the greatest luminescence was when x=0.30 and there was a quenching effect resulting from further addition of Eu^{3+}. Even so the complete connection between Eu^{3+} and Gd^{3+} was unforeseen because they constrained the amount, x from 0 to 0.35 mol %. Li *et. al* [74] in their very recent publication did not agree with Yi

plus they explained that the amount of Eu^{3+} in their experiment on $LiGd_{1-x}Eu_x(MoO_4)_2$ (x=0.01-1) experienced a big effect to the luminescent properties. Li also did not witness any concentration quenching effects through the research carried out. In addition to that, none of the articles documented on the luminous efficacies in the function of increasing Gd^{3+}. Due to that reason, further research on $LiEu_{1-x}Gd_x(MoO_4)_{2-y}(WO_4)_y$ needs to be carried out as well as to response to the discrepancy from the literatures.

The crystal structure details of $LiGd(WO_4)_2$ were found in Postema's article describing the material belonging to space group $I4_1/a$ (see Table Table 3.6) whereas the closest crystal information of $LiGd(MoO_4)_2$ was found in an article written by Rico *et. al* [75]. Rico in 2006 performed a single crystal analysis on $LiGd(MoO_4)_2$ doped with ytterbium and it was found that the crystal structure was tetragonal belonging to the space group I4 with two non-equivalent sites being occupied by the dopant (See Table 3.7). Eight years later Linlin *et. al* [76] suggested that the crystal structure was tetragonal with space group $I4_1/a$. However, only lattice parameters were shown in the article and no margin of errors were provided by the authors as seen in Table 3.8. None of the articles found in relation to the crystal structure of $LiGd(MoO_4)_2$ were published in the ICSD database for further refinement analysis.

Table 3.6: Refined crystallographic data of $LiGd(WO_4)_2$ as outlined by Postema *et. al* [55]

Type	Tetragonal	*x*	0.7500(7)
Space group	$I4_1/a$	*y*	0.5914(8)
a (Å)	5.19904(5)	*z*	0.0372(3)
c (Å)	11.2537(1)	Rwp (%)	6.13
Li/Ln[b] (4*a*)	(1/2,3/4,1/8)	Rp (%)	4.72
W (4*b*)	(1/2,3/4,1/8)		
O (16*f*)	(x,y,z)		

Table 3.7: Refined crystallographic data of $LiGd_{0.936}(MoO_4)_2Yb_{0.064}$ as described by Rico *Rico et. al* [75]

Type	Tetragonal
Space group	$I\bar{4}$
a = b (Å)	5.1814(10)
c (Å)	11.285(3)
Volume ($Å^3$)	302.98(11)
Crystal size (mm)	0.20 × 0.20 × 0.10

Table 3.8: Lattice parameters of $LiGd(MoO_4)_2:Eu_{0.15}$ as described by Linlin *et. al* [76]

Type	Tetragonal
Space group	$I4_1/a$
a = b (Å)	5.1875
c (Å)	11.3300
Volume (Å^3)	304.89

3.7.3 Crystal Structure of $LiAl(MoO_4)_{2-y}(WO_4)_y$

Apart from Y^{3+} and Gd^{3+} being selected as potential candidates in replacing Eu^{3+}, aluminium (III) was also set as another choice of possible cation to replace Eu^{3+}. The incorporation of Al^{3+} was motivated from an interesting discovery established in previous work by Roni Stone [77] in the same laboratory. It was discovered that there exists an infusion (or possibly a vaporization) of europium (III) activators belonging to the tungstate-molybdate phosphor inside the body of an alumina crucible when heated at high temperature. Therefore it would be an interesting experience to learn and examine more about any potentiality the aluminium cations can offer when adapted with red phosphors.

The ionic radius of Al^{3+} is 0.535 Å (at its maximum of 6-coordination) as compared with that of Y^{3+}, Gd^{3+} and Eu^{3+}. The trivalent ions that are nearly half-size ratio to Eu^{3+} is expected to be an 'easy' candidate to successfully replace vacant sites left by Eu^{3+}. However, since the ionic radius of Al^{3+} is very small and can only make up a maximum of 6 coordination's (compared to Eu^{3+} with 8 coordination's in the phosphor) it is possible for the compound to change its crystal symmetry when Al^{3+} cations are incorporated. Also, little is known from previous studies describing the crystal structure of pure $LiAl(MoO_4)_{2-y}(WO_4)_y$ compound. However, besides a report by Klevtsov and Klevtsova [60] over nearly 40 years ago who claimed that the crystal structure of $LiAl(MoO_4)_2$ was triclinic with space group $P\bar{1}$. However, full details about the crystal structure were not entirely disclosed, therefore it is worth analysing the crystal structure of the compound in order to find the correlation between the crystal structure and the related emission intensity. Although the symmetry of the crystal changes as the amount of Al^{3+} increases, it is still worthwhile to note the optimum point where the emission starts degrading. This is due to the fact that Al^{3+} ions sourced from Al_2O_3 starting materials are a lot more economical in comparison to Eu^{3+} found in Eu_2O_3. If there appears to be any useful effects benefited from using Al^{3+} in the phosphor host lattices this will certainly help reduce the necessary cost of producing red phosphors dramatically.

3.8 $CaS:Eu^{2+}$ and $SrS:Eu^{2+}$ Phosphors

Sulfide host lattice phosphors such as $CaS:Eu^{2+}$ and $SrS:Eu^{2+}$ are among red phosphors that absorb strongly in the blue region. This attribute makes them more useful phosphor candidates for improving the colour rendering. However, there are two main drawbacks of these phosphors which are (1) their chemical instabilities towards moisture and (2) inability to emit luminescence at high temperatures due to the thermal quenching effect. Their instability due to moisture results in degradation of these phosphors as a function over time with more issues found when the phosphors are applied to LED chips that have high junction temperatures (up to 200°C), although this problem is removed when the phosphors are used on remote screens when they operate at temperatures close to ambient. In order to assess the effect of relative humidity and temperature on the loss of colour conversion performance of the $CaS:Eu^{2+}$ and $SrS:Eu^{2+}$ phosphors, their ATR-FTIR spectra have also been obtained so that the chemical changes of the sulfide lattices could be monitored spectroscopically as the degradation of the phosphors proceeded. All of the results from this work will be explained further in Chapter 4.

The $CaS:Eu^{2+}$ phosphor was coated with Al_2O_3 by atomic layer deposition in order to protect the sulfide lattice from moisture. The coating was studied using scanning electron microscopy (SEM) to assess the thickness of the coated layer and the PL intensities of the coated and non-coated phosphors have been compared to investigate whether any light emission is lost by applying the coating. Finally, the degradation of the Al_2O_3 coated $CaS:Eu^{2+}$ phosphor has been monitored as a function of ageing over time in an environmental chamber set at 80% relative humidity and temperatures in the range of 50-80°C, in order to assess the effectiveness of protecting the phosphor from moisture with an Al_2O_3 coating.

3.9 Methodology

In general, experimentations in this project are divided into 2 main categories. Category 1 focuses on the sustainability at high humidity levels and temperature of $CaS:Eu^{2+}$ / $SrS:Eu^{2+}$ phosphors coatings. The second category involves searching for cost-effective and efficient phosphors by replacing Eu^{3+} cations in lithium europium tungstate / molybdate (or a combination of the two) with non-activating cations.

3.9.1 Temperature and Humidity Tests on $CaS:Eu^{2+}$ and $SrS:Eu^{2+}$

In order to confirm the chemical stability of alumina coating on phosphor with respect to a certain humidity level and temperature, a sample of $CaS:Eu^{2+}$ and $SrS:Eu^{2+}$ were placed in a humidity chamber. Both $CaS:Eu^{2+}$ and $SrS:Eu^{2+}$ samples were obtained commercially from Phosphor Technology. The $CaS:Eu^{2+}$ phosphor had also been coated with Al_2O_3 by atomic layer deposition with 2 different thicknesses; 400 cycles (40 nm thickness) and 100 cycles (10 nm thickness) by sending the samples to ALD NanoSolutions, Inc. for the coating process in order to protect the sulfide lattice from moisture. The coating was studied using scanning electron microscopy to assess the quality of the coated layer. Furthermore, the PL intensities of the coated and non-coated phosphors were compared to investigate whether any light emission is lost by applying the coating. Finally, the degradation of the Al_2O_3 coated $CaS:Eu^{2+}$ phosphor was monitored as a function of ageing time in an environmental chamber set at 80% relative humidity and temperatures in the range of 50-80 °C, in order to assess the effectiveness of protecting the phosphor from moisture with an Al_2O_3 coating. Environmental temperature and humidity effects on the luminescence of the phosphors were tested and the ageing test of $CaS:Eu^{2+}$ was performed in an A3665-Delta 190-40HS Design Environmental chamber and run for up to 192 hours with 80%RH and 80°C settings. The luminescence of the phosphors was later measured every 24 hours using Bentham spectrometers and excited at 450 nm. Scanning electron microscopy (SEM, Zeiss Supra 35VP), was used to characterize the morphology of the particles and coating layers before and after the exposure. All results are discussed in Chapter 4.

3.9.2 Incorporating Yttriium (III) / Gadolinium (III) / Aluminium (III) on $LiEu_{1-x}M_x(MoO_4)_{2-y}(WO_4)_y$

As explained previously, generating white lights by RGB technique can offer higher efficiencies. However, it is complicated due to the amount of red, green, and blue colour points needing to be properly managed because light as well as colour intensity has its own ageing effect based on the current passing through the devices, temperature, and also time [8]. Alternatively, white lights can possibly be produced by coating the LEDs with synthesized phosphors. One of the most common methods to synthesize red phosphor

is using solid state reaction which is a reaction process that occurs between powders in the solid state.

$LiEu_{1-x}M_x(MoO_4)_{2-y}(WO_4)_y$ (x=0, 0.15, 0.30, 0.45, 0.50, 0.65, 0.75, 0.85 and 1 , M = Al^{3+}, Y^{3+} and Gd^{3+} whereas y = 0, 1 and 2, were prepared by an in house procedure using a solid state reaction method. Lithium carbonate (BDH Chemicals), tungsten (VI) oxide 99.9% (Sigma Aldrich), yttrium oxide 99.99% (Andeke Materials Resource Ltd AMR), gadolinium oxide 99.99% (Ampere Industrie) molybdenum oxide (VI) ≥99.5% (Sigma Aldrich), europium oxide (Eu_2O_3), and aluminium oxide (BDH Chemicals, Brockmann Grade 1) were used as starting materials. The compounds were weighed stoichiometrically, mixed and ground together using a mortar and pestle for 30 minutes and then annealed at 750°C - 800 °C for 4 hours. The resulting phosphor powders were immersed and gently ground to facilitate removal from the crucible. This method was initially employed in making all phosphors in this study due to being cost-effective and simple [3].

There is one more method found in preparing molybdate / tungstate phosphors which is by sol-gel process as reported by H. Wu et al [47, 58] and Hwang et al.[47]. Despite the synthesizing method not being straight forward in comparison to solid state reaction, sol-gel method has been reported to produce smaller particles and better quantum efficiency due to less crystal defects compared to solid state reaction.

3.9.2.1 Improving solid state synthesis of phosphor

We will now move on to look at another important finding we had in getting better red phosphor using solid state reaction after making a modification to the traditional method. Employing solid state reaction using mortar and pestle is a time consuming and exhausting process. Beside the tiring grinding process, this method can also result in an inconsistency in the small sample being made. Firstly, the very light fine powder of starting materials could get spilled out from the mortar potentially causing stoichiometric imbalances to the sample. Secondly, grinding using the hands may cause inconsistency to the rate of grinding which would have an effect on the quality of the samples produced. Therefore, an improved method needs to be found in order to produce phosphor samples of a better quality and consistency throughout the whole series of experiments. After several

attempts to change the grinding method ended with no improvements, we eventually found a new way of preparing the samples by following the exact same steps taken in solid state reaction apart from the grinding operation which was completely removed and replaced with a speed mixer operation. All starting materials were mixed stoichiometrically and weighed to make a sample of 4 grams each. The mixture was then transferred into a polyethylene container and a small amount of acetone was added to the mixture to aid homogenization. The sample was then brought to the speed mixer and run at 2700 rpm for 50 seconds. After that the mixture was taken out and left to dry in the air for 3 hours. The dried mixture was calcined at 800°C for 4 hours and quenched to cool back down to room temperature. It was then ground again and placed into the furnace to undergo a calcination process at the same temperature for another 15 hours.

The most important finding that we experienced from the new synthesis method using the speed mixer was its consistency of producing the right body colour as that gave an indication that the phosphor was correctly synthesized throughout the series of experiments. The body colour of red phosphor made from this new method, as seen in Figure 3.5, looked more reddish and also more regularly distributed compared to the previous method. The phosphor compound synthesized using the speed mixer also produced better intensity if seen under 365 nm (see Figure 3.6) which indicated that the phosphor was better and more efficient. This new and simpler way of synthesis also yields higher luminous efficacy over traditional methods as can be seen in Figure 3.7. Phosphor powder made through the traditional solid state reaction produces patchy powder, making it very difficult to measure the emission spectra out of it, particularly if the powder was positioned wrongly under the spectrometer thus potentially resulting in a lower output. The new method seems to cause more effective reactions between precursors during the time of calcination process and as a consequence produces better luminescence intensity of the phosphor.

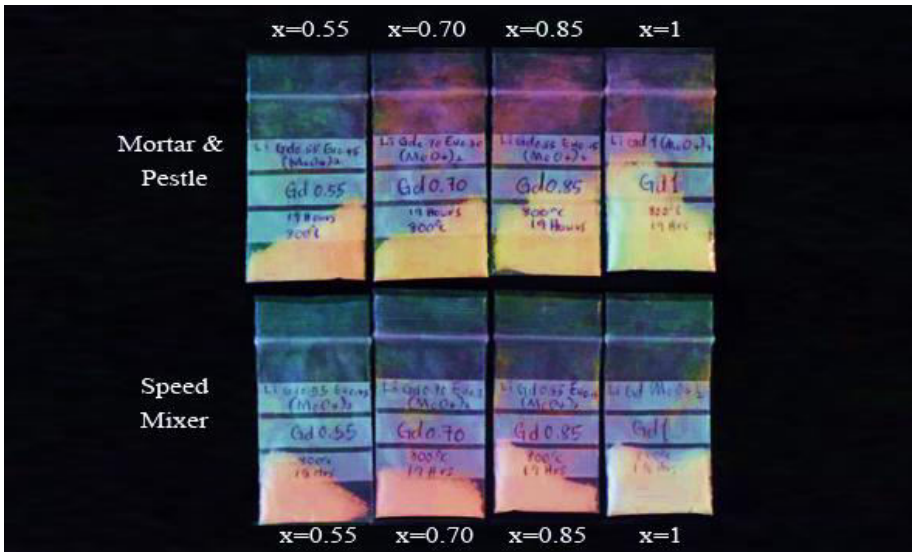

Figure 3.5: Body colour comparison of $LiEu_{1-x}Gd_x(MoO_4)_2$ [x=0.55,0.70, 0.85 and 1] prepared from solid state reaction using mortar and pestle and solid state reaction using speed mixer at 2700 rpm for 50 s.

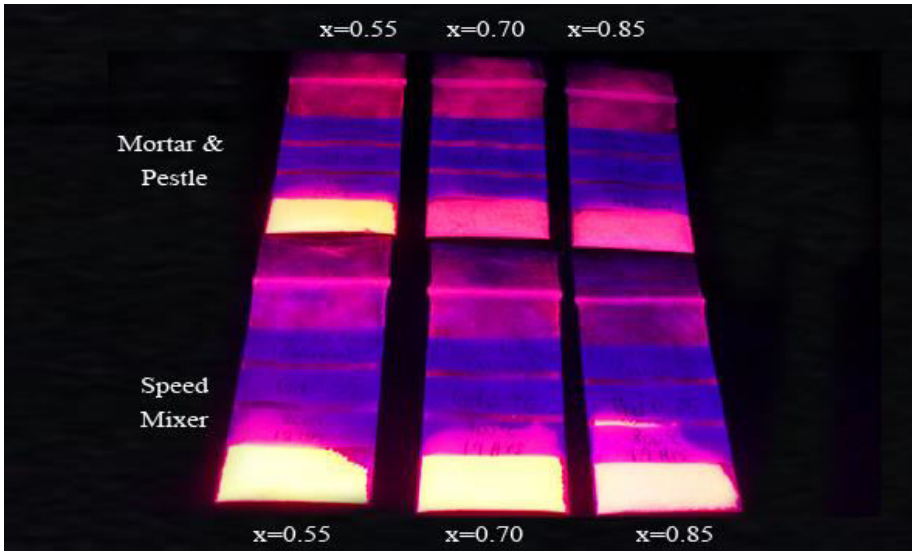

Figure 3.6: Red intensity comparison of $LiEu_{1-x}Gd_x(MoO4)2$ [x=0.55,0.70, 0.85 and 1] under 365 nm solid state reaction using mortar and pestle and solid state reaction using speed mixer at 2700 rpm for 50 s.

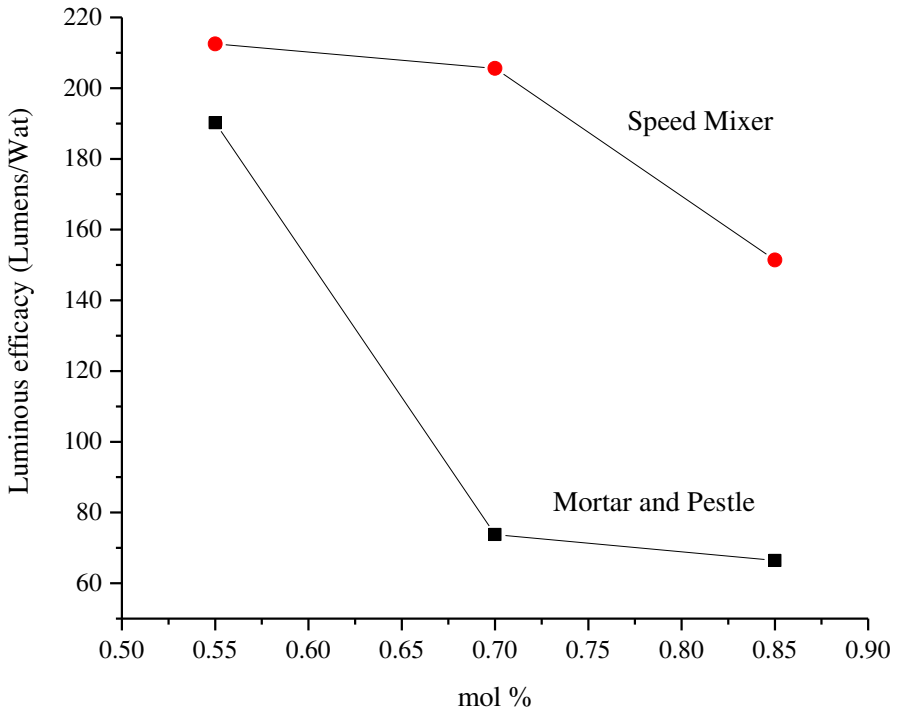

Figure 3.7: Comparison on the emission spectra and luminous efficacy between $LiEu(MoO_4)_2$ samples prepared from (a) solid state reaction using mortar and pestle and (b) solid state reaction using speed mixer at 2700 rpm for 50 s.

Due to the reasons mentioned above, solid state reaction using speed mixer was chosen for the entire synthesis activities in this thesis.

3.10 SEM images of $LiEu(MoO_4)_{(2-y)}(WO_4)_y$

SEM images of the three parent compounds; $LiEu(WO_4)_2$, $LiEu(MoO_4)_2$ and $LiEu(WO_4)(MoO_4)$ were viewed so that the structures and shapes of the particles can be compared and explained later with any excessive starting materials being quickly identified.

Figure 3.8 shows $LiEu(WO_4)_2$ particles that exhibit a mix of spherical and angular shapes from 1-12 µm size range. The particles coalesced forming lumps of larger structures. The particles also looked anisotropic due to distortions or elongations in unclear directions as the material grows, making the particles size irregular with a large range of sizes. Figure 3.9 and Figure 3.10 show $LiEu(MoO_4)_2$ and $LiEu(WO_4)(MoO_4)$ powder which appear to have similar shapes but with less adherence between the particles as compared to $LiEu(WO_4)_2$.

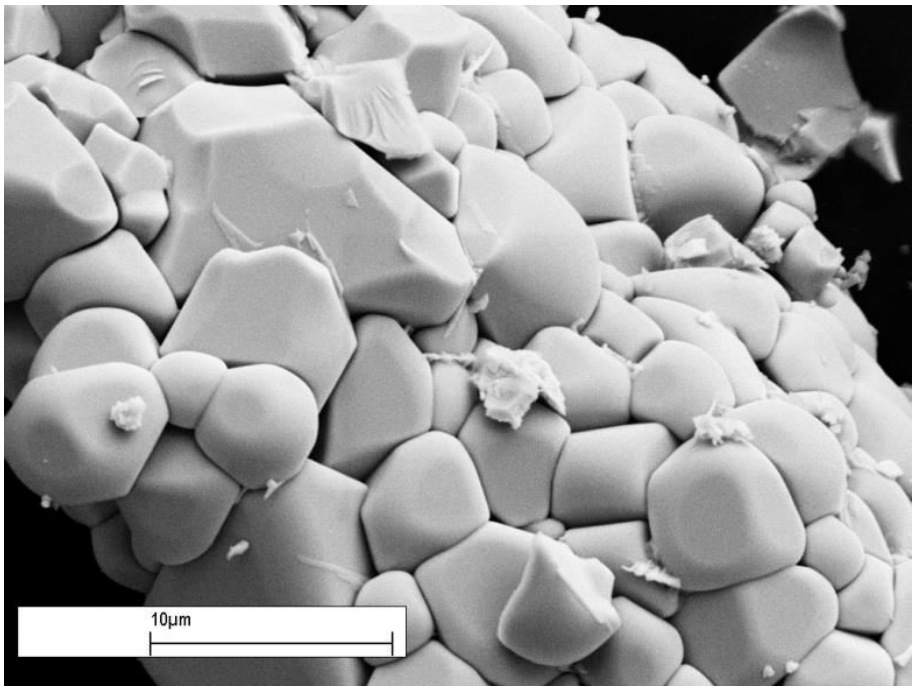

Figure 3.8: SEM images of $LiEu(WO_4)_2$ with 10kx magnification

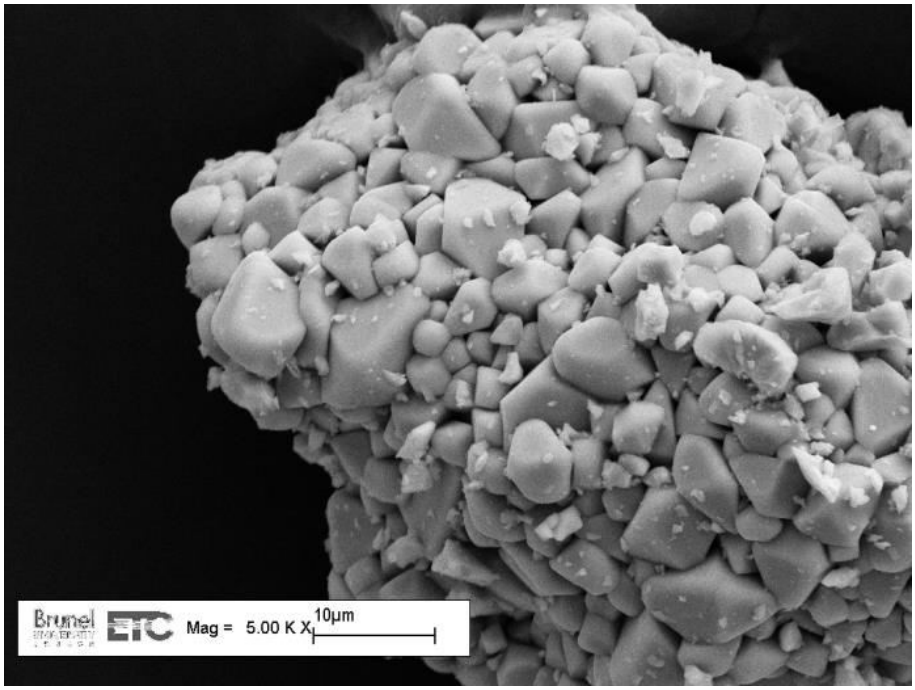

Figure 3.9: SEM images of $LiEu(MoO_4)_2$ with 5kx magnification

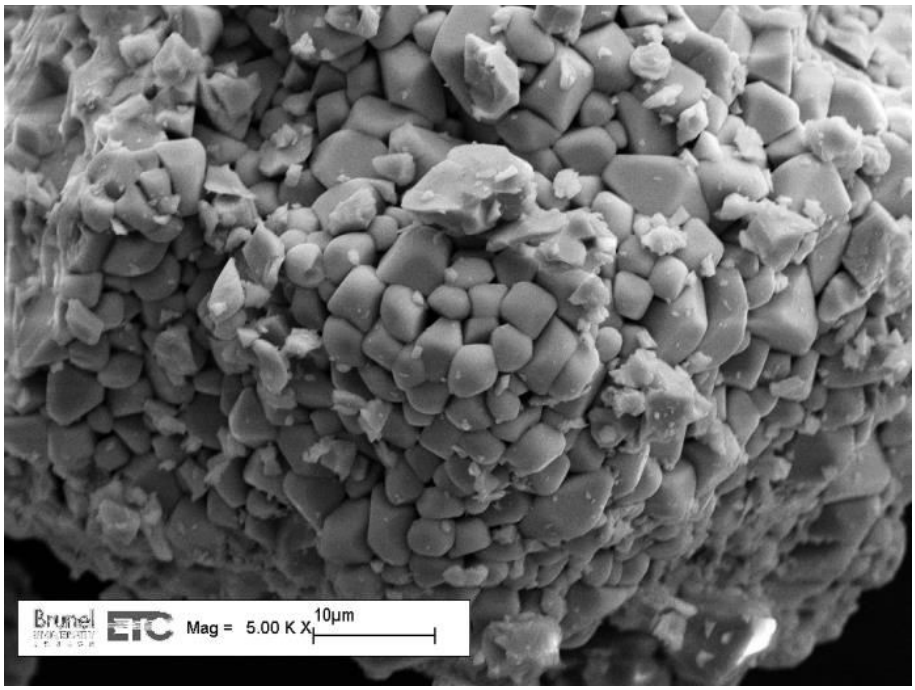

Figure 3.10: SEM images of $LiEu(WO_4)(MoO_4)$ with 5kx magnification

3.11 Conclusion

The findings obtained from this work will help to enhance the lifetime of phosphor therefore contributing to a greener environment whilst at the same time learning the correlation between the changes in the structure of the red phosphors and its luminescence performance as new trivalent cations replace Eu^{3+} dopants inside the phosphor. Since there have been insufficient discussions regarding this correlational relationship the next chapters will discuss further the findings of this new red phosphor. The data gathered from this study will be useful to solid state lighting industries, particularly to a market sector that requires red and white light applications.

3.12 References

1. The British Geological Survey (2010) Rare earth elements: a beginner's guide from the BGS. http://www.bgs.ac.uk/research/highlights/2010/rare_earth_elements.html

2. Sonali P (7 Jan 2015) China's Rare Earths Quotas Go, Possible New Moves Stoke Supply Doubts. http://www.reuters.com/article/china-rareearths-producers-idUSL3N0UL65220150107. *Reuters Online*. Accessed April 20, 2016.

3. Ye S, Xiao F, Pan YX, Ma YY, Zhang QY (2010) Phosphors in phosphor-converted white light-emitting diodes: Recent advances in materials, techniques and properties. *Materials Science and Engineering: R: Reports*, 71(1), 1-34.

4. Zhang Q, Dandeneau CS, Zhou X, Cao G (2009) ZnO Nanostructures for Dye-Sensitized Solar Cells. *Advanced Materials,* 21(41), 4087-4108.

5. George NC, Denault KA, Seshadri R (2013) Phosphors for Solid-State White Lighting. *Annual Review of Materials Research*, 43, 481-501.

6. Nobel Media AB 2014 (20 Apr 2016) The Nobel Prize in Physics 2014. http://www.nobelprize.org/nobel_prizes/physics/laureates/2014/. Accessed April 20, 2016.

7. Amano H (2015) Nobel Lecture: Growth of GaN on sapphire via low-temperature deposited buffer layer and realization of p-type GaN by Mg doping followed by low-energy electron beam irradiation. *Reviews of Modern Physics*, 87(4), 1133.

8. Ronda, C. R. (2007). Luminescence: from theory to applications. *John Wiley & Sons*, pp 105-132.

9. Silver J, Withnall R (2008) Color Conversion Phosphors for LEDS. Luminescent Materials and Applications, *John Wiley & Sons, Ltd*, pp 75-109.

10. Lim KLL, Lee JC, Ng KY (2007) System and method for producing white light using a combination of phosphor-converted white LEDs and non-phosphor-converted color LEDs. U.S. Patent No. 7,256,557. *Washington, DC: U.S. Patent and Trademark Office*.

11. Bessho M, Shimizu K (2012) Latest trends in LED lighting. *Electronics and Communications in Japan*, 95(1), 1-7.

12. Narukawa Y, Ichikawa M, Sanga D, Sano M, Mukai T (2010) White light emitting diodes with super-high luminous efficacy. *Journal of physics D: Applied physics*, 43(35), 354002.

13. Pust P, Weiler V, Hecht C, Tücks A, Wochnik AS, Henß A, Wiechert D, Scheu C, Schmidt PJ, Schnick W (2014) Narrow-band red-emitting Sr $[LiAl_3N_4]$: Eu^{2+} as a next-generation LED-phosphor material, *Nature materials,* 13(9), 891-896.

14. Jia D, Wang X (2007) Alkali earth sulfide phosphors doped with Eu^{2+} and Ce^{3+} for LEDs. *Optical Materials*, 30(3), 375-379.

15. Guo C, Wang S, Chen T, Luan L, Xu Y (2009) Preparation of phosphors AEu $(MoO_4)_2$ (A= Li, Na, K and Ag) by sol-gel method, *Applied Physics A*, 94(2), 365-371.

16. Chen R, Lockwood DJ (2003) Developments in Luminescence and Display Materials Over the Last 100 Years as Reflected in Electrochemical Society Publications, *Journal of The Electrochemical Society*, 149(9), S69-S78.

17. Lei F, Yan B (2008) Hydrothermal synthesis and luminescence of $CaMO_4:RE^{3+}$ (M= W, Mo; RE= Eu, Tb) submicro-phosphors, *Journal of Solid State Chemistry*, 181(4), 855-862.

18. Liu Y, Wang Y, Wang L, Gu Y, Yu S, Lu Z, Sun R (2014) General synthesis of $LiLn(MO_4)_2$: Eu^{3+} (Ln= La, Eu, Gd, Y; M= W, Mo) nanophosphors for near UV-type LEDs, *Royal Society of Chemistry* (4) 4754-4762

19. Macalik L, Hanuza J, Macalik B, Strek W, Legendziewicz J (1996) Comparative studies of optical properties of Eu (III) in $KEu(MoO_4)_2$ and $KEu(WO_4)_2$ crystals. *European journal of solid state and inorganic chemistry*, 33(5), 397-410.

20. Nazarov M, Jeon D, Kang J, Popovici E, Muresan L, Zamoryanskaya M, Tsukerblat B (2004) Luminescence properties of europium–terbium double activated calcium tungstate phosphor. *Solid state communications*, 131(5), 307-311.

21. Neeraj S, Kijima N, Cheetham A (2004) Novel red phosphors for solid-state lighting: the system $NaM(WO_4)_{2-x}(MoO_4)_x:Eu^{3+}$(M= Gd, Y, Bi). *Chemical Physics Letters*, 387(1), 2-6.

22. Sivakumar V, Varadaraju U (2006) A promising orange-red phosphor under near UV excitation. *Electrochemical and solid-state letters*, 9(6), H35-H38.

23. Wang J, Jing X, Yan C, Lin J (2005) $Ca_{1-2x}Eu_xLi_xMoO_4$: A Novel Red Phosphor for Solid-State Lighting Based on a GaN LED. *Journal of The Electrochemical Society, 152(3), G186-G188.*

24. Wang J, Jing X, Yan C, Lin J, Liao F (2005) Photoluminescent Properties of Phosphors in the System $Ca_xCd_{1-x}MoO_4:Eu^{3+}$, Li^+. *Journal of The Electrochemical Society*, *152*(7), G534-G536.

25. Zaushitsyn A, Mikhailin V, Romanenko AY, Khaikina E, Basovich O, Morozov V, Lazoryak B (2005) Luminescence Study of $LiY_{1-x}Eu_x(MoO_4)_2$. *Inorganic materials*, 41(7), 766-770.

26. Jia PY, Liu XM, Yu M, Luo Y, Fang J, Lin J (2006) Luminescence properties of sol–gel derived spherical $SiO_2@Gd_2(WO_4)_3:Eu^{3+}$ particles with core–shell structure. *Chemical physics letters*, 424(4), 358-363.

27. Wang J, Jing X, Yan C, Lin J, Liao F (2006) Influence of fluoride on f–f transitions of Eu^{3+} in $LiEuM_2O_8$ (*M*=Mo, W). *Journal of Luminescence*, 121(1), 57-61.

28. Chiu C, Liu C, Huang S, Chen T (2007) White-light-emitting diodes using red-emitting $LiEu(WO_4)_{2-x}(MoO_4)_x$ phosphors. *Journal of The Electrochemical Society*, 154(7), J181-J184.

29. Liu J, Lian H, Shi C (2007) Improved optical photoluminescence by charge compensation in the phosphor system $CaMoO_4:Eu^{3+}$. *Optical Materials*, 29(12), 1591-1594.

30. Wang X, Xian Y, Wang G, Shi J, Qiang S, Gong M (2007) Luminescence investigation of Eu^{3+} -Sm^{3+} co-doped $Gd_{2-x-y}Eu_xSm_y(MoO_4)_3$ phosphors as red phosphors for UV InGaN-based light-emitting diode. *Optical Materials*, 30(4), 521-526.

31. Wang Z, Liang H, Gong M, Su Q (2007) Luminescence investigation of Eu^{3+} activated double molybdates red phosphors with scheelite structure. *Journal of Alloys and Compounds*, 432(1), 308-312.

32. Zhang Z, Chen H, Yang X, Zhao J (2007) Preparation and luminescent properties of Eu^{3+} and Tb^{3+} ions in the host of $CaMoO_4$. *Materials Science and Engineering: B*, 145(1), 34-40.

33. Zhao X, Wang X, Chen B, Meng Q, Di W, Ren G, Yang Y (2007) Novel Eu^{3+}-doped red-emitting phosphor $Gd_2Mo_3O_9$ for white-light-emitting-diodes (WLEDs) application. J Alloys Compounds. *Journal of alloys and compounds*, 433(1), 352-355.

34. Chiu C, Liu C, Huang S, Chen T (2008) Synthesis and luminescence properties of intensely red-emitting $M_5Eu\ (WO_4)_{4-x}\ (MoO_4)_x$ (M= Li, Na, K) phosphors. *Journal of The Electrochemical Society*, 155(3), J71-J78.

35. Sivakumar V, Varadaraju U (2008) Synthesis, phase transition and photoluminescence studies on Eu^{3+} substituted double perovskites—A novel orange-red phosphor for solid-state lighting. *Journal of Solid State Chemistry*, 181(12), 3344-3351.

36. Su Y, Li L, Li G (2008) Synthesis and optimum luminescence of $CaWO_4$-based red phosphors with codoping of Eu^{3+} and Na^{+}. *Chemistry of Materials*, 20(19), 6060-6067.

37. Wang Y, Sun Y, Zhang J, Ci Z, Zhang Z, Wang L (2008) New red $Y_{0.85}Bi_{0.1}Eu_{0.05}V_{1-y}MyO_4$ (M=Nb, P) phosphors for light-emitting diodes. *Physica B: Condensed Matter*, 403(12), 2071-2075.

38. Zeng Q, Liang H, Gong M, Su Q (2008) Synthesis and luminescence of $Ca_3Ln_2W_2O_{12}$: Eu^{3+} for NUV-InGaN-based red-emitting LED. *Journal of The Electrochemical Society*, 155(10), H730-H733.

39. Zhou L, Wei J, Gong F, Huang J, Yi L (2008) A potential red phosphor $ZnMoO_4$:Eu^{3+} for light-emitting diode application. *Journal of Solid State Chemistry*, 181(6), 1337-1341.

40. Zhu C, Xiao S, Ding J, Yang X, Qiang R (2008) Synthesis and photoluminescent properties of Eu^{3+}-doped$_{(1-x)}CaO–xLi_2O–WO_3$ phosphors. *Materials Science and Engineering: B*, 150(2), 95-98.

41. Cao F, Tian Y, Chen Y, Xiao L, Wu Q (2009) Luminescence investigation of red phosphors $Ca_{0.54}Sr_{0.34-1.5x}Eu_{0.08}Sm_x(MoO_4)_y\ (WO_4)_{1-y}$ for UV-white LED device. *Journal of Luminescence*, 129(6), 585-588.

42. Cao F, Tian Y, Chen Y, Xiao L, QIAN W (2009) Novel red phosphors for solid-state lighting: $Ca_{0.54}\ Sr_{0.34-1.5\,x}\ Eu_{0.08}La_x\ (MoO_4)_y\ (WO_4)_{1-y}$. *Journal of Alloys and Compounds*, 475(1), 387-390.

43. Guo C, Gao F, Xu Y, Liang L, Shi FG, Yan B (2009) Efficient red phosphors $Na_5Ln\ (MoO_4)_4$: Eu^3 (Ln= La, Gd and Y) for white LEDs. *Journal of Physics D: Applied Physics*, 42(9), 095407.

44. Guo C, Yang H, Fu Z, Li L, Choi B, Jeong J (2009) A Potential Red-Emitting Phosphor $BaGd_2\ (MoO_4)_4$: Eu^{3+} for Near-UV White LED. *Journal of the American Ceramic Society*, 92(8), 1713-1718.

45. Haque MM, Kim D (2009) Luminescent properties of Eu^{3+} activated $MLa_2(MoO_4)_4$ based (M = Ba, Sr and Ca) novel red-emitting phosphors. *Materials Letters*, 63(9), 793-796.

46. Shao Q, Li H, Wu K, Dong Y, Jiang J (2009) Photoluminescence studies of red-emitting NaEu $(WO_4)_2$ as a near-UV or blue convertible phosphor. *Journal of Luminescence*, 129(8), 879-883.

47. Hwang K, Jeon Y, Hwangbo S, Kim J (2009) Red-emitting $LiEuW_2O_8$ phosphor for white emitting diodes prepared by sol–gel process. *Optica Applicata*, 39(2), 375-382.

48. Thomas M, Prabhakar Rao P, Deepa M, Chandran M, Koshy P (2009) Novel powellite-based red-emitting phosphors: $CaLa_{1-x}$ $NbMoO_8$:xEu^{3+} for white light emitting diodes. *Journal of Solid State Chemistry*, 182(1), 203-207.

49. Wang S, Koteswara Rao K, Wang Y, Hsu Y, Chen S, Lu Y (2009) Structural Characterization and Luminescent Properties of a Red Phosphor Series: $Y_{2-x}Eu_x(MoO_4)_3$ (x=0.4-2.0). *Journal of the American Ceramic Society*, 92(8), 1732-1738.

50. Xie A, Yuan X, Hai S, Wang J, Wang F, Li L (2009) Enhancement emission intensity of $CaMoO_4$: Eu^3 , Na phosphor via Bi co-doping and Si substitution for application to white LEDs. *Journal of Physics D: Applied Physics*, 42(10), 105107.

51. Xu L, Shen J, Lu C, Chen Y, Hou W (2009) Self-assembled three-dimensional architectures of $Y_2(WO_4)_3$: Eu: controlled synthesis, growth mechanism, and shape-dependent luminescence properties. *Crystal Growth and Design*, 9(7), 3129-3136.

52. Glorieux B, Jubera V, Apheceixborde A, Garcia A (2011) Luminescence properties of tungstates and molybdates phosphors: Illustration on A Ln $(Mo_4)_2$ compounds (A= alikaline cation, Ln= lanthanides, M= W, Mo). 13:460-467

53. Jin Y, Zhang J, Hao Z, Zhang X, Wang X (2011) Synthesis and luminescence properties of clew-like $CaMoO_4$:Sm_{3+}, Eu^{3+}. *Journal of Alloys and Compounds*, 509(38), L348-L351.

54. Mendoza C, Ligny Dd, Panczer G, Peuget S, Bardez-Giboire I, Schuller S (2011) Behaviour of the Eu^{3+} $^5D_0 \rightarrow$ $^7F_0$ transition in $CaMoO_4$ powellite type ceramics under Ar and Pb ions implantation. *Optical Materials*, 34, 386-390.

55. Postema J, Fu W, Ijdo D (2011) Crystal structure of $LiLnW_2O_8$ (Ln = lanthanides and Y): An X-ray powder diffraction study. *Journal of Solid State Chemistry*, 184(8), 2004-2008.

56. Zhou Y, Liu J, Yang X, Yu X, Wang L (2011) Self-assembly and photoluminescence characterization of $CaMoO_4$:Eu^{3+}, Na superstructure via a facile surfactant-free hydrothermal method. *Journal of The Electrochemical Society*, 158(3), K74-K80.

57. Wang D, Yang P, Cheng Z, Wang W, Hou Z, Dai Y, Li C, Lin J (2012) Patterning of $Gd_2(WO_4)_3$: Ln^{3+} (Ln= Eu, Tb) luminescent films by microcontact printing route. *Journal of colloid and interface science*, 365(1), 320-325.

58. Wu H, Hu Y, Zhang W, Kang F, Li N, Ju G (2012) Sol–gel synthesis of Eu^{3+} incorporated $CaMoO_4$: the enhanced luminescence performance. *Journal of sol-gel science and technology*, 62(2), 227-233.

59. Dutta P, Khanna A (2013) Eu^{3+} Activated Molybdate and Tungstate Based Red Phosphors with Charge Transfer Band in Blue Region. *ECS Journal of Solid State Science and Technology*, 2(2), R3153-R3167.

60. Klevtsov P, Klevtsova R (1977) Polymorphism of the double molybdates and tungstates of mono-and trivalent metals with the composition $M^{+}R^{3+}(EO_4)_2$. *Journal of Structural Chemistry*, 18(3), 339-355.

61. Chiu C, Wang M, Lee C, Chen T (2007) Structural, spectroscopic and photoluminescence studies of $LiEu(WO_4)_{2-x}(MoO_4)_x$ as a near-UV convertible phosphor. *Journal of Solid State Chemistry*, 180(2), 619-627.

62. de Moraes JR, Baldochi SL, Soares, Leonardo dos Reis Leano, Mazzocchi VL, Parente CBR, Courrol LC (2012) Growth, structural and optical characterizations of $LiLa_{(1-x)}$ $Eu_x(WO_4)_2$ single-crystalline fibers by the micro-pulling-down method. Mater Res Bull 47:744-749

63. Hwang S, Kang B, Hwangbo S, Kim Y, Kim J (2010) Low-temperature synthesis of $LiEuMo_2O_8$ red phosphor for a white-light-emitting diode. *Materials Research Bulletin*, 47(3), 744-749.

64. Maier A, Provotorov M, Balashov V (1973) Double molybdates and tungstates of the rare earth and alkali metals. *Russian Chemical Reviews*, 42(10), 822.

65. Faculty of Chemical Engineering, University of Applied Sciences Münster (2014) Phosphors Information and Spectra Access (PISA). https://www.fh-muenster.de/fb1/downloads/personal/juestel/juestel/Product_sheet_L-M1-01-Eu_LiEuMo2O8_.pdf. Accessed 10 October 2014

66. Ye S, Wang C, Jing X (2009) Long wavelength extension of the excitation band of LiEuMo2O8 phosphor with Bi3 doping. *Journal of The Electrochemical Society*, 156(6), J121-J124.

67. Schwung S, Rytz D, Gross A, Wesemann V, Enseling D, Jüstel T (2012) On the Luminescence of Single Crystalline $LiEuMo_2O_8$. Poster, *Rare Earth Elements and Compounds (REEC 2012)*.

68. Xie A, Yuan X, Wang J, Wang F (2009) Synthesis and photoluminescence property of red phosphors $LiEu_{1-x}$ Y_x $(WO_4)_{0.5}$ $(MoO_4)_{1.5}$ for white LED. *Science in China Series E: Technological Sciences*, 52(7), 1913-1918.

69. Xie A, Yang W, Zhang M (2012) Red emitting tungsto-molybdate phosphor for near-ultraviolet light-emitting diodes-based solid-state lighting. *Science China Physics, Mechanics and Astronomy,* 55(7), 1229-1234.

70. Kim JS, Lee JC, Cheon CI, Kang H (2006) Crystal Structures and Low Temperature Cofiring Ceramic Property of (1-x)(Li, RE) $W_2O_{8-x}BaWO_4$ Ceramics (RE= Y, Yb). *Japanese journal of applied physics*, 45(9S), 7397.

71. Kolitsch U (2001) The crystal structures of phenacite-type $Li_2(MoO_4)$, and scheelite-type $LiY(MoO_4)_2$ and $LiNd(MoO_4)_2$. *Zeitschrift für Kristallographie-Crystalline Materials*, 216(8), 449-454.

72. Xianju Z, Tonghui Z, Yingmao L, Qiaochun F (2012) $LiY_{1-x}Eu_x(MoO_4)_2$ as a promising red-emitting phosphor of WLEDs synthesized by sol-gel process. *Journal of Rare Earths*, 30(4), 315-319.

73. Yi L, He X, Zhou L, Gong F, Wang R, Sun J (2010) A potential red phosphor $LiGd(MoO_4)_2:Eu^{3+}$ for light-emitting diode application. *Journal of Luminescence*, 130(6), 1113-1117.

74. Li J, Lu C, Lu H, Yang X, Zhu B, Yu H, Sheng J, Che S (2015) Photoluminescent properties of the promising red-emitting phosphor LiGd1−xEux(MoO4)2 for WLEDs. *Ceramics International*, 41, S725-S728.

75. Rico M, Griebner U, Petrov V, Ortega P, Han X, Cascales C, Zaldo C (2006) Growth, spectroscopy, and tunable laser operation of the disordered crystal $LiGd(MoO_4)_2$ doped with ytterbium. *JOSA B*, 23(6), 1083-1090.

76. Li L, Zhang J, Zi W, Gan S, Ji G, Zou H, Xu X (2014) Synthesis and luminescent properties of high brightness MRE $(MoO_4)_2:Eu^{3+}$ (M= Li, Na, K; RE= Gd, Y, Lu) red phosphors for white LEDs. *Solid State Sciences*, 29, 58-65.

77. Stone R, Silver J (September 2011) An Investigation Into Novel Red Emitting Phosphors and Their Applications. Dissertation, Brunel University.

Chapter 4

Accelerated Ageing Studies of CaS:Eu^{2+} and SrS:Eu^{2+} Phosphors

4.1 Introduction and Previous Works on Coating sulfide phosphors from the Literatures

This chapter discusses the effectiveness of alumina coating of CaS:Eu^{2+} and SrS:Eu^{2+} phosphors. As part of the work reported herein the stabilities of both phosphors have been studied when they are subjected to accelerated ageing under conditions of 80% relative humidity and temperatures in the range of 50-80°C. The stability of the CaS:Eu^{2+} phosphor with an ALD coating (supplied by an industrial company) of Al_2O_3 is also investigated.

Although the sulfide phosphors used in this chapter were obtained from industry, it should be noted that the phosphor can easily be synthesized in many ways such as wet chemical synthesis, solid state reaction, microwave heating and solvothermal synthesis [1-4]. The most popular approach to enhance the stability of sulfides is by encapsulating the phosphor particles with transparent layers [1]. Many works on coating sulfide phosphors have been reported in the literatures and one of the early works was in 1982 where Brightwell [5] attempted to enhance the stability of CaS phosphors by applying crystalline layers using vapour phase transport. Since then, numerous encapsulation methods were employed to enhance the stability of sulfide phosphors [6-11] where oxides (such as SiO_2, Al_2O_3, TiO_2, ZnO, and ZrO_2), organic materials and nitrides were utilized as coating layers for sulfide phosphor [7, 11-17]. The encapsulation needs to be thermally and chemically stable, optically transparent (to allow excitation and emission processes to take place) and must be able to be applied uniformly to the surface area of the luminescent particles. These attributes cannot be met by organic coatings which are

unable to withstand high temperature therefore they are not good for coatings on the sulfide particles [1].

Meanwhile for nitride coating, although it has been used as a material for coating due to its transparency and chemical stability, it is still not sufficient to retain decent quantum efficiency as compared to uncoated phosphors [16]. For oxide coatings, a tremendous work has been done by Avci *et. al* [1, 14, 18] and indeed the work reported herein was inspired from their work on high humidity and temperature tests[14, 18]. Avci in 2009 highlighted that the luminescence intensity degradation of 20 nm thickness- Al_2O_3 coated (using the ALD technique) $CaS:Eu^{2+}$ had been improved when exposed to 80% humidity and 80% temperature for 60 hours [18]. They further claimed in another report 2 years later that coating using ALD technique (as they did in Reference [18]) had contributed to negligible degradation as compared to the sol-gel coating technique [14].

Inspired from their work, we took an initiative to replicate the test on $CaS:Eu^{2+}$ and see ourselves how long the ALD coated sulfide phosphors can sustain their luminescence properties at high humidity and temperatures. If this experiment was successful, this coating technique could be the right solution to help improving the performance of other sulfides as well.

Initially the commercial samples of non-coated $CaS:Eu^{2+}$ and non-coated $SrS:Eu^{2+}$ were tested at 80% humidity at a temperature of 80°C in an environmental chamber for 84 hours. The reason of undergoing this ageing test is to determine which phosphor is more sensitive to humidity and high temperature. Based on our hypothesis, $SrS:Eu^{2+}$ should be more susceptible to that environment due to the larger sizes of Sr^{2+} (compared to Ca^{2+}) which would cause the valence electrons to form weaker longer bonds.

4.2 Results and Discussion

4.2.1 Ageing Test of Non-coated $CaS:Eu^{2+}$ Against Non-coated $SrS:Eu^{2+}$

The PL spectra of a non-coated $CaS:Eu^{2+}$ phosphors were aged at a relative humidity of 80% and temperature of 80°C for various times up to 48 hours are shown in Figure 4.1.

The PL intensity from the figure is seen to have decreased to less than one third of its initial value after 84 hours. In comparison, the PL spectra of a non-coated $SrS:Eu^{2+}$ phosphor that has been aged at a relative humidity of 80% and a temperature of 50°C for various times up to 48 hours is presented in Figure 4.2. From the figures it can be observed that although the environment temperature applied on $SrS:Eu^{2+}$ was lower than the one tested on $CaS:Eu^{2+}$, the PL intensity decreased faster to close to zero after just 48 hours. After understanding that the life of non-coated $SrS:Eu^{2+}$ ended after 48 hours whereas non-coated $CaS:Eu^{2+}$ maintains one-third of its intensity in 84 hours even at a higher test temperature, fresh samples of both phosphors were ran at the lower temperature (50°C) at 80% relative humidity. The PL intensities of both the non-coated $CaS:Eu^{2+}$ and $SrS:Eu^{2+}$ phosphors are plotted against ageing time in Figure 4.3 for conditions of 80% relative humidity and 50°C.

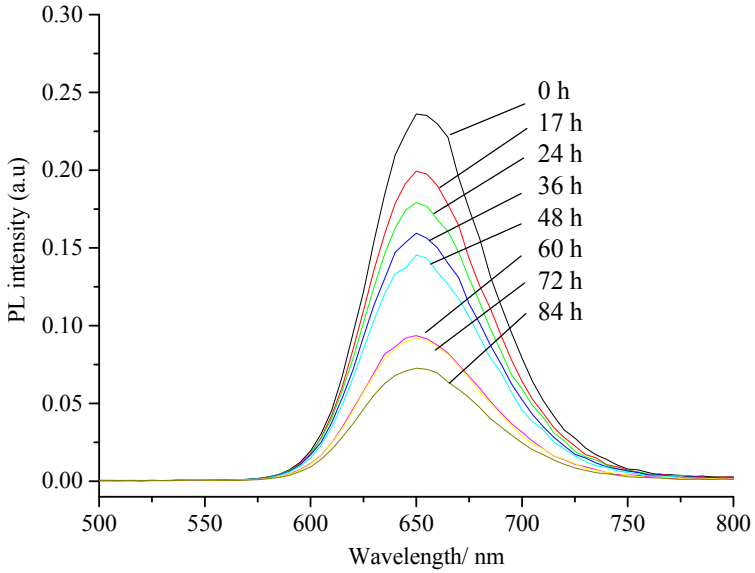

Figure 4.1: PL spectra of $CaS:Eu^{2+}$ (λ_{exc} = 450 nm) before and after accelerated ageing at 80% RH and 80°C over a time period of 84 hours.

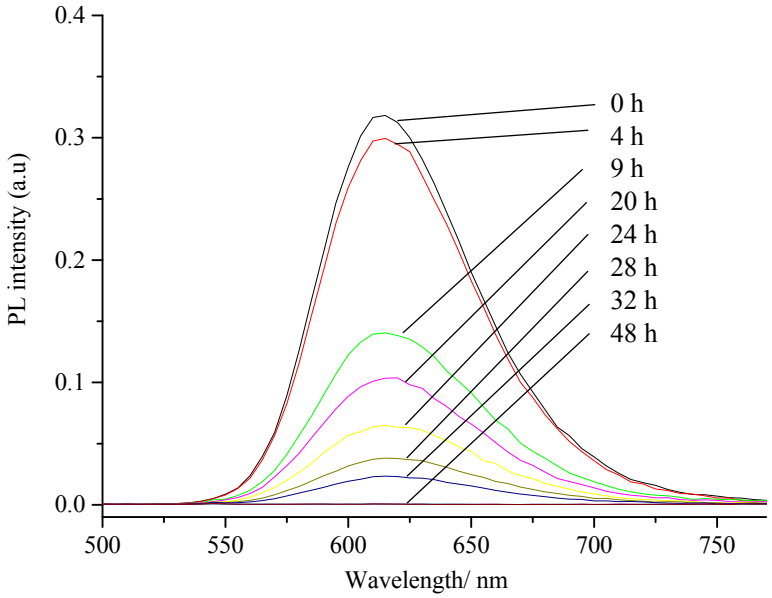

Figure 4.2: PL spectra of SrS:Eu^{2+} (λ_{exc} = 450 nm) before and after accelerated ageing at 80% RH and 50°C over a time period of 48 hours.

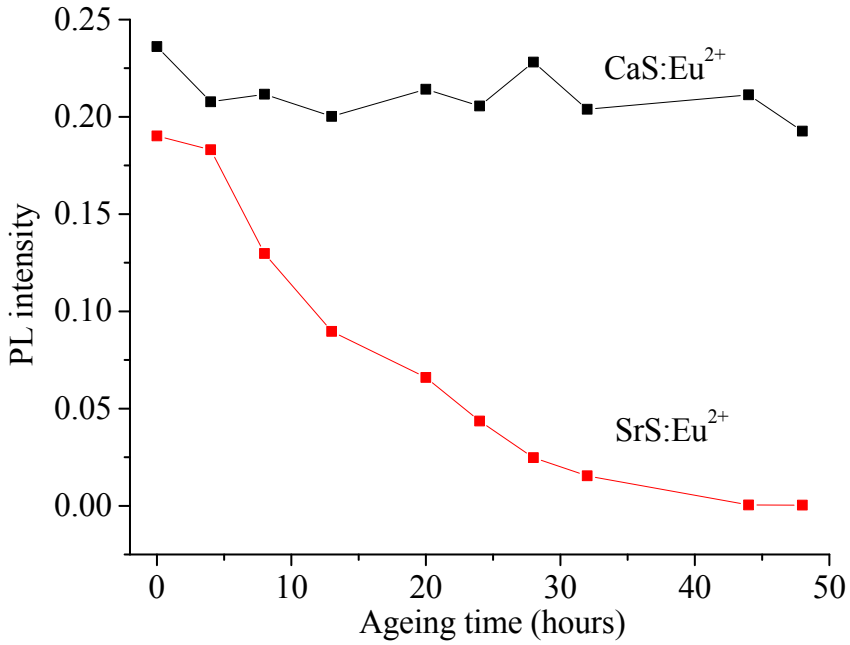

Figure 4.3: PL intensity versus ageing time plots obtained for CaS:Eu^{2+} (black line) and SrS:Eu^{2+} (red line) phosphors under conditions of 80% relative humidity and a temperature of 50°C.

In Figure 4.3, the SrS:Eu^{2+} phosphor is observed to have degraded much more quickly than the CaS:Eu^{2+} phosphor under identical conditions of relative humidity and temperature. This degradation trend is in line with previous literature reports [13, 14] and

the higher susceptibility of the SrS:Eu^{2+} phosphor is attributed to the larger ionic radius of the Sr^{2+} cation (1.32 Å) compared to that of the Ca^{2+} cation (1.14 Å) in a six coordinate environment[2]. Ions with larger ionic radii such as Sr^{2+} cation are more reactive as they hold on to their electrons more loosely, due to them being further from the nucleus compared to the Ca^{2+} cation. Based on these results, CaS:Eu^{2+} was chosen for coating due to it being less reactive in comparison to SrS:Eu^{2+}.

The attenuated total reflectance ATR-FTIR spectra of a CaS:Eu^{2+} phosphor after ageing for various times under conditions of 80% relative humidity and a temperature of 80°C are shown in Figure 4.4. The bands at 883 cm^{-1} and 1300-1600 cm^{-1} are assigned to the calcium carbonate that is formed from reaction of CaS with atmospheric water and carbon dioxide via the following reaction [3]:

$$CaS + H_2O + CO_2 \rightarrow CaCO_3 + H_2S \qquad \textbf{Eq 4.1}$$

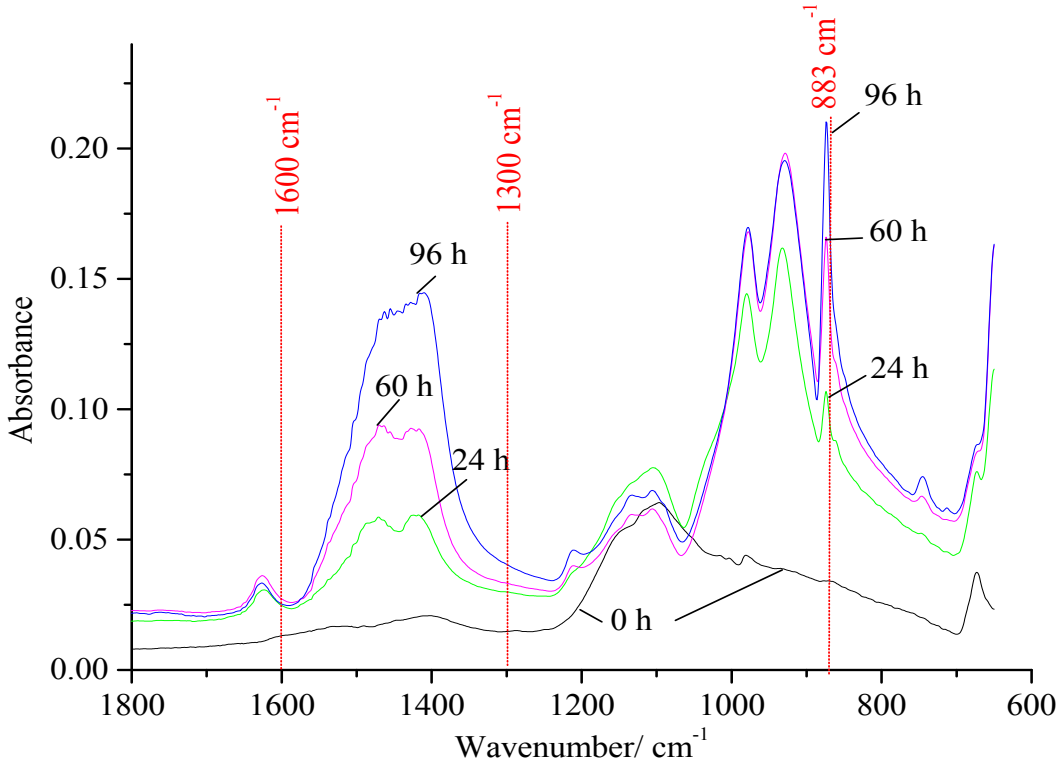

Figure 4.4: ATR FTIR spectra of CaS:Eu^{2+} phosphor after ageing under conditions of 80% relative humidity and a temperature of 80°C for (a) 0, b) 24, c) 60 and d) 96 h.

Likewise, the ATR FTIR spectra of a SrS:Eu^{2+} phosphor after ageing for various times under conditions of 80% relative humidity and a temperature of 50°C are shown in Figure 4.5. The bands in the 1300-1600 region and the two doublets, one with

components at 856 and 872 and the other with components at 679 and 699 cm^{-1}, are assigned to the strontium carbonate that is formed from the reaction of SrS with atmospheric water and carbon dioxide via the following reaction:

$$SrS + H_2O + CO_2 \rightarrow SrCO_3 + H_2S \qquad \textbf{Eq 4.2}$$

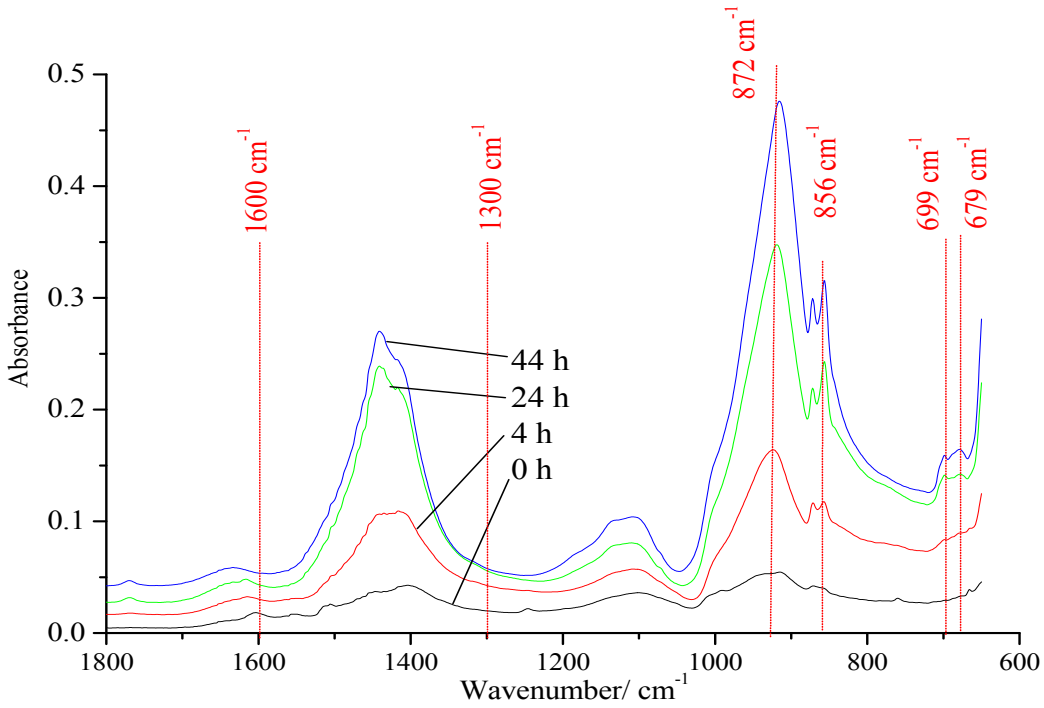

Figure 4.5: ATR FTIR spectra of SrS:Eu^{2+} phosphor under conditions of 80% relative humidity and a temperature of 50°C for (a) 0, b) 4, c) 24 and d) 44 h.

4.2.2 Ageing Test of Non-coated Against Alumina Coated CaS:Eu^{2+}

The CaS:Eu^{2+} phosphor was coated with aluminium oxide using the atomic layer deposition (ALD) method (by an industrial company) and two coating thicknesses of 10 nm and 40 nm were applied. PL spectra were collected from these Al_2O_3 coated CaS:Eu^{2+} phosphors and compared to the PL spectrum of non-coated CaS:Eu^{2+} to investigate any attenuation of the emitted light due to the coatings. As can be seen from Figure 4.6, there is hardly any attenuation of the exciting or emitted light by the Al_2O_3 coatings, proving that the coating layer is optically transparent and suitable in

maintaining the original intensity of uncoated sulfide phosphor. This is also confirmed from the excitation spectra shown in Figure 4.7.

Looking at the sustainability of the coating layers as seen in Figure 4.3 the protective effect of the moisture-sensitive CaS:Eu^{2+} phosphor is clearly demonstrated in ageing studies under conditions of 80% relative humidity and 80°C by a comparison of the PL spectra. For this experiment the non-coated phosphor was placed next to a 40 nm Al_2O_3 coated CaS:Eu^{2+} and the two samples were kept in this environment for 192 hours. The emission intensities as a function of time of exposure for both samples are plotted in Figure 4.8. It can be seen from the figure that the non-coated CaS:Eu^{2+} experienced faster degradation compared to the 40 nm Al_2O_3 coated. The non-coated Cas:Eu^{2+} reduced 58.4% from its initial intensity whilst 40 nm coated CaS:Eu^{2+} only reduced 35.2% after 192 hours in the environmental chamber. Although the degradation of 40 nm thickness Cas:Eu^{2+} is slower than that of uncoated Cas:Eu^{2+}, however the degradation trend on the coated Cas:Eu^{2+} is observed to be faster than that of 20 nm thickness CaS:Eu^{2+} reported by Avci [14].

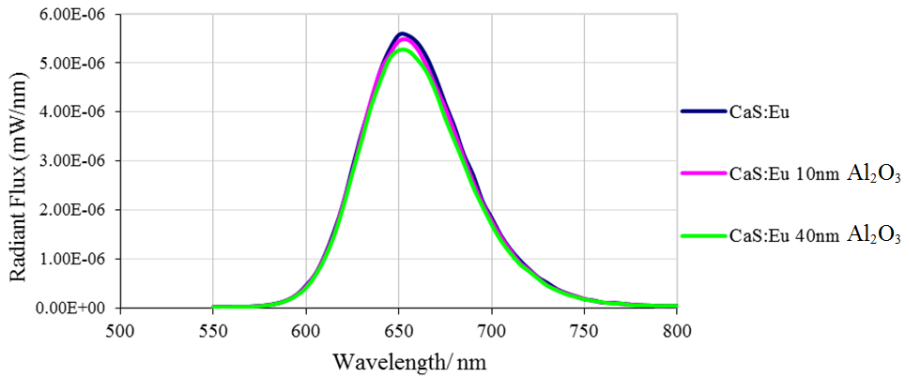

Figure 4.6: PL spectra (λ_{exc} = 450 nm) of CaS:Eu^{2+} phosphor (a) non-coated, b) with a 10 nm thick Al_2O_3 coating, and c) with a 40 nm thick Al_2O_3 coating.

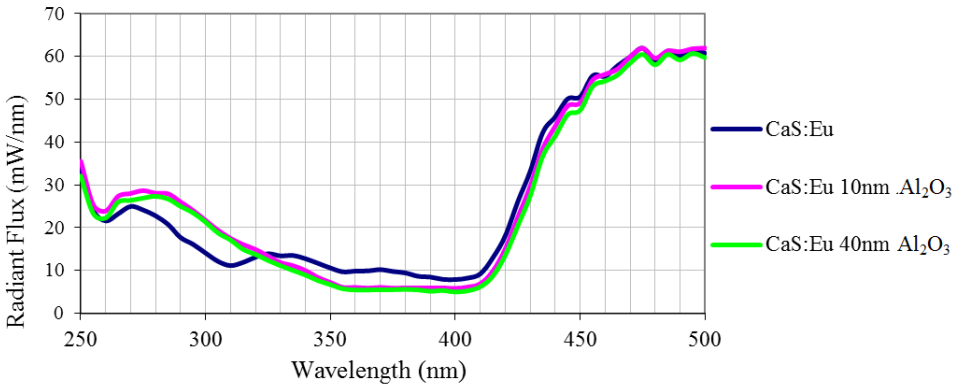

Figure 4.7: PL excitation spectra (monitoring emission at λ = 650 nm) of CaS:Eu^{2+} phosphor (a) non-coated, b) with a 10 nm thick Al_2O_3 coating, and c) with a 40 nm thick Al_2O_3 coating.

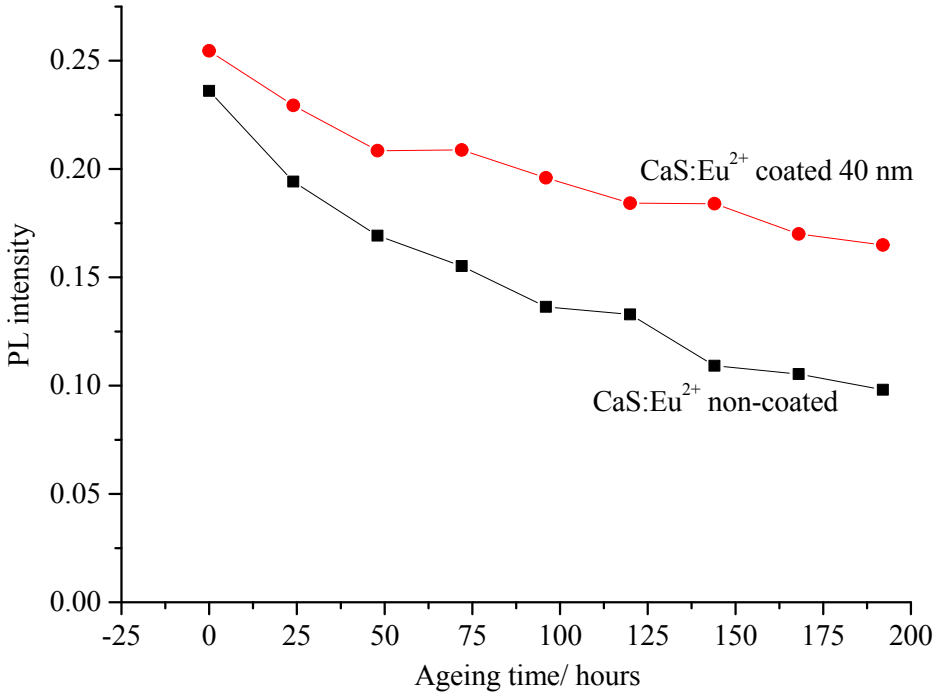

Figure 4.8: PL intensity versus ageing time plots obtained for coated CaS:Eu^{2+} (red line) and non-coated CaS:Eu^{2+} (black line) phosphors under conditions of 80% relative humidity and a temperature of 80°C.

SEM images of the sample particles of both non-coated and Al_2O_3 coated CaS:Eu^{2+} before and after the ageing processes takes place are shown in Figure 4.9 and Figure 4.10. In Figure 4.9, it can be seen that the uncoated particles have drastically changed with carbonate layers ($CaCO_3$) encapsulating the particles after they were exposed to 192 hours of 80% relative humidity and a temperature of 80°C. However the coated particles seem to be less susceptible to atmospheric water and high temperature. The degradation in emission intensity still occurred probably due to degradation of the particles in areas where they did not have complete coatings. In these uncoated or partially coated areas on the particles a reaction with CO_2 and water to form $CaCO_3$ occurred as explained in Eq 4.1 and seen clearly in Figure 4.10 (a). The fresh coated particles (before undergoing the ageing process) had very fine coatings on their surfaces of almost fully uniform encapsulated layers of Al_2O_3 though some parts of the surface were still uncoated and therefore exposed to the outside environment. Figure 4.10 (b) shows the coated particles after exposed to 192 hours of 80% relative humidity and a temperature of 80°C. The surface on the coated particles after ageing seems to have less carbonate layers as compared to non-coated particles due to less chemical reaction with

the humidity and high temperature from the environment. The shapes of the particles also remained unchanged except for new growth from the carbonate layers.

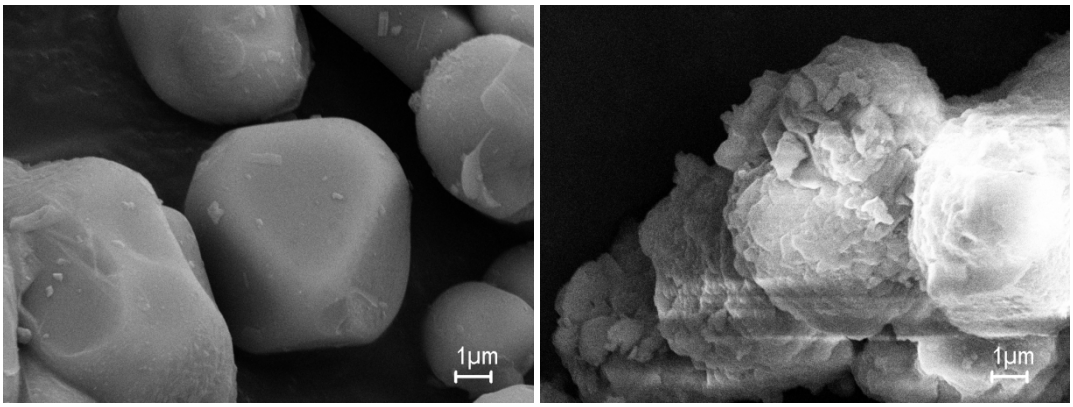

(a) (b)

Figure 4.9: SEM images of non-coated CaS:Eu^{2+} magnified at 25kc (a) at 0 hour (b) after 192 hours in 80% relative humidity and a temperature of 80°C

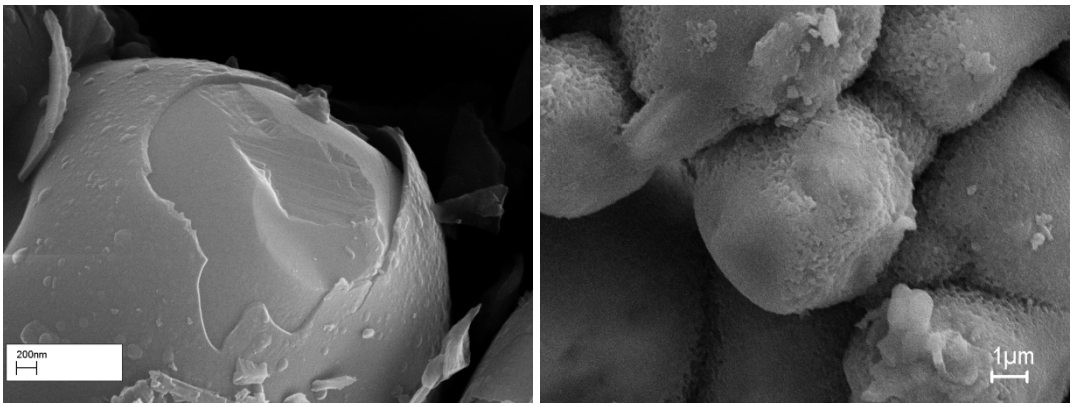

(a) (b)

Figure 4.10: SEM images of 40 nm coated CaS:Eu^{2+} (a) at 0 hour magnified at 70.69kx (b) after 192 hours in 80% relative humidity and a temperature of 80°C magnified at 25kx

4.2.3 Conclusion

From this work a number of conclusions could be made and are offered as a caveat when coating metal sulfide based phosphor particles;

1. CaS:Eu^{2+} and SrS:Eu^{2+} phosphors have been shown to be moisture sensitive in accelerated ageing studies under conditions of 80% relative humidity and temperatures in the range of 50-80°C .

2. $SrS:Eu^{2+}$ phosphor samples are shown to degrade much more quickly than $CaS:Eu^{2+}$ phosphor samples under the same conditions of relative humidity and temperature.
3. The ATR FTIR spectra indicated that $CaCO_3$ and $SrCO_3$ are formed from reaction of CaS and SrS, respectively, with atmospheric water and carbon dioxide.
4. Al_2O_3 coatings, which were applied to the $CaS:Eu^{2+}$ phosphor by ALD, did not significantly attenuate the exciting or emitted light.
5. The Al_2O_3 coatings protected the $CaS:Eu^{2+}$ phosphor from moisture and the protection can be improved further if the Al_2O_3 layer uniformly covered the $CaS:Eu^{2+}$ surface area.
6. The Al_2O_3 coated $CaS:Eu^{2+}$ and $SrS:Eu^{2+}$ phosphors could be used as colour conversion materials for generating red light from blue LEDs if the environmental conditions experienced by the latter are not too hard on the coated phosphors.

4.2.4 References

1. Avci N (2012) Sol-gel Processes for Protection and Synthesis of Luminescent Materials. Dissertation, Ghent University.

2. Van Haecke J, Smet P, Poelman D (2004) The influence of source powder composition on the electroluminescence of $Ca_{1-x}Sr_xS$:Eu thin films. *Spectrochimica Acta Part B: Atomic Spectroscopy*, 59(10), 1759-1764.

3. Van Haecke J, Smet P, De Keyser K, Poelman D (2007) Single crystal CaS: Eu and SrS: Eu luminescent particles obtained by solvothermal synthesis. *Journal of The Electrochemical Society*, 154(9), J278-J282.

4. Sun B, Yi G, Chen D, Zhou Y, Cheng J (2002) Synthesis and characterization of strongly fluorescent europium-doped calcium sulfide nanoparticles. *Journal of Materials Chemistry*, 12(4), 1194-1198.

5. Brightwell J, Ray B, Buckley C (1982) Preparation, crystal growth and luminescence in calcium sulphide. *Journal of Crystal Growth*, 59(1), 210-216.

6. Shin HH, Kim JH, Han BY, Yoo JS (2008) Failure analysis of a phosphor-converted white light-emitting diode due to the CaS: Eu phosphor. *Japanese Journal of Applied Physics*, 47(5R), 3524.

7. Guo C, Chu B, Wu M, Su Q (2003) Oxide coating for alkaline earth sulfide based phosphor. *Journal of luminescence*, 105(2), 121-126.

8. Guo C, Chu B, Su Q (2004) Improving the stability of alkaline earth sulfide-based phosphors. *Applied Surface Science*, 225(1), 198-203.

9. Yoo S, Kim C (2009) Nanocomposite encapsulation of CaS: Eu light-emitting diode phosphors for the enhancement of the stability against moisture. *Journal of The Electrochemical Society*, 156(7), J170-J173.

10. Suchea M, Christoulakis S, Androulidaki M, Koudoumas E (2008) CaS: Eu, Sm and CaS: Ce, Sm films grown by embedding active powder into an inert matrix. *Materials Science and Engineering: B*, 150(2), 130-134.

11. Gang S, Kim D, Kim S, Hwang N, Lee K (2012) Improvement in the moisture stability of CaS:Eu phosphor applied in light-emitting diodes by titania surface coating. *Microelectronics Reliability*, 52(9), 2174-2179.

12. Xue L, Kajiyoshi K, Sasaoka H, Nishimura K (2008) Preparation of uniform titania nanocoating on ZnS-based phosphors by a sol–gel process. *Thin Solid Films*, 516(15), 4833-4838.

13. Do H, Kim E, Hong S (2010) Improved moisture resistance of SrS:Eu2+ phosphors with nanoscale SiO2 coating. *Journal of Luminescence*, 130(8), 1400-1403.

14. Avci N, Cimieri I, Smet PF, Poelman D (2011) Stability improvement of moisture sensitive CaS:Eu^{2+} micro-particles by coating with sol-gel alumina. *Optical Materials*, 30(7), 1032-1035.

15. Lin J, Huang Y, Bando Y, Tang C, Golberg D (2009) BN tubular layer-sheathed CaS: Eu2 nanowires as stable red-light-emitting nanophosphors. *Chem. Commun.*, (43), 6631-6633.

16. Musschoot J, Xie Q, Deduytsche D, Van den Berghe S, Van Meirhaeghe R, Detavernier C (2009) Atomic layer deposition of titanium nitride from TDMAT precursor. *Microelectronic Engineering*, 86(1), 72-77.

17. Bogush G, Tracy M, Zukoski C (1988) Preparation of monodisperse silica particles: control of size and mass fraction. *Journal of non-crystalline solids*, 104(1), 95-106.

18. Avci N, Musschoot J, Smet P, Korthout K, Avci A, Detavernier C, Poelman D (2009) Microencapsulation of Moisture-Sensitive CaS:Eu^{2+} Particles with Aluminum Oxide. *Journal of The Electrochemical Society*, 156(11), J333-J337.

Chapter 5

Incorporating Yttrium (III) on Tungstate/Molybdate Host Lattices

This chapter discusses the results of incorporating yttrium (III) in three different series of scheelite compounds. The parent compounds studied in this chapter are $LiEu(WO_4)_2$, $LiEu(MoO_4)_2$ and $LiEu(MoO_4)(WO_4)$. Their properties are discussed in 5.1 below and latter discussions are based on how Y^{3+} substitution for Eu^{3+} impacts on the luminous efficacy and the way it correlates with the crystal structure of the original compounds. The parent Eu^{3+} compounds and all of the substituted compounds are of the general formula $LiEu_{(1-x)}Y_x(MoO_4)_{(2-y)}(WO4)_y$ as described in Chapter 3.

There were 3 specific reports, discussed in Chapter 3 that were undertaken to examine the effects of incorporating of Y^{3+} into $LiEu_{(1-x)}Y_x(MoO_4)_{(2-y)}(WO4)_y$ and its correlation with the photoluminescence of the phosphors. Zaushitsyn *et, al* [1] in 2005 with compounds formula $LiY_{1-x}Eu_x(MoO_4)_2$ and Xie An *et. al* [2] on $LiEu_{1-x}Y_x(WO_4)_{0.5}(MoO_4)_{1.5}$ reported that the best emission intensity appeared to be in the event that the concentrations of Eu^{3+} and Y^{3+} are balanced (at 0.5 mol each). Xianju *et, al.*[3] also examined the influence of $Eu^{3+}$and Y^{3+}on the luminescence emission of $LiY_{1-x}Eu_x(MoO_4)_2$. However, Eu^{3+} mol was only set from 0.01 to 0.1 and they did not give any explanation on the whole series from x=0 until x=1. However neither of these papers reported on luminous efficacies.

5.1 Lithium Europium Tungstate and Molybdate host lattices.

5.1.1 Powder Crystallography

Figure 5.1 presents the XRPD pattern of $LiEu(WO_4)_2$ as in ICSD collection code 261832 created by Postema *et al* [4] whereas Figure 5.2 shows three XRPD patterns of the powder samples; $LiEu(WO_4)_2$, $LiEu(MoO_4)_2$ and $LiEu(WO_4)(MoO_4)$

which were prepared by solid state reactions developed in our laboratories (see Chapter 2). It can be seen that all the main diffraction peaks from the three samples are in agreement with the reference pattern presented in Figure 5.1 The parent compound $LiEu(WO_4)_2$ is clearly isostructural with that given in ICSD collection code 261832 fitting the tetragonal space group $I4_1/a:2$ in accordance with other reports [1, 5-8]. This structure is commonly referred to as the scheelite structure. The most intense diffractions in the XRPD patterns are found at $2\theta \approx 29°$corresponding to the (112) reflection. Other reflections can also be seen at $2\theta \approx$ 18.8°, 31.7° 34.4° and 47.5° respectively corresponding to the (101), (004), (200) and (204) reflections.

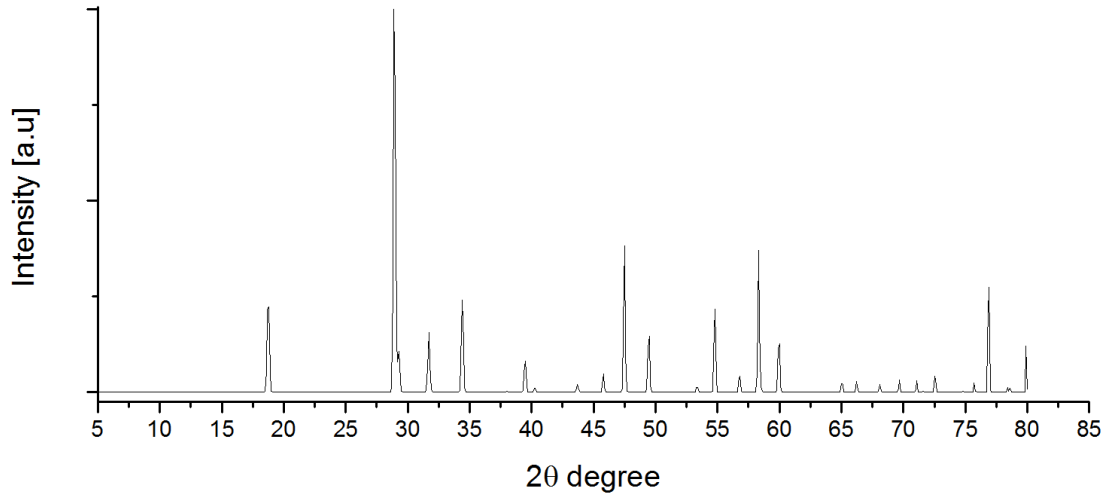

Figure 5.1: XRPD pattern of $LiEu(WO_4)_2$ as described by Postema et al [4]. (ICSD collection code 261832)

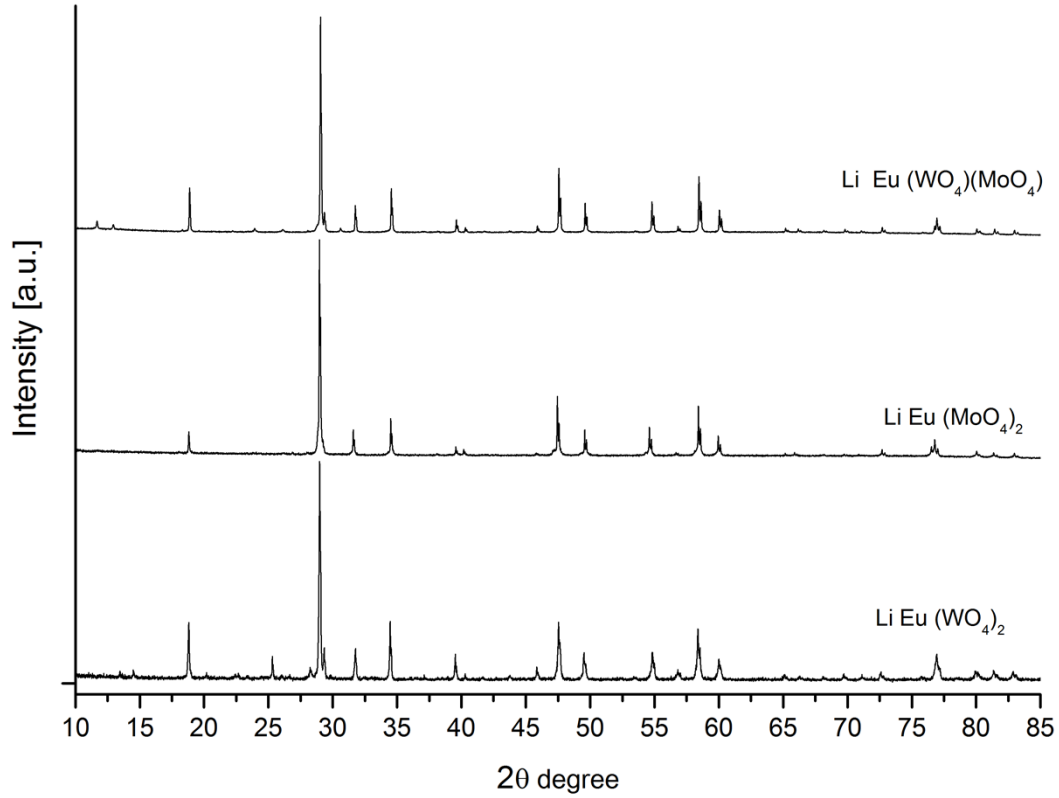

Figure 5.2: XRPD diffraction patterns of $LiEu(WO_4)_2$, $LiEu(MoO_4)_2$ and $LiEu(WO_4)(MoO_4)$

5.1.2 Photoluminescence properties

Excitation and emission spectra of phosphors are influenced by the selection rules that depend upon the symmetry of the host lattice sites as well as the inherent properties of the activator(s). These spectra depend on how the transition takes place, if the bands are broad this often indicates a charge transfer (C-T) process and allowed transitions (i.e. d-f). Charge transfer (C-T) is a process involving valence electrons originally from the ligands moving into the vacant orbitals of the metallic cations [9, 10]. In the spectra of the trivalent rare earth elements as in our samples, as shown in Figure 5.3 and Figure 5.4, sharp emission bands are seen. These are due to forbidden f-f transitions which are manifest as narrow emission bands around 615 nm. Both figures show that the samples have very good absorption band at 395 nm and 465 nm and emit around 615 nm (red light). The narrow emission lines as represented by dashed blue and red lines in Figure 5.3 and Figure 5.4 are found to have CIE colour coordinates (x, y) of (0.6386, 0.3183) for the tungstates; (0.6407, 0.3190) for the molybdates and (0.6387, 0.3170) for the tungstate/molybdate compounds which are

all very similar. The coordinates of the three compounds are plotted in a CIE chromaticity diagram as shown in Figure 5.5.

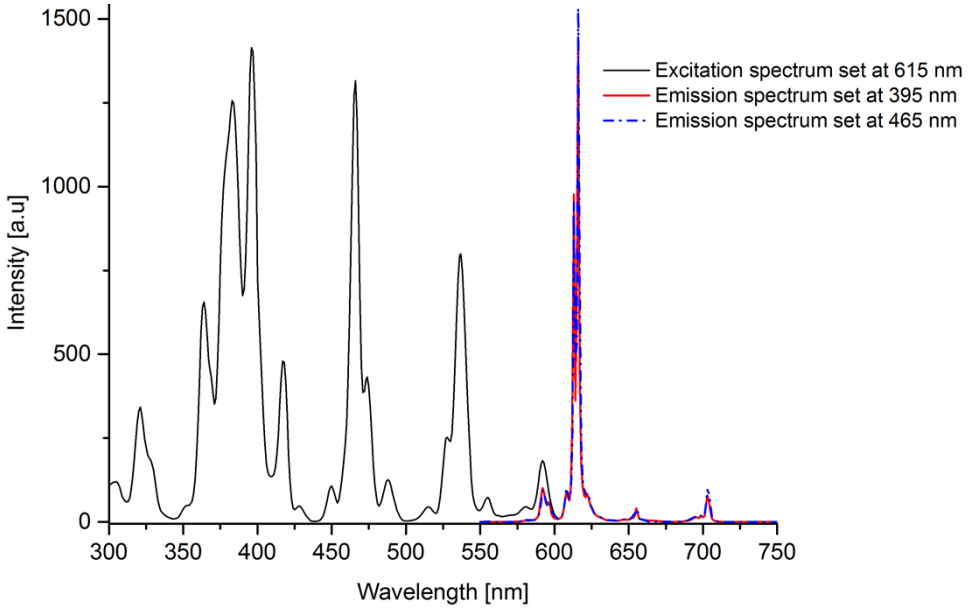

Figure 5.3: Emission and excitation spectra of $LiEu(WO_4)_2$

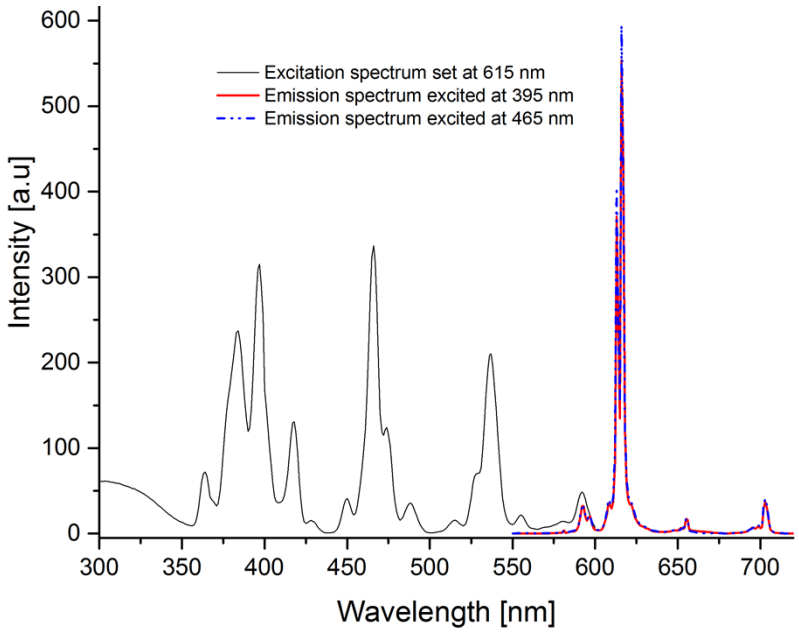

Figure 5.4: Excitation and emission spectra of $LiEu(MoO_4)_2$

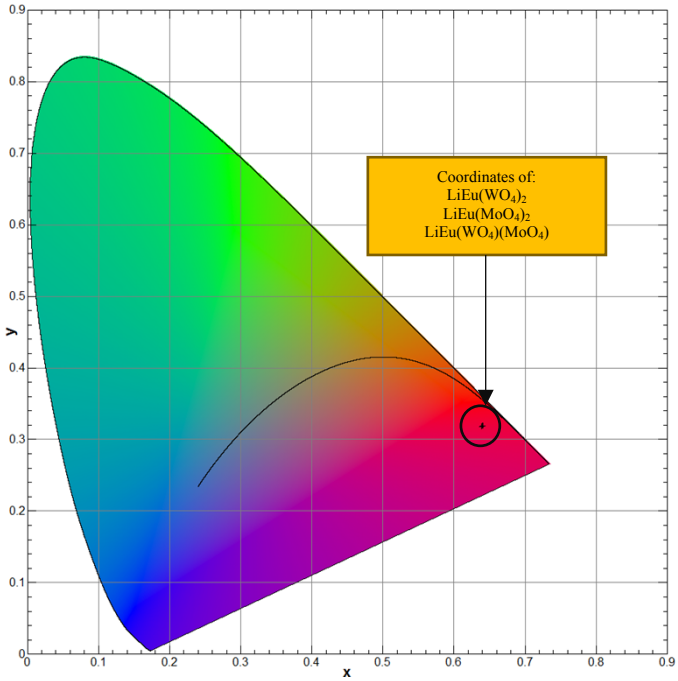

Figure 5.5: CIE chromaticity coordinates of $LiEu(WO_4)_2$, $LiEu(MoO_4)_2$ and $LiEu(WO_4)(MoO_4)$

In contrast to the case of allowed transitions, which have a good chance of occurrence and are observed as broad bands as seen on Europium (II) dopant cations in Chapter 4. The latter transitions have a shorter lifetime and the phosphors have been used to convert blue LED light to other colours. In the present cases these Eu^{3+}phosphors that undergo forbidden transitions will experience longer lifetimes.

5.2 Effects of Substituting Eu^{3+} in Lithium Europium Tungstate and Molybdate Phosphors with Y^{3+} cations.

The discussion of the results begins with selection of yttrium (III) as a potential substitute in these scheelite compounds. It has been understood that yttrium has been shown to be a very essential element in host lattices for many phosphor compounds such as the popular yellow phosphor $Y_3Al_5O_{12}:Ce^{3+}$ [11]. The reason yttrium (III) is chosen for this work as a substitute is primarily because it has chemical similarities with the lanthanides yet has no luminescent properties itself. Its ionic radius is slightly smaller than Eu^{3+} (Y^{3+} 1.019 Å < Eu^{3+} 1.066 Å) thus it can easily substitute for Eu^{3+} and settle down in the same site where the Eu^{3+} cation was positioned. Hence it is expected that as the concentration of Y^{3+} increases, the emission spectrum should be unchanged (in form, not intensity) until/if the initial parent Eu^{3+} structure changes. Even though Y^{3+}cannot act as a luminescent centre like Eu^{3+} attributable to zero f

orbitals unlike lanthanides, the cost of manufacturing tungstate/molybdate phosphors using yttrium (III) to substitute for europium (III) can be significantly reduced as the former is much cheaper.

5.2.1 Incorporation of Y^{3+} into Tungstate host lattices

5.2.1.1 Powder Crystallography

The first set of samples that were substituted with Y^{3+} for Eu^{3+} had the general formula of $LiEu_{(1-x)}Y_x(WO_4)_2$ where x is in the range from 0 to 1, the XRPD results are presented in Figure 5.6 as an overlay. The figure summarizes how the initial phase of tetragonal $LiEu(WO_4)_2$ changes as the proportion of Y^{3+} gradually increases from 0 to 100%. It can be observed from the figure that as the concentration of Y^{3+} reaches 50%, it still does not significantly change the initial tetragonal structure of $LiEu(WO_4)_2$. However the phase starts to change slightly when 0.55 mol of Y^{3+} is substituted in and a significant phase-change can be observed afterwards until Y^{3+} completely replaces Eu^{3+} to change the structure to that of monoclinic $LiY(WO_4)_2$.

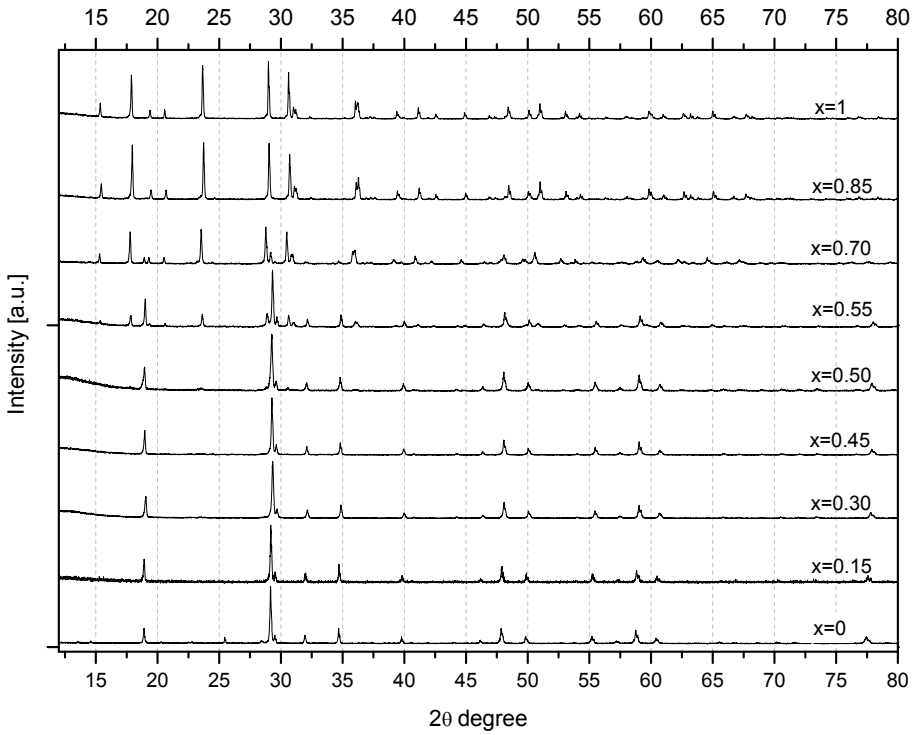

Figure 5.6: XRPD patterns of $LiEu_{(1-x)}Y_x(WO_4)_2$

The XRPD results obtained from the samples $LiEu_{(1-x)}Y_x(WO_4)_2$ were then fitted using Retvield refinement analysis and the fit for the $LiY(WO_4)_2$ pattern after

refinement is shown in Figure 5.7. The model chosen for the Retvield analysis was based on a refinement model carried out by Postema et, al. [4] instead of a model assigned by K.J Seog et al. [12] who suggested that the space group of $LiY(WO_4)_2$ compound should be P2. The latter model was rejected due to high standard deviations on some of the refinement data presented in the article. Furthermore the *x* and *z* coordinates of W atoms were also questionable as it was detected to have an *n-glide* perpendicular to *b-axis* [1][4] which makes the P2/n model preferred in refining the XRPD results reported herein. Figure 5.7 confirms the crystal structure is monoclinic with space group P2/n with weighted profile factor, R_{wp}12.57. Although the computed R_{wp} is not minimal, the visual observation as seen in Figure 5.7 demonstrates that the fitting is sufficient to claim the structure as P12/n1(13).

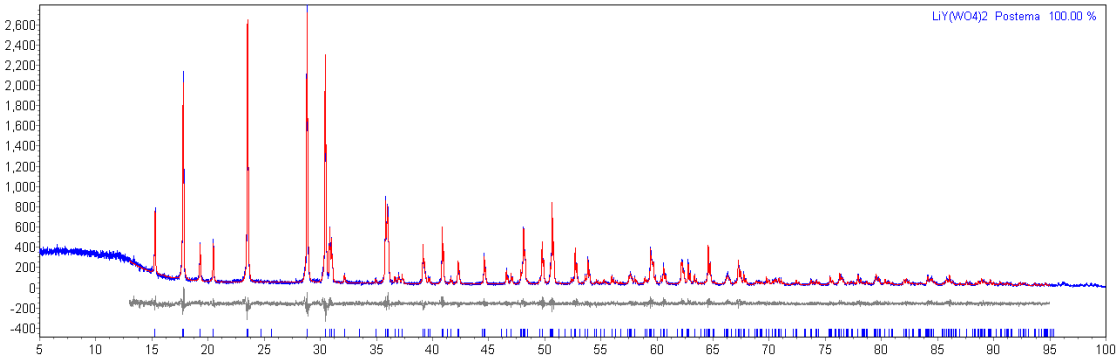

Figure 5.7: Retvield refinement analysis of monoclinic $LiY(WO_4)_2$ against ICSD collection code 261840 [4]

In an effort to learn how the phases present in the $LiEu_{1-x}Y_x(WO_4)_2$ system transform from tetragonal I41/a:2 to monoclinic P2/n as the concentration of Y^{3+} increases all the XRPD patterns of the samples were refined as discussed below for Table 5.1 for three different scenarios. All three scenarios are summarized in Table 5.1 and the best results are presented in Table 5.2. As discussed above, from Figure 5.6 the tetragonal phase appears to remain unaffected from 0 to 50 % and it starts transforming as soon as 55 % concentration of Y^{3+} is introduced, the phase is seen to be completely transformed to a pure monoclinic structure when 85 % of Y^{3+} is in the sample. To fully assess how the structures change three different sets of refinements were carried out. The first set of refinements were made by taking into account the worst scenario that there could possibly be an unseen (by eye in Figure 5.6) second phase (monoclinic) present when Y^{3+} concentration is in the range 15 % to 85 % until it becomes purely monoclinic at 100 % of Y^{3+}.

Table 5.1: Summary of three scenarios employed in XRPD refinement analysis on $LiEu_{1-x}Y_x(WO_4)_2$

	x (mol)	Phases assumption
Scenario no. 1	0	1 phase
	0.15	2 phases
	0.30	
	0.45	
	0.50	
	0.55	
	0.70	
	0.85	
	1	1 phase

	x (mol)	Phases assumption
Scenario no. 2	0	1 phase
	0.15	
	0.30	
	0.45	
	0.50	
	0.55	2 phases
	0.70	2 phases
	0.85	2 phases
	1	1 phase

	x (mol)	Phases assumption
Scenario no. 3	0	1 phase
	0.15	
	0.30	
	0.45	
	0.50	
	0.55	2 phases
	0.70	2 phases
	0.85	1 phase
	1	

The second scenario was made with a presumption that the second phase takes place when Y^{3+} concentrations are in between 55% to 85% due to an observation made in Figure 5.6 in which no new noticeable peaks were observed before 55% of Y^{3+}. The third scenario was that 2 phases only exist from 55 % to 75 % of Y^{3+} whereas at 85 % concentration of Y^{3+} refined as single phase. The third scenario was based on the fact that the fit tried for the tetragonal phase at 85% Y^{3+}gave no real evidence for the presence of this phase as shown in Table 5.2 (see fit in Appendix A). All refinements were set for 1000 iterations to ensure the TOPAS software would converge to the nearest parameters possible to the XRPD results measured from the samples. After considering the resultant fits the third scenario was the favoured choice. The resulting data is presented in Table 5.2 and the discarded data from scenarios 1 and 2 is presented in Appendix A. As far as the XRPD patterns of $LiEu_{0.15}Y_{0.85}(WO_4)_2$ and $LiY(WO_4)_2$ are concerned they are identical to one another and there is no evidence of a tetragonal phase in the 85% Y^{3+} concentration.

Table 5.2: Lattice parameters of tetragonal I41/a:2 and monoclinicP2/n refined on $LiEu_{(1-x)}Y_x(WO_4)_2$

Y^{3+} (mol)		0	0.15	0.3	0.45	0.5	0.55	0.7	0.85	1
Tetragonal I41/a:2	a (Å)	5.2082(1)	5.2005(1)	5.19172(9)	5.18318(7)	5.1812(1)	5.17865(9)	5.1778(2)	N/A	N/A
	c (Å)	11.2809(3)	11.2593(3)	11.2421(3)	11.2183(2)	11.2140(4)	11.2070(3)	11.2057(7)		
	Vol (Å^3)	306.00(1)	304.51(2)	303.02(1)	301.38(1)	301.04(2)	300.55(1)	300.42(3)		
	%	100	100	100	100	100	65(1)	12(1)		
Monoclinic P12/n1	a (Å)	N/A	N/A	N/A	N/A	N/A	10.0474(6)	10.0293(2)	10.0128(2)	9.9899(1)
	b (Å)						5.8092(3)	5.8043(1)	5.80065(7)	5.79480(6)
	c (Å)						5.0106(3)	5.0055(1)	5.00420(8)	5.00271(5)
	β (°)						94.522(4)	94.400(1)	94.3111(9)	94.1986(7)
	Vol (Å^3)						291.55(3)	290.52(1)	289.825(8)	288.827(5)
	%						35(1)	88(1)	100	100
R_{wp}		10.81	16.71	15.3	14.74	16.87	13.72	13.33	13.68	12.57

The cell volumes and lattice parameters from the refined $LiEu_{(1-x)}Y_x(WO_4)_2$ are plotted in Figure 5.8 and Figure 5.9 (a) and (b) respectively. It can be observed from Figure 5.8 that both tetragonal $I4_1/a:2$ and monoclinic P2/n cell volumes of the $LiEu_{(1-x)}Y_x(WO_4)_2$ series decrease as the amount of Y^{3+} increases. This reduction occurs due to the substitution of Y^{3+} which has a smaller ionic radius than Eu^{3+} and therefore the substitution of Eu^{3+} with Y^{3+} results in volume contractions on both structures. In Figure 5.9 (a) and (b) the cell parameters do not show dramatic changes with the Y^{3+}concentration, but it can be seen that the cell contractions are most apparent as reductions on *c* cell parameter of the lattices. This is not surprising as the *c* cell parameters are the longest cell lengths.

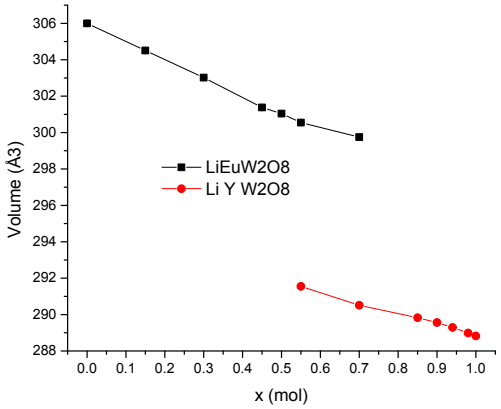

Figure 5.8: Cell volumes of tetragonal $LiEu(WO_4)_2$ and monoclinic $LiY(WO_4)_2$

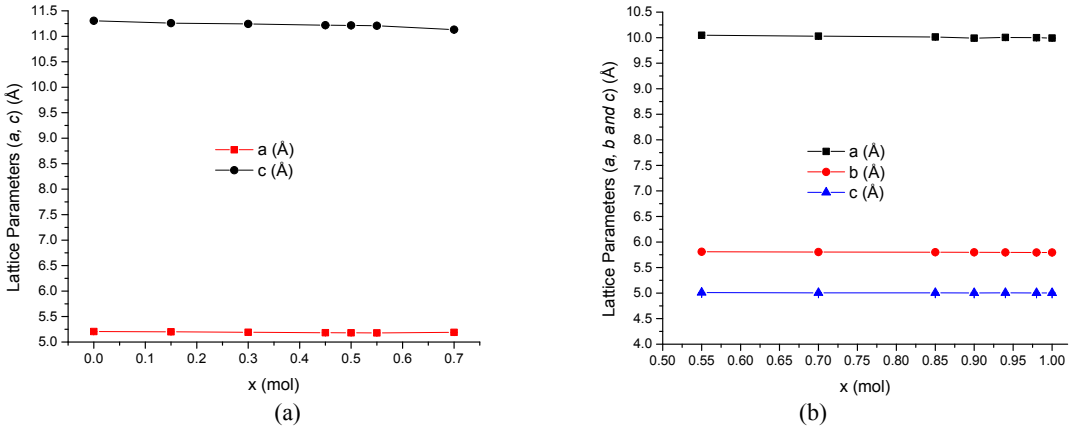

Figure 5.9: Lattice parameters of (a) tetragonal $LiEu(WO_4)_2$ and (b) monoclinic $LiY(WO_4)_2$

Figure 5.10 shows schematic diagrams representing the refined crystal structures of (a) the $LiEu(WO_4)_2$ sample which has a tetragonal structure I41/a:2 and (b) $LiY(WO_4)_2$ which has a monoclinic structure P2/n after Eu^{3+} has been completely

substituted with Y^{3+}. Li/Eu ions in $LiEu(WO_4)_2$ have eight coordination while W^{6+} ions are surrounded by 4 oxygen ions in a tetrahedral coordination. Whereas $LiY(WO_4)_2$ is assigned to a structure where Li, Y and W ions are all surrounded by oxygen ions in a well-organized octahedral coordination with slightly deformed lattice angles.

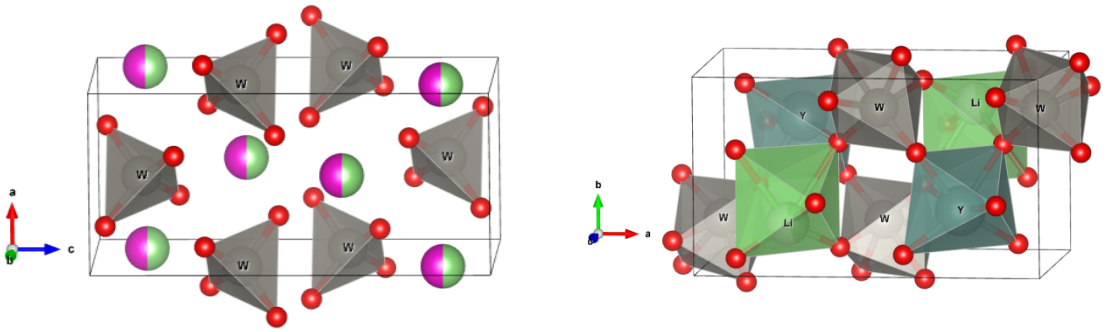

(a) (b)

Figure 5.10: Modelled crystal structure of (a) tetragonal $LiEu(WO_4)_2$ and (b) monoclinic $LiY(WO_4)_2$

5.2.1.2 Photoluminescence properties

The next focus is on the photoluminescence properties of the substituted compounds presented in Figure 5.11 and Figure 5.12. The emission spectrum of the parent unsubstituted Eu^{3+} compound is in the wavelength range from 585 nm to 720 nm. Particularly the bands near 615 nm related to $^5D_0 \rightarrow {}^7F_2$ transition experience notable loss of intensity with increase in Y^{3+} concentration when excited at 395 nm. Such a declining trend appears to agree with the overlaid XRPD results in Figure 5.6 which suggests that although the symmetry of the emission centres is not altered when more Y^{3+} cations (below 50%) are incorporated into the lattice, there is less Eu^{3+} present and so the overall emission decreases. Until 50% Y^{3+} concentration the emission reduces gradually as presented in Figure 5.11, above 50% Y^{3+} concentration the rate of decline is much greater in line with the change in structure to the monoclinic $LiY(WO_4)_2$. Clearly from these results the emission properties of the Eu^{3+} cations in the monoclinic $LiY(WO_4)_2$ lattice are inferior to those of the same cation in the tetragonal $LiEu(WO_4)_2$ lattice or that in the former phase the Eu^{3+} cations do not emit (if they do emit they must be in a lattice site that is identical to that of the tetragonal structure as the spectra shows no signs of new emission bands). In addition the spectra in Figure 5.11 and Figure 5.12 do both show some emission for the 85% Y^{3+} concentration suggesting that either the emission arises from a very small amount

of the tetragonal phase being present (though there is no evidence from the XRPD analysis set out above) or the monoclinic phase emits the same spectra as the tetragonal phase.

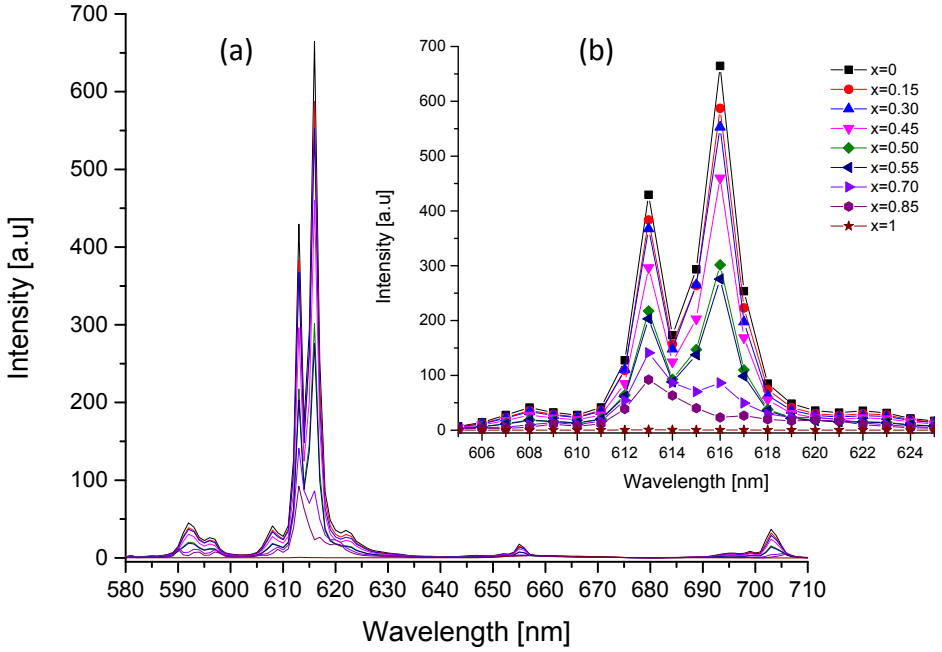

Figure 5.11: Emission spectra of $LiEu_{(1-x)}Y_x(WO_4)_2$ excited at 395nm as seen (a) from range of 585-720 nm and (b) at closer range from 610 – 620 nm

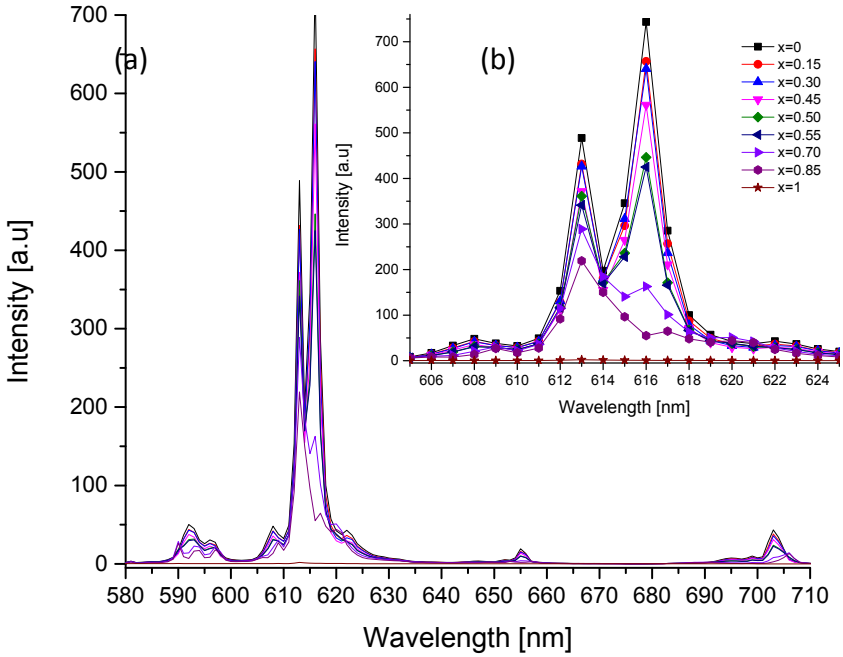

Figure 5.12: Emission spectra of $LiEu_{(1-x)}Y_x(WO_4)_2$ excited at 465nm as seen (a) from 585-720 nm and (b) close up 610 – 620 nm

The Luminous efficacies of the spectra obtained from the measurements are listed in Table 5.3. The highest luminous efficacy is found to be associated with the parent Eu^{3+} compound with 172.7 lm/W when excited at 395 nm and 202.6 lm/W when excited at 465 nm. The luminous efficacies drop gradually till a concentration of 45% Y^{3+}, then drop more swiftly almost by 50% when the concentration ratio of Y^{3+} and Eu^{3+} are equal. After that the luminous efficacies measured at both excitation wavelengths drop much further as Y^{3+}concentration reaches 0.85 mol and they disappear when Eu^{3+} is completely substituted. The trends of luminous efficacies as observed in Figure 5.13 (a) and (b) again confirms that the luminous efficacy of the $LiEu(WO_4)_2$ phosphor is highly affected when $Y^{3+}$is incorporated. Such demise in luminous efficacy above 50% Y^{3+} concentration is due to a change in crystal structure of the compound which has affected the symmetry of the Eu^{3+}site. However at 45% Y^{3+} substitution the luminous efficacy is still around 66% of that the parent tetragonal $LiEu(WO_4)_2$ phosphor. So substitution of 45% Eu^{3+} only reduces the emission by one third. So it is advantageous to replace the expensive Eu^{3+} cations with the much less expensive Y^{3+} cations up to this value.

Table 5.3: Luminous efficacies of $LiEu_{(1-x)}Y_x(WO_4)_2$ excited at (a) 395nm and (b) 465 nm

x (Mol)	Luminous Efficacy (lm/W)	
	exc 395 nm	exc 465 nm
0	172.7	202.6
0.15	153.7	182.2
0.3	133.6	168.0
0.45	119.4	159.6
0.5	86.3	138.5
0.55	78.2	130.4
0.7	46.4	77.2
0.85	24.9	46.3
1	0	0

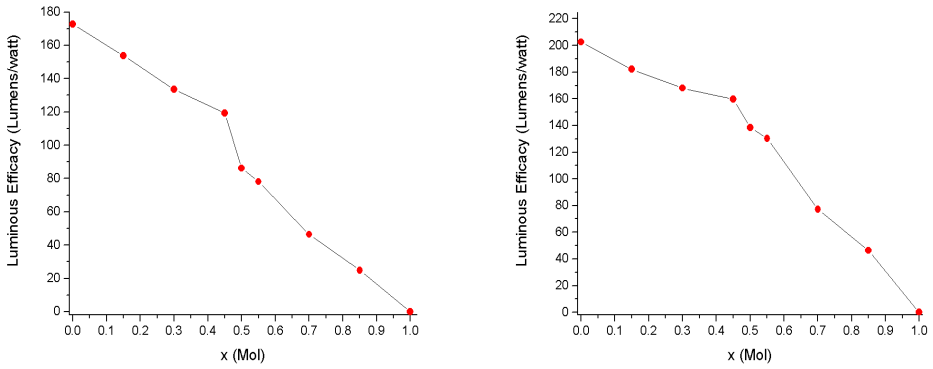

(a) (b)

Figure 5.13: Luminous efficacies of $LiEu_{(1-x)}Y_x(WO_4)_2$ excited at (a) 395nm and (b) 465 nm

The CIE colour coordinates and colour temperature of these phosphors are listed in Table 5.4 whereas the positions of the coordinates in the CIE diagram are shown in Figure 5.15 and Figure 5.16. As can be seen from the table and figures when the phase of the crystal structure of the compound changes, it slightly influences the colour coordinates of the emissions from the compound. Therefore the colour emitted from this compound is sensitive to any changes of Eu^{3+}electronic environment. With increasing Y^{3+} concentration it slowly moves to higher colour temperature which is indicative of quenching in the higher Eu^{3+} concentrations. Again this also shows that although the substitution of Eu^{3+} does change the colour coordinates slightly, it also increases the relevant efficacies as it cuts down on the quenching. It must be stated however, that there was little evidence of line broadening in the higher Eu^{3+} concentrations which would have been further evidence of quenching (see the normalized spectra of $LiEu_{(1-x)}Y_x(WO_4)_2$ in Figure 5.14).

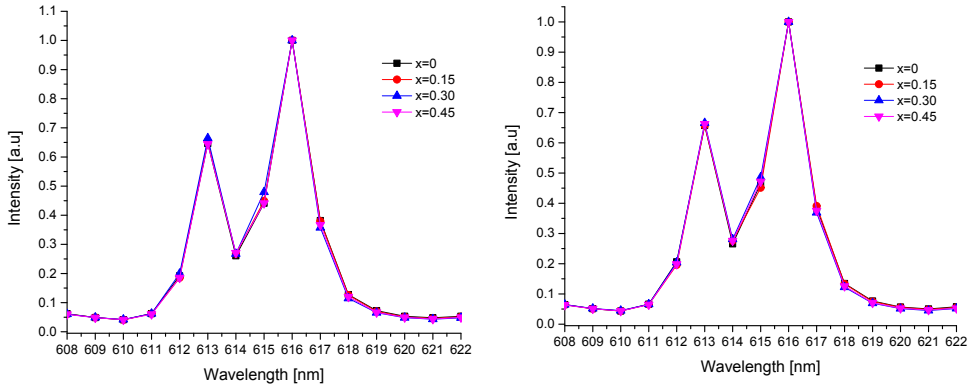

Figure 5.14: Normalized spectra of $LiEu_{(1-x)}Y_x(WO_4)_2$ excited at (a) 395 nm and (b) 465 nm

Table 5.4: CIE Colour coordinates of $LiEu_{(1-x)}Y_x(WO_4)_2$

No.	Y^{3+} Concentration (mol)	Exc 395 nm			Exc 465 nm		
		Coordinates		Colour temp	Coordinates		Colour temp
		x	y		x	y	
1	0	0.6692	0.3306	889 K	0.6692	0.3306	889 K
2	0.15	0.6694	0.3304	887 K	0.6693	0.3305	888 K
3	0.30	0.6693	0.3305	888 K	0.6692	.3305	888 K
4	0.45	0.6691	0.3306	889 K	0.6691	0.3307	890 K
5	0.50	0.6689	0.3309	891 K	0.6683	0.3315	895 K
6	0.55	0.6683	0.3315	895 K	0.6687	0.3310	892 K
7	0.70	0.6672	0.3326	903 K	0.6668	0.3329	892 K
8	0.85	0.6664	0.3334	909 K	0.6660	0.3338	912 K
9	1	N/A					

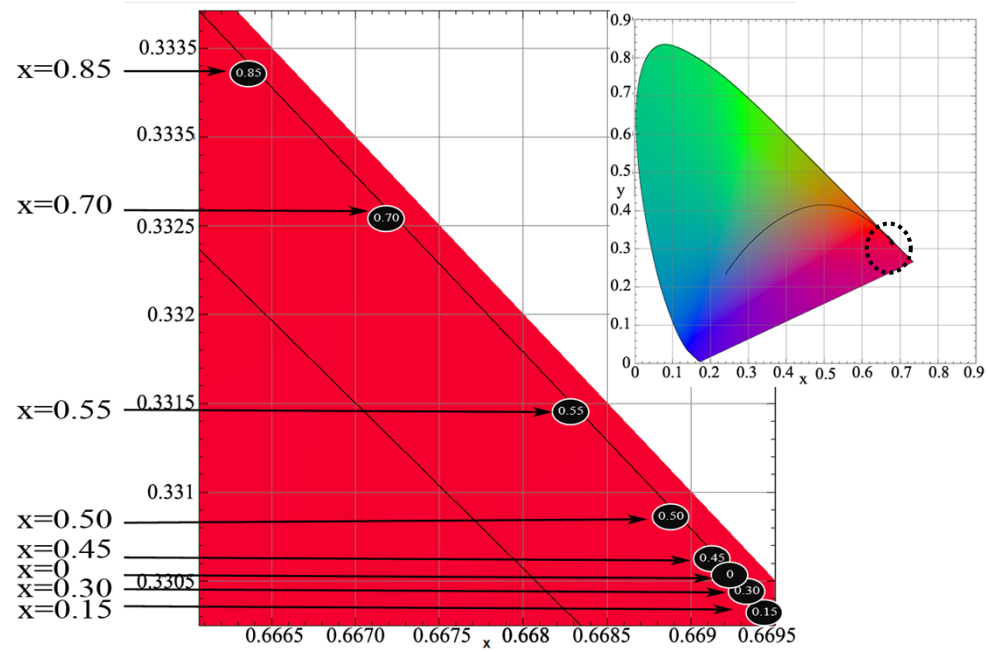

Figure 5.15: CIE diagram for $LiEu_{(1-x)}Y_x(WO_4)_2$ excited at 395 nm

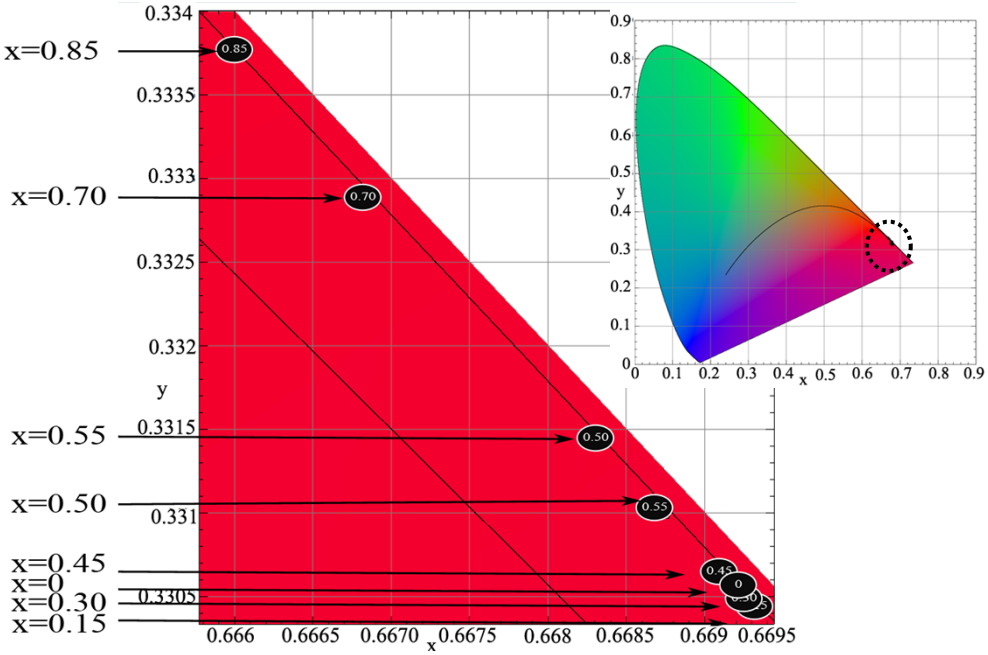

Figure 5.16: CIE diagram for $LiEu_{(1-x)}Y_x(WO_4)_2$ excited at 465 nm

5.2.2 Incorporation of Y^{3+} into Molybdate host lattices

5.2.2.1 Powder Crystallography

Figure 5.17 shows the XRPD results for the series of $LiEu_{(1-x)}Y_x(MoO_4)_2$ XRPD results acquired (where x ranges from 0 to 1). The figure implies that there is

no major phase transformation experienced by the initial tetragonal $LiEu(MoO_4)_2$ structure. There are however, other possible explanations on little shifts on most of the diffracted lines when $2\theta \approx$ 29.5, 34.5, 49.5, 55 and 60 towards higher values of the diffraction angle. This is because an alteration in composition leads to changes in lattice parameters and therefore results in a shift of diffraction lines. Such changes in the lattice by swapping Eu^{3+} with smaller Y^{3+} decreases the lattice parameters as the ionic radius of Y^{3+} is slightly smaller than that of Eu^{3+}. The tetragonal phase of $LiY(MoO_4)_2$ is in a good agreement with a number of findings [1-3, 13, 14]and particularly from Kolitsch [15] who reported details on the crystal structure of $LiY(MoO_4)_2$.

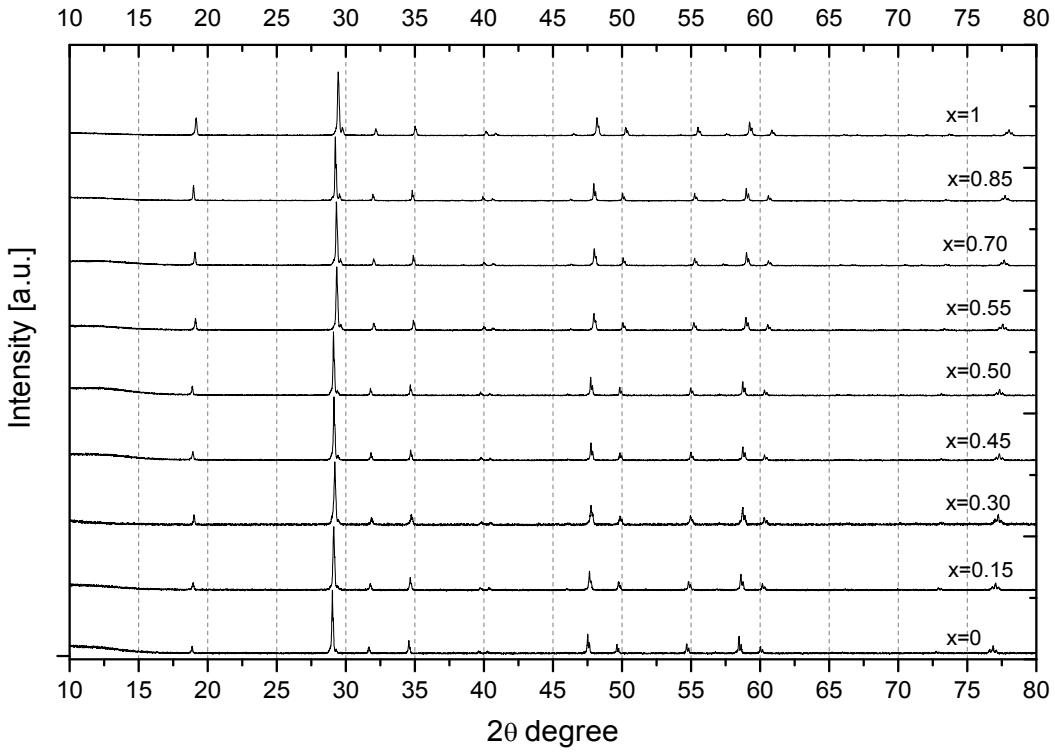

Figure 5.17: XRPD patterns of the $LiEu_{(1-x)}Y_x(MoO_4)_2$ series (where x is in the range 0 to 1)

All XRPD results of $LiEu_{(1-x)}Y_x(MoO_4)_2$ were subsequently refined using Retvield refinement with the aid of TOPAS software. Considering that during the time of this work undertaken there was no $LiEu(MoO_4)_2$ reference model obtainable in the ICSD database (although the details of the crystal structure have been reported [15]); Therefore the nearest reference model needed to be selected. $LiEu(WO_2)_4$ was chosen for the reference model for the Retvield analysis. This selection was made due to a presumption that the $LiEu_{(1-x)}Y_x(MoO_4)_2$ materials should possess similar scheelite type crystal structures as in $LiEu(MoO_4)_2$ as found in the literature [1, 14-

17]. In addition the ionic radii of both W^{6+} and Mo^{6+} are both close (0.42 Å for W^{6+} and 0.41 Å for Mo^{6+} and both sizes are referred based on 8 coordination numbers).

Since no changes were observed in the diffraction peaks of the overlaid XRPD patterns in Figure 5.17, the crystal structures of all samples were regarded as unaltered through the entire experiments. However the reference model selected was modified to fit sensibly with the real samples especially by changing the Eu^{3+} with Y^{3+} and substituting the original W^{6+} with Mo^{6+}. The lattice parameters and cell volumes based on the Retvield refinement of the XRPD results are presented in Table 5.5 which shows that the lattice's volume decreases about 3.4 % from 306.548 $Å^3$ to 296.1859 $Å^3$.

Table 5.5: Lattice parameters changes of $LiEu_{(1-x)}Y_x(MoO_4)_2$

Y^{3+} (mol)	Tetragonal I41/a:2			R_{wp}
	a (Å)	c (Å)	Vol ($Å^3$)	
0	5.20138(9)	11.3308(3)	306.55(1)	9.81
0.15	5.1936(1)	11.3114(3)	305.11(1)	9.59
0.30	5.1848(2)	11.2878 (5)	303.44(2)	11.23
0.45	5.17659(8)	11.2646 (2)	301.86(1)	9.65
0.50	5.17324(7)	11.2582(2)	301.30(1)	9.57
0.55	5.17042(8)	11.2510(2)	300.77(1)	9.30
0.70	5.16218(6)	11.2286(2)	299.220(9)	9.28
0.85	5.15454(4)	11.2032(1)	297.661(6)	9.25
1	5.14629(6)	11.1835(2)	296.186(8)	9.73

The lattice parameters listed in Table 5.5 are plotted as presented in Figure 5.18 (a) and (b). From the graphs, the contraction of the volumes are more affected by the *c* cell dimension compared to the *a=b* cell dimensions. The figures show gradual decreases of both cell volumes and lattice parameters when the concentration of Y^{3+} rises.

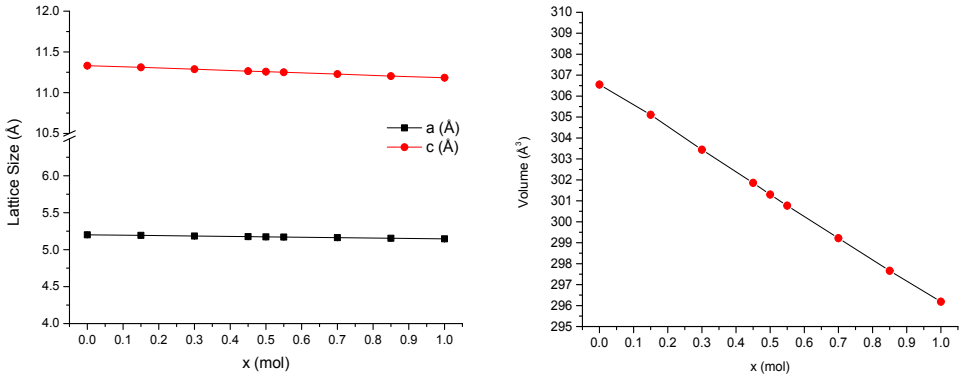

Figure 5.18: (a) Cell volumes and (b) Lattice parameters of $LiEu_{(x-1)}Y_x(MoO_4)_2$

The image of refinement fitting presented in Figure 5.19 suggests that the XRPD profile fits nicely with $LiY(MoO_4)_2$ model with R_{wp} 9.73. This result was obtained by keeping the occupancy of Mo^{6+} fixed to 1, whilst Li^+ and Y^{3+} cations were set from the software to share occupancies in the same sites. The site occupancies of $LiY(MoO_4)_2$ as presented in Table 5.6 indicate that Y^{3+} occupies the site with an occupancy factor of 0.4867 while Li^+ are found to occupy the site of Y^{3+} with occupancy factor of 0.5133. The occupancy factors are pertinent after taking into consideration the fitting of the refined data it is apparent that both Li^+ and Y^{3+} cations occupy the same lattice sites in approximately a 1:1 ratio.

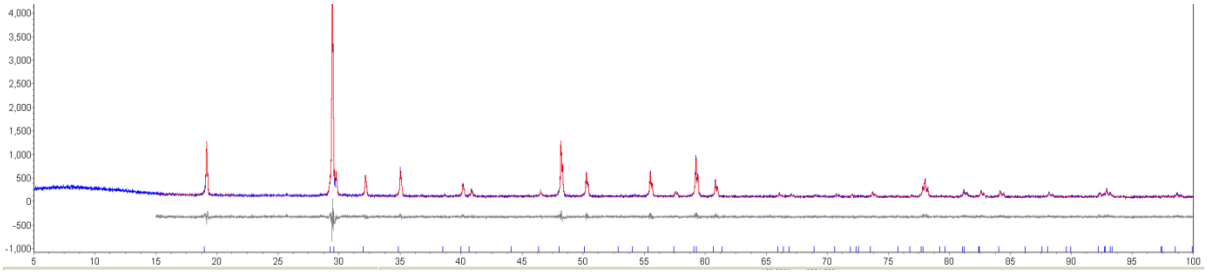

Figure 5.19: Retvield refinement of $LiY(MoO_4)_2$ against ICSD collection code 261840 [4]

Table 5.6: Site occupancies of $LiY(MoO_4)_2$

Np	Site	x	y	z	Atom	Occ
Mo	4	0.50000	0.75000	0.12500	Mo^{+6}	1
Y	4	0.00000	0.25000	0.12500	Y^{+3}	0.4867(36)
					Li^{+1}	0.5133(36)
O	16	0.74031(86)	0.0902(12)	-0.03893(40)	O^{-2}	0.914(12)

A model of the compound structure was generated and is presented in Figure 5.20 (a) and (b) detailing the scheelite structure of $LiY(MoO_4)_2$. The figures present a single lattice that consists of 3 formulae of $LiY(MoO_4)_2$ with eight oxygens surrounding Y^{3+} or Li^+ cations as presented in Figure 5.20 (a)and each Mo^{6+} has four oxygens coordinated to it making an overall tetrahedral shape isolating $(MoO_4)^{2-}$ in the lattice. Such coordination of oxygens to the other neighbouring elements shows that the Li^+ and Y^{3+}cations have eight coordination. Table 5.5 shows the way in which the tetragonal 141/a lattice's volume decreases 3.38 % from 306.548 $Å^3$ to 296.1859 $Å^3$ as the concentration of Y^{3+} increases. The contraction of the volume seems to be more affected by *c* cell dimension of the lattice rather than *a=b* cell dimensions as discussed earlier based on Figure 5.13.

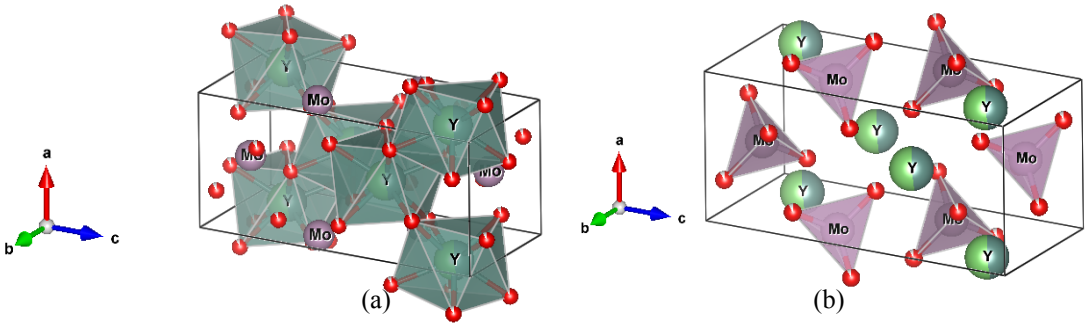

Figure 5.20: Scheelite modelled structure of $LiY(MoO_4)_2$ that shows (a) eight oxygen anions surrounding Eu/Li cations and (b) the tetrahedral shape of oxygens isolating $(MoO_4)^{2-}$ in a lattice.

5.2.2.2 Photoluminescence Properties

Figure 5.21 and Figure 5.22 show the emission spectra of $LiEu_{(1-x)}Y_x(MoO_4)_2$ excited at 395 nm and 465 nm respectively. No significant shifts from the spectra can be observed from the figures and the changes in intensity between the highest and the lowest luminescence spectra are also not too wide, showing that the intensities do not decline so obviously as a function of falling Eu^{3+} concentration. The emission bands observed at a few wavelength ranges at 588–600 nm ($^5D_0 \rightarrow {}^7F_1$ transition), 610–630 nm ($^5D_0 \rightarrow {}^7F_2$ transition), 650–660 nm ($^5D_0 \rightarrow {}^7F_3$ transition) and 690–710 nm ($^5D_0 \rightarrow {}^7F_4$ transition) are all related to the transitions of the excited state of Eu^{3+}in these phosphors. Interestingly unlike the results for the $LiEu_{(1-x)}Y_x(WO_4)_2$ series described above, as Y^{3+} was incorporated the observed emission spectra of $LiEu_{0.15}Y_{0.85}(MoO_4)_2$ series still achieves about three quarter of the initial $LiEu(MoO_4)_2$ intensity when excited at 395nm and about a half when excited at 465 nm at very high Y^{3+} concentrations.

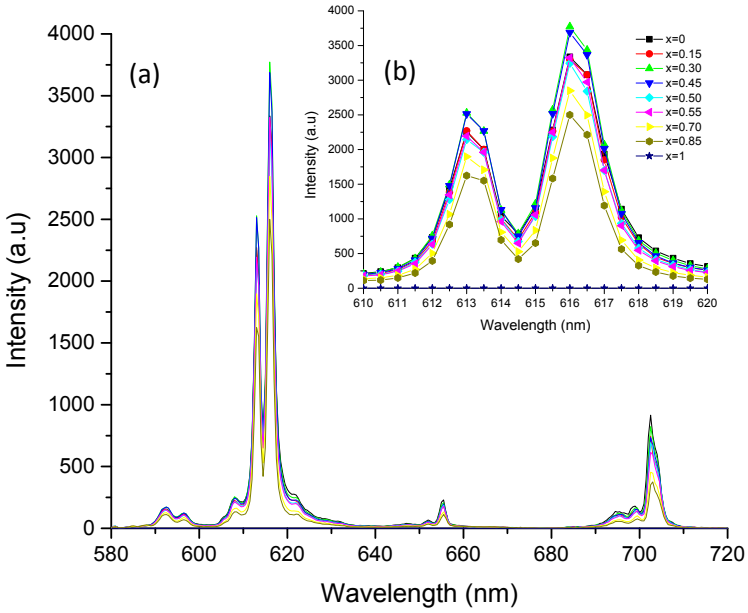

Figure 5.21: Emission spectra of Li $Eu_{(1-x)}Y_x(MoO_4)_2$ excited at 395nm as seen (a) from range of 580-720 nm and (b) at closer range from 610 – 620 nm

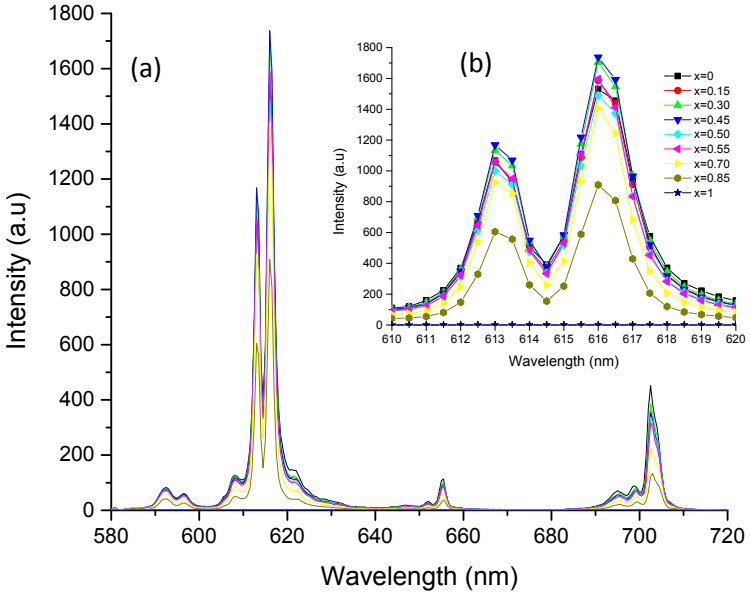

Figure 5.22: Emission spectra of $LiEu_{(1-x)}Y_x(MoO_4)_2$ excited at 465nm as seen (a) from range of 570-720 nm and (b) at closer range from 610 – 620 nm

Luminous efficacies are listed in Table 5.7 and plotted inFigure 5.24 (a) and (b). The luminous efficacies measured for $LiEu_{(1-x)}Y_x(MoO_4)_2$ when excited at 395nm as in Figure 5.24(a) reveal that $LiEu(MoO_4)_2$ produces 163.33 lm/W whereas $LiEu_{0.15}Y_{0.85}(MoO_4)_2$ still yields 122.36 lm/W. Likewise the luminous efficacies of

$LiEu(MoO_4)_2$ and $LiEu_{0.15}Y_{0.85}(MoO_4)_2$ when excited at 465 nm are 199.28 lm/W and 118.28 lm/W respectively. The results of Y^{3+} concentration on the luminous efficacy as seen on $LiEu_{0.15}Y_{0.85}(MoO_4)_2$ indicate that as the concentration of Eu^{3+}falls the luminous efficacies remain fairly constant. The reason for this is obviously due to a number of factors but one is that in this series of phosphors the initial tetragonal phase of the parent Eu^{3+} compound does not change.

This means that the substitution of Eu^{3+} by Y^{3+} in $LiEu_{1-x}Y_x(MoO_4)_2$ has no effect on the site symmetry of the emission centres by at least until the ratio between Y^{3+} and Eu^{3+} ratio reaches 0.55:0.45 and even then the luminescent centre is not highly affected when the ratio is up to 0.85:0.15. The unaffected symmetry of the luminescent centre therefore allows the same interaction to happen between the Eu^{3+} (due to the same energy level of the activator) and the host efficiently. Figure 5.24 (a) and (b) also shows gradual rises of the luminous efficacies as the amount of Eu^{3+}cations are substituted with Y^{3+}cations until it reaches the maximum peak at 0.45 mol of Y^{3+}. This must be due to the change in volume of the lattice induced by the inclusion of the Y^{3+} cations. It appears that the lattice size around 45% inclusion of Y^{3+} manifests the highest luminous efficacies then as the lattice gets smaller still the luminous efficacies decrease.

In Figure 5.23, the spectra are normalised and it is apparent that the line-width decreases as a function of falling Eu^{3+} concentration. This indicates that in the parent $LiEu(MoO_4)_2$ phosphor concentration quenching is taking place. It is well known that too much concentration of activator in a compound can result in a quicker migration of excited energy across the material via cross relaxation process and this leads to a lowering of the desired emission. Therefore for $LiEu_{(1-x)}Y_x(MoO_4)_2$compound, Y^{3+} at 0.45 mol appears to be the most effective concentration and it can be employed in acquiring the most efficient luminescence. It is therefore apparent that cheaper phosphors than $LiEu(MoO_4)_2$ can be made by incorporating 45% or more of Y^{3+} into the lattice depending on the desired luminous efficacy. The Y concentration can be increased to 70% without a dramatic drop when excited at 465nm.

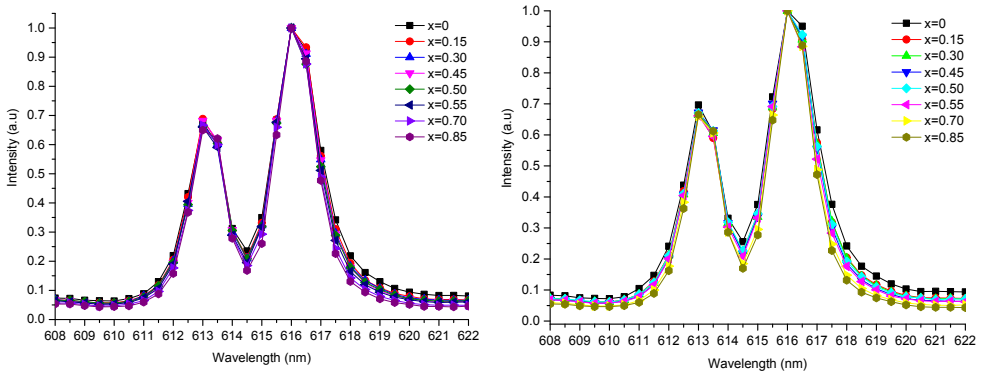

(a) (b)

Figure 5.23: Normalized spectra of $LiEu_{(1-x)}Y_x(MoO_4)_2$ excited at (a) 395nm and (b) 465 nm

Table 5.7: Luminous efficacies of $LiEu_{(1-x)}Y_x(MoO_4)_2$ excited at (a) 395nm and (b) 465 nm

x (mol)	Luminous Efficacy	
	exc 395 nm	exc 465 nm
0	163.33	199.28
0.15	162.41	204.56
0.3	175.66	215.04
0.45	176.49	217.17
0.5	161.78	204.86
0.55	162.69	207.68
0.7	139.40	182.91
0.85	122.37	118.28
1	0	0

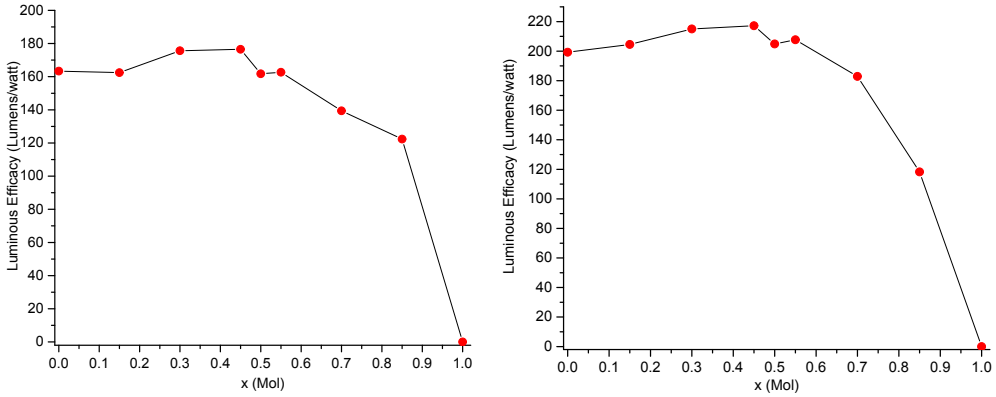

(b) (b)

Figure 5.24: Luminous efficacies of $LiEu_{(1-x)}Y_x(MoO_4)_2$ excited at (a) 395nm and (b) 465 nm

Table 5.8 shows the CIE colour coordinates of $LiEu_{(1-x)}Y_x(MoO_4)_2$ from x=0 until x=1. It can be observed from the table that the colour temperature of the phosphor is largely unaffected by the presence of Y^{3+} thus the colour temperature does

not change much until it reaches x=0.55 and only starts changing notably afterwards (see the CIE diagrams in Figure 5.25 and Figure 5.26).

Table 5.8: CIE Colour coordinates of Li $Eu_{(1-x)}Y_x(MoO_4)_2$ when excited at 395 nm

No.	Yttrium Concentration (mol)	Exc 395 nm			Exc 465 nm		
		Coordinates		Colour temp	Coordinates		Colour temp
		x	y		x	y	
1	0	0.6720	0.3278	870 K	0.6718	0.3280	869 K
2	0.15	0.6716	0.3282	943 K	0.6713	0.3285	871 K
3	0.30	0.6715	0.3283	949 K	0.6711	0.3286	872 K
4	0.45	0.6712	0.3286	950 K	0.6708	0.3289	874 K
5	0.50	0.6711	0.3291	954 K	0.6704	0.3293	875 K
6	0.55	0.6706	0.3302	962 K	0.6700	0.3297	878 K
7	0.70	0.6695	0.3305	990 K	0.6686	0.3311	886 K
8	0.85	0.6668	0.3312	1029 K	0.6653	0.3343	906 K
9	1	0.5142	0.4858	N/A	0.5125	0.4816	N/A

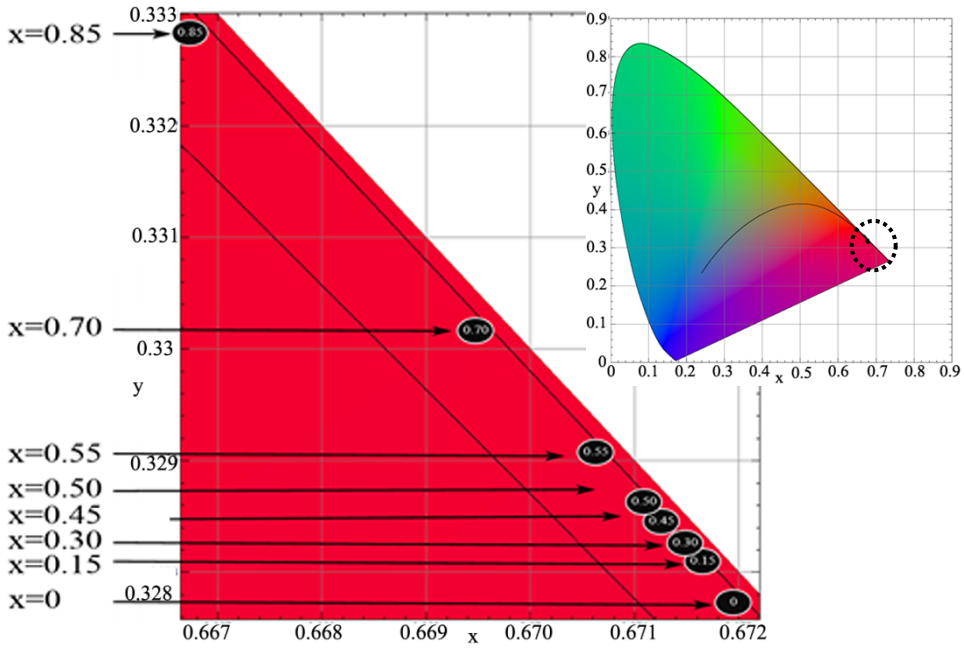

Figure 5.25: CIE diagram for $LiEu_{(1-x)}Y_x(MoO_4)_2$ excited at 395nm

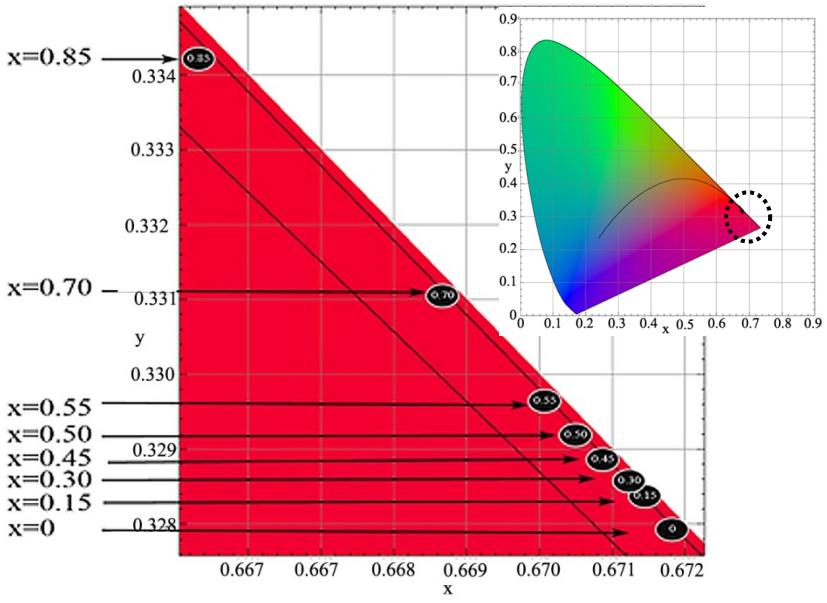

Figure 5.26: CIE diagram for $LiEu_{(1-x)}Y_x(MoO_4)_2$ excited at 465nm

5.2.3 Incorporating of Y^{3+} into Molybdate-Tungstate host lattices

5.2.3.1 Powder Crystallography

After observing that;-

a) the phase of tetragonal double tungstate phosphor compounds (see above) changes as concentration of Y^{3+} increases raises and that

b) no phase changes were seen in the double molybdate compounds (see above),

the obvious next step was to look at the effect of substituting Eu^{3+} with Y^{3+} in a series of molybdate-tungstate; $LiEu_{(1-x)}Y_x(WO_4)(MoO_4)$ compounds. Figure 5.27 presents the XRPD diffraction patterns in overlay of $LiEu_{(1-x)}Y_x(WO_4)(MoO_4)$ where x is ranged from 0 to 1. The results of the XRPD studies indicate that the molybdate-tungstate phosphor does not experience phase changes as Eu^{3+} in the compound is substituted by Y^{3+}. The only observed differences between the $LiEu_{(1-x)}Y_x(WO_4)(MoO_4)$ compounds is that there are noticeable shifts of the diffraction peaks to higher angles which are due to the effect of smaller ions (Y^{3+}) that settle in the lattice leading to a reduction in cell size. This is in keeping with what happened to the double molybdate compounds.

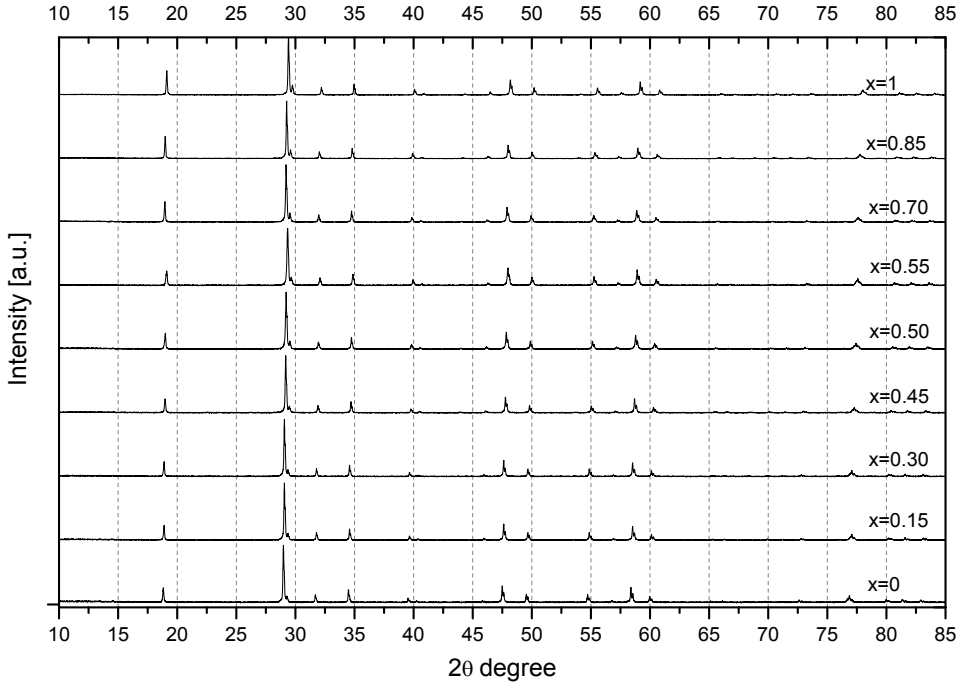

Figure 5.27: XRPD patterns of Li $Eu_{(1-x)}Y_x(WO_4)(MoO_4)$

The details of the cell volumes and lattice parameters as calculated using Retvield refinement on $LiEu_{(1-x)}Y_x(WO_4)(MoO_4)$ are presented in Table 5.9. The same model of $LiEu(WO_4)_2$ compound as discussed in 5.1.1 was chosen again as the reference since that was the closest reference can be obtained from the ICSD online database. The model was however modified in TOPAS software mainly by changing the Eu^{3+} to Y^{3+} ratio and one site occupied by W^{6+} was replaced with Mo^{6+} to become $LiY(WO_4)(MoO_4)$. The changes were made to ensure that the model could be set as close as possible to the patterns obtained in the XRPD results. The R_{wp} values as can be observed from Table 5.9 are higher than those obtained for the $LiEu_{(1-x)}Y_x(MoO_4)_2$. Although the R_{wp} values are slightly larger than usual the difference between calculated and measured data is visually minimal and can be judged from the grey line as presented in Figure 5.28.

The Mo^{6+} and W^{6+} were arranged so that they occupy identical sites with both occupancy factors fixed at 0.5. Concurrently Li^+ and Y^{3+} cations were refined by setting both elements to be in the same sites. Table 5.10 suggests that Y^{3+} occupies the site with an occupancy factor of 0.5077 whereas Li^+ presently occupies the site with 0.4923 factors. These findings are in good agreement with the 1:1 ratio found in the formulation in the parent compound. Figure 5.29 (a) shows the graph of the cell volumes as the amount of Y^{3+}cations increases substituting for the Eu^{3+} cations. From

the figure it can be seen that the cell volume of the initial parent compound $LiEu(WO_4)(MoO_4)$ reduces linearly as the smaller Y^{3+} cations are substituted into the cell. This indicates that Y^{3+} has successfully substituted Eu^{3+} in the original sites. The result of the shrinking volumes is elaborated by looking at Figure 5.29 (b) which again indicates the *c* cell dimension is more affected than the *a*=*b* cell dimensions and this leads to the shrinkage of the lattice as a whole.

Table 5.9: Lattice parameters of $LiEu_{(1-x)}Y_x(WO_4)(MoO_4)$

Y^{3+} (mol)	Tetragonal I41/a:2			R_{exp}	R_{wp}	R_p
	a (Å)	c (Å)	Vol (Å^3)			
0	5.20657 (9)	11.3088 (3)	306.562 (12)	12.48	13.61	10.83
0.15	5.1968938 (8)	11.2857 (2)	304.802 (11)	11.88	13.35	10.62
0.30	5.18818 (8)	11.2634 (2)	303.180 (11)	12.46	13.86	11.05
0.45	5.17955 (9)	11.2415 (3)	301.584 (13)	13.16	15.07	12.04
0.50	5.17321 (9	11.2582 (3)	301.292 (12)	8.78	11.74	8.97
0.55	5.17514 (7)	11.2283 (2)	300.718 (10)	12.11	13.42	10.60
0.70	5.16643 (6)	11.2068 (2)	299.1323 (89)	12.17	13.70	10.78
0.85	5.15876 (5)	11.1849 (2)	297.6619 (73)	12.36	14.06	10.98
1	5.15042 (5)	11.1612 (1)	296.0703 (66)	12.78	14.81	11.46

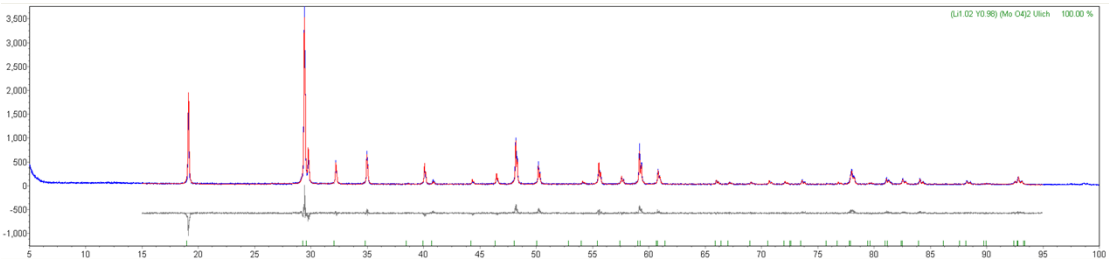

Figure 5.28: Retvield refinement of $LiY(WO_4)(MoO_4)$

Table 5.10: Site occupancies of $LiY(WO_4)(MoO_4)$

Site	Np	x	y	z	Atom	Occ
Mo/W	4	0.50000	0.75000	0.12500	Mo^{+6}	0.5
					W^{+6}	0.5
Y	4	0.00000	0.25000	0.12500	Y^{+3}	0.508(3)
					Li^{+1}	0.492(3)
O	16	0.7517(9)	0.091(1)	-0.0391(5)	O^{-2}	0.94(1)

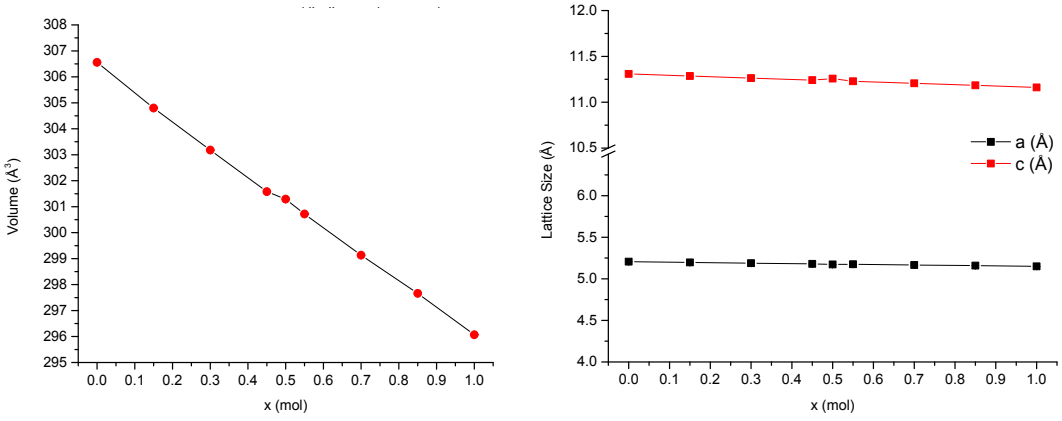

Figure 5.29: (a) Cell volumes and (b) lattice parameters of $LiEu_{(1-x)}Y_x(WO_4)(MoO_4)$

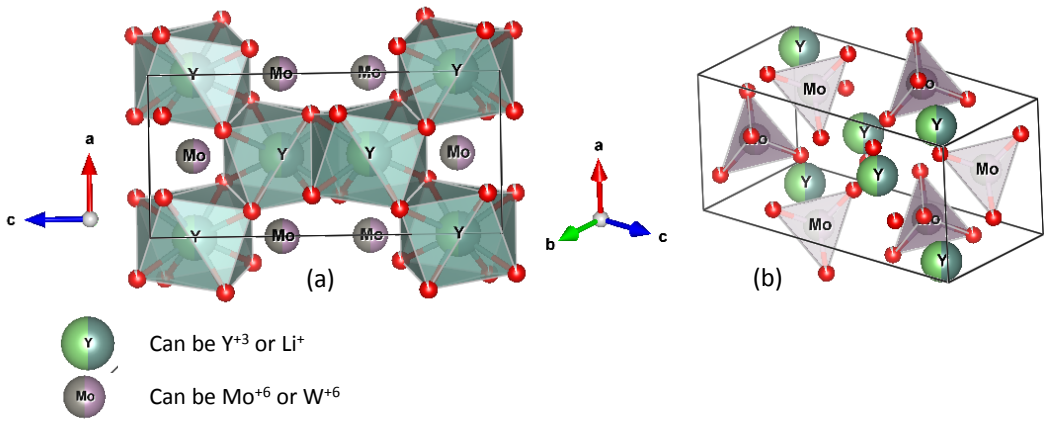

Figure 5.30: Scheelite modelled structure of $LiEu_{(1-x)}Y_x(WO_4)(MoO_4)$that shows (a) eight oxygen anions surrounding Y^{3+}/Li^{+} cations, (b) the tetrahedral shape of oxygens isolating$(WO_4)^{2-}$ and $(MoO_4)^{2-}$ in a lattice.

5.2.3.2 Photoluminescence Properties

Figure 5.31 and Figure 5.32 show emission spectra of the samples when excited at 395 nm and 465 nm respectively. All emission spectra (except the unseen spectrum of x=1) fall in regions between 588–600 nm ($^5D_0 \rightarrow {}^7F_1$), 610–630 nm ($^5D_0 \rightarrow {}^7F_2$), 610–630 nm ($^5D_0 \rightarrow {}^7F_2$), 640–662 nm ($^5D_0 \rightarrow {}^7F_3$), and 681–710 nm ($^5D_0 \rightarrow {}^7F_4$) which are no different from the parent $LiEu(WO_4)(MoO_4)$ compound. The figures also give evidence that the spectral intensity reduces as amount of Y^{3+}increases. Figure 5.33 (a) and Table 5.11 reveal that the overall trend of the luminous efficacies when excited at 395 nm is not highly affected until the ratio of Eu^{3+} to Y^{3+} reaches 0.5:0.5. In fact the phosphor still maintains nearly three quarters of the initial value as it was recorded to have 173.95 lm/W.

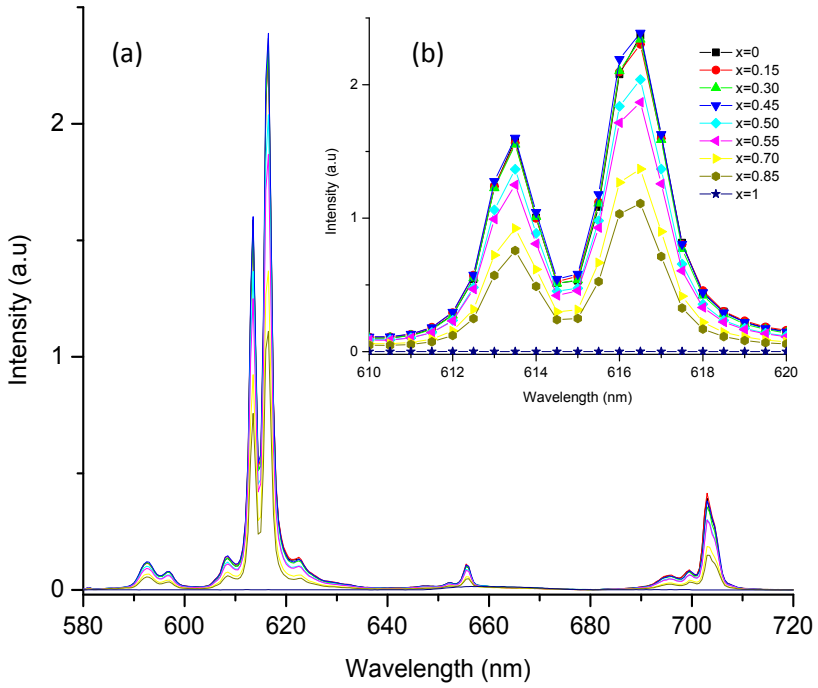

Figure 5.31: Emission spectra of $LiEu_{(1-x)}Y_x(WO_4)(MoO_4)$ excited at 395nm as seen (a) from range of 580-720 nm and (b) at closer range from 610 – 620 nm

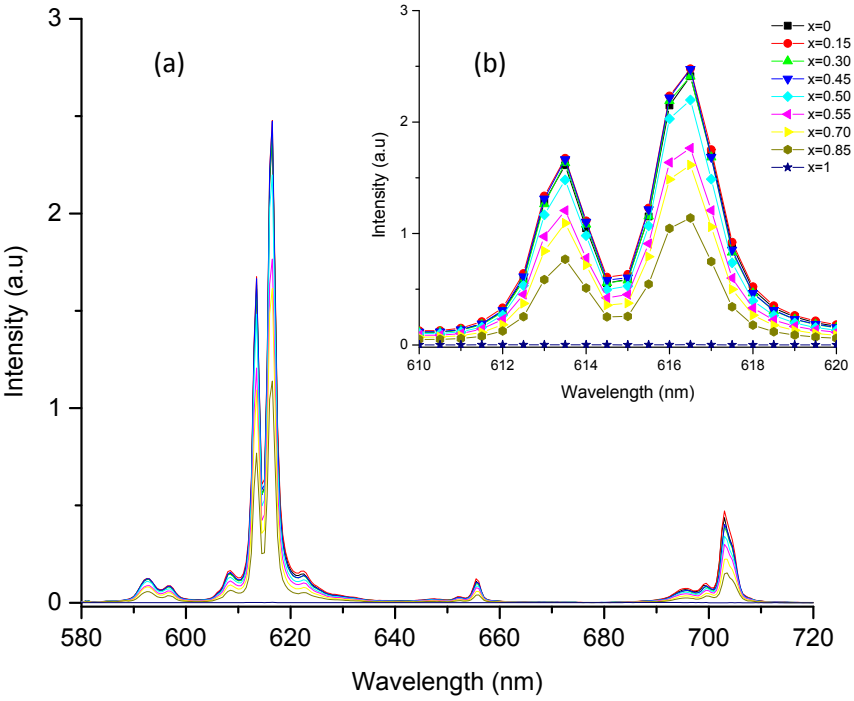

Figure 5.32: Emission spectra of $LiEu_{(1-x)}Y_x(WO_4)(MoO_4)$ excited at 465nm as seen (a) from range of 580-720 nm and (b) at closer range from 610 – 620 nm

Similarly, the luminous efficacy of the emission spectra when excited at 465 nm as shown in Figure 5.33 (b) and Table 5.11 also manifest a similar trend where the luminous efficacy only drops only about 12% when x=0.55 and it still sustains about

60% of its efficacy when x=0.85. In addition, the reddish body colour of the compound can obviously be seen degrading to become pale reddish when x=0.85. Interestingly the luminous efficacies are maximum around a volume size of 301.5Å^3, similar to the value of the maximum in the $LiEu_{(1-x)}Y_x(MoO_4)_2$ series discussed above where the best values were for a cell volume of around 301.8Å^3.

Table 5.11: Luminous efficacies of Li $Eu_{(1-x)}Y_x(WO_4)(MoO_4)$ excited at (a) 395nm and (b) 465 nm

x (Mol)	Luminous Efficacy (lm/W)	
	exc 395 nm	exc 465 nm
0	236.38	243.78
0.15	238.14	248.06
0.3	231.03	241.84
0.45	236.63	243.94
0.5	219.78	230.44
0.55	214.04	214.54
0.7	174.80	190.15
0.85	124.65	150.15
1	N/A	N/A

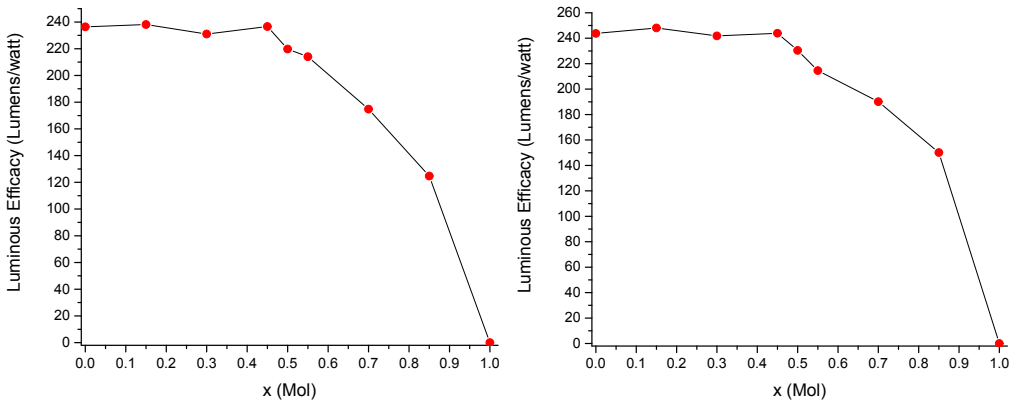

(a) (b)

Figure 5.33: Luminous efficacies of $LiEu_{(1-x)}Y_x(WO_4)(MoO_4)$ excited at (a) 395nm and (b) 465 nm

The normalized spectra when excited at 395 nm and 465 nm (see Figure 5.34) indicate that again the line-width decreases with respect to the falling Eu^{3+} concentration. This explains that in the parent $LiEu(WO_4)(MoO_4)$ phosphor concentration quenching is already taking place. CIE colour coordinates of these compounds are presented in Table 5.12 and the coordinates are plotted in the CIE diagram shown in Figure 5.35 and Figure 5.36. It can be observed from the table and figures that the colour coordinates are not significantly affected as the concentration of Y^{3+} increases replacing the Eu^{3+}cations until concentrations of 0.70 mol and above.

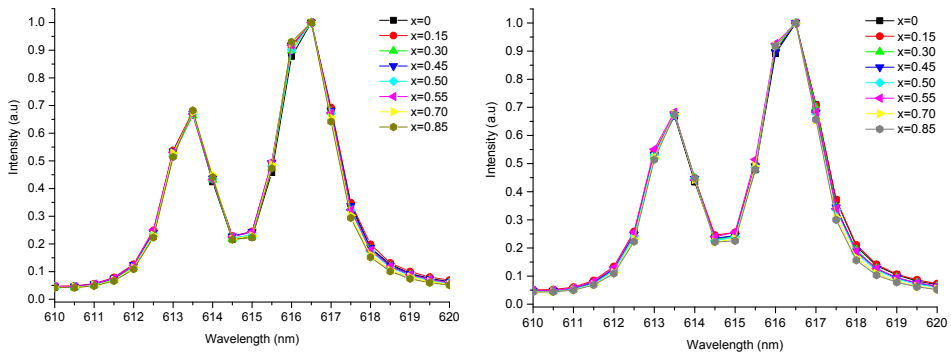

(a) (b)

Figure 5.34: Normalized spectra of $LiEu_{(1-x)}Y_x(MoO_4)(WO_4)$ excited at (a) 395nm and (b) 465 nm

Table 5.12: CIE Colour coordinates of Li $Eu_{(1-x)}Y_x(MoO_4)(WO_4)$ when excited at 395 nm and 465 nm.

No.	Yttrium Concentration (mol)	Exc 395 nm			Exc 465 nm		
		Coordinates		Colour temp	Coordinates		Colour temp
		x	y		x	y	
1	0	0.6715	0.3282	872 K	0.6705	0.3290	878 K
2	0.15	0.6723	0.3275	866 K	0.6720	0.3278	869 K
3	0.30	0.6721	0.3277	868 K	0.6716	0.3282	872 K
4	0.45	0.6719	0.3279	869 K	0.6715	0.8283	872 K
5	0.50	0.6718	0.3279	870 K	0.6713	0.3285	873 K
6	0.55	0.6718	0.3280	870 K	0.6713	0.3285	873 K
7	0.70	0.6713	0.3285	873 K	0.6706	0.3292	878 K
8	0.85	0.6706	0.3292	878 K	0.6697	0.3301	885 K
9	1	N/A					

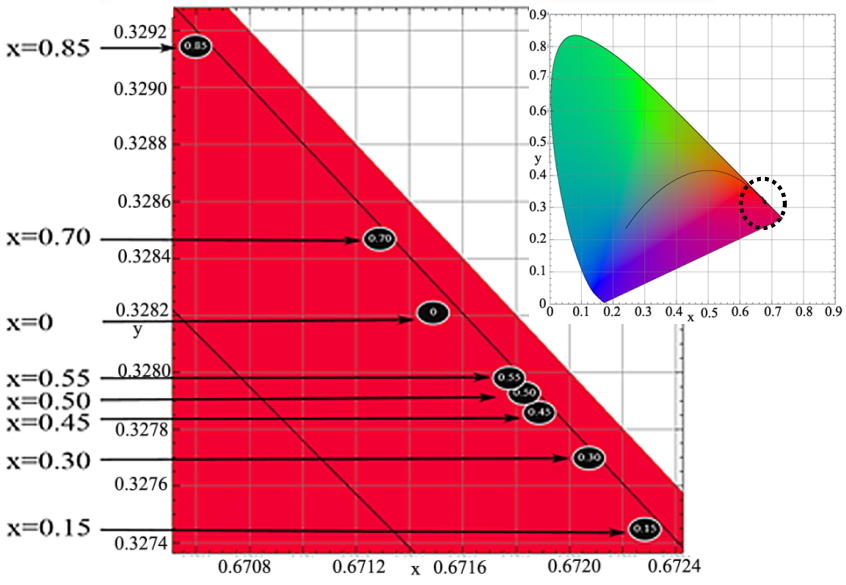

Figure 5.35: CIE diagram for $LiEu_{(1-x)}Y_x(MoO_4)(WO_4)$ excited at 395nm

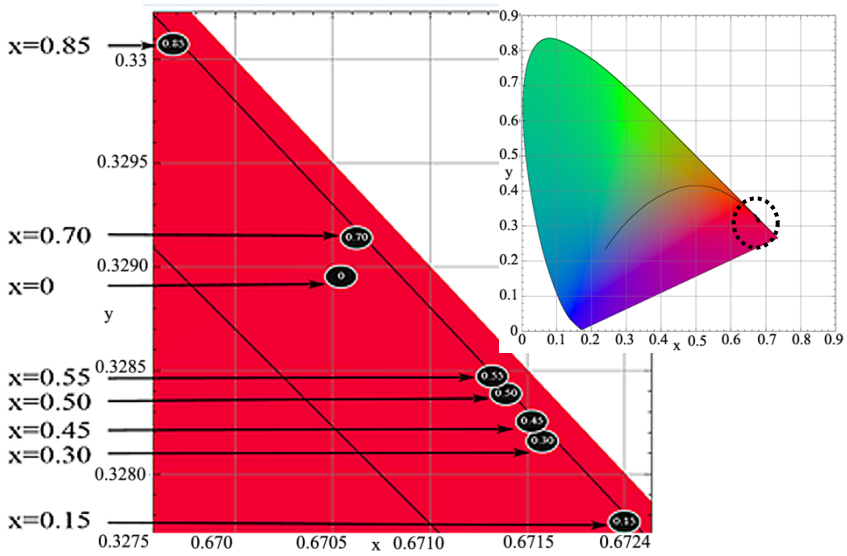

Figure 5.36: CIE diagram for $LiEu_{(1-x)}Y_x(MoO_4)(WO_4)$ excited at 465nm

In common with the findings for the double molybdate phosphors, these tungstate-molybdate phosphors starts to change their colour coordinates significantly when the molarity ratio of Y^{3+} to Eu^{3+} reaches 0.85:0.15 and move towards colder temperature region.

5.3 SEM images

Unlike the tetragonal $LiEu(WO_4)_2$ particles that exhibited a spherically shaped surface morphology, the morphological view of the monoclinic $LiY(WO_4)_2$ powder shows angular shapes without any admixture of any impurity phases (see Figure 5.37). However, the grain shapes of the other two samples of $LiY(MoO_4)_2$ and $LiY(WO_4)(MoO_4)$ as respectively shown in Figure 5.38 and Figure 5.39 remain in rounded irregular shapes with the majority of the grain sizes in the range from 1 – 5 µm. The change of particle shapes on $LiY(WO_4)_2$ and the unchanged particle shapes of $LiY(MoO_4)_2$ and $LiY(WO_4)(MoO_4)$ are in line with the XRPD results discussed in this chapter.

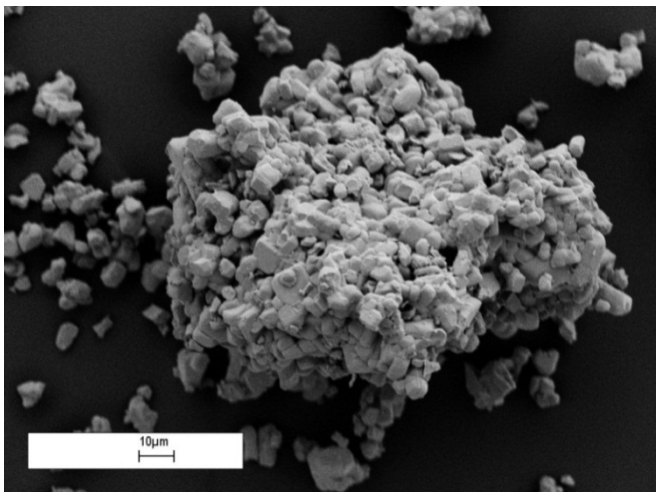

Figure 5.37: SEM images of $LiY(WO_4)_2$ with 2k magnification.

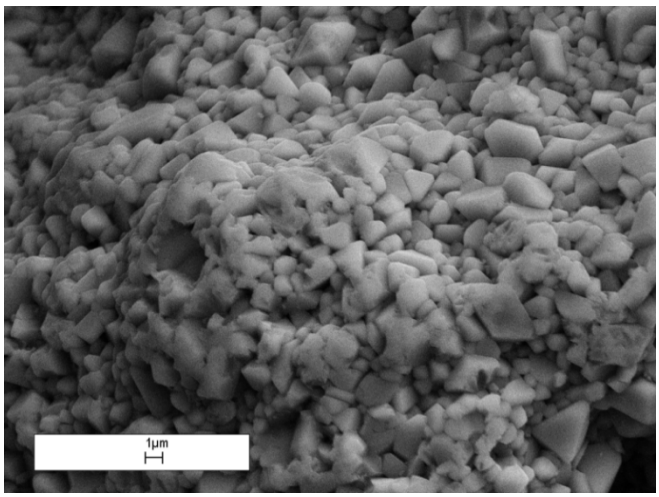

Figure 5.38: SEM images of $LiY(MoO_4)_2$ with 5k magnification.

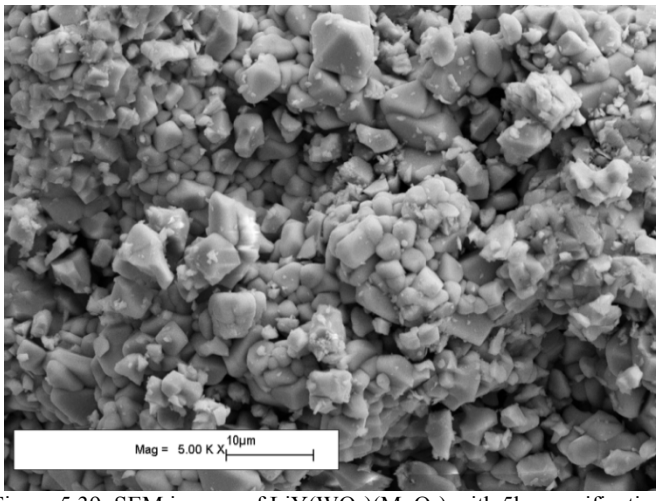

Figure 5.39: SEM images of $LiY(WO_4)(MoO_4)$ with 5k magnification.

5.4 Conclusions

In conclusion, $LiEu(WO_4)_2$ changes its phase from tetragonal to monoclinic when Eu^{3+} is replaced with Y^{3+}. The luminous efficacy of the phosphors in the series $LiEu_{(1-x)}Y_x(WO_4)_2$ show a gradual decline until 45% Y^{3+} concentration then they decrease almost linearly as the concentration of Y^{3+} increases. In contrast both the $LiEu_{(1-x)}Y_x(MoO_4)_2$ compounds and $LiEu_{(1-x)}Y_x(WO_4)(MoO_4)$ compounds remain in tetragonal phase until Eu^{3+} is completely substituted by Y^{3+} cations.

$LiEu_{0.55}Y_{0.45}(WO_4)_2$ is a decent alternative for lighting applications (depending on applications) as it contains less Eu^{3+} than the parent $LiEu(WO_4)_2$; hence is less expensive to prepare. However $LiEu_{0.55}Y_{0.45}(MoO_4)_2$ and $LiEu_{0.55}Y_{0.45}(MoO_4)(WO_4)$ were found to be the most efficient phosphors and if not for other drawbacks discussed earlier would be potential candidates for solid state lighting devices particularly for blue LED as alternatives to the parent phosphors. The colour temperature of the compounds moves very slightly towards colder regions in the presence Y^{3+}.

The $LiEu_{(1-x)}Y_x(WO_4)_2$ phosphors are the most significantly affected among the three phosphor series by a change in phase at greater Y^{3+} concentrations. In spite of this new finding, there is no clear evidence to explain why $LiEu_{(1-x)}Y_x(WO_4)_2$ experienced a phase change in contrast to the other two phosphor series. Although it has been mentioned by others in the literature [4] that the phase change happens depending on the size of the lanthanides, the findings from these experiments do not seem to be consistent with that statement.

5.5 References

1. Zaushitsyn A, Mikhailin V, Romanenko AY, Khaikina E, Basovich O, Morozov V, Lazoryak B (2005) Luminescence Study of $LiY_{1-x}Eu_x(MoO_4)_2$. *Inorganic materials*, 41(7), 766-770.

2. Xie A, Yuan X, Wang J, Wang F (2009) Synthesis and photoluminescence property of red phosphors $LiEu_{1-x}Y_x(WO_4)_{0.5}(MoO_4)_{1.5}$ for white LED. *Science in China Series E: Technological Sciences*, 52(7), 1913-1918.

3. Xianju Z, Tonghui Z, Yingmao L, Qiaochun F (2012) $LiY_{1-x}Eu_x(MoO_4)_2$ as a promising red-emitting phosphor of WLEDs synthesized by sol-gel process. *Journal of Rare Earths*, 30(4), 315-319.

4. Postema J, Fu W, Ijdo D (2011) Crystal structure of $LiLnW_2O_8$ (Ln = lanthanides and Y): An X-ray powder diffraction study. *Journal of Solid State Chemistry*, 184(8), 2004-2008.

5. Wang Z, Liang H, Zhou L, Wu H, Gong M, Su Q (2005) Luminescence of $(Li_{0.333}Na_{0.334}K_{0.333})Eu(MoO_4)_2$ and its application in near UV InGaN-based light-emitting diode. *Chemical Physics Letters*, 412(4), 313-316.

6. Wang J, Jing X, Yan C, Lin J, Liao F (2006) Influence of fluoride on f–f transitions of Eu^{3+} in $LiEuM_2O_8$ (*M*=Mo, W). *Journal of Luminescence*, 121(1), 57-61.

7. Wang Z, Liang H, Gong M, Su Q (2007) Luminescence investigation of Eu^{3+} activated double molybdates red phosphors with scheelite structure. J Alloys Compounds. *Chemical Physics Letters*, 412(4), 313-316.

8. Hwang K, Jeon Y, Hwangbo S, Kim J (2009) Red-emitting $LiEuW_2O_8$ phosphor for white emitting diodes prepared by sol–gel process. *Optica Applicata*, 39(2), 375-382.

9. Wang Y, Guo X, Endo T, Murakami Y, Ushirozawa M (2004) Identification of charge transfer (CT) transition in (Gd,Y)BO_3:Eu phosphor under 100–300nm. *Journal of Solid State Chemistry*, 177(7), 2242-2248.

10. Stone R, Silver J (September 2011) An Investigation Into Novel Red Emitting Phosphors and Their Applications. Dissertation, Brunel University.

11. Greenwood NN, Earnshaw A (1997) 20 - Scandium, Yttrium, Lanthanum and Actinium. In: Anonymous Chemistry of the Elements (Second Edition), *Butterworth-Heinemann, Oxford*, pp 944-953.

12. Kim JS, Lee JC, Cheon CI, Kang H (2006) Crystal Structures and Low Temperature Cofiring Ceramic Property of (1-x)(Li, RE) $W_2O_{8-x}BaWO_4$ Ceramics (RE= Y, Yb). *Japanese journal of applied physics*, 45(9S), 7397.

13. Liu Y, Wang Y, Wang L, Gu Y, Yu S, Lu Z, Sun R (2014) General synthesis of $LiLn(MO_4)_2$: Eu^{3+} (Ln= La, Eu, Gd, Y; M= W, Mo) nanophosphors for near UV-type LEDs. *RSC ADVANCES*, 4(9), 4754-4762.

14. Glorieux B, Jubera V, Apheceixborde A, Garcia A (2011) Luminescence properties of tungstates and molybdates phosphors: Illustration on A Ln $(Mo_4)_2$ compounds (A= alikaline cation, Ln= lanthanides, M= W, Mo). *Solid State Sciences*, 13(2), 460-467.

15. Kolitsch U (2001) The crystal structures of phenacite-type $Li_2(MoO_4)$, and scheelite-type $LiY(MoO_4)_2$ and LiNd $(MoO_4)_2$. *Zeitschrift für Kristallographie-Crystalline Materials*, 216(8), 449-454.

16. Le Page Y, Strobel P (1980) Structure of lithium yttrium bismolybdate (VI). *Acta Crystallographica Section B: Structural Crystallography and Crystal Chemistry*, 36(8), 1919-1920.

17. Kumari LS, Gopchandran KG (2015) Enhanced Red Emission in $LiY_{1-x}Mo_2O_8$: $_xEu^{3+}$ Phosphors for White Light Emitting Diodes. *Materials Today: Proceedings*, 2(3), 1007-1011.

Chapter 6

Incorporating Gadolinium (III) on Tungstate / Molybdate Host Lattices

This chapter discusses findings emerged from incorporating gadolinium (III) in three different parent compounds; $LiEu(WO_4)_2$, $LiEu(MoO_4)_2$ and $LiEu(MoO_4)(WO_4)$. The work is similar to that reported in Chapter 5 but herein instead of incorporating Y^{3+}, Eu^{3+} were substituted with Gd^{3+}. The properties of the three series of phosphors are discussed in this chapter in relation to each other and the phosphors reported in Chapter 5. Finally the luminous efficacies are discussed and how they correlate with the initial crystal structure of the parent compounds.

Our literature studies as discussed in Chapter 3 had shown that there has been a number of experiments were conducted to identify the correlation relationship, in terms of photoluminescence properties between the Eu^{3+} and Gd^{3+} in $LiEu_{1-x}Gd_x(MoO_4)_{2-y}(WO_4)_y$. Yi *et. al*,[1] investigated the relative photoluminescence effect of the doped Eu^{3+} in the $LiGd_{1-x}(MoO_4)_2:Eu_x^{3+}$ phosphors with respect to the photoluminescence intensity. From the experiment, they found that the highest luminescence was when x=0.30 and there was a quenching effect due to further addition of Eu^{3+}. However the full relationship between Eu^{3+} and Gd^{3+} was unknown as they limited the concentration, *x* from 0 to 0.35 mol. Very recently, Li *et. al* [2] disagreed with Yi in which they stated that the amount of Eu^{3+} in their experiment on $LiGd_{1-x}Eu_x(MoO_4)_2$ (x=0.01–1) had a big influence on the lattice. They also indicated that there was no evidence of concentration quenching observed from their work. Apart from this, none of the papers reported on the luminous efficacies as a function of increasing Gd^{3+}. Further investigation on $LiEu_{1-x}Gd_x(MoO_4)_{2-y}(WO_4)_y$ needs to be carried out in order to answer the discrepancy from the literature.

6.1.1 Incorporation of Gd^{3+} into Tungstate host lattices

The method of synthesizing $LiEu_{(1-x)}Gd_x(WO_4)_2$ was reported in Chapter 3 for the other phosphor samples. However as there seemed to be interesting effects observed in the body colour of the phosphors they were prepared a number of times. It was found that the body colour of the phosphor did not change in proportion to the falling of Gd^{3+}concentration (see Figure 6.1). The first sample $LiEu(WO_4)_2$ was found to have a light-red body colour and the next sample's body colour (x=0.15) turned out to be pale red. The body colour of the next sample came out even paler (near to yellow) but then in the next samples the red colour came back brighter at x=0.45 and onwards. The difficulties in making a consistent series of phosphor body colours also occurred in the $LiEu_{(1-x)}Y_x(WO_4)_2$ series of phosphors as discussed in Chapter 5 where it was seen that the luminous efficacy did not fall with a linear trend as the concentration of Eu^{3+} decreased until later on. It was deduced that the change was due to the phase-transformation from tetragonal to monoclinic structure in the phosphor series. Therefore for this phosphor series several attempts were made to ensure the samples were properly prepared but the consistency issue in the body colours was still not fully resolved.

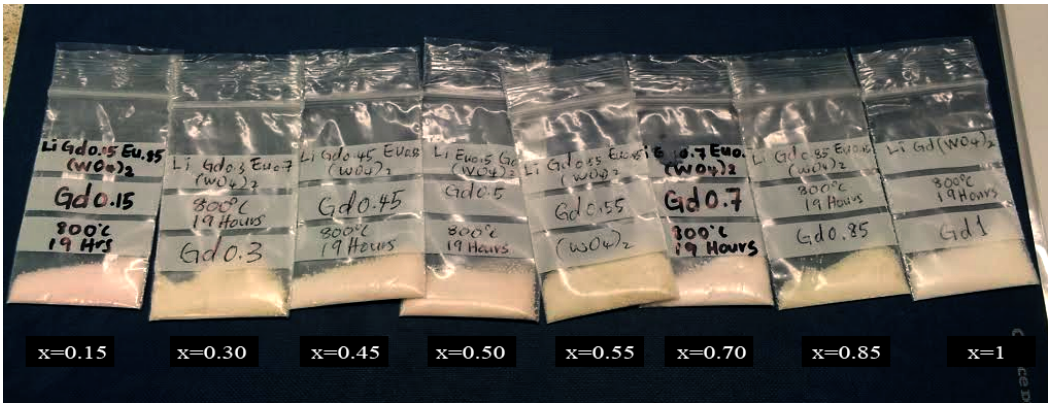

Figure 6.1: Body colours of $LiEu_{(1-x)}Gd_x(WO_4)_2$ powder samples

6.1.1.1 Powder Crystallography

In Figure 6.2 the overlaid XRPD patterns of $LiEu_{(1-x)}Gd_x(WO_4)_2$ (from x=0 to x=1) are presented. The diffraction patterns displayed in the figure indicate that the initial crystal structure of $LiEu(WO_4)_2$ did not change as the amount of Gd^{3+} substituting for Eu^{3+} increased. The peaks in the diffraction patterns were not

obviously seen to shift to the right as the Gd^{3+} cations were substituted into the structures for Eu^{3+}cations, in contrast to the findings for the $LiEu_{(1-x)}Y_xM_2O_8$ and $LiEu_{(1-x)}Y_x(WO_4)(MoO_4)$ series. The peaks mainly remain at the same angles as the radius of Gd^{3+} that is larger than Y^{3+} but is still smaller than Eu^{3+} (Y^{3+} 1.019 Å < Gd^{3+} 1.053 Å < Eu^{3+} 1.066 Å). This means that the ionic radius of Gd^{3+} is closer to Eu^{3+} as compared to Y^{3+} and therefore should not affect the size of lattice cells. The unchanged patterns in the XRPD results therefore confirm that $LiGd(WO_4)_2$ also has a tetragonal crystal structure with space group $I4_1/a:2$ and this finding is in line with the literature [3, 4].

The XRPD data of the samples were refined in TOPAS software. Since no phase changes can be noted as Gd^{3+} increased as seen in Figure 6.2 the same refinement model used in refining $LiEu(WO_4)_2$ was used for analysis in this section. Except for the fact that the occupancy of Eu^{3+} sites was substituted by Gd^{3+} the rest of the refining configuration was maintained as it was in parent compounds. The process of refining the XRPD results at the same time can help determine changes in all lattice parameters of the compound. As a result, Table 6.1 presents the refined lattice parameters (a=b, c and cell volumes) for the whole series of $LiEu_{(1-x)}Gd_x(WO_4)_2$.

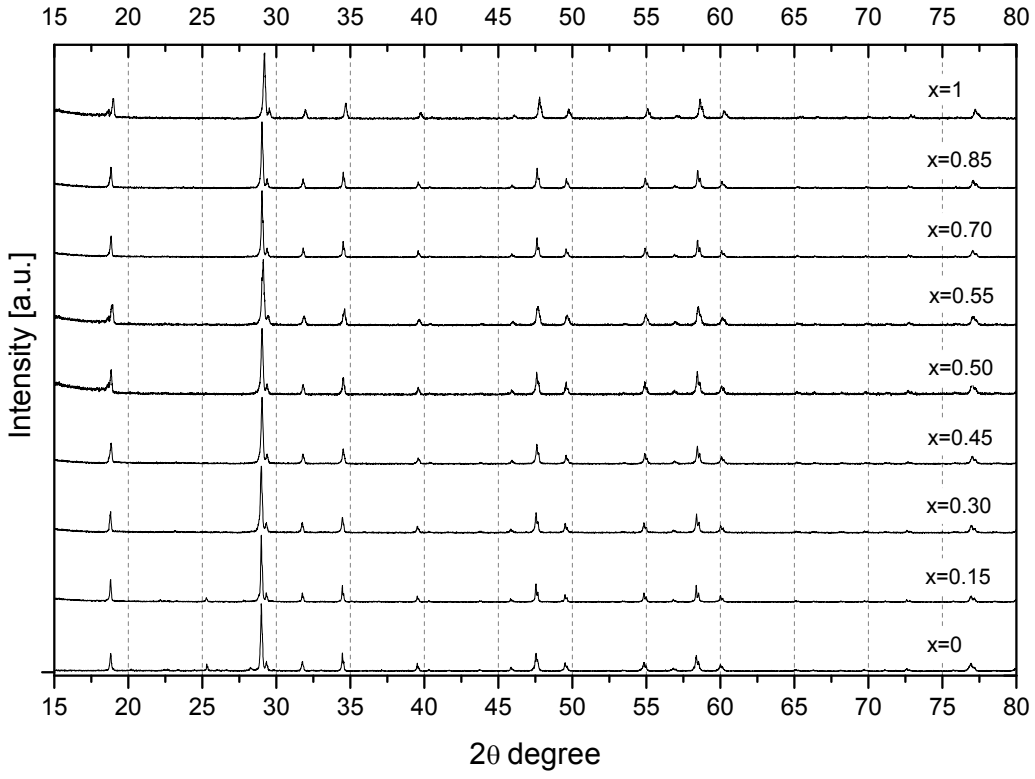

Figure 6.2: XRPD patterns of $LiEu_{(1-x)}Gd_x(WO_4)_2$

Table 6.1 shows that the R_{wp} of the $LiGd(WO_4)_2$ is15.22 and although the R_{wp} is relatively high (more than 10%) and the high R_p value also gives an indication that the background has noise from one angle to another, but looking at the fitting image shown in Figure 6.3 explains that the refinement agrees that the Gd^{3+}cations have substituted for the Eu^{3+} cations and settle in the same lattice sites as the Eu^{3+}cations of the parent compound. To determine how well the crystal structure of the compound fits to the scheelite structure all XRPD results from the samples $LiEu_{(1-x)}Gd_x(WO_4)_2$ were then refined in TOPAS software and then each fit was collected. A typical fit of one of them [$LiGd(WO_4)_2$] is shown in Figure 6.3. In the case of $LiGd(WO_4)_2$ the reference model was taken based on the same reference model used in Chapter 5 except the Eu^{3+} was substituted with Gd^{3+} to ensure the refinement can be carried out as close as possible to the reference model. It is interesting to note from Figure 6.3 that the XRPD measurement fitted well with the refinement model $LiGd(WO_4)_2$.

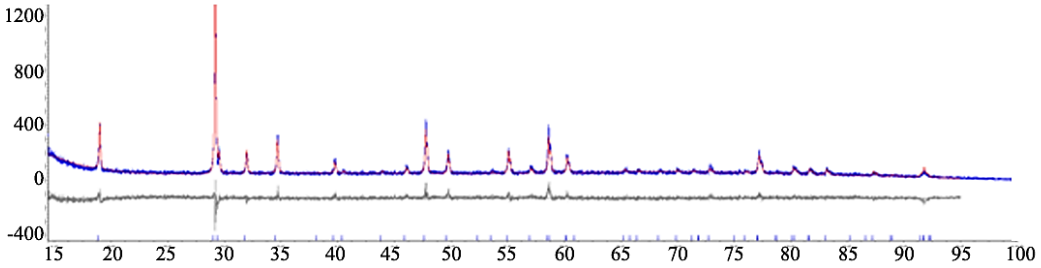

Figure 6.3: Profile fit of $LiGd(WO_4)_2$

The process of refining XRPD results at the same time determines all the lattice parameters of the compound. As a result, Table 6.1 presents the lattice parameters (a=b, and c cell volumes) for the whole series of $LiEu_{(1-x)}Gd_x(WO_4)_2$.

Table 6.1: Lattice parameters of tetragonal $I4_1/a$:2 $LiEu_{(1-x)}Gd_x(WO_4)_2$

Gd^{3+} (mol)	Tetragonal $I4_1/a$:2			R_{exp}	R_{wp}	R_p
	a (Å)	c (Å)	Vol (Å^3)			
0	5.2082(1)	11.2809(3)	306.00(1)	3.92	10.81	7.01
0.15	5.20743(7)	11.2761(2)	305.78(1)	10.84	13.91	10.77
0.30	5.2055(1)	11.2722(3)	305.45(1)	10.45	13.37	10.69
0.45	5.2050(2)	11.2701(5)	305.33(2)	12.32	15.15	12.00
0.50	5.2040(2)	11.2671(5)	305.13(2)	13.37	16.86	13.56
0.55	5.2024(1)	11.265(3)	304.89(2)	10.59	13.10	10.39
0.70	5.20050(9)	11.2623(3)	304.59(1)	11.43	13.58	10.80
0.85	5.1987(1)	11.2589(3)	304.29(1)	11.31	13.89	11.11
1	5.1965(1)	11.2546(4)	303.91(2)	12.02	15.22	12.12

As can be seen from Table 6.1, it is apparent that the R_{wp} of the refinements seems to be good (near to 10%) taken in conjunction with each of the refined images (Figure 6.3 as for an example) and indeed none of the mean errors were seen as

significant as all error values were small. The lattice parameters listed in Table 6.1 are plotted as presented in Figure 6.4 (a) and (b). From the graphs, the rate of contraction was seen to be smaller than what was encountered in Chapter 5 due here to the presence of the larger Gd^{3+} being incorporated into the lattice rather than the Y^{3+} cations. The result was that it was more difficult to identify which lattice sides were more affected in this series of phosphors. The refinement results on the $LiGd(WO_4)_2$ also confirms that Li^+ and Gd^{3+} share the same site with occupancy factor 0.55(1) and 0.45(1) respectively (See Table 6.2).

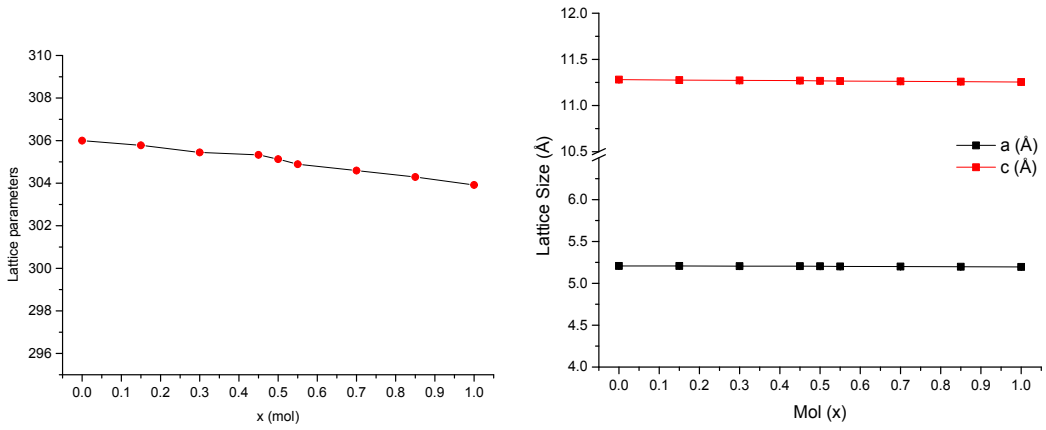

(a) (b)

Figure 6.4: (a) Cell volumes and (b) Lattice parameters of $LiEu_{(1-x)}Gd_x(MoO_4)_2$

Table 6.2: Site occupancies of $LiGd(WO_4)_2$

Site	Np	x	y	z	Atom	Occ
W	4	0.50000	0.75000	0.12500	W^{+6}	1
Gd	4	0.00000	0.25000	0.12500	Gd^{+3} Li^{+1}	0.55(1) 0.45(1)
O	16	0.74280	0.09480	-0.04000	O^{-2}	1

Following the substitution of Eu^{3+} with Gd^{3+} a model of the compound structure was generated based on the refined result of the XRPD data and is presented in Figure 6.5 (a) and (b) detailing the scheelite structure of $LiGd(WO_4)_2$. Both figures present the lattice of $LiGd(WO_4)_2$ with four oxygen ions around each W^{6+} cations as presented in Figure 6.5 (a) establishing tetrahedral shapes whereas each Li^+(and or the Gd^{3+} that is in the same site) has eight oxygen ions coordinated to it. No significant differences were found between this model and the parent compound $LiEu(WO_4)_2$ and therefore such coordination again confirms that $LiGd(WO_4)_2$ maintains the tetragonal crystal structure. The decrease in the lattice's volume (that decreased less

than 1% from 306.00(1) Å^3 to 303.91(2) Å^3) as the concentration of Gd^{3+}cations increased was foreseeable as the ionic radius of Gd^{3+} is larger than Y^{3+} as discussed in 6.1.1.1.

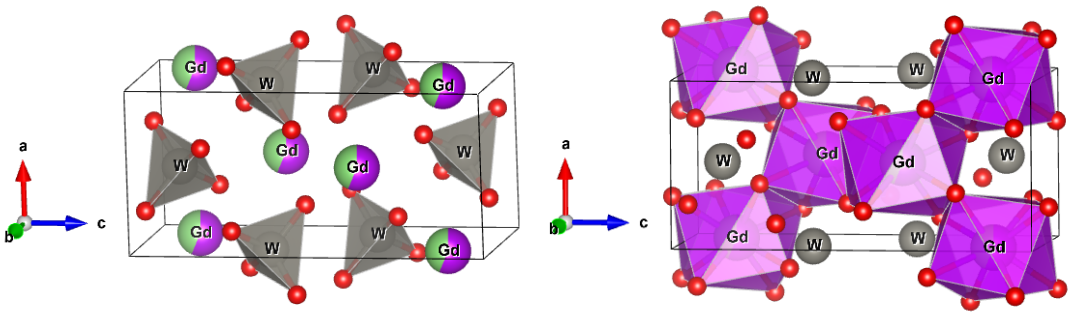

Figure 6.5: Modelled crystal structure of tetragonal $LiGd(WO_4)_2$

6.1.1.2 Photoluminescence properties

Figure 6.6 and Figure 6.7 present the emission spectra of the $Eu_{(1-x)}Gd_x(WO_4)_2$ series of phosphors excited at 395 nm and 465 nm respectively. The emission spectra shown in both figures are displayed in the wavelength range from 580 nm to 720 nm which is associated with the principle transitions of the excited state of Eu^{3+}. The emission bands can notably be seen particularly at 613 nm and 616 nm related to the transition from $^5D_0 \rightarrow {}^7F_2$. The overlaid emission spectra excited at 395 nm presented in Figure 6.6 shows that the spectral intensity only dropped to about half of that of the parent $LiEu(WO_4)_2$ as the concentration of Gd^{3+} reached 0.85 mol. The same situation can also be observed in Figure 6.7 when the phosphor was excited at 465 nm. All spectral shapes are in the same forms throughout the whole series of samples proving that the symmetry of the emission centre was not affected by the presence of Gd^{3+} as it substituted Eu^{3+}. This was in line with what was found in the XRPD results (see Figure 6.2).

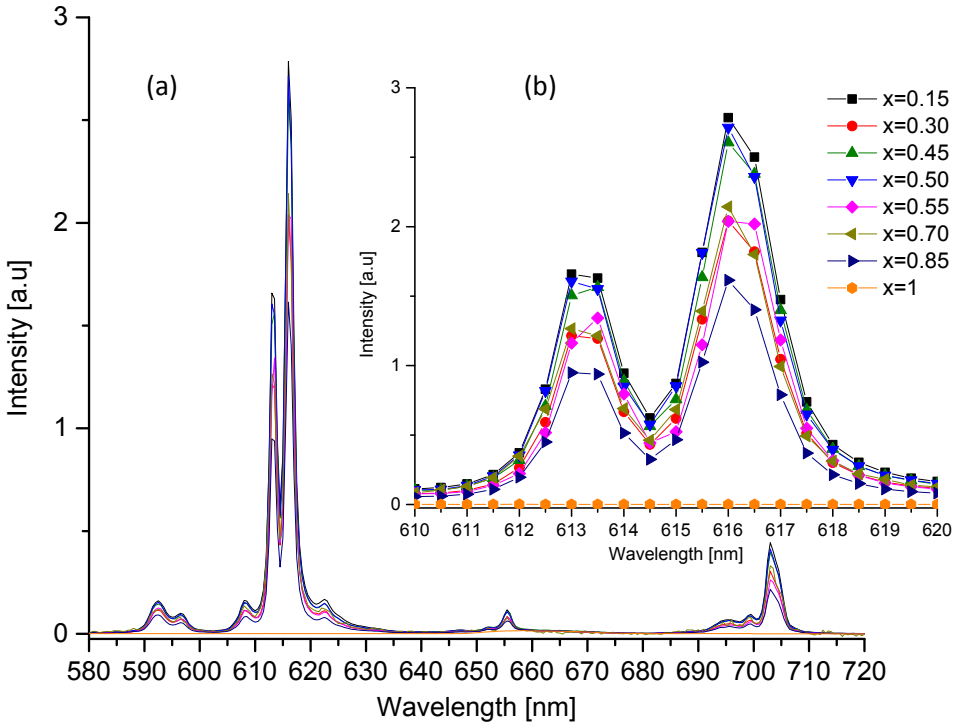

Figure 6.6: Emission spectra of $LiEu_{(1-x)}Gd_x(WO_4)_2$ excited at 395nm as seen (a) from range of 580-720 nm and (b) at closer range from 610 – 620 nm

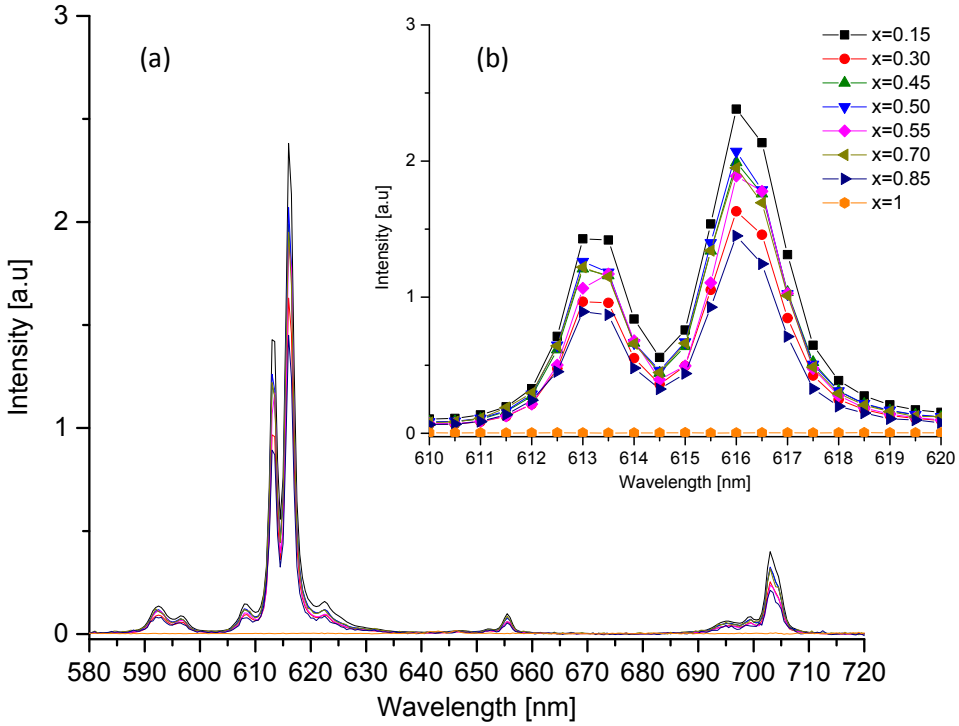

Figure 6.7: Emission spectra of $LiEu_{(1-x)}Gd_x(WO_4)_2$ excited at 465nm as seen (a) from range of 580-720 nm and (b) at closer range from 610 – 620 nm

Table 6.3 shows the measured luminous efficacies while Figure 6.8 (a) and (b) show the plots from all samples when excited at 395 nm and 465 nm respectively. The

results of the efficacies are quite revealing and show a different behaviour to those shown in Chapter 5. Both graphs in Figure 6.8 (a) and (b) display a marked decrease in luminous efficacy when Gd^{3+} was added from x=0.15 to x=0.30 and then interestingly, there was a significant rise-backup at x=0.45. The luminous efficacy when excited at 395 nm then slowly decreased until x=0.85 whilst the efficacy excited at 465 nm seems to be stable until the concentration of Gd^{3+} reached 0.85 mol. The trends of luminous efficacies had already been expected due to the body colour appearance of the samples (See Figure 6.1). The decline of efficacy as seen in Figure 6.8 was due to the gradual loss of Eu^{3+} and this can be confirmed by looking at the form of the spectra at x=0.15 and x=0.30 which are identical with the parent $LiEu(WO_4)_2$ compound and therefore the symmetry of the luminescent centre was likely not affected. This judgement is also based on the evidence observed in the XRPD results discussed earlier in Figure 6.2. As to the rise of efficacy when x=0.45 and x=0.50 in spite of matching with the body colour of the compound the reason behind this enhancement is difficult to explain but might well be associated with the Gd^{3+} concentration influencing the lattice and raising the efficacy of the Eu^{3+} emission. If the lattice size is optimised for the emission of the Eu^{3+} at around 45 to 55% this would suggest that a value of 305.13(2) $Å^3$ for the cell volume is optimum. This value is close to the optimum found of 301 $Å^3$ in the Y^{3+} materials in Chapter 5 and of course Gd^{3+} is larger than Y^{3+}.

Table 6.3: Luminous efficacies of $LiEu_{(1-x)}Gd_x(WO_4)_2$ excited at (a) 395nm and (b) 465 nm

x (Mol)	Luminous Efficacy (lm/W)	
	exc 395 nm	exc 465 nm
0	172.684	202.5578
0.15	155.5445	200.9759
0.3	113.1573	137.6185
0.45	147.9703	167.9133
0.5	146.7164	174.6666
0.55	125.5896	159.4586
0.7	111.9269	164.5373
0.85	87.1954	122.3507
1	0	0

Further analysis on the concentration quenching as seen in Figure 6.9 revealed that the line broadening are hardly seen except on the parent compound which would have been further evidence of quenching. Despite the intensity of Gd^{3+} substituted

compounds being less than the parent pure Eu^{3+} compound the values for 45 % – 50% of Gd^{3+} are good and indicate that these phosphors are usable and because of containing less Eu^{3+} they will be half the price of the pure Eu^{3+} compound.

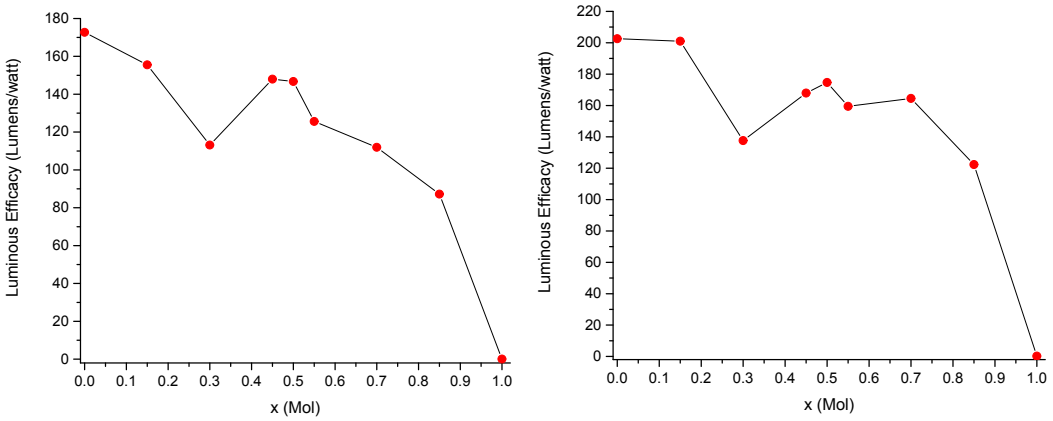

Figure 6.8: Luminous efficacies of $LiEu_{(1-x)}Gd_x(WO_4)_2$ excited at (a) 395nm and (b)465 nm

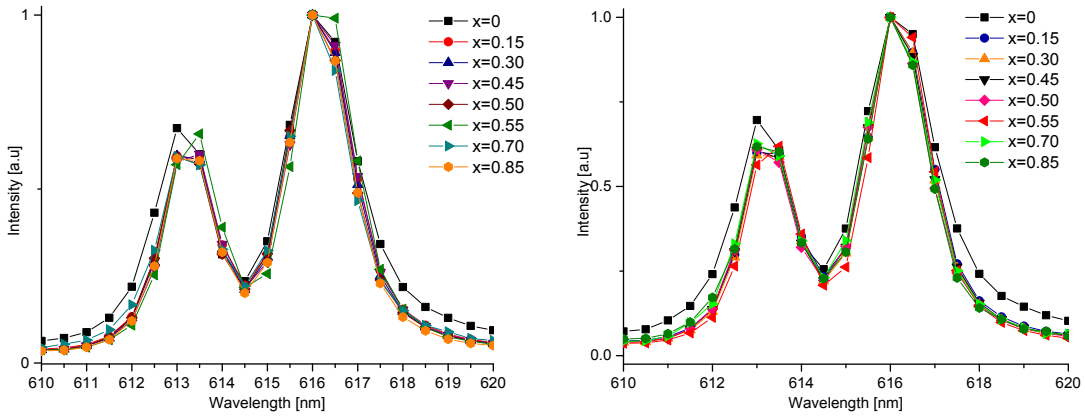

Figure 6.9: Normalized emission spectra of $LiEu_{(1-x)}Gd_x(WO_4)_2$ excited at (a) 395nm and (b) 465 nm

Table 6.4 shows the CIE colour coordinates of $LiEu_{(1-x)}Gd_x(WO_4)_2$ from x=0 until x=1. The colour temperature of the phosphor as listed in the table was basically not affected by the presence of Gd^{3+} primarily from x=0.50 and below. Thereby the colour temperature did not change significantly (see the CIE diagrams in Figure 6.10 and Figure 6.11) till 55% Gd^{3+}. Then the colour temperature and the x and y coordinates do show a change but remain in the red region.

Table 6.4: CIE Colour coordinates of $LiEu_{(1-x)}Gd_x(WO_4)_2$

No.	Gd^{3+} Concentration (mol)	Exc 395 nm			Exc 465 nm		
		Coordinates		Colour temp	Coordinates		Colour temp
		x	y		x	y	
1	0	0.6692	0.3306	889 K	0.6692	0.3306	889 K
2	0.15	0.6709	0.3288	876 K	0.6706	0.3292	879 K
3	0.30	0.6708	0.3290	877 K	0.6703	0.3295	881 K
4	0.45	0.6709	0.3289	876 K	0.6702	0.3295	881 K
5	0.50	0.6707	0.3291	878 K	0.6702	0.3296	881 K
6	0.55	0.6672	0.3325	903 K	0.6679	0.3318	898 K
7	0.70	0.6697	0.3301	885 K	0.6676	0.3321	900 K
8	0.85	0.6690	0.3307	890 K	0.6663	0.3334	909 K
9	1	N/A					

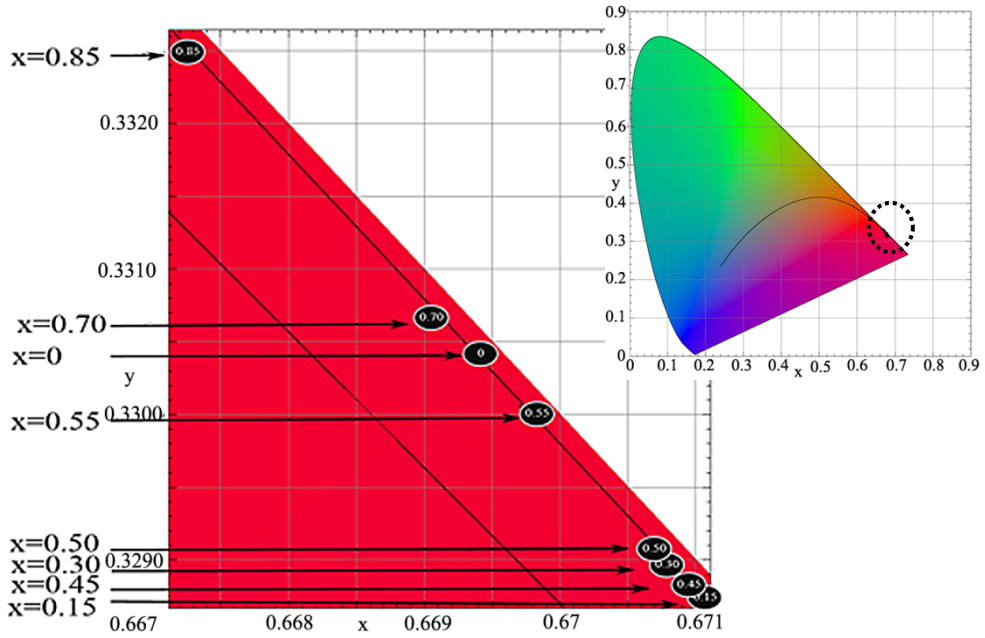

Figure 6.10: CIE diagram for $LiEu_{(1-x)}Gd_x(WO_4)_2$ excited at 395nm

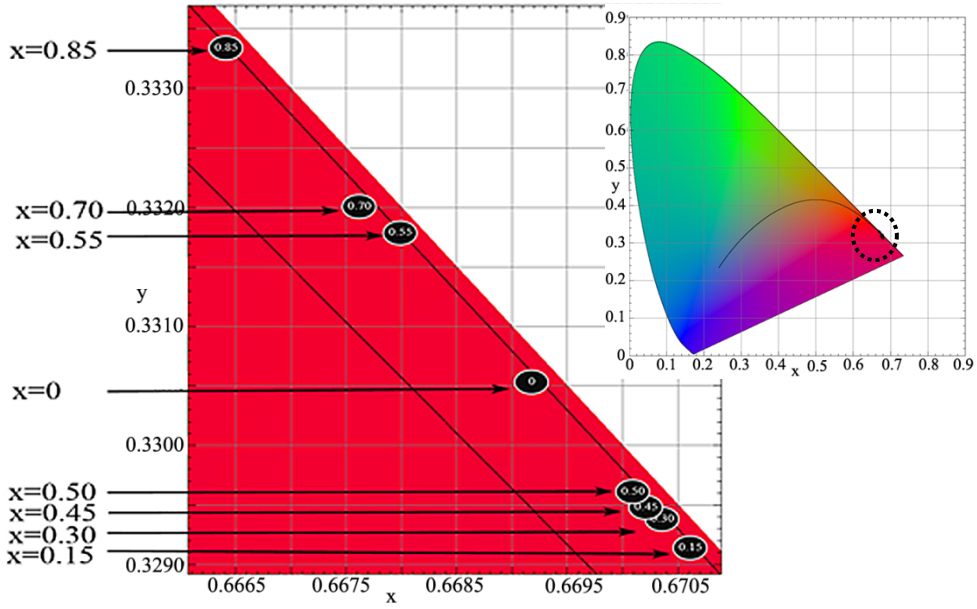

Figure 6.11: CIE diagram for $LiEu_{(1-x)}Gd_x(WO_4)_2$ excited at 465nm

6.1.2 Incorporation of Gd^{3+} into Molybdate host lattices

6.1.2.1 Powder Crystallography

As discussed in the introduction to this chapter and after what has been reported in the previous section (see 6.1.1 and Chapter 5), the experimental evidence on the incorporation of gadolinium (III) into a series of $LiEu_{(1-x)}Gd_xM_2O_8$ samples will now be presented and discussed. Figure 6.12 shows overlaid XRPD patterns of $LiEu_{(1-x)}Gd_xM_2O_8$ where x is in the range from 0 to 1. The overlaid pattern again gives evidence that the initial scheelite structure of $LiEu(MoO_4)_2$ did not change in correlation with the function of falling Eu^{3+}. The diffraction peaks of the parent compound can still be observed especially at $2\theta \approx 29°$which corresponds to the (112) reflection and other peaks seen at $2\theta \approx$ 18.8°(101), 31.7°(004), 34.4° (200) and 47.5°(204) remained unchanged as the concentration of Gd^{3+} increased. The unchanged XRPD diffraction peaks throughout the whole series of $LiEu_{(1-x)}Gd_xM_2O_8$ indicate that the compound did not undergo any phase transformations as concentration of $Eu^{3+}$was reduced and substituted with Gd^{3+}. It was also in line with Gd^{3+}, which is slightly smaller than Eu^{3+} (in comparison with Y^{3+} - Eu^{3+}experiments where Y^{3+} is much smaller than Eu^{3+} as discussed in Chapter 5).

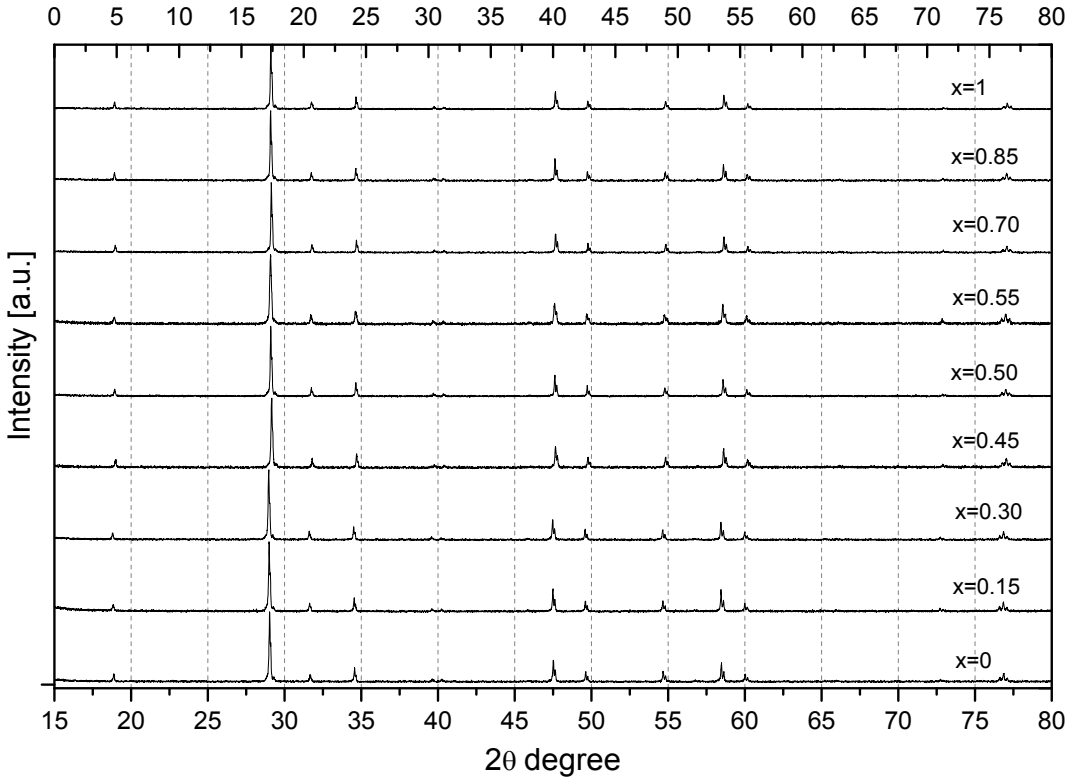

Figure 6.12: XRPD patterns of $LiEu_{(1-x)}Gd_x(MoO_4)_2$

As no phase transformations were observed in the overlaid XRPD patterns in Figure 6.12 all samples were then refined using TOPAS. Table 6.5 lists all refined parameters from TOPAS based on the same parent $LiEu(WO_4)_2$ model used in Chapter 5 and again the reference model selected was customized to fit appropriately with the actual samples by replacing the Eu^{3+} with Gd^{3+} and W^{6+} was replaced with Mo^{6+}. An example of the refined image of $LiGd(MoO_4)_2$ as shown in Figure 6.13 indicates that the XRPD results matched closely with the standard model. The lattice parameters and cell volumes based on the refined results in Table 6.5 shows that the lattice's volume only decreases slightly by around 0.75 % (from 306.55 $Å^3$ to 304.24 $Å^3$) due to the substitution of $Gd^{3+}$with Eu^{3+} in the Eu^{3+} lattice site. Table 6.5 also reveals the $LiGd(MoO_4)_2$ XRPD profile had a good fit against the $LiGd(MoO_4)_2$ reference model with R_{wp} 8.21.

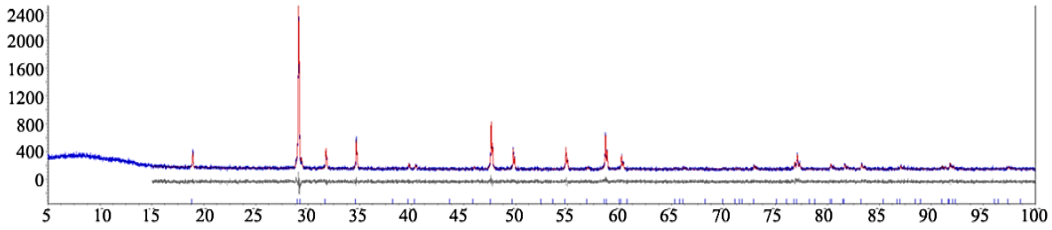

Figure 6.13: Retvield refinement of $LiGd(MoO_4)_2$

Table 6.5: Lattice parameters of tetragonal $I4_1/a:2$ $LiEu_{(1-x)}Gd_x(MoO_4)_2$

Gd^{3+} (mol)	Tetragonal $I4_1/a:2$			R_{exp}	R_{wp}	R_p
	a (Å)	c (Å)	Vol (Å^3)			
0	5.20138(9)	11.3308(3)	306.55(1)	8.99	9.81	7.80
0.15	5.200(1)	11.327(3)	306.28(1)	9.08	10.03	7.98
0.30	5.19816(9)	11.3241(3)	305.99(1)	8.75	9.48	7.59
0.45	5.1966(1)	11.3191(3)	305.66(2)	9.47	10.26	8.15
0.50	5.19529(8)	11.3176(2)	305.47(1)	8.37	8.94	7.12
0.55	5.1944(1)	1.3156(4)	305.32(2)	9.24	9.95	7.94
0.70	5.19263(8)	11.3115(2)	305.00(1)	8.24	8.69	6.92
0.85	5.19087(8)	11.3068(2)	304.66(1)	8.33	8.76	6.99
1	5.18824(8)	11.3025(2)	304.24(1)	7.80	8.21	6.51

The lattice parameters listed in Table 6.5 are plotted in Figure 6.14 (a) and (b). The graphs show a gradual decline of cell volumes as a function of rising Gd^{3+}concentration. As discussed above, there was no surprise as the contraction of the lattice parameters this time was less than what had been witnessed in the work on Y^{3+} in reported Chapter 5.

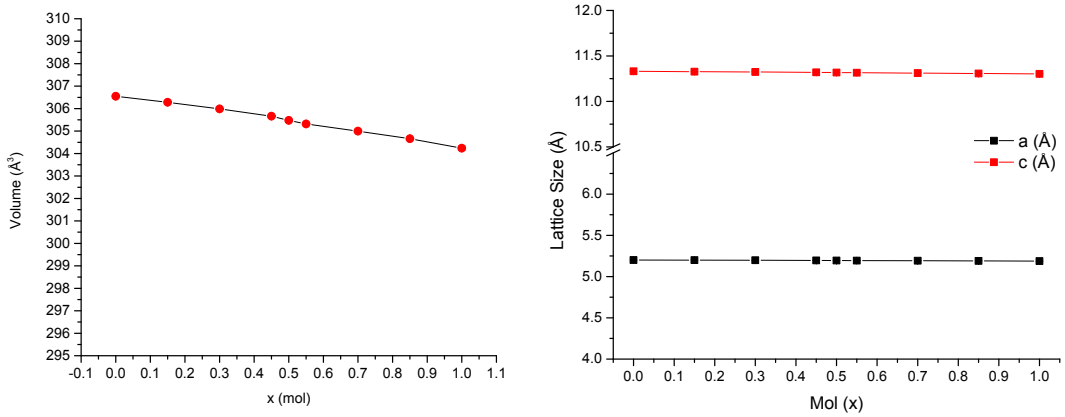

(a) (b)

Figure 6.14: (a) Cell volumes and (b) Lattice parameters of $LiEu_{(1-x)}Gd_x(MoO_4)_2$

The site occupancies of $LiGd(MoO_4)_2$ presented in Table 6.6 imply that Gd^{3+} occupies the site with occupancy factor of 0.488(7) while Li^+ occupied in the site of Gd^{3+} with occupancy factor of 0.512(7). The determination of the site occupancies are

relevant after taking into consideration the net charge of the compound is -0.096 (very near to zero). Moreover as Li only has a very small number of electrons compared to Gd^{3+} such a small difference is not unreasonable and hence we can assume that the formulation is correct as $LiGd(MoO_4)_2$.

Table 6.6: Site occupancies of $LiGd(MoO_4)_2$

Site	Np	x	y	z	Atom	Occ
Mo	4	0.50000	0.75000	0.12500	Mo^{+6}	1
Gd	4	0.00000	0.25000	0.12500	Gd^{+3}	0.488(7)
					Li^{+1}	0.512(7)
O	16	0.74280	0.09480	-0.04000	O^{-2}	1

A model of the compound's structure has been calculated and is shown in Figure 6.15 (a) and (b) demonstrating the particular scheelite structure of $LiGd(MoO_4)_2$. Both figures show a modelled lattice consists of $LiGd(MoO_4)_2$ with eight oxygens surround Gd^{3+} or Li^{+} cations as presented in Figure 6.15(a) and each Mo^{6+} has four oxygen ions coordinated to it making a tetrahedral shape. These images are similar to what has been found in parent compound $LiEu(WO_4)_2$.

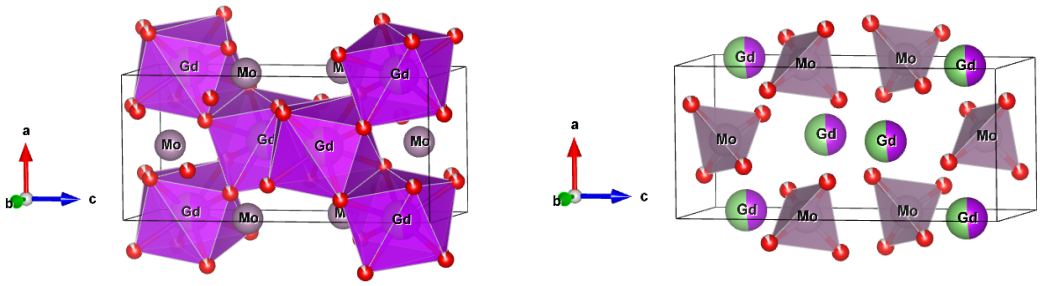

Figure 6.15: Scheelite modelled structure of $LiEu_{(1-x)}Gd_xM_2O_8$

6.1.2.2 Photoluminescence Properties

Figure 6.16 and Figure 6.17 show the emission spectra of $LiEu_{(1-x)}Gd_x(MoO_4)_2$ excited at 395 nm and 465 nm respectively. Typical Eu^{3+}emission bands are observed at 588–600 nm the $^5D_0 \rightarrow {}^7F_1$ transition and the intense emission observed at 610–630 nm was due to the $^5D_0 \rightarrow {}^7F_2$ transition and a small emission band is seen at 690–710 nm (the$^5D_0 \rightarrow {}^7F_4$ transition). Interestingly, the trend of falling intensity is observed to be similar with the work on $LiEu_{(1-x)}Y_x(MoO_4)_2$ (see chapter 5) where no significant

reduction can be seen when the concentration of Gd^{3+}rises. This positive result is observed under both excitation energies until the concentration of Gd^{3+}reaches 0.70 mol (in for substituting Eu^{3+}). Indeed the luminescence intensity of $LiEu_{0.15}Gd_{0.85}(MoO_4)_2$ can still be seen to be near to half of the maximum intensity of the parent compound when excited at 465 nm. Meanwhile Figure 6.18 shows that there was evidence of band-broadening as the amount of Eu^{3+} increases on both excitations. This broadening effect is a manifestation of concentration quenching at high Eu^{3+} concentrations.

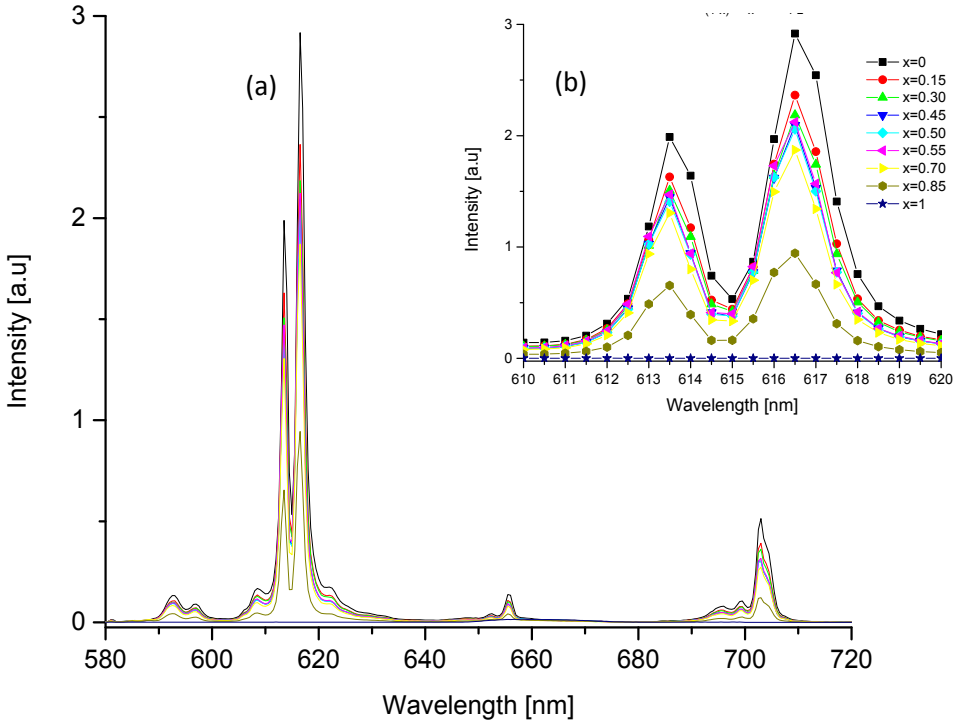

Figure 6.16: Emission spectra of LiEu(1-x)Gdx(MoO4)2 excited at 395nm as seen (a) from range of 570-720 nm and (b) at closer range from 610 – 620 nm

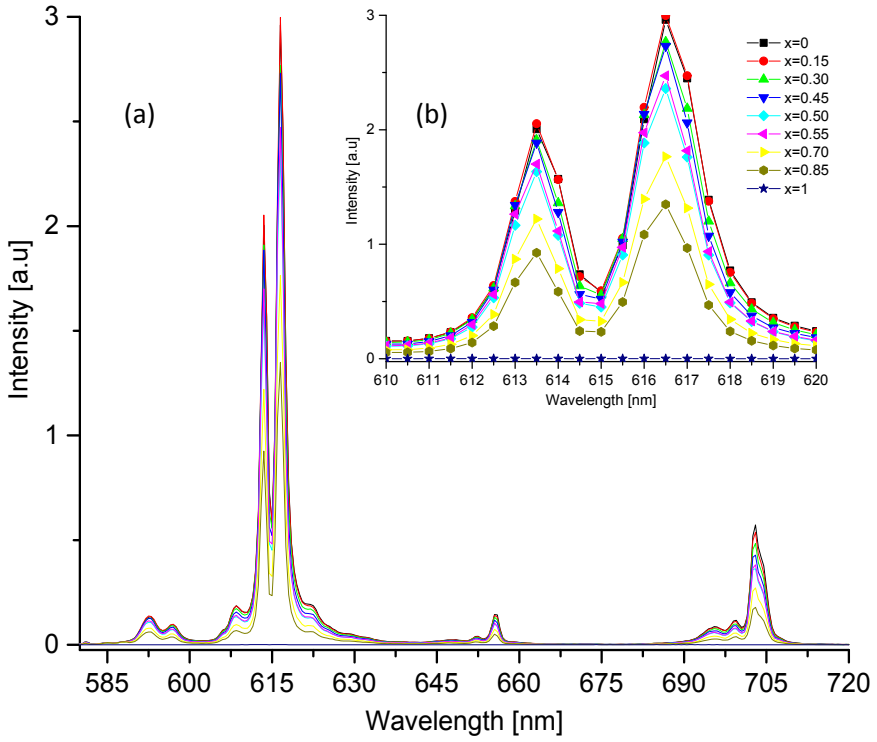

Figure 6.17: Emission spectra of LiEu(1-x)Gdx$(MoO_4)_2$ excited at 465nm as seen (a) from range of 570-720 nm and (b) at closer range from 610 – 620 nm

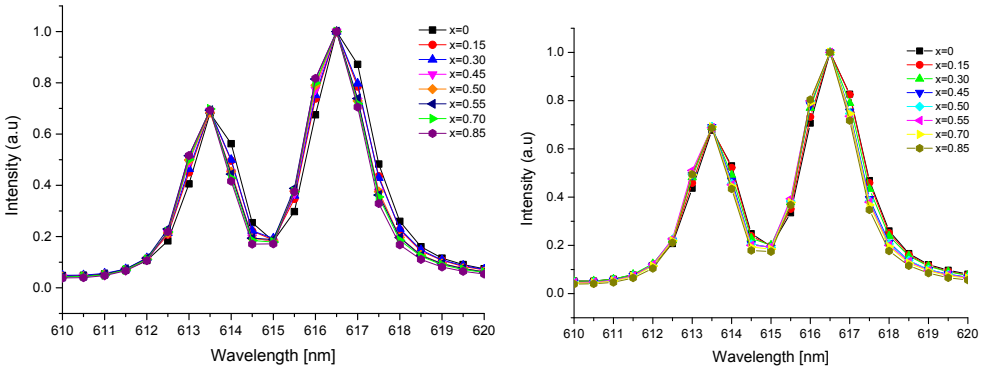

(a) (b)

Figure 6.18: Normalized spectra of $LiEu_{(1-x)}Gd_x(MoO_4)_2$ excited at (a) 395nm and (b) 465 nm

Table 6.7 shows the luminous efficacies of the $LiEu_{(1-x)}Gd_x(MoO_4)_2$ phosphors while Figure 6.19 shows how they behave as a function of increasing Gd^{3+}. The luminous efficacy when excited at 395 nm as shown in Figure 6.19 (a) was found to slip back from 163.33 lm/W to 148.67 lm/W and then started to increase slowly to the maximum value at x=0.30. The luminous efficacy then reduced steadily to 139.09 lm/W at x=0.70. No significant differences were found for excitations at 465 nm as shown in Figure 6.19 (b) except that it started with a little lower luminous efficacy

before rising to a maximum of 211.51 lm/W. The graph then remained at high efficacy values (with a small variation) until a luminous efficacy value of 210.77 lm/W at x=0.45.

Table 6.7: Luminous efficacies of $LiEu_{(1-x)}Gd_x(MoO_4)_2$ excited at (a) 395nm and (b) 465 nm

x (Mol)	Luminous Efficacy (lm/W)	
	exc 395 nm	exc 465 nm
0	163.33	199.28
0.15	148.67	211.51
0.3	153.47	205.40
0.45	149.74	210.77
0.5	139.06	195.52
0.55	143.77	200.57
0.7	139.09	171.81
0.85	89.202	120.35
1	0	0

A common observation from both sets of results (taken with the two different excitation wavelengths) shows that no substantial changes of luminous efficacy can be observed between x=0 to x=0.70 except they reached their top values in the presence of Gd^{3+} (somewhere about x=0.30 to 0.50) and then they started to drop dramatically after x = 0.70. Based on the earlier observations reported in Chapter 5 (5.2.3.2), the luminous efficacy could seems to be enhanced when the lattice volume is reduced to about 301.5 – 301.8 $Å^3$.

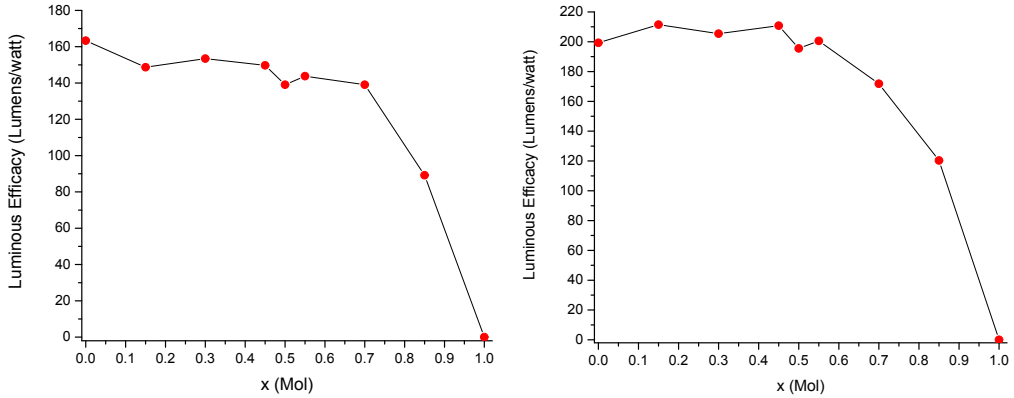

Figure 6.19: Luminous efficacies of Li $Eu_{(1-x)}Gd_x(MoO_4)_2$ excited at (a) 395nm and (b) 465 nm

CIE colour coordinates of these compounds are presented in Table 6.8 and the coordinates are plotted in the CIE diagram shown in Figure 6.20 and Figure 6.21. It can be observed from the table and figures that the colour coordinates did not

significantly change as the concentration of Gd^{3+} increased until concentrations of 0.85 mol. were reached This is again evidence that the spectral emission which comes from the excited Eu^{3+} is relatively unaffected by the introduction of $Gd^{3+}$and therefore is again in line with what has been discussed in section 6.1.2.1.

Table 6.8: CIE Colour coordinates of $LiEu_{(1-x)}Gd_x(MoO_4)_2$

No.	Gd^{3+} Concentration (mol)	Exc 395 nm			Exc 465 nm		
		Coordinates		Colour temp	Coordinates		Colour temp
		x	y		x	y	
1	0	0.6730	0.3267	861 K	0.6692	0.3306	889 K
2	0.15	0.6728	0.3270	863 K	0.6706	0.3292	879 K
3	0.30	0.6726	0.3272	865 K	0.6703	0.3295	881 K
4	0.45	0.6721	0.3277	868 K	0.6702	0.3295	881 K
5	0.50	0.6720	0.3278	869 K	0.6702	0.3296	881 K
6	0.55	0.6719	0.3279	869 K	0.6676	0.3321	900 K
7	0.70	0.6712	0.3286	874 K	0.6679	0.3318	898 K
8	0.85	0.6694	0.3303	887 K	0.6663	0.3334	909 K
9	1	N/A					

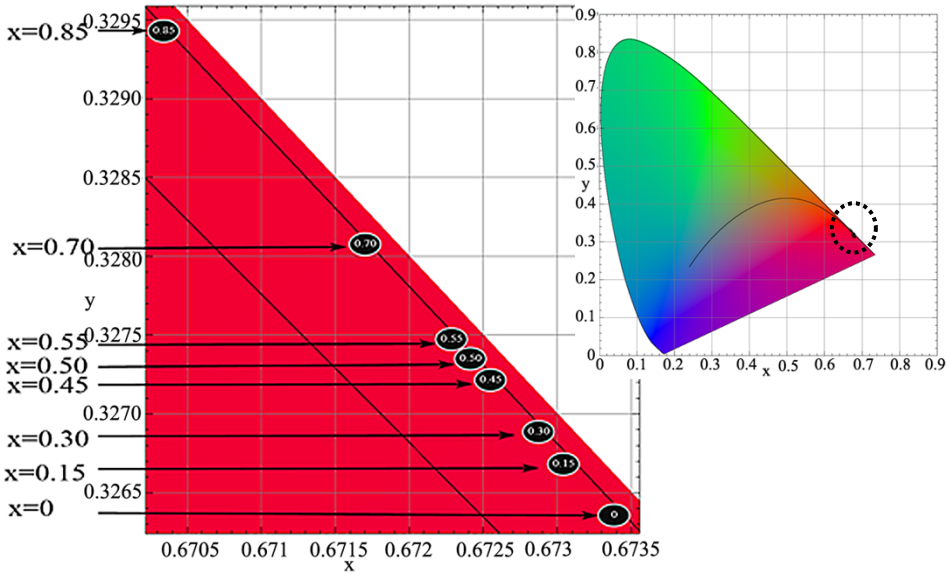

Figure 6.20: CIE diagram for $LiEu_{(1-x)}Gd_x(MoO_4)_2$ excited at 395nm

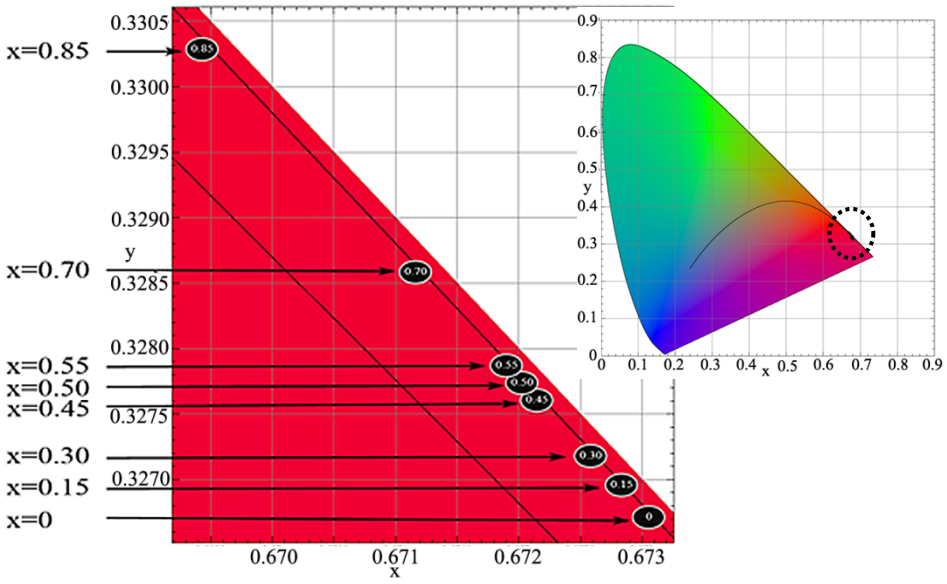

Figure 6.21: CIE diagram for $LiEu_{(1-x)}Gd_x(MoO_4)_2$ excited at 465nm

6.1.3 Incorporation of Gd^{3+} into Molybdate-Tungstate host lattices

6.1.3.1 Powder Crystallography

This section reports studies carried out on incorporating gadolinium (III) into a series of tungstate-molybdate lattices of the formulation $LiEu_{(1-x)}Gd_x(WO_4)(MoO_4)$. Figure 6.22 shows the XRPD diffraction patterns in overlay of $LiEu_{(1-x)}Gd_x(WO_4)(MoO_4)$ where x is ranges from 0 to 1. As can be seen from the figure the crystal structure of these molybdate-tungstate phosphors does not experience changes as Gd^{3+} increases substituting for the Eu^{3+} cations. Following the addition of Gd^{3+} as shown in Figure 6.22, the only differences noted are the slight shifts of certain diffraction peaks to higher angles which were due to the effect of smaller Gd^{3+}ions that settle in the lattice causing the cell to contract. This is in keeping with the findings reported for the double molybdate compounds discussed above as well as those for the tungstate - molybdate compounds discussed in Chapter 5.

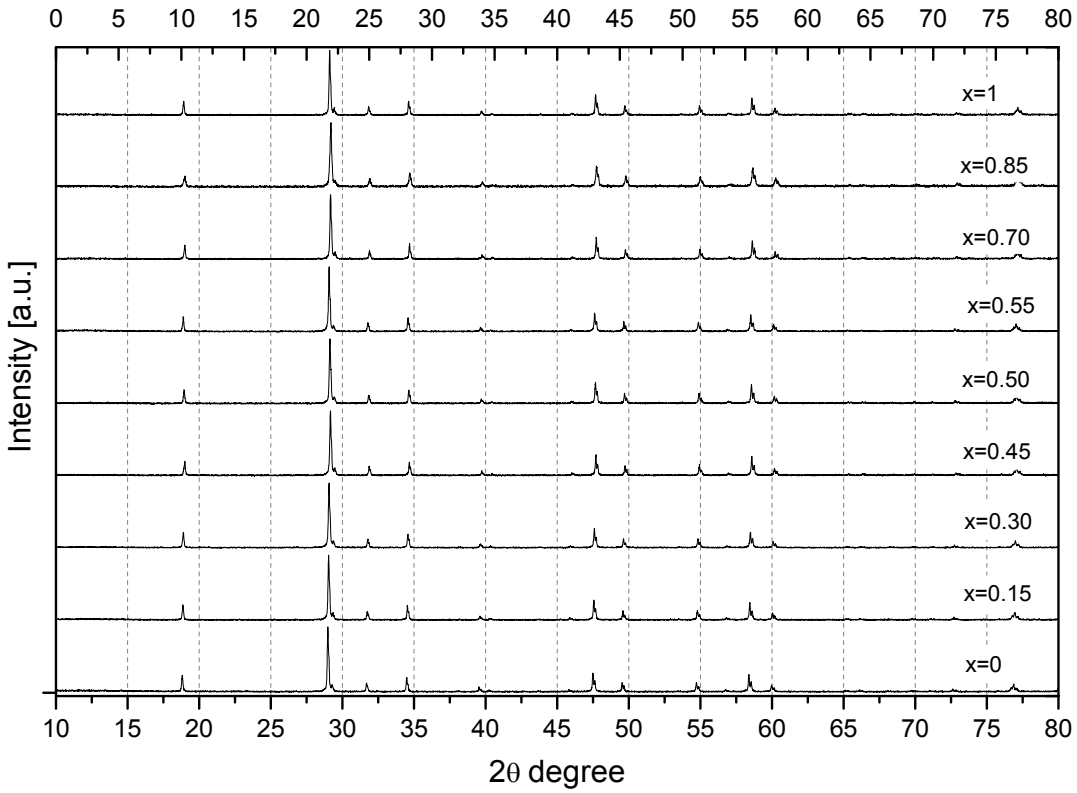

Figure 6.22: XRPD patterns of $LiEu_{(1-x)}Gd_x(WO_4)(MoO_4)$

The cell volumes and lattice parameters in the refinement of $LiEu_{(1-x)}Gd_x(WO_4)(MoO_4)$ are shown in Table 6.9. The same model of $LiEu(WO_4)_2$ was selected once again as the starting point for the refinements. In agreement with the previous work reported in this chapter and chapter 5 this model was adjusted by replacing the $Eu^{3+}$with Gd^{3+} and the site occupied by W^{6+} was given a shared occupation with 50% Mo^{6+} (to become 1:1 ratio) in order to satisfy the formulation of $LiGd(WO_4)(MoO_4)$. From the table it can be observed that the R_{wp} values are in the range 11.79 to 14.46. In spite of the fact that the R_{wp} values were slightly higher than usual in the refinement, the visible difference between the refined model and the measured data was very little to the eye as can be observed as the grey line as displayed in Figure 6.23.

Table 6.10 shows that the Gd^{3+}cations occupied the same lattice site as the Li^+ cations having an occupancy factor of 0.480(9) while Li^+ occupies the site with 0.521(9). This data is sensible for the reason that the net charge of the compound was considerably neutral (near to 0 net charge), moreover the Li^+ cations have few electrons and so the fit will not be expected to be precise. Figure 6.24 (a) presents the graph of the cell volumes and shows a gradual decline as the amount of Gd^{3+} cations increased substituting Eu^{3+} cations causing the cell to contract. From the figure it is

obvious that the downward trend was not as sharp as that seen in $LiEu_{(1-x)}Y_x(WO_4)(MoO_4)$ in Chapter 5. The cell sizes change only slightly and though apparent in the figure, it is difficult to distinguish which cell dimensions were more affected (the a = b cell dimensions or the c cell dimensions as shown in Figure 6.24 (b)) because the cell volume only reduced less than 1 % from the starting size of the parent compound.

Table 6.9: Lattice parameters of tetragonal $I4_1/a:2$ $LiEu_{(1-x)}Gd_x(WO_4)(MoO_4)$ Tetragonal $I4_1/a:2$

Gd^{3+} (mol)	a (Å)	c (Å)	Vol (Å^3)	R_{exp}	R_{wp}	R_p
0	5.20657 (9)	11.3088 (3)	306.562 (12)	12.48	13.61	10.83
0.15	5.204493(88)	11.30311(26)	306.165(12)	11.81	13.49	10.80
0.30	5.202624(83)	11.29846(24)	305.819(12)	11.10	12.42	9.93
0.45	5.20072(11)	11.29403(31)	305.475(15)	12.89	14.46	11.44
0.50	5.19954(11)	11.29150(31)	305.268(15)	12.51	14.75	11.78
0.55	5.19885(10)	11.29028(29)	305.154(14)	11.78	13.52	10.78
0.70	5.19672(10)	11.28461(29)	304.751(14)	12.42	14.08	11.14
0.85	5.19417(19)	11.27889(53)	304.298(26)	13.23	15.91	12.48
1	5.192978(92)	11.27453(27)	304.041(13)	11.79	12.82	10.26

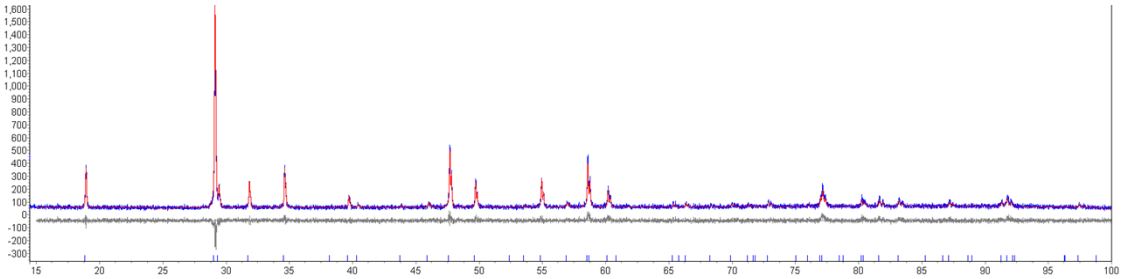

Figure 6.23: Retvield refinement of $LiGd(WO_4)(MoO_4)$

Table 6.10: Site occupancies of $LiGd(WO_4)(MoO_4)$

Site	**Np**	**x**	**y**	**z**	**Atom**	**Occ**
Mo/W	4	0.50000	0.75000	0.12500	Mo^{+6} W^{+6}	0.5 0.5
Gd	4	0.00000	0.25000	0.12500	Gd^{+3} Li^{+1}	0.480(9) 0.521(9)
O	16	0.7592(31)	-0.0861(55)	0.0352(13)	O^{-2}	0.86(5)

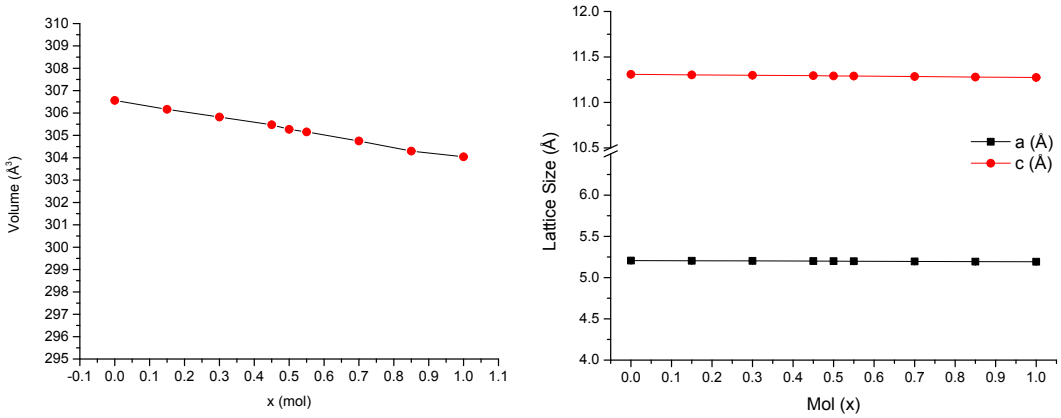

(a) (b)

Figure 6.24: (a) Cell volumes and (b) Lattice parameters of $LiEu_{(1-x)}Gd_x(WO_4)(MoO_4)$

The refined $LiGd(WO_4)(MoO_4)$ result was then exported to VISTA software to generate a modelled structure presented in Figure 6.25(a) and (b). It is no surprise that there was no difference in how the oxygen ions are coordinated in this particular lattice compared with earlier findings (apart from those of $LiY(WO_4)_2$) given that the crystal structure of this compound did not transform. As expected each Gd^{3+} is surrounded by eight oxygen ions as seen in Figure 6.25 (a) and also every Mo^{6+} / W^{6+} ion comes with four oxygen ions building tetrahedral shapes as shown Figure 6.25(b).

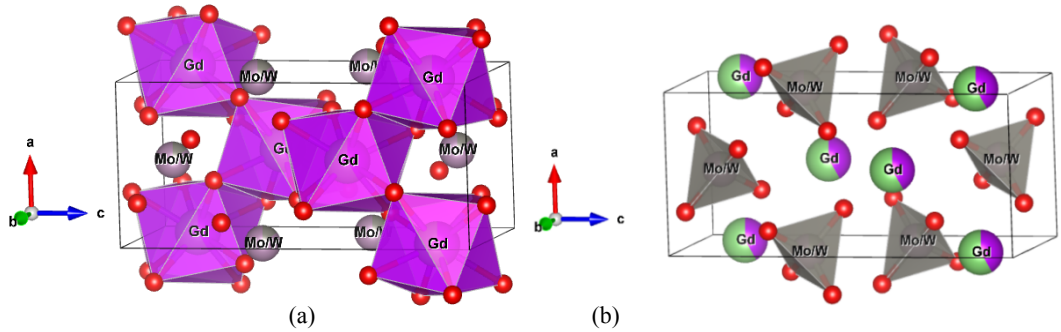

(a) (b)

Figure 6.25: Scheelite modelled structure of $LiEu_{(1-x)}Gd_x(WO_4)(MoO_4)$ that shows (a) eight oxygen anions surrounding Gd^{3+}/Li^{+} cations, (b) the tetrahedral shape of oxygens isolating $(WO_4)^{2-}$ and $(MoO_4)^{2-}$ in a lattice.

6.1.3.2 Photoluminescence Properties

Figure 6.26 and Figure 6.27 show the emission spectra of the samples when excited at 395nm and 465 nm respectively. The spectra from both figures show emission bands which manifest transitions from the excited state of Eu^{3+}(at 588–600 nm due to $^5D_0 \rightarrow {}^7F_1$ transition, the brightest 610–630 nm ($^5D_0 \rightarrow {}^7F_2$), 640–662 nm ($^5D_0 \rightarrow {}^7F_3$), and also at681–710 nm ($^5D_0 \rightarrow {}^7F_4$)). The figures also show that the spectral intensity especially the emission which relates to $^5D_0 \rightarrow {}^7F_2$ transition at 616

nm manifests a slight reduction as the amount of Gd^{3+} increases until x=0.70. The luminescence intensities on both excitations still looked good until they experienced sudden drops near to half of the initial intensity for $LiEu_{(0.15)}Gd_{0.85}(MoO_4)(WO_4)$ at around 90%Gd^{3+} before losing the entire intensity when no more Eu^{3+} was present in the pure Gd material.

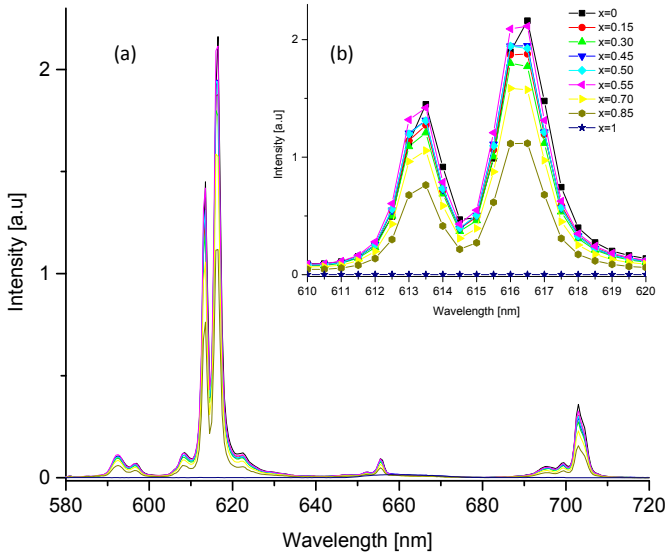

Figure 6.26: Emission spectra of $LiEu_{(1-x)}Gd_x(MoO_4)(WO_4)$ excited at 395nm as seen (a) from range of 580-720 nm and (b) at closer range from 610 – 620 nm

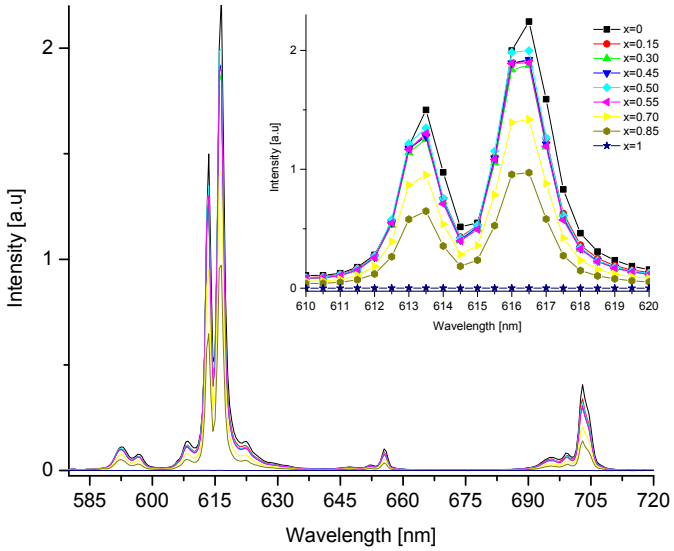

Figure 6.27: Emission spectra of $LiEu_{(1-x)}Gd_x(MoO_4)(WO_4)$ excited at 465nm as seen (a) from range of 580-720 nm and (b) at closer range from 610 – 620 nm

Table 6.1 shows the values of luminous efficacies measured from these phosphors and plotted in Figure 6.28(a) and (b). It was interesting to observes from the graphs that the values overall remained fairly steady for 395 nm excitation and just fall a little for 465 nm excitations as the concentration of Eu^{3+} decreased but then

there was a rise which can be seen when the concentration of Gd^{3+} reached a 1:1 ratio with Eu^{3+}. $LiEu(WO_4)(MoO_4)$ was measured to produce 195.38lm/W and reached its peak at $LiEu_{0.50}Gd_{0.50}(WO_4)(MoO_4)$ with 212.53 lm/W when excited at 395 nm. The same parent compound yielded 243.78lm/W when excited at 465 nm and although it went down a little, the luminous efficacy started improving at Gd^{3+} = 0.55 mol. The explanation for this can be of course the consequence of a several factors but one is the fact that in this series of phosphors the initial tetragonal phase of the parent Eu^{3+} compound did not transform.

Table 6.11: Luminous efficacies of $LiEu_{(1-x)}Gd_x(WO_4)(MoO_4)$ excited at (a) 395nm and (b) 465 nm

x (Mol)	Luminous Efficacy (lm/W)	
	exc 395 nm	exc 465 nm
0	195.38	243.78
0.15	193.56	225.87
0.3	192.65	223.90
0.45	197.35	217.35
0.5	204.50	238.85
0.55	212.53	235.31
0.7	205.58	214.35
0.85	151.41	155.99
1	N/A	N/A

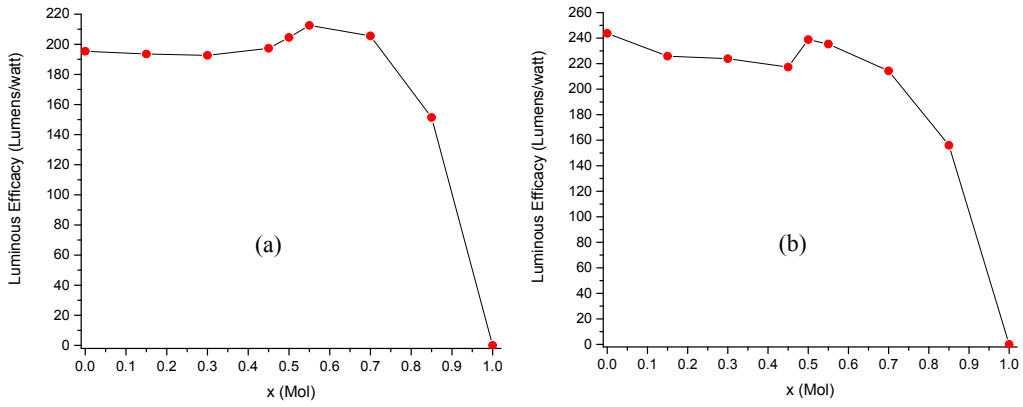

Figure 6.28: Luminous efficacies of $LiEu_{(1-x)}Gd_x(WO_4)(MoO_4)$ excited at (a) 395nm and (b) 465 nm

The spectra were normalised as shown in Figure 6.29 and it is apparent that with an increasing Eu^{3+} concentration, the emission lines started to broaden indicating that in the parent $LiEu(MoO_4)(WO_4)$ phosphor, concentration quenching was already in place. Therefore for the $LiEu_{(1-x)}Gd_x(MoO_4)(WO_4)$ compound Gd^{3+} at about 0.50 mol – 0.55 mol can be the right candidate for the most efficient luminescence. So

more economical phosphors with improved luminescence can be had by incorporating about 50% of Gd^{3+} into the lattice depending on the desired luminous efficacy.

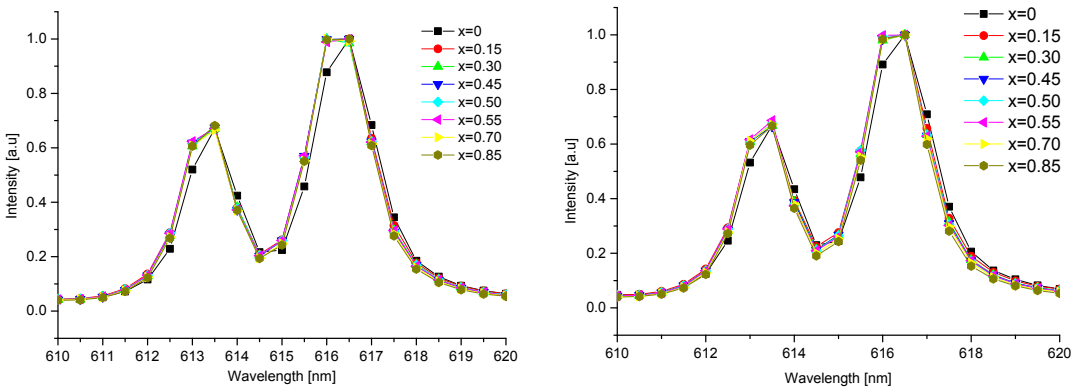

Figure 6.29: Normalized spectra of $LiEu_{(1-x)}Gd_x(WO_4)(MoO_4)$ excited at (a) 395nm and (b) 465 nm

Table 6.12 shows the CIE colour coordinates of $LiEu_{(1-x)}Gd_x(WO_4)(MoO_4)$ from x=0 until x=1. Again it can be seen from the table that the colour coordinates of the phosphor are not affected much as the Gd^{3+}concentration increases, thus it can be concluded that the colour temperature did not move significantly. Even so the CIE coordinates of all samples which are shown in Figure 6.30 and Figure 6.31 do move a little towards the colder temperature region as a function of falling Eu^{3+}concentration.

Table 6.12: CIE Colour coordinates of $LiEu_{(1-x)}Gd_x(WO_4)(MoO_4)$

No.	Gd^{3+} Concentration (mol)	Exc 395 nm			Exc 465 nm		
		Coordinates		Colour temp	Coordinates		Colour temp
		x	y		x	y	
1	0	0.6715	0.3283	872 K	0.6705	0.3290	878 K
2	0.15	0.6718	0.3279	870 K	0.6715	0.3283	872 K
3	0.30	0.6716	0.3282	871 K	0.6713	0.3285	874 K
4	0.45	0.6714	0.3284	873 K	0.6711	0.3287	875 K
5	0.50	0.6715	0.3283	872 K	0.6711	0.3287	875 K
6	0.55	0.6714	0.3284	873 K	0.6709	0.3288	876 K
7	0.70	0.6710	0.3288	876 K	0.6705	0.3293	879 K
8	0.85	0.6703	0.3295	881 K	0.6695	0.3303	887 K
9	1	N/A					

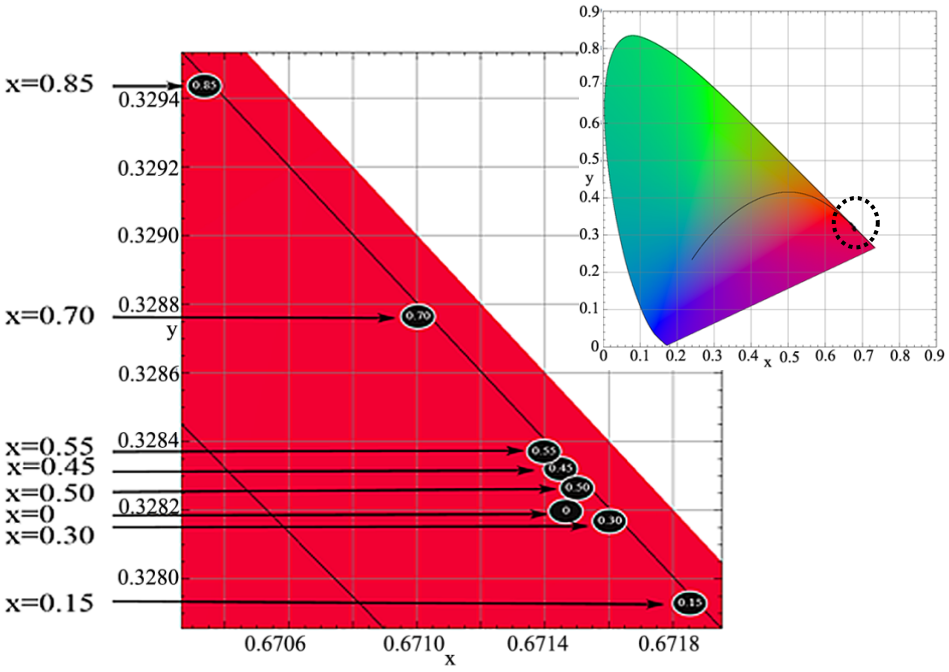

Figure 6.30: CIE diagram for $LiEu_{(1-x)}Gd_x(WO_4)(MoO_4)$ excited at 395nm

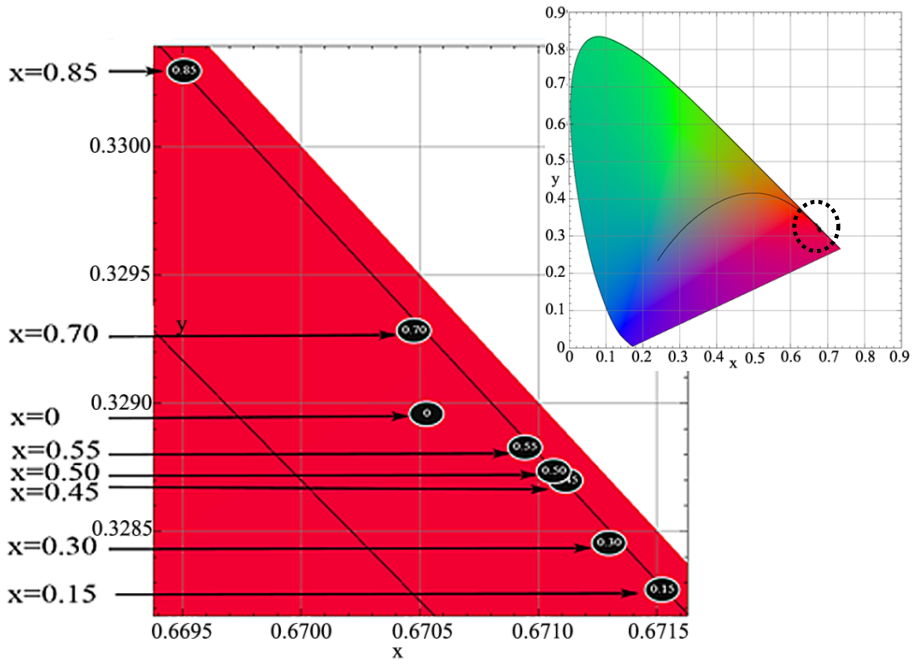

Figure 6.31: CIE diagram for $LiEu_{(1-x)}Gd_x(WO_4)(MoO_4)$ excited at 465nm

6.2 SEM Images

Figure 6.32 shows that the $LiGd(WO_4)_2$ particles exhibit a spherically shaped surface morphology within 1-4 µm size range. There also seems to be a strong adherence among the particles in the compound. The concave imprints as seen on the

top left of the figure were probably due to the physical force used during the separation from the crucibles or also may be due to some effects after grinding the samples to become powder. Figure 6.33 shows the $LiGd(MoO_4)_2$ powder in which the crystallites have more angular-shapes with less adherence between the particles compared to those of $LiGd(WO_4)_2$. The particles also looked anisotropic due to distortions or elongations in certain preferential directions as the material grows which makes the particles size irregular with a larger size range. Figure 6.34 shows a view of the morphology of the $LiGd(WO_4)(MoO_4)$ material where there is also clearly less adherence between the particles. The shapes of the particles also seemed to be more spherical as compared to the $LiGd(MoO_4)_2$ as seen in Figure 6.33.

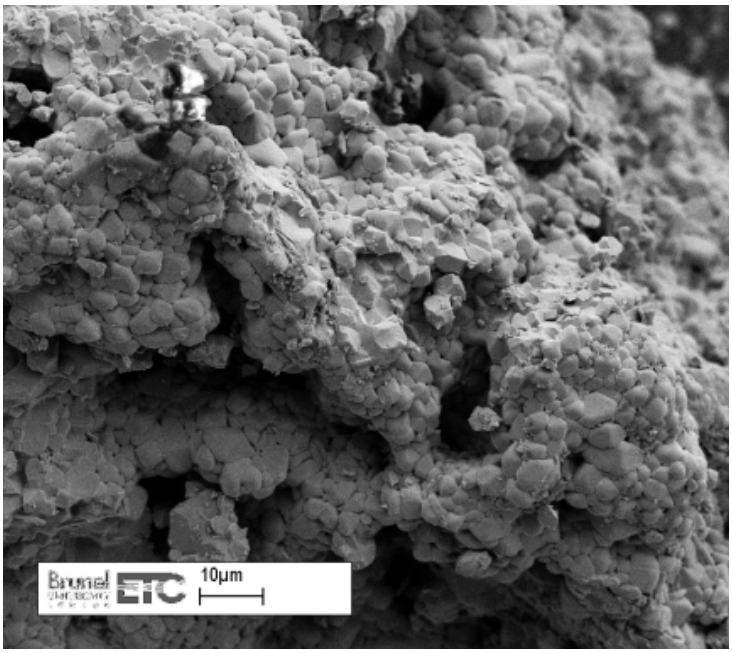

Figure 6.32: SEM images of $LiGd(WO_4)_2$ with 5kx magnification

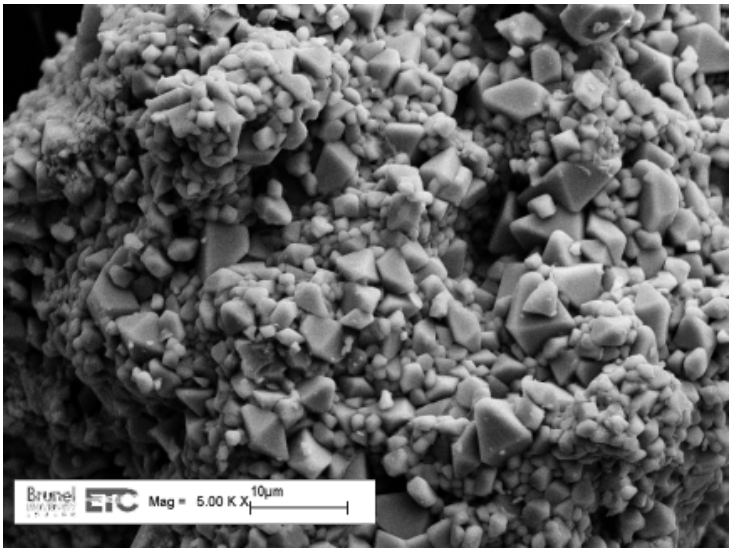

Figure 6.33: SEM images of $LiGd(MoO_4)_2$ with 5kx magnification

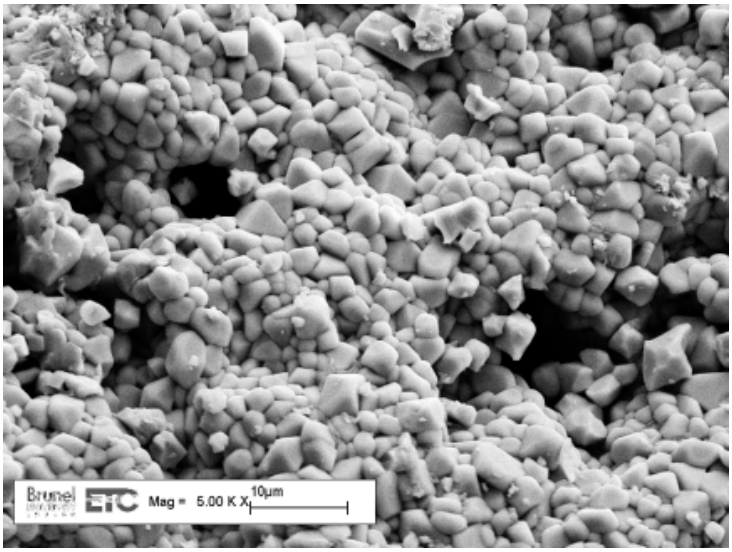

Figure 6.34: SEM images of $LiGd(WO_4)(MoO_4)$ with 5kx magnification

6.1 Conclusions

After observing and analysing all results in this chapter, there are a number of conclusions can be made;

1) $LiEu_{(1-x)}Gd_x(WO_4)_2$ compound does not change to a different phase as Gd^{3+} increases. The phosphor was found to be very difficult to yield good results consistently. This did not happen to the other two sets of samples $LiEu_{(1-x)}Gd_x(WO_4)(MoO_4)$ and $LiEu_{(1-x)}Gd_x(MoO_4)_2$. After several attempts to remake the samples, although the luminous efficacy dropped at certain concentrations it can be agreed that $LiEu_{0.5}Gd_{0.5}(WO_4)_2$ still can be a decent option for the parent compound.
2) For $LiEu_{(1-x)}Gd_x(MoO_4)_2$ and $LiEu_{(1-x)}Gd_x(WO_4)(MoO_4)$, Gd^{3+} can be incorporated up to 70% in replacing Eu^{3+} content without much intensity loss; therefore it offers cheaper cost as compared with the parent compound. Additionally, the best composition at Gd^{3+}=0.55 mol for $LiEu_{(1-x)}Gd_x(WO_4)(MoO_4)$ indeed gives higher luminous efficacy compared to its parent compound.
3) The luminous efficacies recorded in $LiEu_{(1-x)}Gd_x(MoO_4)_2$ and $LiEu_{(1-x)}Gd_x(WO_4)(MoO_4)$ are slightly lower than the sets of samples that incorporated Y^{3+} as in Chapter 5. Based on our initial observation, the best efficiency turned out to be optimized when the lattice volumes were in the range of 301.5 $Å^3$ - 301.8 $Å^3$ which were not achieved for all samples in this chapter. Although the lattice volume can reach down to 304.298 $Å^3$, at that stage the concentration of $Eu^{3+}$is too low therefore it will not have an ideal distance between the activators to yield efficient emission.

6.2 References

1. Yi L, He X, Zhou L, Gong F, Wang R, Sun J (2010) A potential red phosphor $LiGd(MoO_4)_2:Eu^{3+}$ for light-emitting diode application. *Journal of Luminescence*, 130(6), 1113-1117.

2. Li J, Lu C, Lu H, Yang X, Zhu B, Yu H, Sheng J, Che S (2015) Photoluminescent properties of the promising red-emitting phosphor $LiGd_{1-x}Eu_x(MoO_4)_2$ for WLEDs. *Ceramics International*, 41, S725-S728.

3. Glorieux B, Jubera V, Apheceixborde A, Garcia A (2011) Luminescence properties of tungstates and molybdates phosphors: Illustration on A Ln $(Mo_4)_2$ compounds (A= alkaline cation, Ln= lanthanides, M= W, Mo). *Solid State Sciences*, 13(2), 460-467.

4. Postema J, Fu W, Ijdo D (2011) Crystal structure of $LiLnW_2O_8$ (Ln = lanthanides and Y): An X-ray powder diffraction study. *Journal of Solid State Chemistry*, 184(8), 2004-2008.

Chapter 7

Incorporating Aluminium (III) on Tungstate / Molybdate Host Lattices

The focus of this chapter is on investigating the possibility of minimizing the use of Eu^{3+} by replacing the rare earth cations with aluminium Al^{3+}. Instead of using Y^{3+} and Gd^{3+} as discussed in Chapter 5 and 6, Al^{3+} was selected as a potential candidate to replace Eu^{3+} in the lithium europium molybdate/tungstate host lattices. In Chapter 3 it was discussed that there is very limited information regarding the impact of Al^{3+} cations on the luminescent properties of molybdate/tungstate based phosphors. The fact that Al^{3+} has a very small atomic radius in comparison to those of Y^{3+}, Gd^{3+} and Eu^{3+} and that it has a maximum coordination number of 6 makes it an interesting and potentially good candidate for improving the tungstate / molybdate phosphors. In addition, Al^{3+} originating in Al_2O_3 (the starting material used in this experiment) is much cheaper than any Eu^{3+} starting material. Earlier work from our laboratories has shown that it is indeed possible to incorporate Al^{3+} into tungstate / molybdate lattices, and that the resulting phosphors have interesting properties [1]. The research in this chapter was aimed at studying this incorporation in greater detail. Phosphor samples with a general formula $LiEu_{1-x}Al_x(MoO_4)_{2-y}(WO_4)_y$ (x=0, 0.15, 0.30, 0.45, 0.50, 0.60, 0.75, 0.95 and 1 whereas y=0, 1 and 2) were prepared by solid state reaction as explained in Chapter 3 and associated results are presented herein.

7.1 Incorporation of Al^{3+} into Tungstate host lattices

7.1.1 Powder Crystallography

The XRPD patterns of all phosphor samples $LiEu_{(1-x)}Al_x(WO_4)_2$ are displayed in Figure 7.1. The parent compound $LiEu(WO_4)_2$ is isostructural with other parent Eu^{3+} phosphors as discussed in the previous chapters fitting the tetragonal space group $I4_1/a$:2. The most intense diffraction peak at $2\theta \approx 29°$ is due to the (112) reflection. Other peaks at $2\theta \approx$ 18.8°, 31.7° 34.4° and 47.5° respectively correspond to (101), (004), (200) and (204) reflections. No noticeable changes can be seen from the XRPD

patterns as x increases from x=0 to x=0.45 but a second phase is detected starting at x=0.50 and this is increasing until significant changes arise when x=0.75 until x=1.

There is clear evidence for the systematic growth of a second unknown phase above x=0.45 throughout the phosphors presented in Figure 7.1. However, the tetragonal phase of the parent x=0 compound is still seen to persist up to x=0.75 (as seen in Figure 7.7), but there is no evidence of it in the x=0.95 material, indicating that the initial tetragonal structure remains in the phosphors produced until x=0.75. While starting from x=0.50, new diffraction peaks can be seen clearly, particularly at $2\theta \approx 25.0°, 33.0°$, indicating that at least two phases were present (one with the tetragonal crystal phase and another unknown phase). Although the latter phase clearly grows as Al^{3+} increases, its XRPD data cannot be fitted in TOPAS software as its structure is unknown.

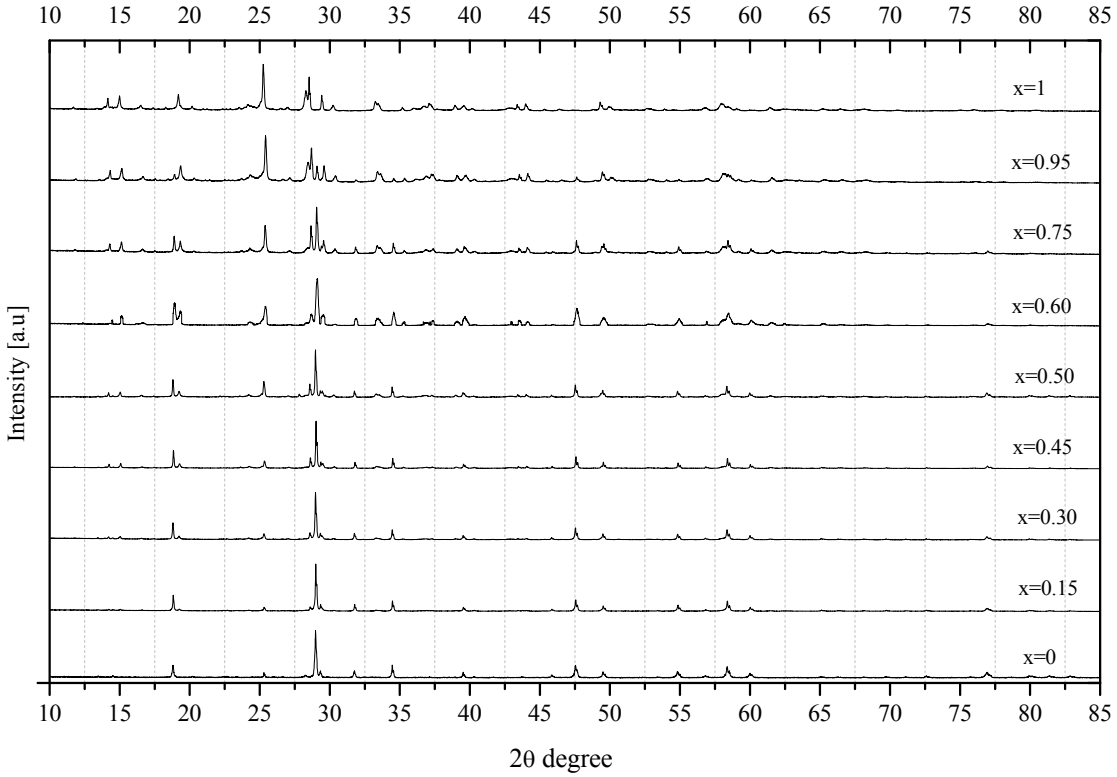

Figure 7.1: XRPD patterns of $LiEu_{(1-x)}Al_x(WO_4)_2$

As the crystal structure of $LiAl(WO_4)_2$ cannot be identified with any ICSD crystal database (including the starting materials used during synthesis), the stoichiometry was initially prepared as a large sample before being divided into a number of smaller samples and fired at different temperatures as shown in Figure 7.2.

The reason for this was to test if it was a single phase presented or to answer the question:- "Is there any possibility that the correct firing temperature had changed in the presence of aluminium oxide?".

Figure 7.2 shows the XRPD patterns of the compound when fired at 600 °C, 700 °C, 750 °C, 800 °C and 850 °C in comparison with the "parent" Eu^{3+} sample (in red) when fired at 750 °C. The figure indicates that there are differences between each of the firing temperatures. As for the sample which was fired at 600 °C, the diffraction peak which used to be found at $2\theta \approx 28.5°$ is not present indicating that the structure is not tetragonal. Although the profile fitting cannot be performed by TOPAS software due to the inability of the relevant data in the ICSD database, a scan from the EVA software as seen in Figure 7.3 gives some evidence that the starting material WO_3 used during the synthesis does not properly react when sintered at 600 °C. The peaks that represent WO_3 can be clearly detected at $2\theta \approx 23°, 23.5°$ and $24.5°$. The EVA software also clearly matched peaks belonging to lithium tungsten oxides with formulae $Li_2(W_2O_7)$ and $Li_2W_2O_4$. For the sample that had been fired at 700 °C as shown in Figure 7.4, the diffraction peaks of the triclinic $Li_2(W_2O_7)$, particularly at $2\theta \approx 13°, 14.5°$, were found to rise, indicating the growth of the crystal structure was occurring. The trace of WO_3 can still be observed from the figure suggesting that 700 °C is not yet a suitable firing temperature for this compound. The use of EVA in matching any possible materials on the compound fired at 750 °C were negative as none could be seen matched to the peaks of the compound but the trace of WO_3 had gone. There were also no more peaks of $Li_2(W_2O_7)$, WO_3, $Li_2W_2O_4$ or any other materials that can be matched by the EVA software. Interestingly none of the peaks matched to any of the EVA wide databases (that are sensible) and this makes the structure of the "compound" or compounds unknown.

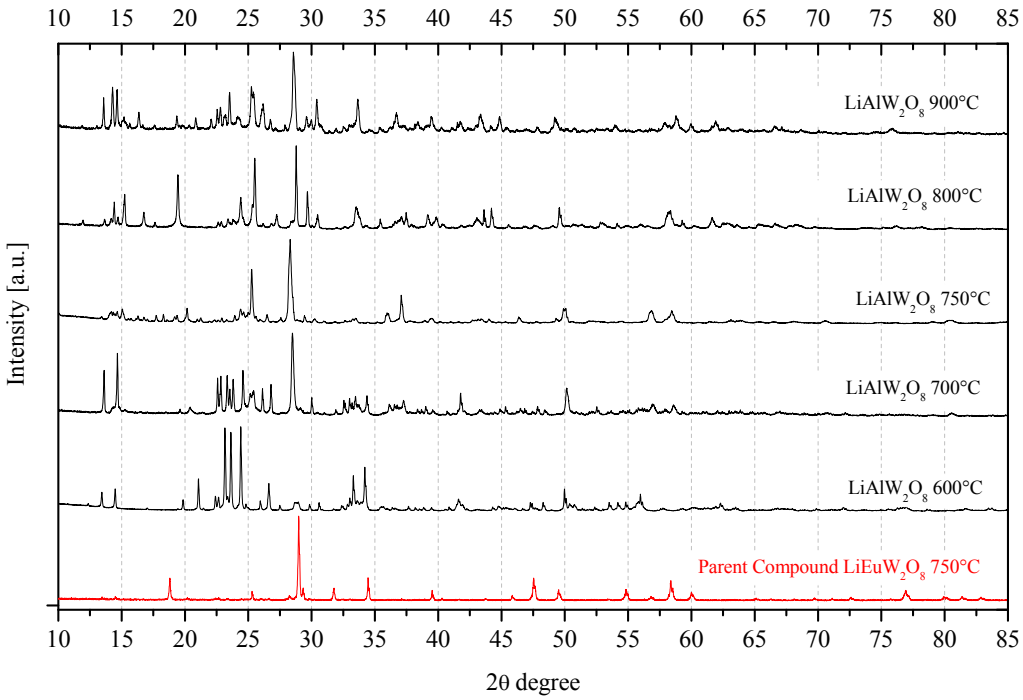

Figure 7.2: XRPD patterns of $LiAl(WO_4)_2$ sintered at different temperature in comparison to the $LiEu(WO_4)_2$ parent compound (red line)

For the compound that was fired at 800 °C, the EVA software matched the major peaks of the compound with $LiAl(WO_4)_2$ suggesting the peaks may belong to $LiAl(WO_4)_2$ which is in the literature but the structure has not been elucidated [2] (See Figure 7.5). However, the quality and reliability of the data is very low and questionable unless the model can be created and fitted with the sample. The XRPD peaks of the compound that was fired at 900 °C also suggest that there exists $LiAl(WO_4)_2$ in the compound (see Figure 7.6) but again without any details disclosed regarding the matching information. If this match is true, this means that the best firing temperature so far is in the range of 800 °C to 900 °C. However, nothing can be concluded as the fitting analysis cannot be done to support a given structure. The materials also contain impurities due to the formation of other materials in the same stoichiometry "compound".

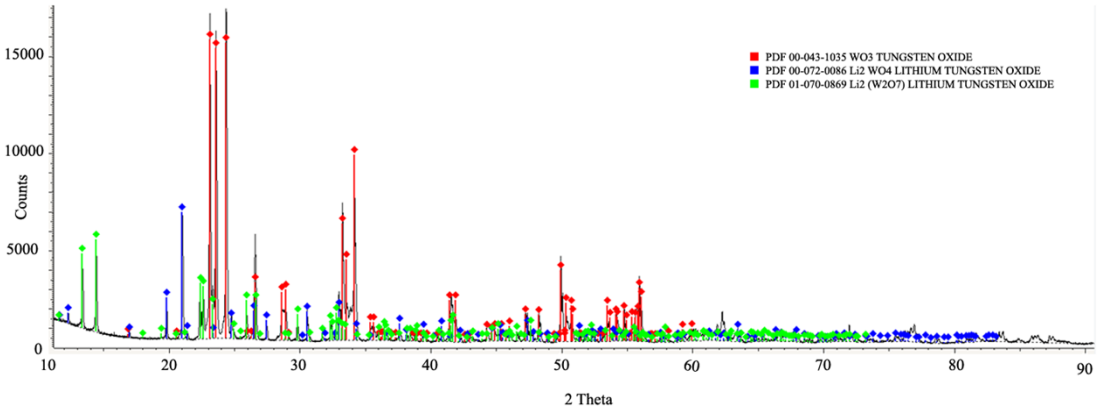

Figure 7.3: Materials matching using EVA software on $LiAl(WO_4)_2$ fired at 600°C

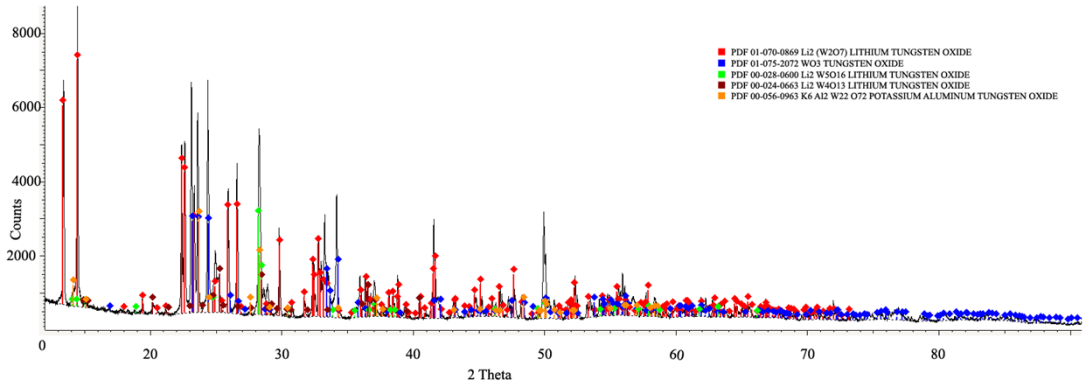

Figure 7.4: Materials matching using EVA software on $LiAl(WO_4)_2$ fired at 700°C

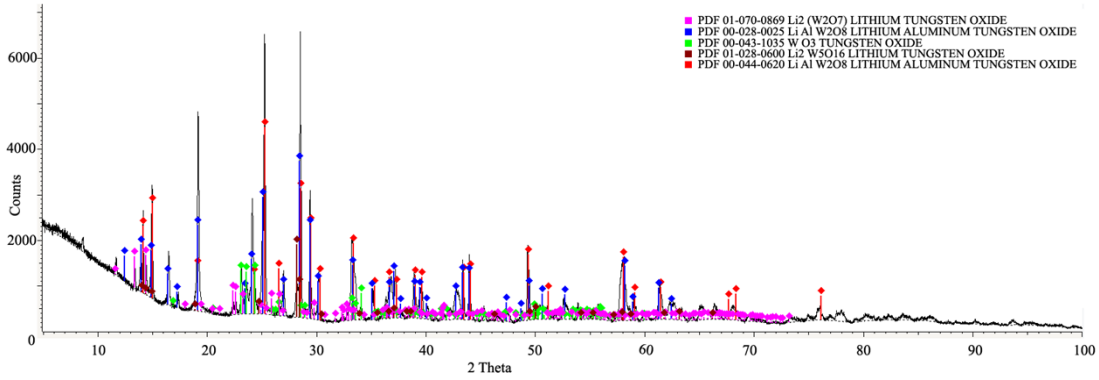

Figure 7.5: Materials matching using EVA software on $LiAl(WO_4)_2$ fired at 800°C

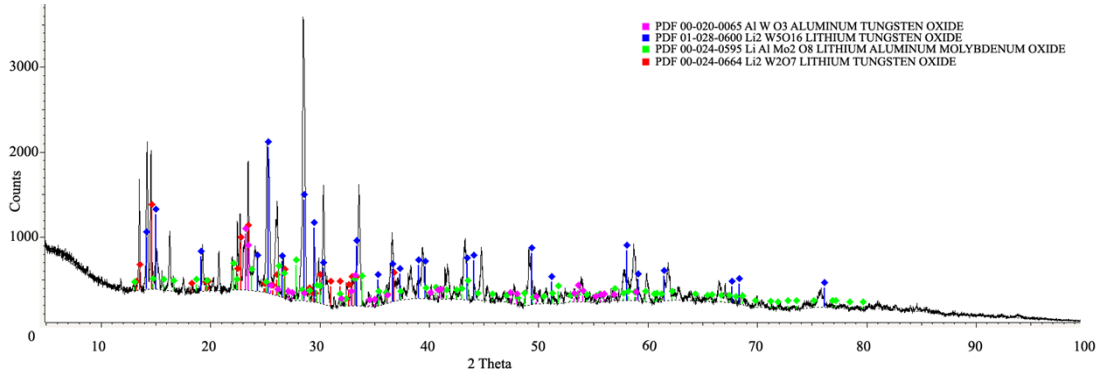

Figure 7.6: Materials matching using EVA software on $LiAl(WO_4)_2$ fired at 900°C

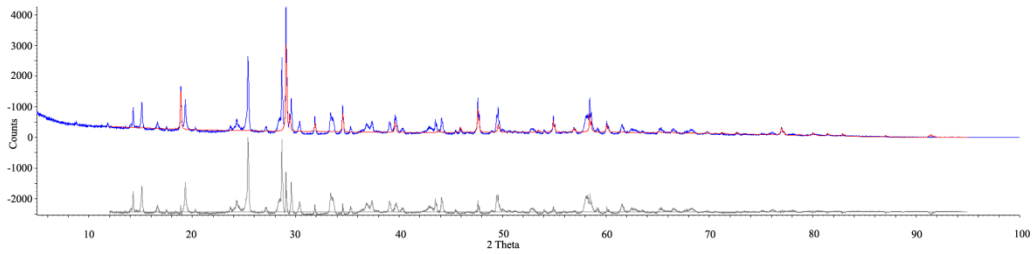

Figure 7.7: Partial refinement fit for $LiEu_{0.25}Al_{0.75}(WO_4)_2$

Table 7.1 shows the cell sizes and crystallite size arising from fitting the scheelite phase from x=0 until x=0.75. The results were initially refined with small margins of errors (R_{wp}s) but the value increases as the concentration of the Al^{3+} cations rises in keeping with progressively less of this phase being present. The cell volumes and lattice parameters were separately plotted as presented in Figure 7.8 (a) and (b). There is no specific trend that can be described on the impact of cell volumes and the lattice parameters. Despite the cell volume appearing slightly fluttered in the function of the increasing amount of Al^{3+}, the lattice parameters in Figure 7.8 (b) actually prove that the compound does not have significant lattice changes. The unchanged size of the lattice suggests that if the Al^{3+} cations are indeed entering the lattice they are not reducing the cell size or distorting it as might have been expected. The questions that therefore arise are:- "Do the Al^{3+} cations enter the lattice at all?" or if they do not enter "What happens to them?" In order to answer these questions other questions need to be asked such as:- "Is there other evidence that they are present for instance in the luminescent spectra?" This latter question will be explored below.

It may not be surprising that the Al^{3+} cations do not affect the lattice size as the Li^{+} cations occupy the same sites as the much larger Eu^{3+} cations. Therefore the lattice may in fact tolerate Al^{3+} cations replacing some of the Eu^{3+} cations before x=0.50.

Table 7.1: Lattice parameters of tetragonal $I4_1/a$:2 $LiEu_{(1-x)}Al_x(WO_4)_2$

Al^{3+} (mol)	Tetragonal $I4_1/a$:2			R_{exp}	R_{wp}	R_p
	a (Å)	c (Å)	Vol (Å^3)			
0	5.2082(1)	11.2809(3)	306.00(1)	3.92	10.81	7.01
0.05	5.2186(3)	11.3005(7)	307.76(4)	10.05	21.52	16.48
0.15	5.21049(11)	11.2816(3)	306.286(16)	7.59	26.13	18.51
0.30	5.20974(12)	11.2793(4)	306.136(18)	6.91	29.72	21.30
0.45	5.2021(2)	11.2923(5)	305.59(3)	6.30	42.27	31.28
0.50	5.21028(15)	11.2793(4)	306.20(2)	3.97	23.38	15.97
0.60	5.2144(3)	11.2879(9)	306.92(4)	9.49	31.73	23.19
0.75	5.2117(3)	11.2811(8)	306.42(4)	6.97	38.89	29.56
0.95			N/A			
1			N/A			

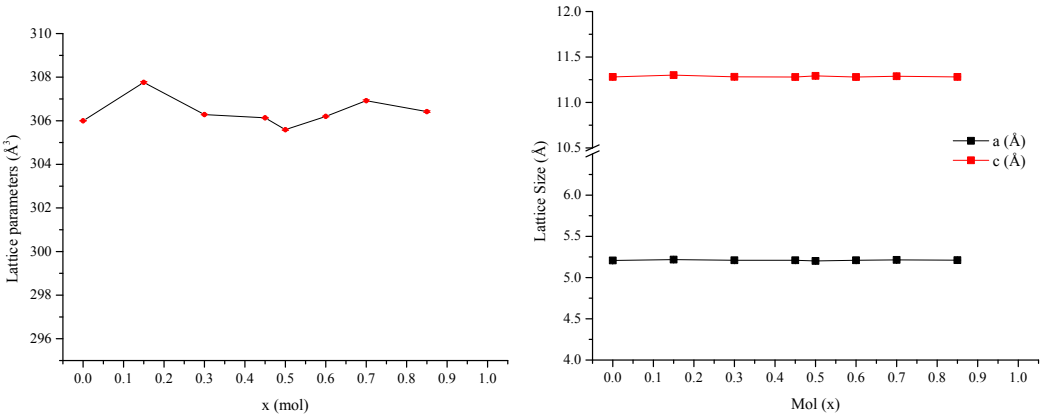

(a) (b)

Figure 7.8: (a) Cell volumes and (b) lattice parameters tetragonal of $LiEu_{(1-x)}Al_x(WO_4)_2$

7.1.2 Photoluminescence properties

The emission spectra excited at 395 nm and 465 nm of $LiEu_{(1-x)}Al_x(WO_4)_2$ are shown in Figure 7.9 to Figure 7.14. Two well resolved peaks are observed at 613 nm and 616 nm in both figures and are assigned to the $^5D_0 \rightarrow {}^7F_2$ transition of Eu^{3+} ions. The overlaid emission spectra excited at 395 nm presented in Figure 7.9 to Figure 7.11 implies that the spectral intensity dropped gradually whilst increasing Al^{3+} up to a value of x=0.45. It then increased again at x=0.50 and x=0.60 before decreasing rapidly. The same situation can also be observed in Figure 7.12 to Figure 7.14 when the phosphor was excited at 465 nm. All spectral forms are similar across the entire series of samples confirming that the symmetry of the emission centre had not been affected by the presence of Al^{3+} in the compound.

Since there are clearly two different types of patterns, as discussed in section 7.1.1, on the presence of scheelite phase and the phase based on $LiAl(WO_4)_2$, this also means that the two phases are not isostructural. Therefore it can be expected that the Eu^{3+} cations are not in identical environments in the two structures. If the Eu^{3+} cations were in very different electronic environments in both structures, this would manifest in the photoluminescent emission spectra of the different x values by the positions of the emission bands. In fact as seen in Figure 7.15 to Figure 7.19, there is no evidence for significant change in the band positions in the emission spectra so the electronic environments of the Eu^{3+} cations in the two structures must be very similar. Moreover, the excitation spectra of all the Eu^{3+} containing phosphors (x = 0 to 0.95)

are almost identical. An alternative explanation could be that all the Eu^{3+} cations are confined to the $LiEu_{(1-x)}Al_x(WO_4)_2$ which will be reviewed in this section.

It is clear to see from the results that the emission properties of the Eu^{3+} cations, if they go into the unidentified phase (*e.g.* as seen in samples x=0.75 and x=0.95), are inferior to those from the cation in the tetragonal $LiEu(WO_4)_2$ lattice. There are two possible explanations about the emission spectra coming from the unknown phase samples x=0.75 and x=0.95 although there is no tetragonal phase detected in the XRPD. The reason behind the emission spectra is either:

i) the emission is produced by an incredibly small amount of the tetragonal $LiEu_{(1-x)}Al_x(WO_4)_2$ phase being present (though there is no evidence from the XRPD analysis set out above). The unknown phase Eu^{3+} cations do not emit because should they do so they must be in a lattice site that is similar to the tetragonal structure as the spectra displayed no indication of different emission bands. OR

ii) the Eu^{3+} activator from the unknown phase itself emits identical spectra as seen in the tetragonal phase.

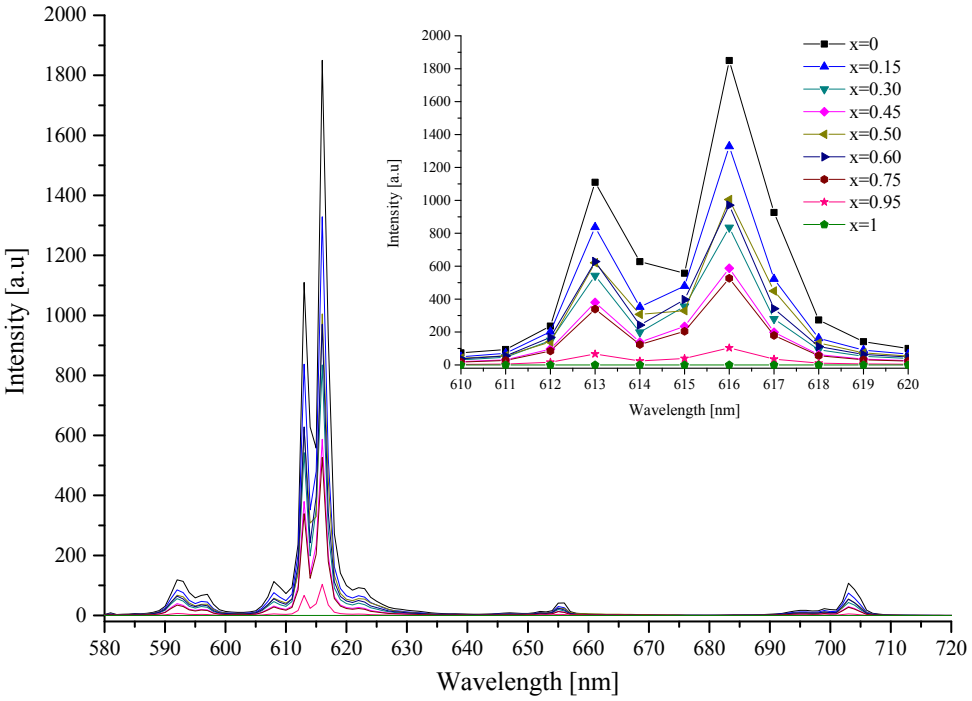

Figure 7.9: Emission spectra of $LiEu_{(1-x)}Al_x(WO_4)_2$ excited at 395 nm

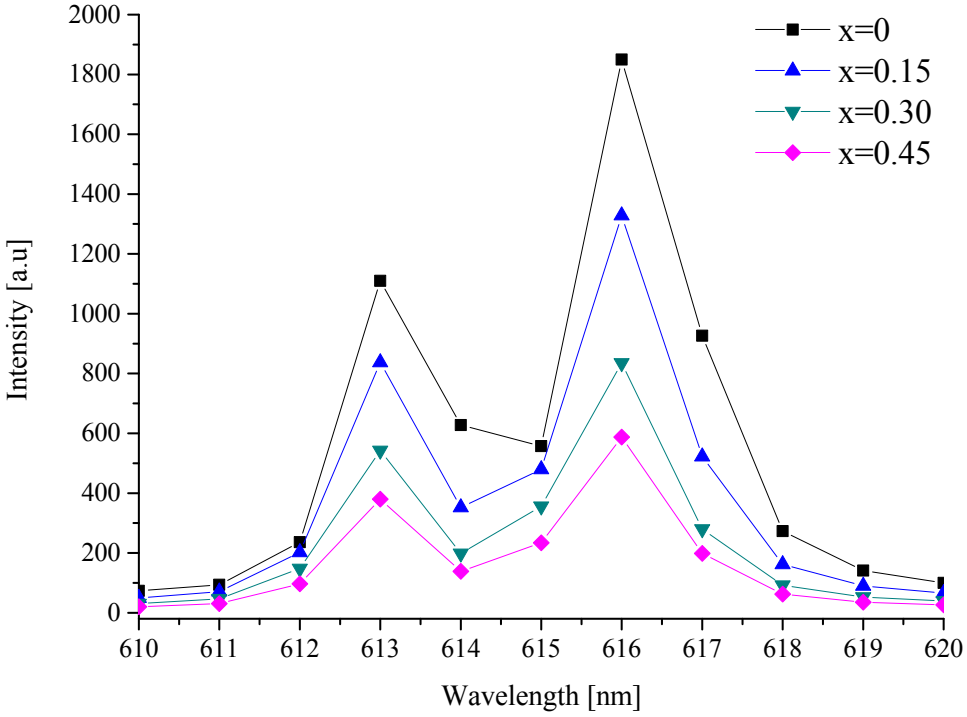

Figure 7.10: Emission spectra ranged from 610 nm – 620 nm of $LiEu_{(1-x)}Al_x(WO_4)_2$ excited at 395 nm (x=0 to 0.45)

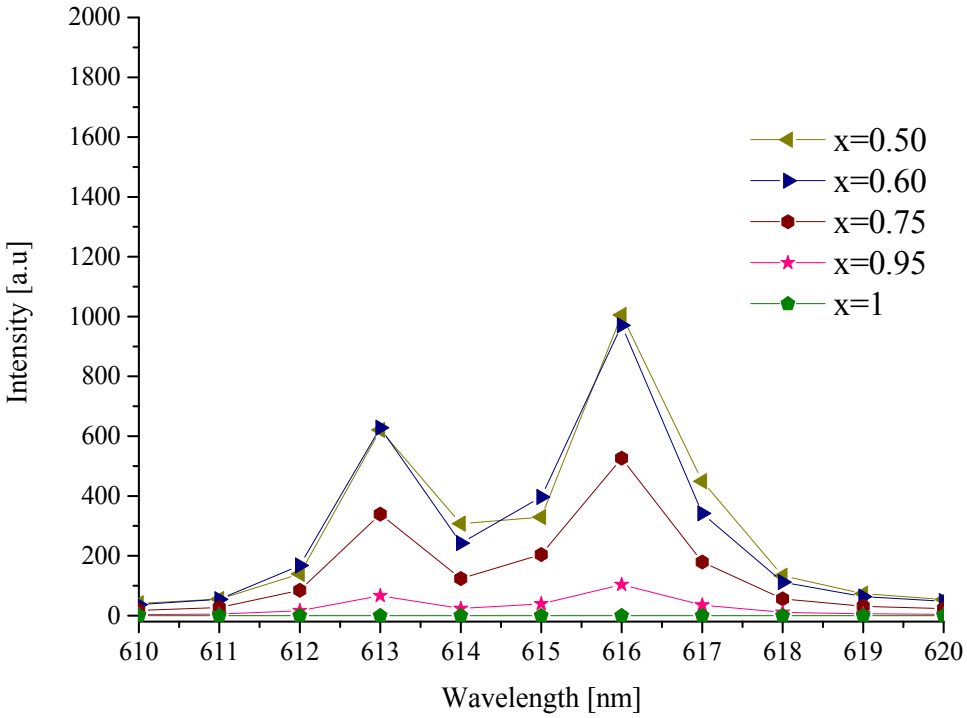

Figure 7.11: Emission spectra ranged from 610 nm – 620 nm of $LiEu_{(1-x)}Al_x(WO_4)_2$ excited at 395 nm (x=0.50 to 1)

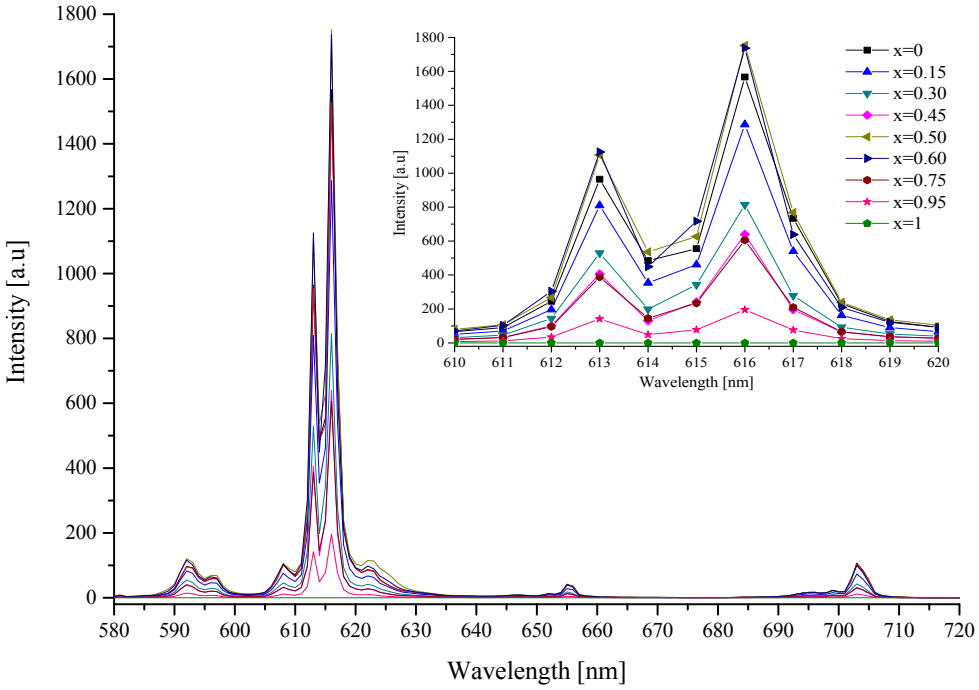

Figure 7.12: Emission spectra of $LiEu_{(1-x)}Al_x(WO_4)_2$ excited at 465 nm

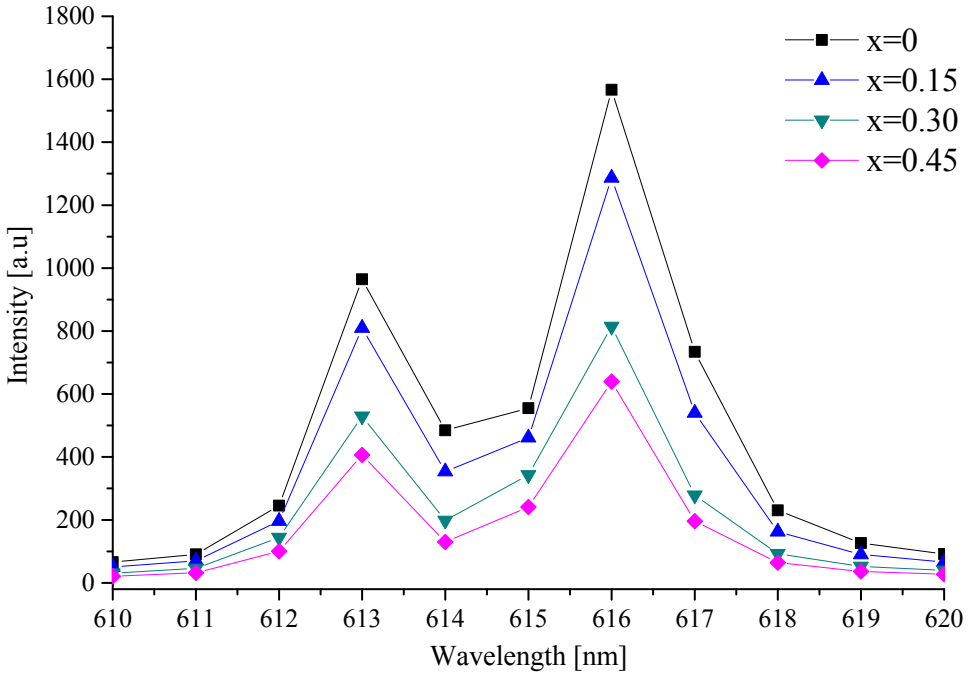

Figure 7.13: Emission spectra ranged from 610 nm – 620 nm of $LiEu_{(1-x)}Al_x(WO_4)_2$ excited at 465 nm (x=0 to 0.45)

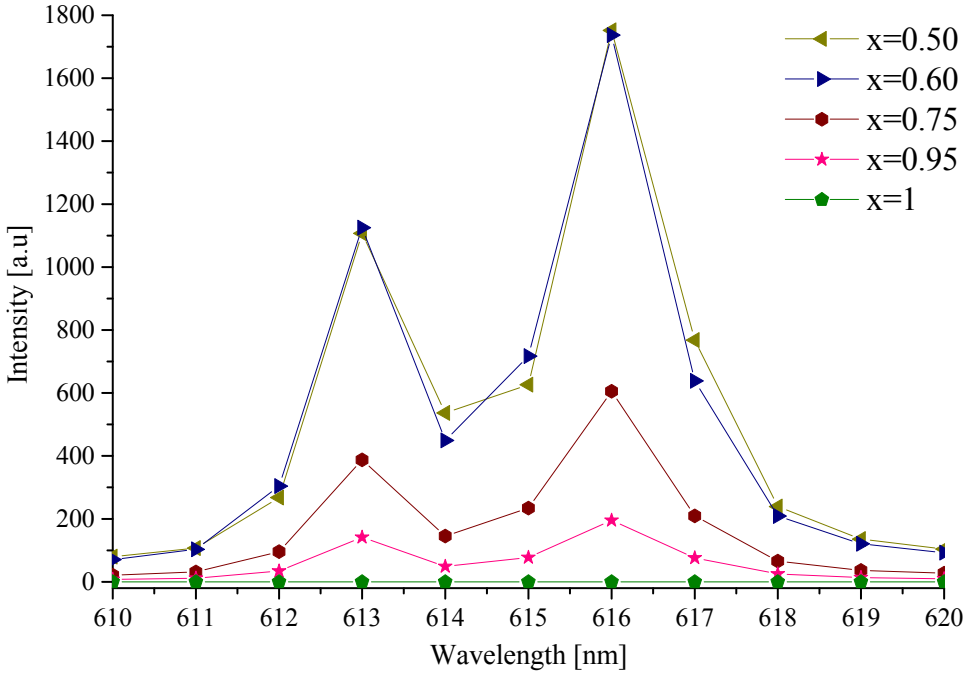

Figure 7.14: Emission spectra ranged from 610 nm – 620 nm of $LiEu_{(1-x)}Al_x(WO_4)_2$ excited at 465 nm (x=0.50 to 1)

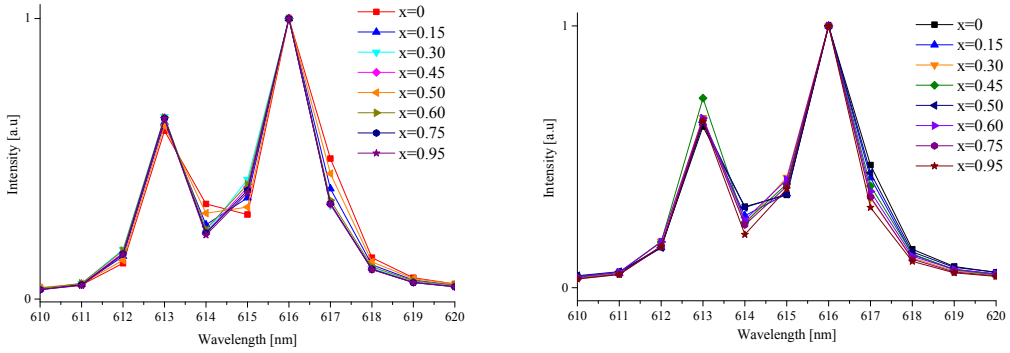

(a) (b)

Figure 7.15: Normalized emission spectra of $LiEu_{(1-x)}Al_x(WO_4)_2$ excited at (a) 395 nm and (b) 465 nm.

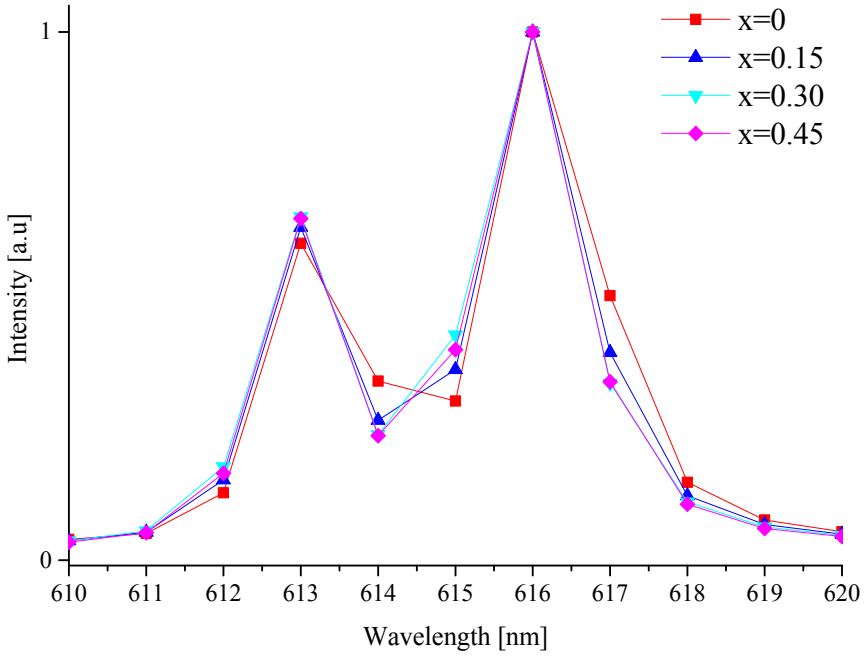

Figure 7.16: Normalized emission spectra of $LiEu_{(1-x)}Al_x(WO_4)_2$ excited at 395 nm (x = 0 to 0.45)

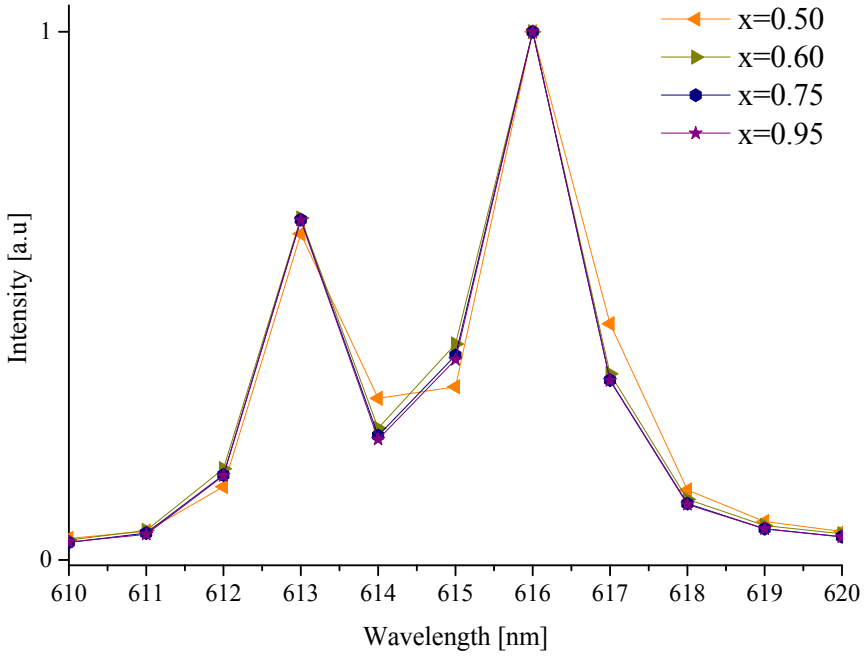

Figure 7.17: Normalized emission spectra of $LiEu_{(1-x)}Al_x(WO_4)_2$ excited at 395 nm (x = 0.50 to 0.95)

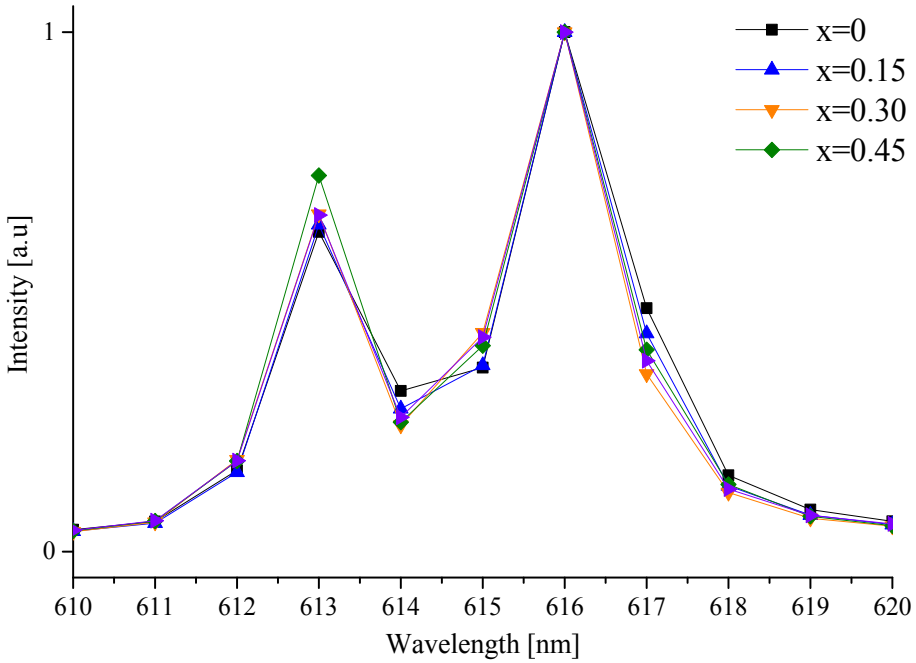

Figure 7.18: Normalized emission spectra of $LiEu_{(1-x)}Al_x(WO_4)_2$ excited at 465 nm (x = 0 to 0.45)

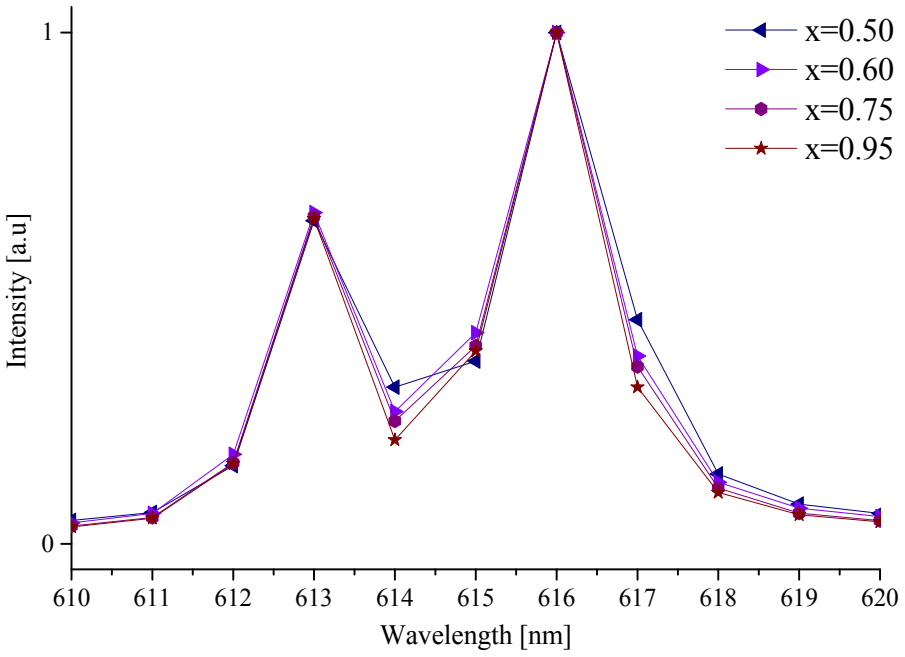

Figure 7.19: Normalized emission spectra of $LiEu_{(1-x)}Al_x(WO_4)_2$ excited at 465 nm (x = 0.50 to 0.95)

It is apparent from Figure 7.9 to Figure 7.13 that the decrease in the intensity of the emission from x=0.15 to x=0.45 occurs with a concomitant decrease in the line width of the two major emission lines. This indicates that the Eu^{3+} cation concentration is decreasing in the lattice as the narrowing spectral lines are indicative of less quenching in the emission. The fact that there is an increase in intensity in the

x=0.50 and x=0.60 data suggests that a major substitution of the Eu^{3+} has occurred. The increase followed by a further decrease in the line width also suggests the substitution of Al^{3+} cations into the lattice has taken place.

Table 7.2 shows the luminous efficacies while Figure 7.20 (a) and (b) show the plots coming from all samples excited at 395 nm and 465 nm. The results exhibit a different behaviour to those demonstrated in Chapter 5 where it was found that there was a phase transformation when Y^{3+} was introduced into $LiEu(WO_4)_2$. It is clear that although the tetragonal phase appears to be unaltered by the presence of Al^{3+} cations as discussed in section 7.1.1, the luminous efficacy results can only be explained if the Al^{3+} cations are entering the $LiEu(WO_4)_2$ lattice. If no Al^{3+} cations entered the lattice then it would be expected that the amount of $LiEu(WO_4)_2$ would decrease continuously as the Al^{3+} cations were added. However, this would result in a continuous drop in luminous efficacy and therefore does not account for the increase observed at x=0.50. Both graphs in Figure 7.20 (a) and (b) display a gradual decrease in luminous efficacy when Al^{3+} was added from x=0.15 to x=0.45 and then interestingly, there is a significant rise-back up at x=0.50. Indeed the sample of x=0.50, when excited from 450 nm wavelength, shows even greater efficacy than the parent $LiEu(WO_4)_2$. The luminous efficacy above x=0.60 then slowly decreases until x=0.95. The initial decline of efficacy (x=0 to x=0.45) was clearly due to the gradual loss of Eu^{3+}. This can be confirmed by looking at the consistent form of the normalised spectra in Figure 7.15 and Figure 7.19 which are similar to the parent $LiEu(WO_4)_2$ compound so the symmetry of the luminescent centre was not affected. The increase in efficacy when x=0.50 is due to the Eu^{3+} to Eu^{3+} distances are increasing so less quenching of the luminescence takes place, resulting in more of the light being emitted from the phosphor. The tetragonal lattice volume of the optimized compound at x=0.50 is 306.20 $Å^3$ which is larger than the volumes of the optimized phosphors obtained in Chapters 5 and 6.

Table 7.3 lists all colour coordinates of the $LiEu_{(1-x)}Al_x(WO_4)_2$ phosphors with their colour temperatures plotted in Figure 7.21 and Figure 7.22. The table and figures show that there was only a very small shift of colour coordinates and colour temperature that is consistent with the changes in the line widths of the two main emission bands.

It is apparent that the shift of CIE coordinates for the x=0.60, 0.75 and 0.95 values is reversed for the excitations at 395nm compared to that at 465nm.

Table 7.2: Luminous efficacies of $LiEu_{(1-x)}Al_x(WO_4)_2$ excited at 395 nm and 465nm

x (mol)	Exc 395 nm	Exc 465 nm
0	172.68	202.56
0.15	138.71	163.20
0.30	107.85	126.48
0.45	74.45	121.68
0.50	115.90	253.74
0.60	114.51	248.64
0.75	64.71	110.53
0.95	1.50	25.60
1	0.02	0.55

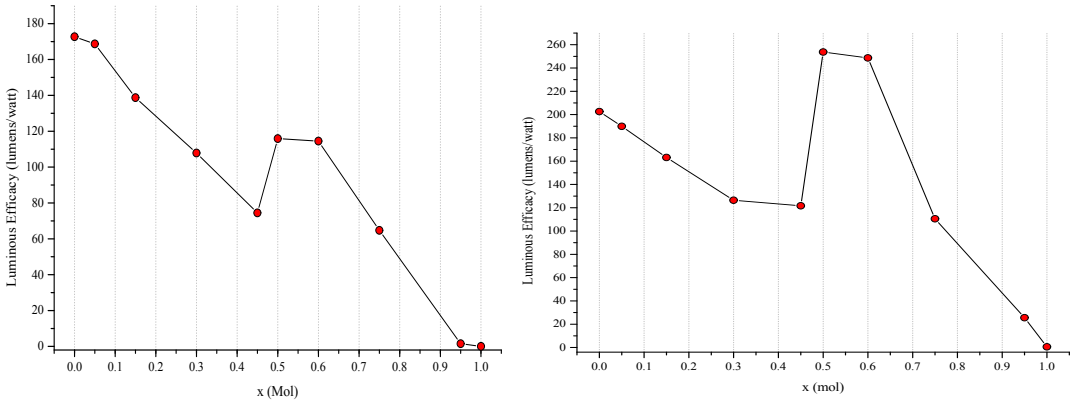

(a) (b)

Figure 7.20: Luminous efficacy of $LiEu_{(1-x)}Al_x(WO_4)_2$ excited at (a) 395 nm and (b) 465 nm

Table 7.3: CIE Colour coordinates of $LiEu_{(1-x)}Al_x(WO_4)_2$

No.	Al^{3+} Concentration (mol)	Exc 395 nm			Exc 465 nm		
		Coordinates		Colour temp	Coordinates		Colour temp
		x	y		x	y	
1	0	0.6690	0.3300	885 K	0.6696	0.3302	886 K
2	0.15	0.6697	0.3301	885 K	0.6693	0.3304	887 K
3	0.30	0.6696	0.3301	885 K	0.6692	0.3305	889 K
4	0.45	0.6696	0.3301	886 K	0.6691	0.3307	889 K
5	0.50	0.6695	0.3303	887 K	0.6688	0.3309	905 K
6	0.60	0.6695	0.3303	887 K	0.6690	0.3307	890 K
7	0.75	0.6696	0.3302	886 K	0.6687	0.3311	892 K
8	0.95	0.6696	0.3302	886 K	0.6680	0.3318	898 K
9	1	N/A					

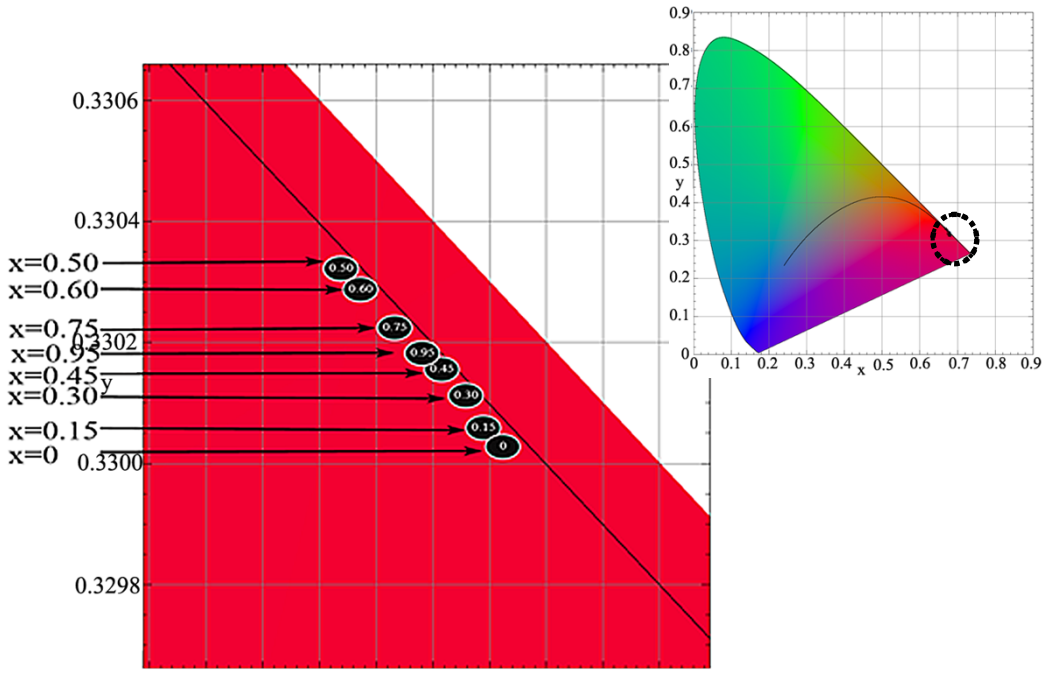

Figure 7.21: CIE diagram for $LiEu_{(1-x)}Al_x(WO_4)_2$ excited at 395nm

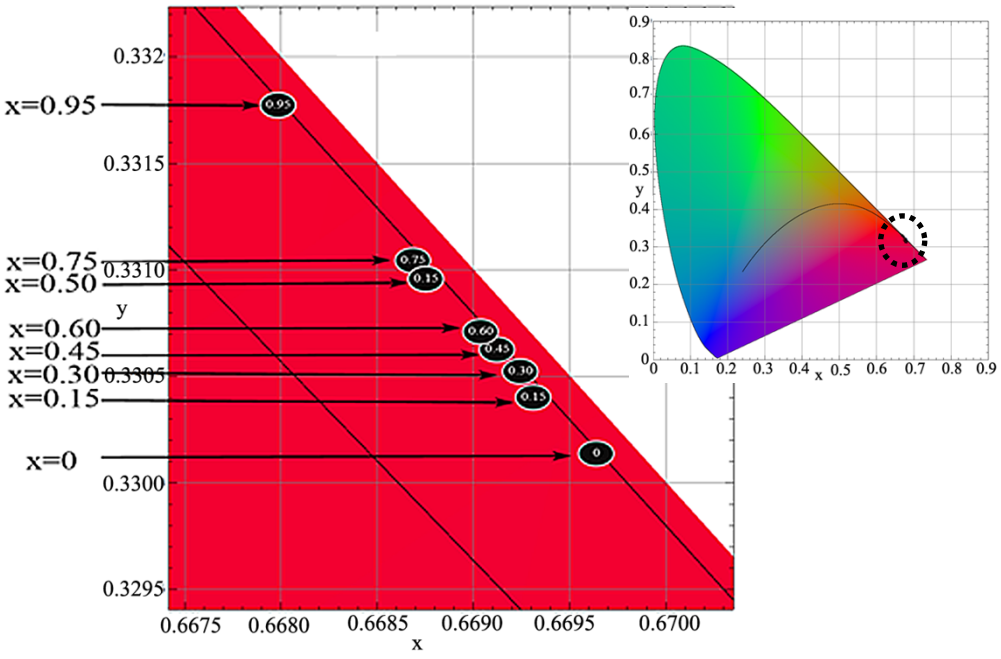

Figure 7.22: CIE diagram for $LiEu_{(1-x)}Al_x(WO_4)_2$ excited at 465 nm

7.2 Incorporation of Al^{3+} into Molybdate host lattices

7.2.1 Powder Crystallography

Figure 7.23 presents overlaid XRPD patterns of the $LiEu_{(1-x)}Al_x(MoO_4)_2$ where x is within the range of 0 to 1. The overlaid pattern provides evidence of how the original tetragonal phase of $LiEu(MoO_4)_2$ transforms to a different phase in correlation with the decreasing Eu^{3+} cation concentration. The diffraction peaks of the tetragonal compound at $2\theta \approx 29°$ corresponding to (112) reflection as well as other peaks witnessed at $2\theta \approx 18.8°$ (101), 31.7°(004), 34.4° (200) and 47.5°(204) slowly disappeared up to x=0.95 and all peaks were absent at x=1. The changes of the XRPD diffraction peaks across the series of $LiEu_{(1-x)}Al_xM_2O_8$ signify that the compound experiences a phase transformation as a function of the declining Eu^{3+} concentration as the Al^{3+} cation concentration increases. There is no sign of phase-changes before x=0.45 until then the compound seems to maintain the tetragonal structure. The new phase as seen in Figure 7.23 starts growing in the material from x=0.45 with the peaks clearly present when the concentration of Al^{3+} reaches 0.75 mol.

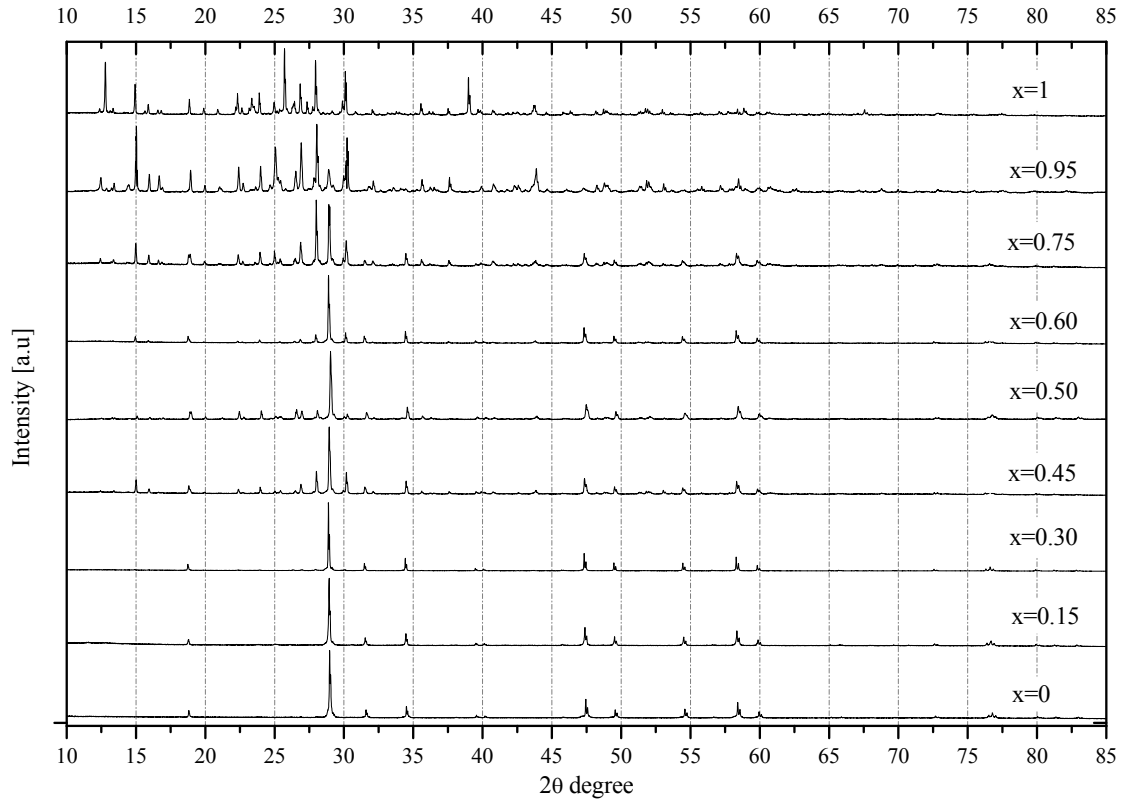

Figure 7.23: XRPD patterns of $LiEu_{(1-x)}Al_x(MoO_4)_2$

The XRPD results were then matched using EVA software and only around half of the diffraction peaks were found to fit the $LiAl(MoO_4)_2$ pattern which belongs to the triclinic structure with the space group $P\bar{1}$. The result was then fitted using Retvield refinement analysis despite a few major peaks belonging to an unidentified material(s). However, the closest fit was to the $LiAl(MoO_4)_2$ pattern (triclinic with the space group $P\bar{1}$) reported by Soloveva in the ICSD database [3] as shown in Figure 7.24. All samples were then refined using TOPAS and the process of refinement was made by taking into consideration 2 possible scenarios:

i) Scenario 1: There is a new phase that starts to grow from x=0.45 to x values greater than this, as there is no visual evidence of the new phase below x=0.45.

ii) Scenario 2: The new phase starts to grow as early as x=0.15 (although there is visually no evidence seen in Figure 7.23 but perhaps there is a very small amount of this new phase).

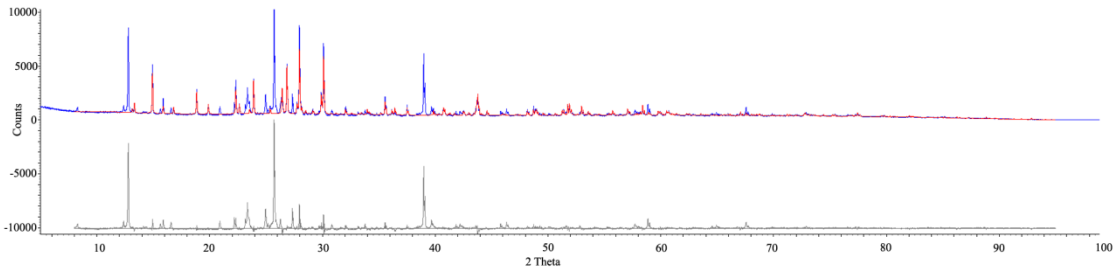

Figure 7.24: Refinement fit for $LiEuAl(MoO_4)_2$

Table 7.4 and Table 7.5 list all refined parameters of $LiEu_{(1-x)}Al_x(MoO_4)_2$ based on scenario 1 and scenario 2 respectively along with the calculated amount of each phase present. Crystal structure models used for reference in refining the data were the tetragonal $I4_1/a$:2 compound of $LiEu(MoO_4)_2$ (the same model used in refining $LiEu(MoO_4)_2$ in Chapter 5 and Chapter 6) and triclinic model $LiAl(MoO_4)_2$ from Soloveva [3].

Means of errors (R_{wp}s) at x=0.15 and x=0.30 on both tables were compared and it can be observed that R_{wp}s on the two samples in Table 7.5 are slightly less than that of Table 7.4. Although the R_{wp}s are slightly improved in Table 7.5 than the single-phase refinements in Table 7.4 because more variables were included in the refinement of the 2-phase analysis such an improvement was meaningless and consequently discarded. Therefore Table 7.4 is chosen instead of Table 7.5 and this decision is also in line with what has been observed in Figure 7.23 as there were no changes observed as Al^{3+} concentration increased from 0 to 30%. Lattice parameters of the tetragonal and triclinic

phases are plotted in Figure 7.25 (a) and (b) respectively. There is no sign of an effect on the size of the tetragonal lattice parameters as Al^{3+} concentration increases due to the lattice size not changing. This indicates that the Al^{3+} anions do not distort the lattice site previously occupied by the Eu^{3+} anions. In the next section further evidence for the incorporation of Al^{3+} cations is presented.

Table 7.4: Lattice parameters of tetragonal $I4_1/a$:2 $LiEu_{(1-x)}Al_x(MoO_4)_2$ (Scenario 1)

Al^{3+} (mol)		0	0.15	0.3	0.45	0.5	0.6	0.75	0.95	1
Tetragonal $I4_1/a$:2	a (Å)	5.20138(9)	5.20693(7)	5.20788(4)	5.20794(8)	5.20622(7)	5.20853(6)	5.20963(11)	5.2207(7)	
	c (Å)	11.3308(3)	11.3576(2)	11.36359(12)	11.3774(3)	11.3568(2)	11.37284(17)	11.3809(4)	11.393(3)	N/A
	Vol (Å^3)	306.55(1)	307.928(10)	308.204(6)	308.584(12)	307.824(10)	308.532(8)	308.881(17)	310.51(11)	
	%	100	100	100	40.1(10)	45.1(11)	57.1(11)	19.2(5)	6.0(2)	N/A
Triclinic $P\bar{1}$	a (Å)	N/A	N/A	N/A	7.0403(5)	7.0363(2)	7.0400(6)	7.0397(4)	7.0393(3)	7.0432(4)
	b (Å)				7.1665(4)	7.1710(2)	7.1678(4)	7.1693(3)	7.1689(3)	7.1616(3)
	c (Å				6.63628(18)	6.6360(2)	6.6368(2)	6.63672(18)	6.63589(17)	6.6372(2)
	Vol (Å^3)				299.38(3)	299.412(19)	299.48(3)	299.52(2)	299.47(2)	299.39(2)
	alpha (°)	N/A	N/A	N/A	110.920(4)	110.936(3)	110.916(4)	110.916(3)	110.916(2)	110.887(3)
	beta (°)	N/A	N/A	N/A	105.310(4)	105.269(3)	105.296(5)	105.299(3)	105.283(3)	105.324(3)
	gamma (°)	N/A	N/A	N/A	90.926(6)	90.940(3)	90.922(8)	90.929(5)	90.943(4)	90.926(5)
	%	N/A	N/A	N/A	59.9(10)	54.9(11)	42.9(11)	80.8(5)	94.0(2)	100
R_{exp}		8.99	6.2	5.45	5.31	3.16	5.48	5.39	2.41	4.23
R_{wp}		9.81	13.1	16.58	16.74	6.28	13.11	14.87	17.44	27.05
R_p		7.8	8.52	10.15	10.26	4.51	8.38	9.91	11.11	16.89

Table 7.5: Lattice parameters of tetragonal $I4_1/a$:2 $LiEu_{(1-x)}Al_x(MoO_4)_2$ (Scenario 2)

Al^{3+} (mol)		0	0.15	0.3	0.45	0.5	0.6	0.75	0.95	1
Tetragonal $I4_1/a$:2	a (Å)	5.20138(9)	5.20694(7)	5.20791(4)	5.20794(8)	5.20622(7)	5.20853(6)	5.20963(11)	5.2207(7)	
	c (Å)	11.3308(3)	11.3575(2)	11.36370(11)	11.3774(3)	11.3568(2)	11.37284(17)	11.3809(4)	11.393(3)	N/A
	Vol (Å^3)	306.55(1)	307.928(10)	308.210(6)	308.584(12)	307.824(10)	308.532(8)	308.881(17)	310.51(11)	
	%	100	60(6)	81(2)	40.1(10)	45.1(11)	57.1(11)	19.2(5)	6.0(2)	
Triclinic $P\bar{1}$	a (Å)	N/A	7.178(10)	7.058(2)	7.0403(5)	7.0363(2)	7.0400(6)	7.0397(4)	7.0393(3)	7.0432(4)
	b (Å)		7.087(9)	7.1275(18)	7.1665(4)	7.1710(2)	7.1678(4)	7.1693(3)	7.1689(3)	7.1616(3)
	c (Å		6.570(9)	6.6409(12)	6.63628(18)	6.6360(2)	6.6368(2)	6.63672(18)	6.63589(17)	6.6372(2)
	alpha (°)		111.77(15)	110.74(2)	110.920(4)	110.936(3)	110.916(4)	110.916(3)	110.916(2)	110.887(3)
	beta (°)		104.6(2)	105.34(3)	105.310(4)	105.269(3)	105.296(5)	105.299(3)	105.283(3)	105.324(3)
	gamma (°)		90.9(2)	90.74(3)	90.926(6)	90.940(3)	90.922(8)	90.929(5)	90.943(4)	90.926(5)
	Vol (Å^3)		298.2(9)	299.21(14)	299.38(3)	299.412(19)	299.48(3)	299.52(2)	299.47(2)	299.39(2)
	%		40(6)	19(2)	59.9(10)	54.9(11)	42.9(11)	80.8(5)	94.0(2)	100
R_{exp}		8.99	6.19	5.45	5.31	3.16	5.48	5.39	2.41	4.23
R_{wp}		9.81	12.85	15.68	16.74	6.28	13.11	14.87	17.44	27.05
R_p		7.8	8.23	9.14	10.26	4.51	8.38	9.91	11.11	16.89

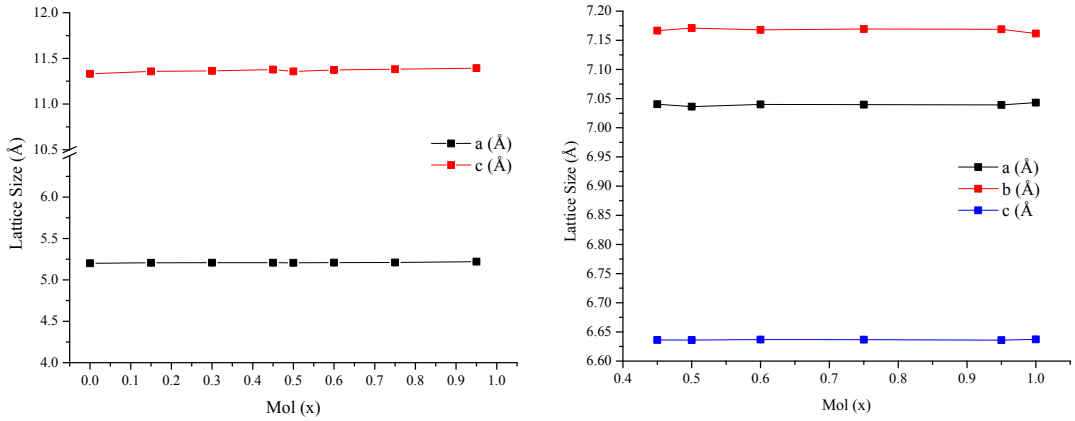

Figure 7.25: Lattice parameters tetragonal of $LiEu_{(1-x)}Al_x(WO_4)_2$ (a) based on tetragonal model of $LiEu(MoO_4)_2$ and (b) based on triclinic structure of $LiAl(MoO_4)_2$

7.2.2 Photoluminescence Properties

Eu^{3+} emission bands at 613 nm and 616 nm can be observed in all the samples (x=0 to x = 0.95) as shown in Figure 7.27 to Figure 7.31 after excitation at 395 nm and 465 nm respectively. The emission bands at 588–600 nm are due to the $^5D_0 \rightarrow {}^7F_1$ transition and the intense emission bands at 613 nm and 616 nm arise from the $^5D_0 \rightarrow {}^7F_2$ transitions and again a small emission band is seen at 690–710 nm which is due to the $^5D_0 \rightarrow {}^7F_4$ transition. Interestingly, the trend of falling intensity starts early at x=0.15 (for 395 nm excitation energy) or x=0.30 (at 465 nm excitation energy) unlike the other samples measured in Chapter 5 and Chapter 6. All luminescence spectra were also normalised to the 616 nm as shown in Figure 7.32 to Figure 7.36. It can be understood from the figures that there was again some small evidence of concentration quenching that takes place at low values of x. This explanation is due to the observation on the narrowing bands seen in the function of increasing Al^{3+} in Figure 7.32 to Figure 7.36.

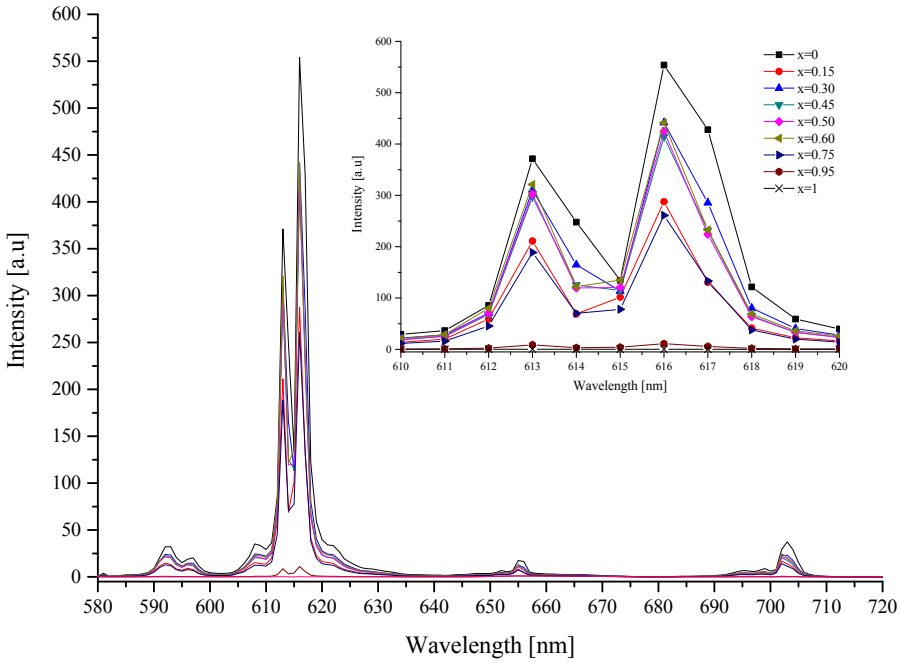

Figure 7.26: Emission spectra of $LiEu_{(1-x)}Al_x(MoO_4)_2$ excited at 395 nm

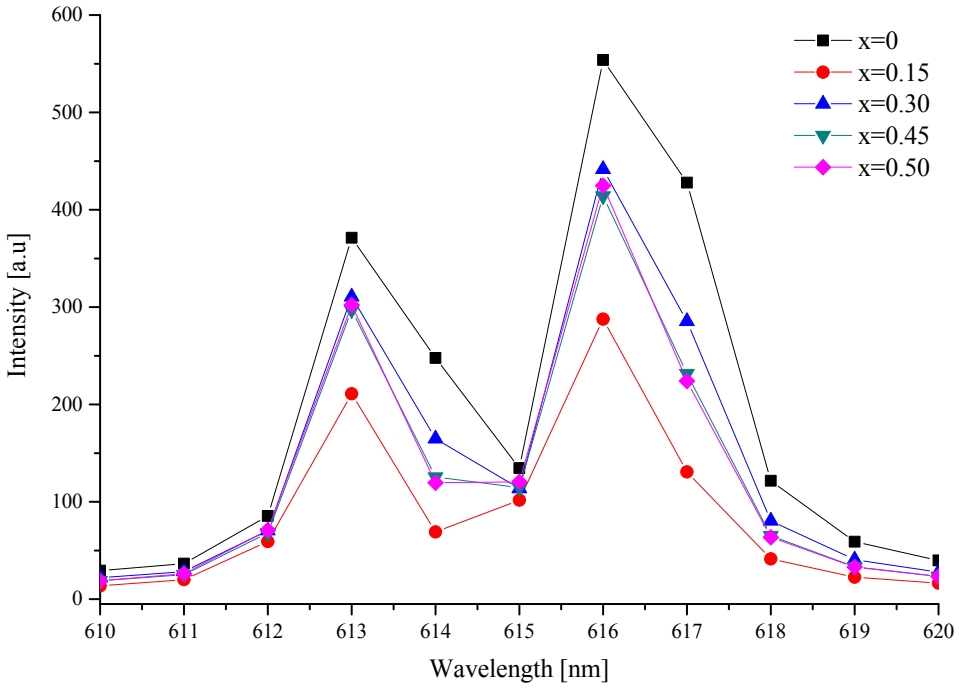

Figure 7.27: Emission spectra ranged from 610 nm to 620 nm of $LiEu_{(1-x)}Al_x(MoO_4)_2$ excited at 395 nm (x=0 to 0.50)

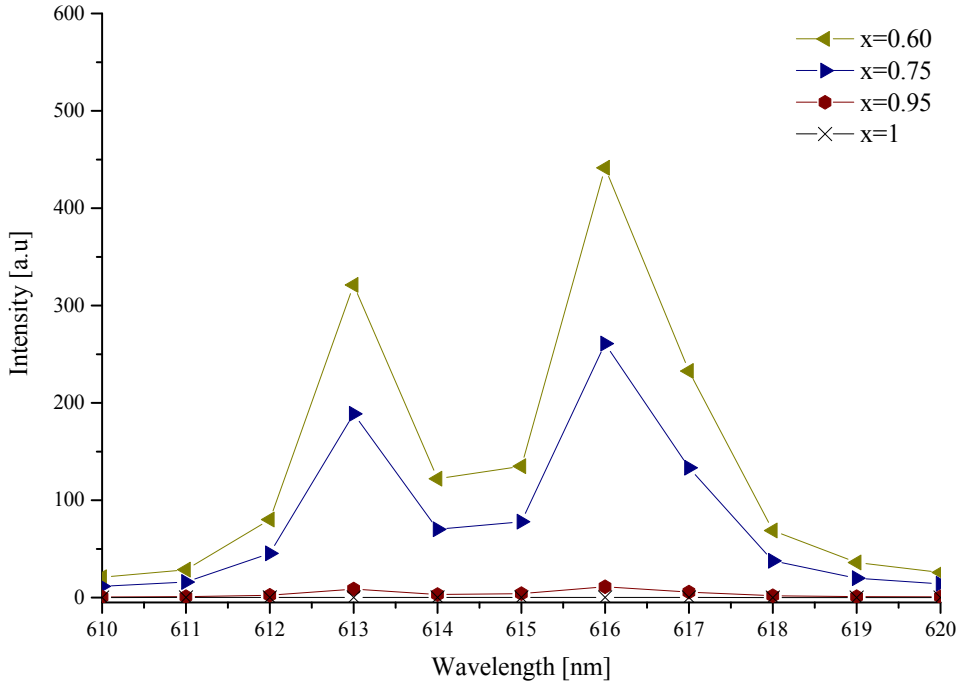

Figure 7.28: Emission spectra ranged from 610 nm to 620 nm of $LiEu_{(1-x)}Al_x(MoO_4)_2$ excited at 395 nm (x=0.60 to 1)

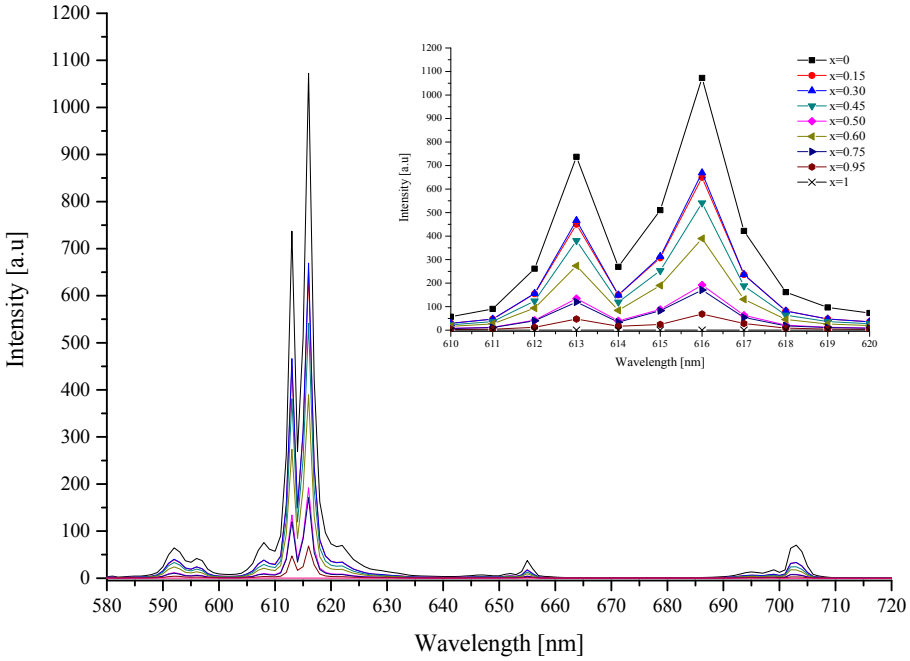

Figure 7.29: Emission spectra of $LiEu_{(1-x)}Al_x(MoO_4)_2$ excited at 465 nm

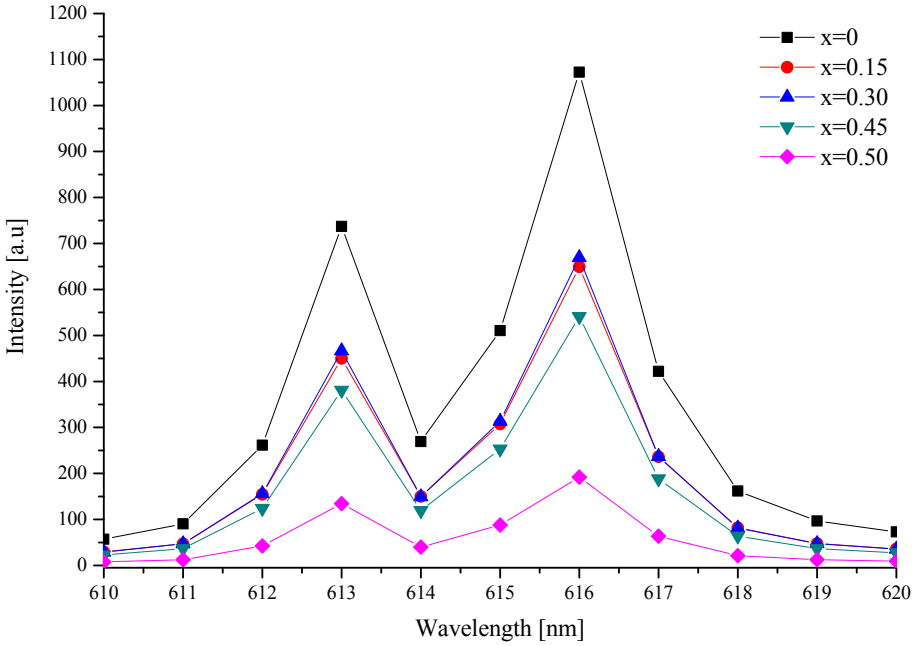

Figure 7.30: Emission spectra ranged from 610 nm to 620 nm of $LiEu_{(1-x)}Al_x(MoO_4)_2$ excited at 465 nm (x=0 to 0.50)

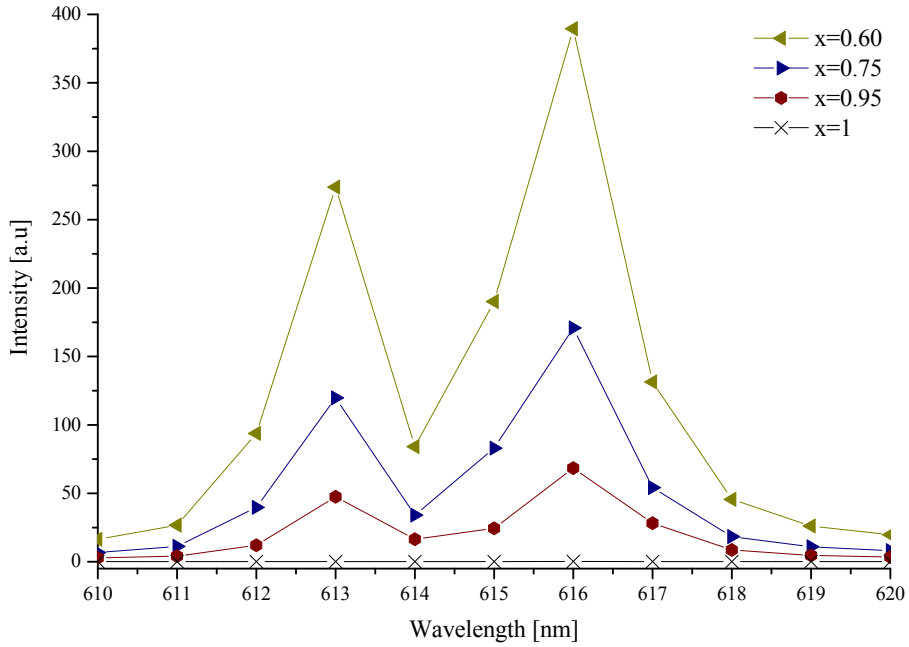

Figure 7.31: Emission spectra ranged from 610 nm to 620 nm of $LiEu_{(1-x)}Al_x(MoO_4)_2$ excited at 465 nm (x=0.60 to 1)

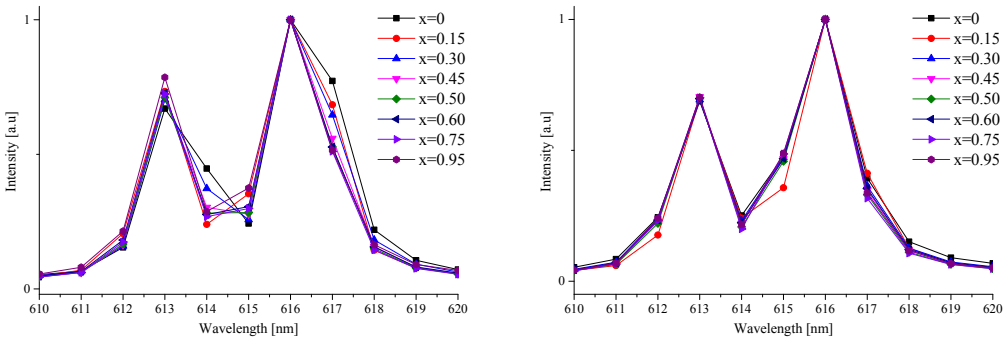

(a) (b)

Figure 7.32: Normalized emission spectra of $LiEu_{(1-x)}Al_x(MoO_4)_2$ excited at (a) 395 nm and (b) 465 nm

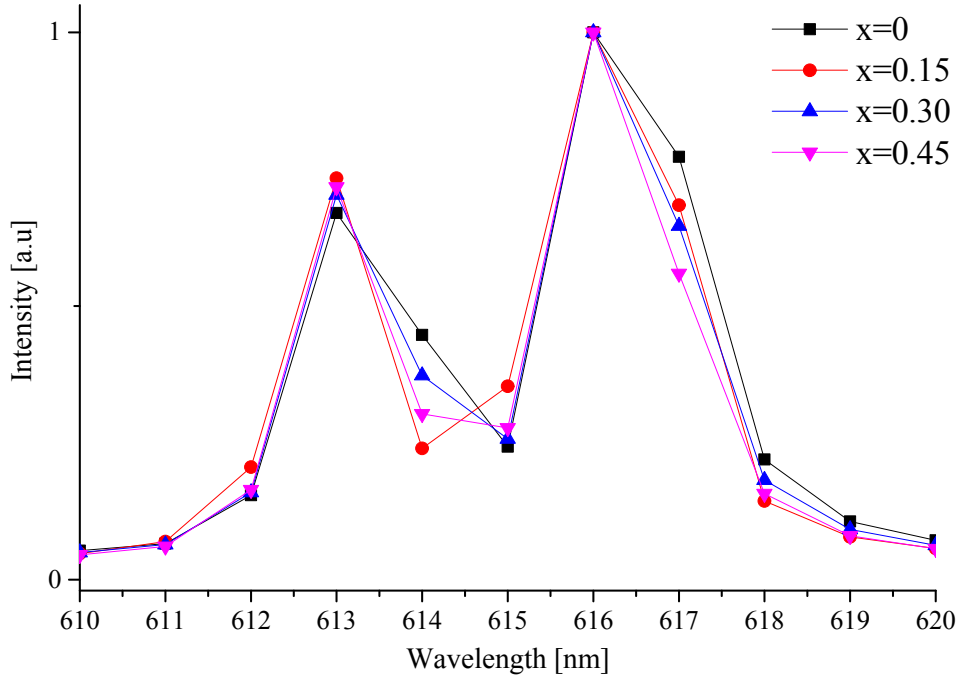

Figure 7.33: Normalized emission spectra of $LiEu_{(1-x)}Al_x(MoO_4)_2$ excited at 395 nm (x = 0 to 0.45)

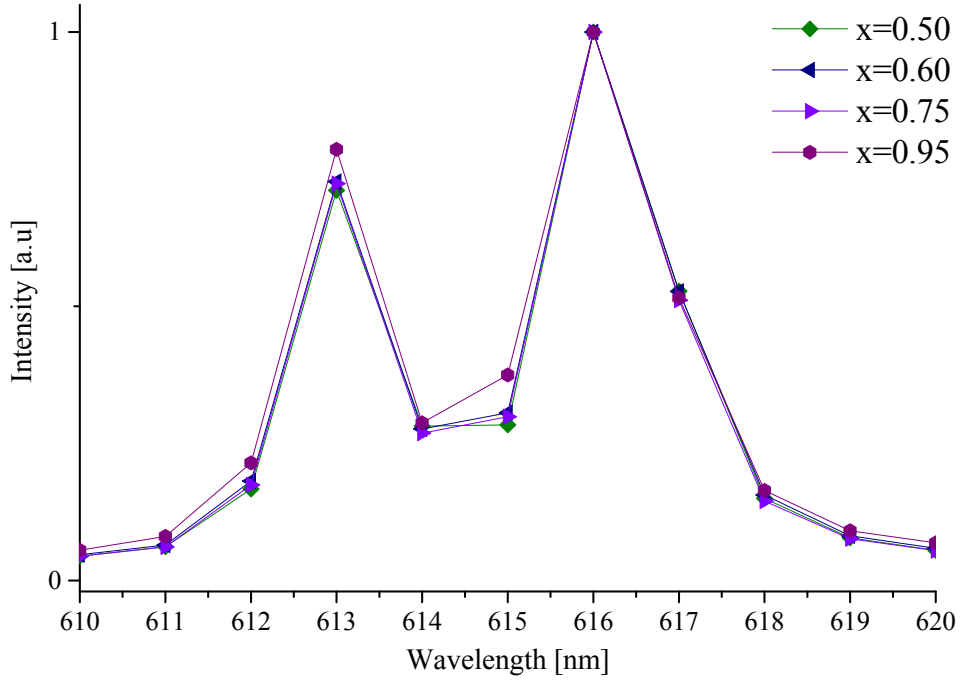

Figure 7.34: Normalized emission spectra of $LiEu_{(1-x)}Al_x(MoO_4)_2$ excited at 395 nm (x = 0.50 to 0.95)

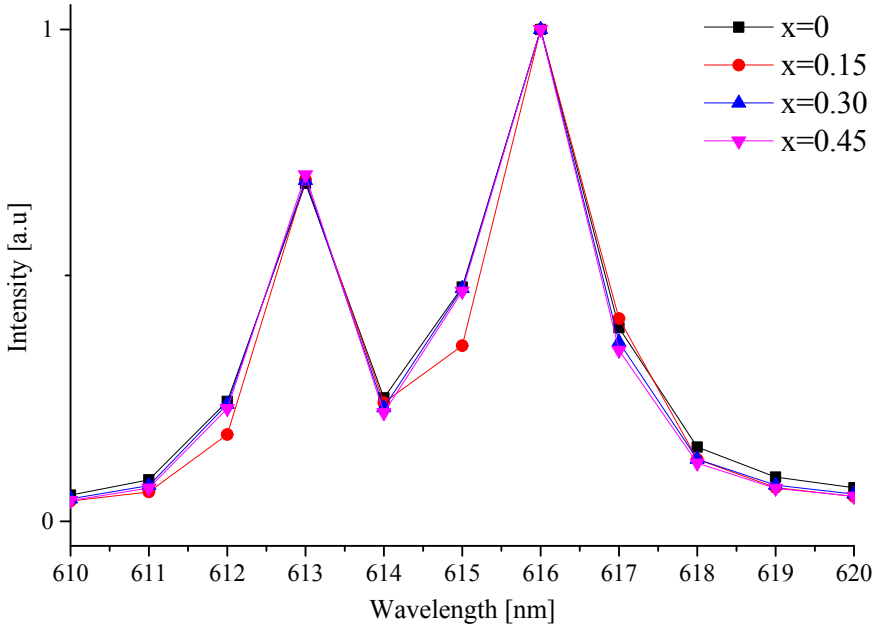

Figure 7.35: Normalized emission spectra of $LiEu_{(1-x)}Al_x(MoO_4)_2$ excited at 465 nm (x = 0 to 0.45)

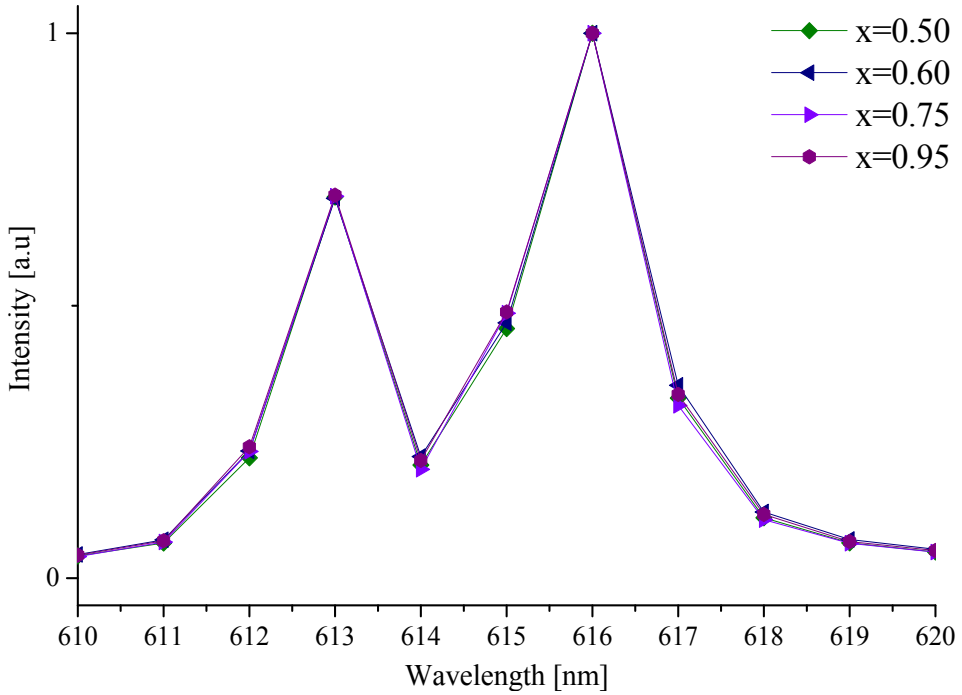

Figure 7.36: Normalized emission spectra of $LiEu_{(1-x)}Al_x(MoO_4)_2$ excited at 465 nm (x = 0.50 to 0.95)

Table 7.6 shows the luminous efficacies measured on the samples $LiEu_{(1-x)}Al_x(MoO_4)_2$ while all values in Table 7.6 are plotted in Figure 7.37 (a) and (b). As the luminous efficacy was investigated, there was an obvious similarity with the emission spectra as observed in Figure 7.26 to Figure 7.31 where the value dropped nearly half at x=0.15 down to 74.7 lm/W under 395nm excitation, whereas the sample which was excited at 465 nm was found to have reduced to 136.67 lm/W. The most important finding to appear from the data collected is how the luminous efficacy rose to the highest value at x=0.60 which was measured to have 210.77 lm/W when excited at 465 nm. The graph measured for x=0.60 also shows a huge rise when excited at 395 nm. The result of a rise in the luminous efficacy at x=0.60 proves that:

i) The distances amongst the emission centres were shorter than the optimum distance due to high concentration for x values below 0.60. Therefore the energy was transferred from one cation to another neighbouring identical cation through cross relaxation and energy migration processes instead of all the light being emitted from the lattice.

ii) Removing 60% of the amount of Eu^{3+} had given the optimum distance amongst the emission centres to reduce the energy quenching mechanisms, therefore the luminescence intensity increased to the maximum.

iii) A linear decline after x=0.60 is due to the continuing drop in the concentration of the Eu^{3+} activators.

The emission only appears to come from the tetragonal phase of $LiEu(MoO_4)_2$, this is evident from the decline of the luminous efficacy from x=0.60 to x=1. If there was an emission from the second phase (triclinic $P\bar{1}$), the electronic environment of the emission centre must be almost identical to that of the tetragonal $LiEu(MoO_4)_2$ (due to the similar shape seen in their spectral properties as in Figure 7.32). There is no evidence for emission from the triclinic phase however, such emission would have been expected to add intensity, contradicting point (iii) above.

Table 7.6: Luminous efficacies of $LiEu_{(1-x)}Al_x(MoO_4)_2$ excited at (a) 395nm and (b) 465 nm

x (Mol)	Luminous Efficacy (lm/W)	
	exc 395 nm	exc 465 nm
0	163.33	199.28
0.15	74.7	150.7
0.3	100.53	136.67
0.45	107.2	175.23
0.50	111.30	
0.6	133.37	210.77
0.75	71.61	93.33
0.95	4.13	1.15
1	0	0

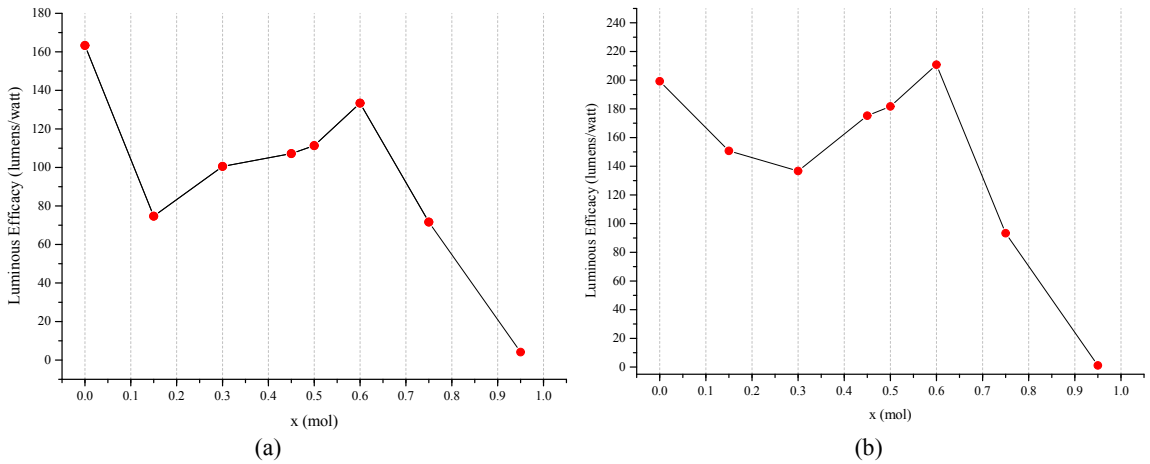

(a) (b)

Figure 7.37: Luminous efficacy of $LiEu_{(1-x)}Al_x(MoO_4)_2$ excited at (a) 395 nm and (b) 465 nm

Table 7.7 lists all colour coordinates and colour temperatures of the samples $LiEu_{(1-x)}Al_x(MoO_4)_2$ and the data was again plotted in Figure 7.38 and Figure 7.39. The table and figures show that there was only a small change of colour coordinates and colour temperature. In this phosphor system there were no obvious trends in the CIE coordinates.

Table 7.7: CIE Colour coordinates of $LiEu_{(1-x)}Al_x(MoO_4)_2$

No.	Al^{3+} Concentration (mol)	Exc 395 nm			Exc 465 nm		
		Coordinates		Colour temp	Coordinates		Colour temp
		x	y		x	y	
1	0	0.6718	0.3280	870 K	0.6715	0.3283	872 K
2	0.15	0.6718	0.3279	870 K	0.6715	0.3283	872 K
3	0.30	0.6719	0.3279	870 K	0.6715	0.3283	872 K
4	0.45	0.6717	0.3282	871 K	0.6712	0.3286	874 K
5	0.50	0.6717	0.3281	870K	0.6712	0.3283	872 K
6	0.60	0.6717	0.3281	870 K	0.6715	0.3282	872 K
7	0.75	0.6717	0.3281	869 K	0.6714	0.3283	874 K
8	0.95	0.6720	0.3278	875 K	0.6719	0.3278	872 K
9	1				N/A		

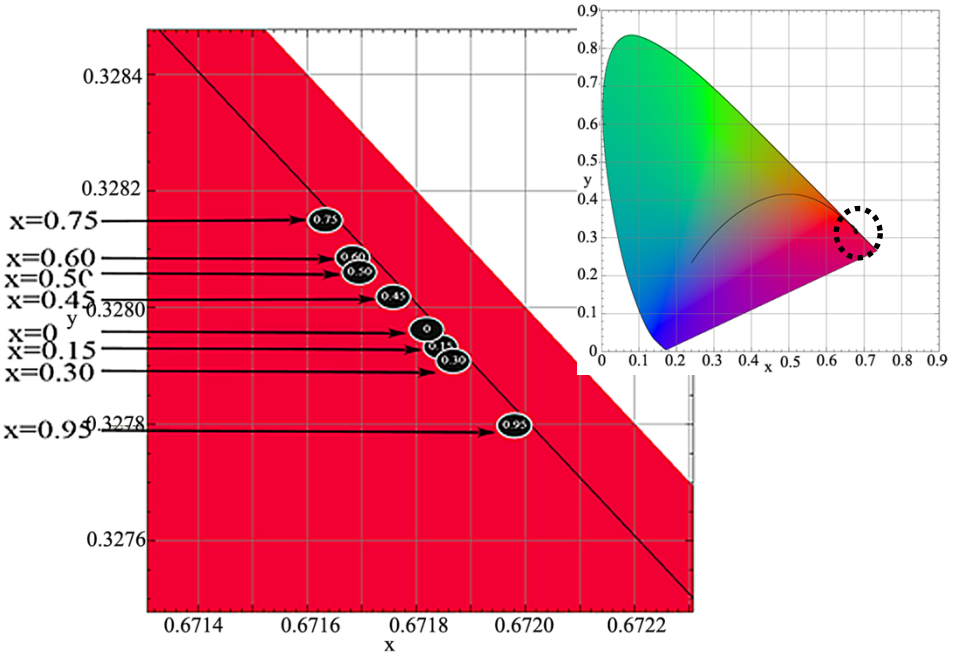

Figure 7.38: CIE diagram for $LiEu_{(1-x)}Al_x(MoO_4)_2$ excited at 395nm

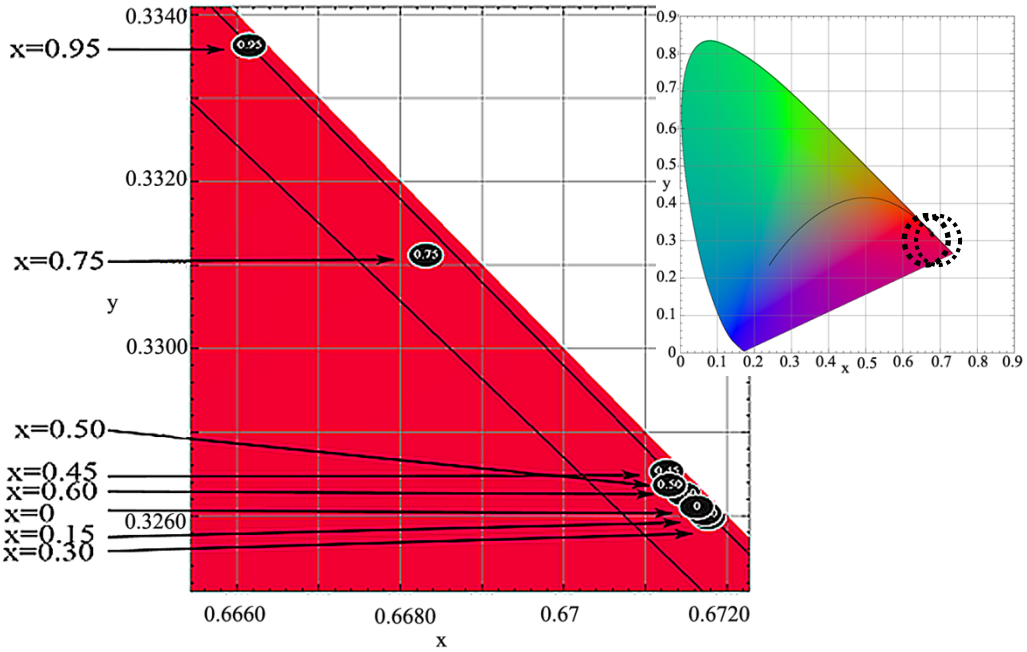

Figure 7.39: CIE diagram for $LiEu_{(1-x)}Al_x(MoO_4)_2$ excited at 465nm

7.3 Incorporating of Al^{3+} into Molybdate-Tungstate host lattices

As the $LiEu_{(1-x)}Al_x(WO_4)_2$ phosphor series changed from tetragonal to an unknown phase whilst the $LiEu_{(1-x)}Al_x(MoO_4)_2$ phosphors changed to a phase believed to be a triclinic $P\bar{1}$ with increasing x values, it was thought worthwhile to explore what occurs in the intermediate phosphor system $LiEu_{(1-x)}Al_x(WO_4)(MoO_4)$. Another reason to test these series of materials was to find a conclusive correlation between the lattice size of the crystal structure and the luminous efficacy of the materials.

7.3.1 Powder Crystallography

Figure 7.40 presents the XRPD diffraction patterns in overlay of $LiEu_{(1-x)}Al_x(WO_4)(MoO_4)$ where x has values from 0 to 1. New peaks at $2\theta \approx$ 22.5˚, 23.5˚, 26.0˚, 27.0˚, 36.0˚ and 43.5˚ started to grow as soon as 15% of Al^{3+} was introduced, indicating that the system systematically generated a new phase in the presence of Al^{3+} cations while the peaks belonging to the tetragonal phase $I4_1/a$:2 $LiEu(WO_4)(MoO_4)$remained in the system until x=0.95. No suitable matches were found in the EVA software for the new phase. However, further analysis on the crystal structure of the new phase, based on the refinement model of $LiAl(MoO_4)_2$ used in 7.2.1, indicated that its diffraction pattern was neither identical to that of $LiEu(MoO_4)_2$ nor $LiEu(WO_4)_2$ as seen in Figure 7.41. As discussed earlier for precaution purposes the sample of x=1 was re-synthesized again for a second time (see Figure 7.42) to test for reproducibility. The result from the second synthesis again gives no obvious difference to that of the first sample. So both the old and the new samples of $LiAl(WO_4)(MoO_4)$ manifested the same XRPD data.

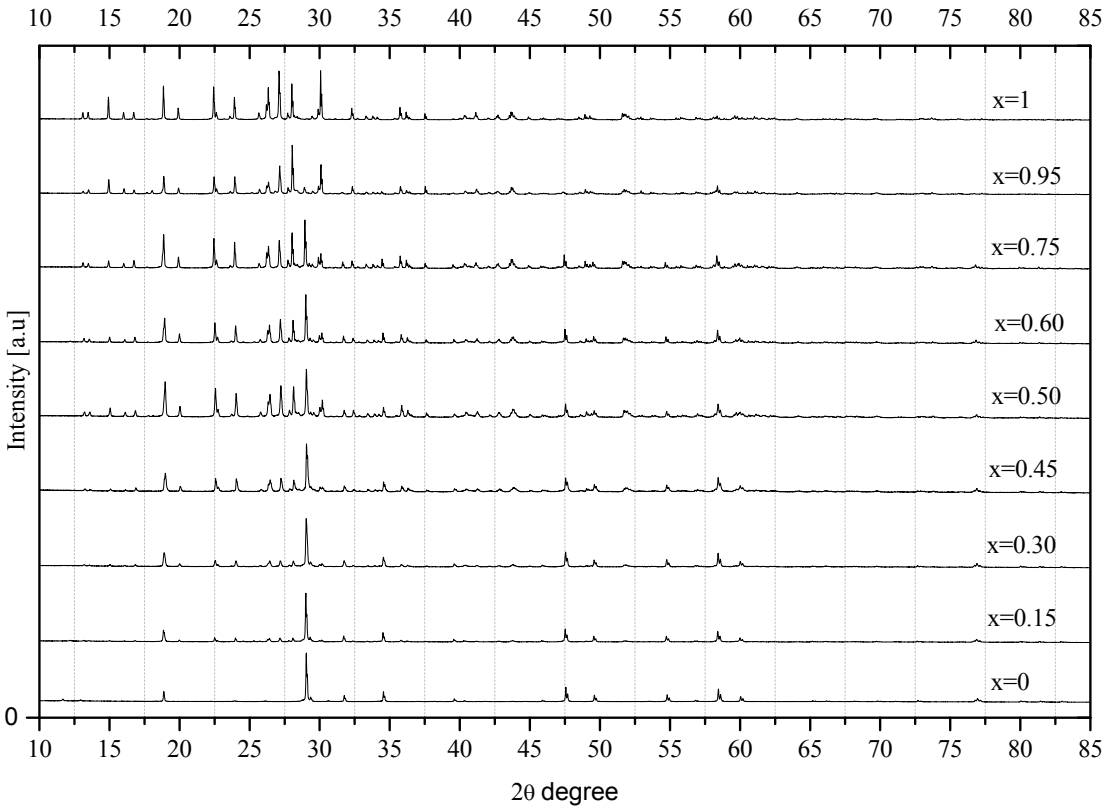

Figure 7.40: XRPD patterns of $LiEu_{(1-x)}Al_x(WO_4)$((MoO_4)

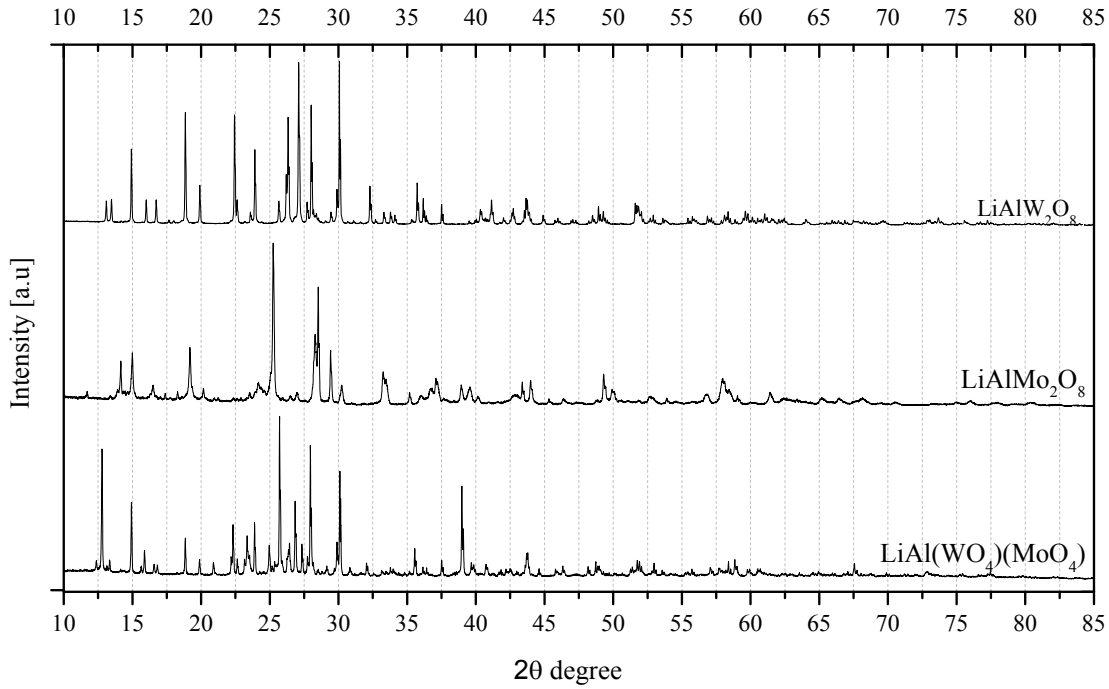

Figure 7.41: XRPD patterns of $LiAl(WO_4)_2$, and $LiAl(MoO_4)_2$, $LiAl(WO_4)(MoO_4)$

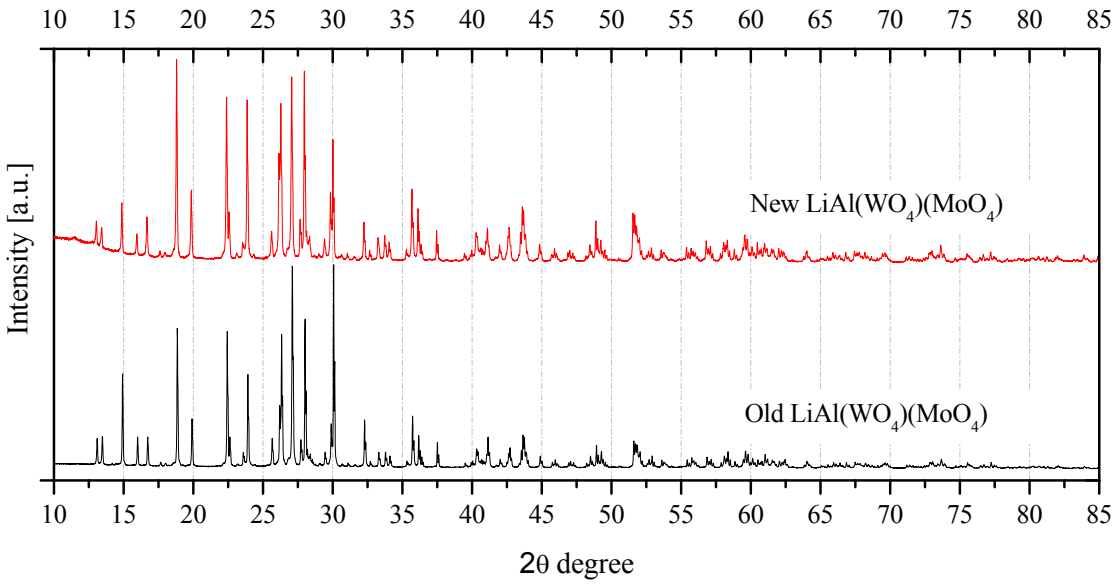

Figure 7.42: XRPD patterns of $LiAl(WO_4)(MoO_4)$(old vs new)

Figure 7.43 shows the refinement fit of $LiAl(MoO_4)(WO_4)$ which was performed using TOPAS software. The fitting model $LiAl(MoO_4)_2$ reported by Soloveva[3] was again employed due to being unable to perfectly fit the measured data. Soloveva's structure was chosen as it was considered to be a relevant structure close to the XRPD measured data. However, the *.cif file was adjusted by having additional W^{6+} on the Mo^{6+} sites so that the refinement process could go to the closest fit to the measured data. The mean of errors (R_{wp}s) from the refined data as listed in Table 7.8 is acceptable and the observed fitting of this crystal structure (as seen in Figure 7.43) was better in comparison to the fitting of $LiAl(MoO_4)_2$. Both lattices parameters were plotted, as shown in Figure 7.44, which explains that the relationship between the two phases is insignificant since no obvious trend (incline or decline) can be observed as the amount of Al^{3+} rises. The lattice size of triclinic $LiAl(WO_4)(MoO_4)$ had also changed significantly from what had been recorded for $LiAl(MoO_4)_2$ as both the a and b parameters were now closer to each other at 7.08 Å.

Table 7.8 shows the site occupancies of all refined ions (except O^{-2} ions that were not adjusted and were instead fixed to the default amount set in the *.cif file) in proving that the fitting on triclinic $P\bar{1}$ is chemically sensible. Clearly the triclinic structure gives a different scenario in the lattice compared to the tetragonal parent compound of $LiEu(MoO_4)(WO_4)$. Figure 7.45 shows the way six oxygen anions surround Al^{3+} revealing that the cations have (of its maximum) 6-coordination. Oxygen ions can have 6 maximum bonds with other atoms (unlike Eu^{3+} that can have the maximum of 8 coordination

numbers) therefore such replacement between Eu^{3+} and Al^{3+} will not give a similar crystal symmetry. Nevertheless the oxygen anions as seen in Figure 7.45 still isolate $(MoO_4)^{2-}$ or $(WO_4)^{2-}$ with tetrahedral shapes in the lattice.

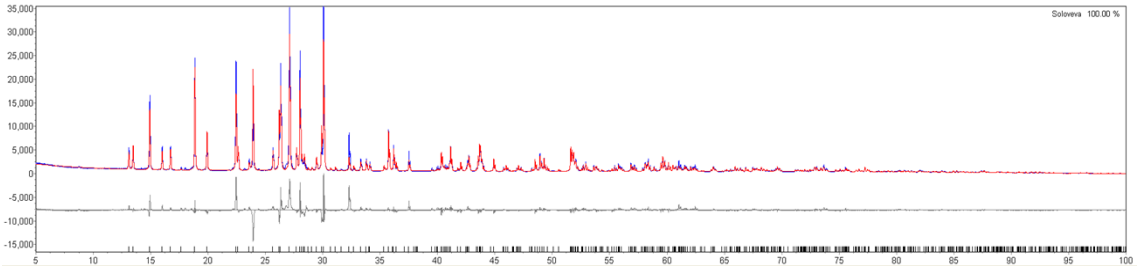

Figure 7.43: Refinement fit for $LiAl(MoO_4)(WO_4)$

Table 7.8: Lattice parameters of tetragonal $I4_1/a$:2 $LiEu_{(1-x)}Al_x(MoO_4)(WO_4)$

Al^{3+} (mol)		0	0.15	0.3	0.45	0.5	0.6	0.75	0.95	1
Tetragonal $I4_1/a$:2	a (Å)	5.20657(9)	5.20719(5)	5.20720(6)	5.21035(8)	5.20861(8)	5.20902(5)	5.20859(4)	5.2156(2)	N/A
	c (Å)	11.3088(3)	11.3127(1)	11.3121(2)	11.3222(3)	11.3165(3)	11.3215(2)	11.3179(2)	11.343(1)	
	Vol (Å³)	306.562(12)	306.741(7)	306.729(8)	307.37(1)	307.01(1)	307.195(8)	307.047(7)	308.57(4)	
	%	100	68(1)	60(1)	45(1)	19.1(9)	26.5(9)	21.5(8)	4(1)	
Triclinic P	a (Å)	N/A	7.0807(2)	7.0807(2)	7.0841(2)	7.0826(1)	7.0833(1)	7.08313(7)	7.0861(1)	7.08347(4)
	b (Å)		7.0863(2)	7.0861(2)	7.0853(2)	7.0814(1)	7.08096(9)	7.08263(7)	7.0775(1)	7.08270(4)
	c (Å		6.6436(2)	6.6437(2)	6.6458(2)	6.6437(1)	6.64433(9)	6.64431(6)	6.6449(1)	6.64474(4)
	alpha (°)		110.626(3)	110.618(3)	110.624(2)	110.616(1)	110.615(1)	110.6180(7)	110.603(1)	110.6176(4)
	beta (°)		105.679(3)	105.677(3)	105.689(2)	105.701(1)	105.704(1)	105.6981(7)	105.718(1)	105.7028(4)
	gamma (°)		90.636(3)	90.629(3)	90.629(3)	90.627(1)	90.624(1)	90.6300(8)	90.611(2)	90.6312(4)
	Vol (Å³)		298.27(2)	298.30(2)	298.47(2)	298.142(9)	298.181(7)	298.243(5)	298.19(1)	298.272(3)
	%		32(1)	40(1)	55(1)	80.9(9)	73.5(9)	78.5(8)	96(1)	100
R_{exp}		12.48	3.43	3.79	4.55	3.31	3.36	3.16	3.28	3.04
R_{wp}		13.61	8.8	9.25	10.46	10.88	10.11	9.3	15.55	16.2
R_p		10.83	5.8	6.1	7.29	7.61	7.06	6.73	11.32	11.93

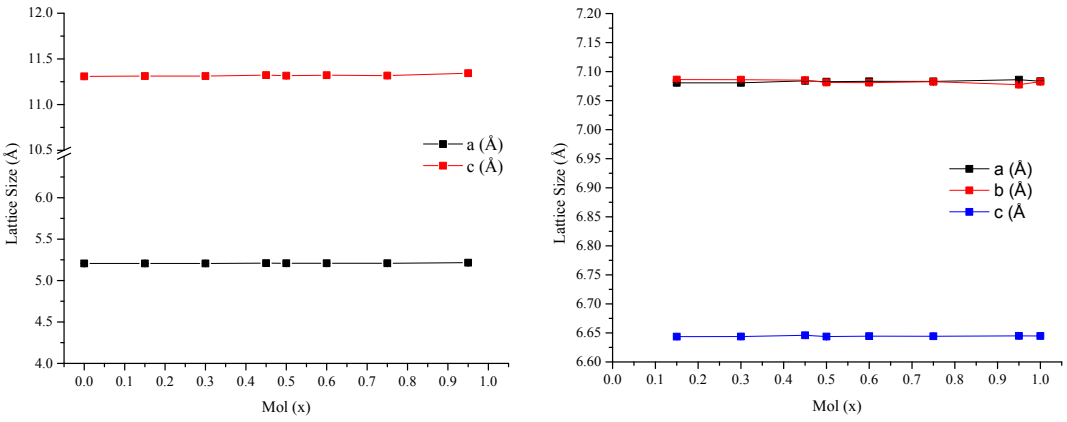

(a) (b)

Figure 7.44: Lattice parameters of $LiEu_{(1-x)}Al_x(WO_4)(MoO_4)$ based on (a) tetragonal model of $LiEu(WO_4)(MoO_4)$ and (b) triclinic structure $LiAl(WO_4)(MoO_4)$

Table 7.9: Site occupancies of $LiAl(WO_4)(MoO_4)$

Site	Np	x	y	z	Atom	Occ
Mo/W	2	0.03350	0.28490	0.67760	Mo^{+6} W^{+6}	0.81(1) 0.19(1)
Mo/W	2	0.42320	0.20700	0.16780	Mo^{+6} W^{+6}	0.855(1) 0.145(1)
Al	2	0.10020	0.82580	0.91320	Al^{+3}	1
Li	2	0.55600	0.20200	0.71300	Li^{+}	1

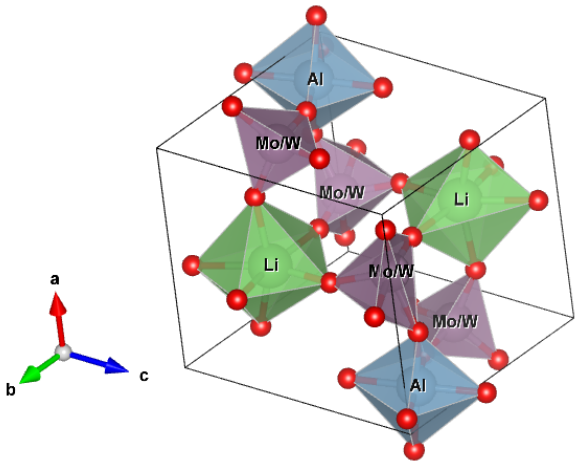

Figure 7.45: Triclinic refined model $LiAl(WO_4)(MoO_4)$

7.3.2 Photoluminescence Properties

Figure 7.46 to Figure 7.51 show the emission spectra of the samples when excited at 395nm and 465 nm respectively. All emission spectra (except x=1) fall in regions of 588–600 nm ($^5D_0 \rightarrow {}^7F_1$), 610–630 nm ($^5D_0 \rightarrow {}^7F_2$), 640–662 nm ($^5D_0 \rightarrow {}^7F_3$), and 681–710 nm ($^5D_0 \rightarrow {}^7F_4$) and are therefore similar to the parent $LiEu(WO_4)(MoO_4)$ compound. The similar spectral forms can be explained as supporting the premise that the emission spectra came from the same luminescent centre of the parent compound up to an x value of 0.95. This result is in line with the XRPD results in Figure 7.40 which has been discussed earlier, confirming the presence of the parent compound throughout this phosphor system. There is evidence for emission band-narrowing effects that can be seen in the normalized spectra as shown in Figure 7.52 to Figure 7.56 in the function of increasing Al^{3+} cation concentration. This can be explained because Al^{3+} concentration addition does limit the concentration quenching by increasing the Eu^{3+} to Eu^{3+} distances.

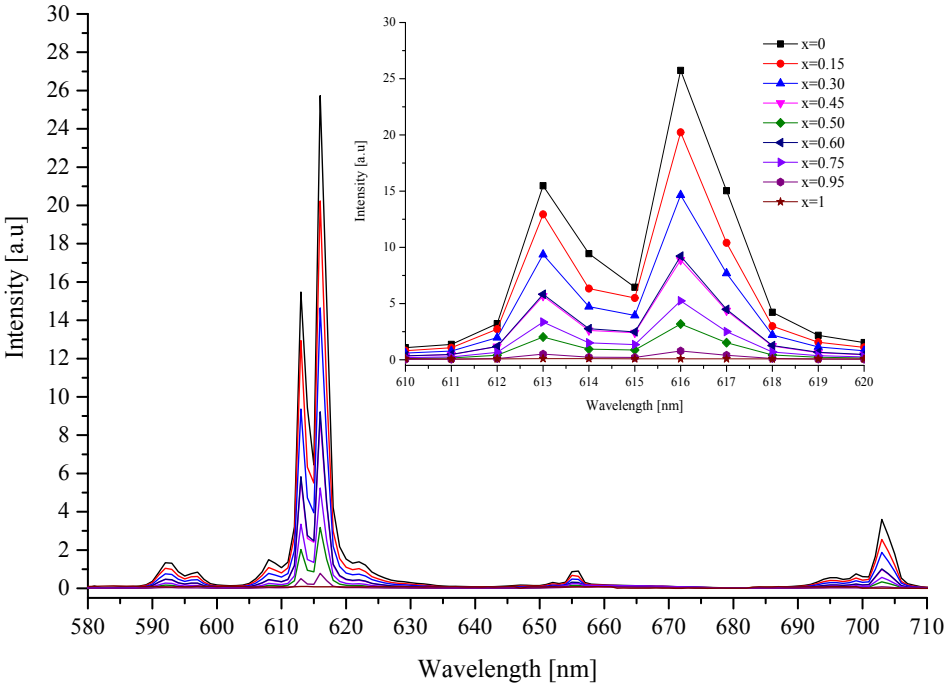

Figure 7.46: Emission spectra of $LiEu_{(1-x)}Al_x(WO_4)(MoO_4)$ excited at 395 nm

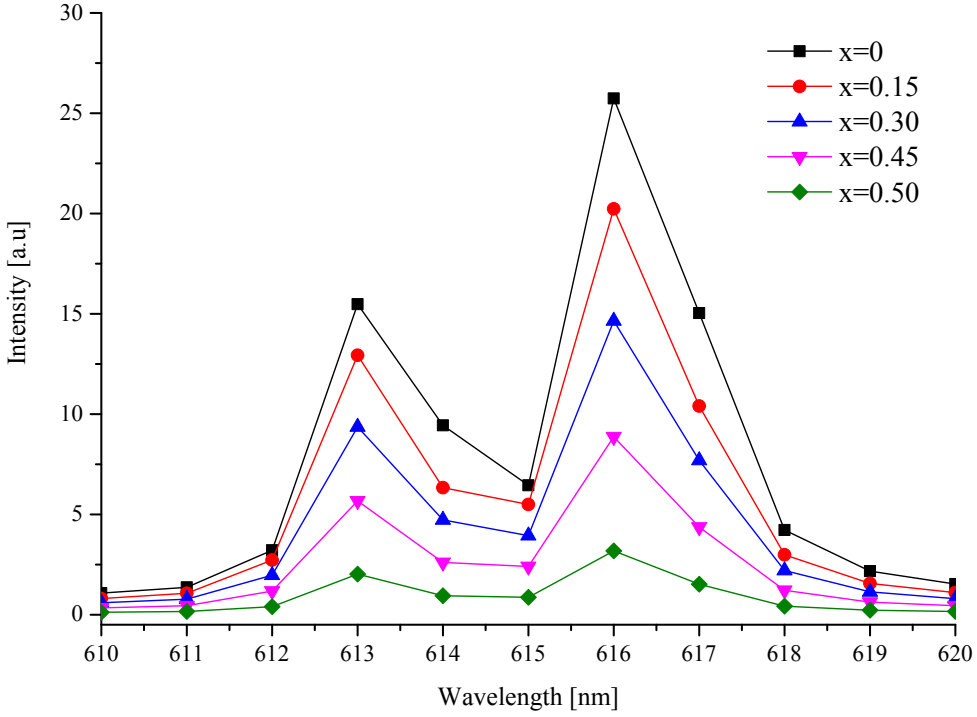

Figure 7.47: Emission spectra ranged from 610 nm to 620 nm of $LiEu_{(1-x)}Al_x(WO_4)(MoO_4)$ excited at 395 nm (x=0 to 0.50)

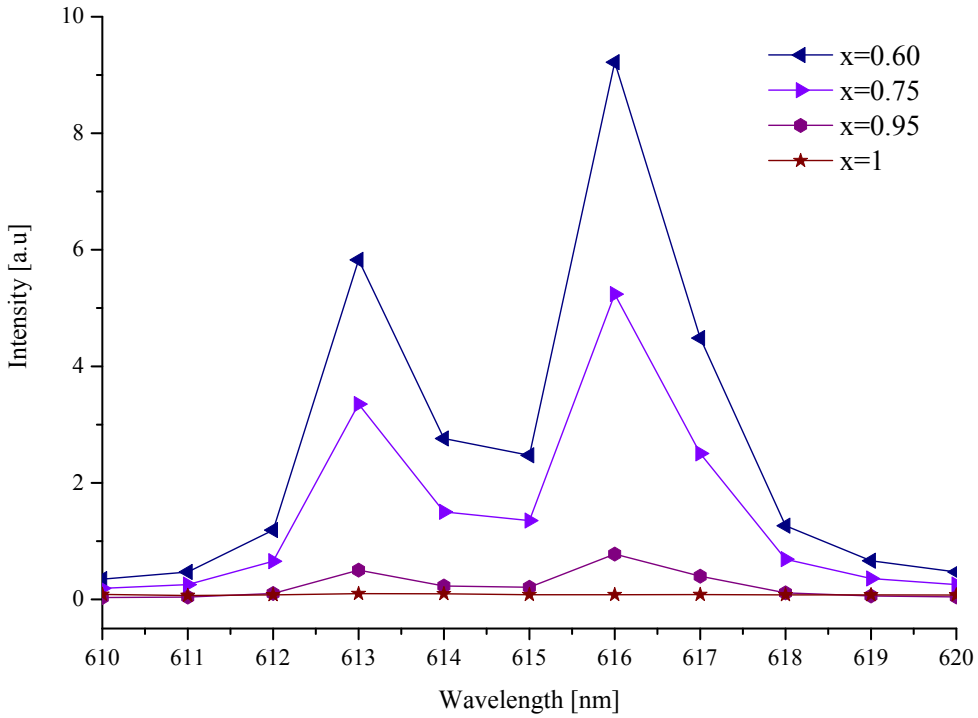

Figure 7.48: Emission spectra ranged from 610 nm to 620 nm of $LiEu_{(1-x)}Al_x(WO_4)(MoO_4)$ excited at 395 nm (x=0.60 to 1)

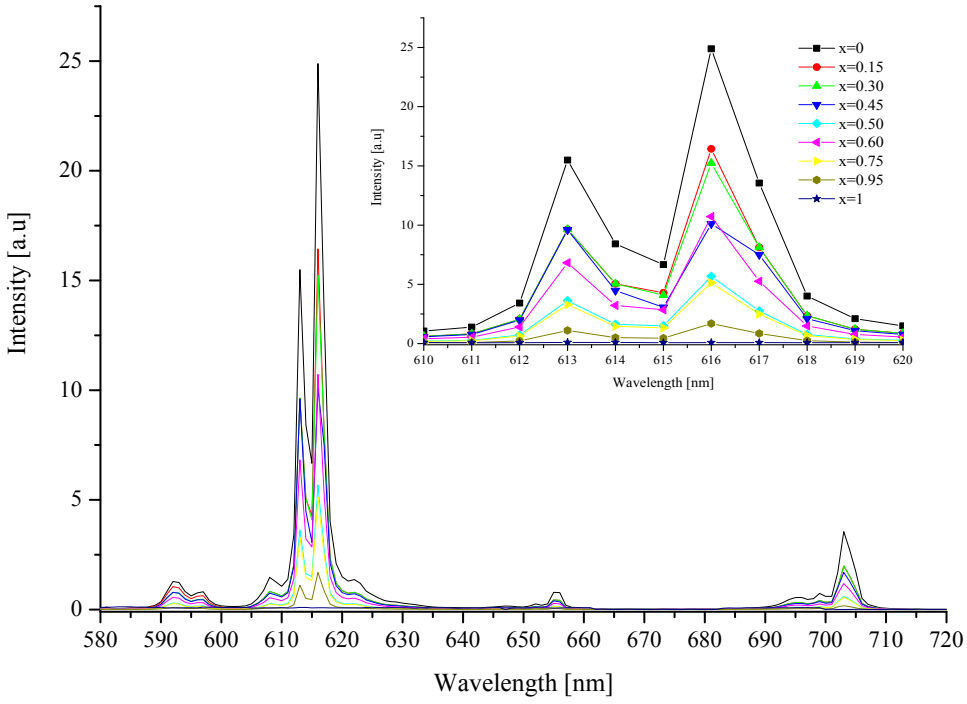

Figure 7.49: Emission spectra of $LiEu_{(1-x)}Al_x(WO_4)(MoO_4)$ excited at 465 nm

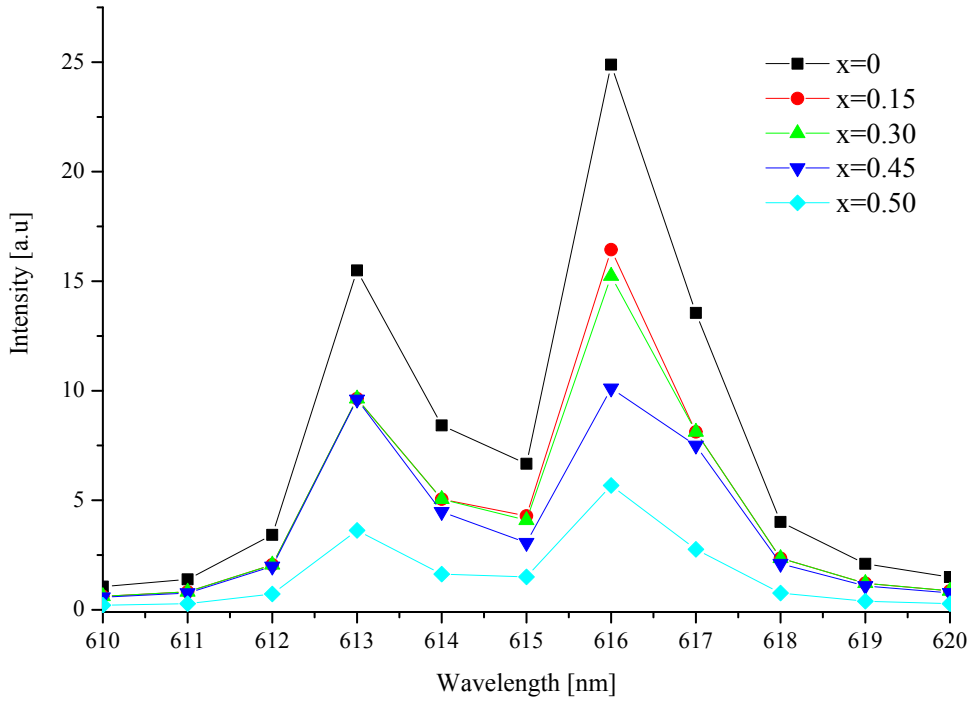

Figure 7.50: Emission spectra ranged from 610 nm to 620 nm of $LiEu_{(1-x)}Al_x(WO_4)(MoO_4)$ excited at 465 nm (x=0 to 0.50)

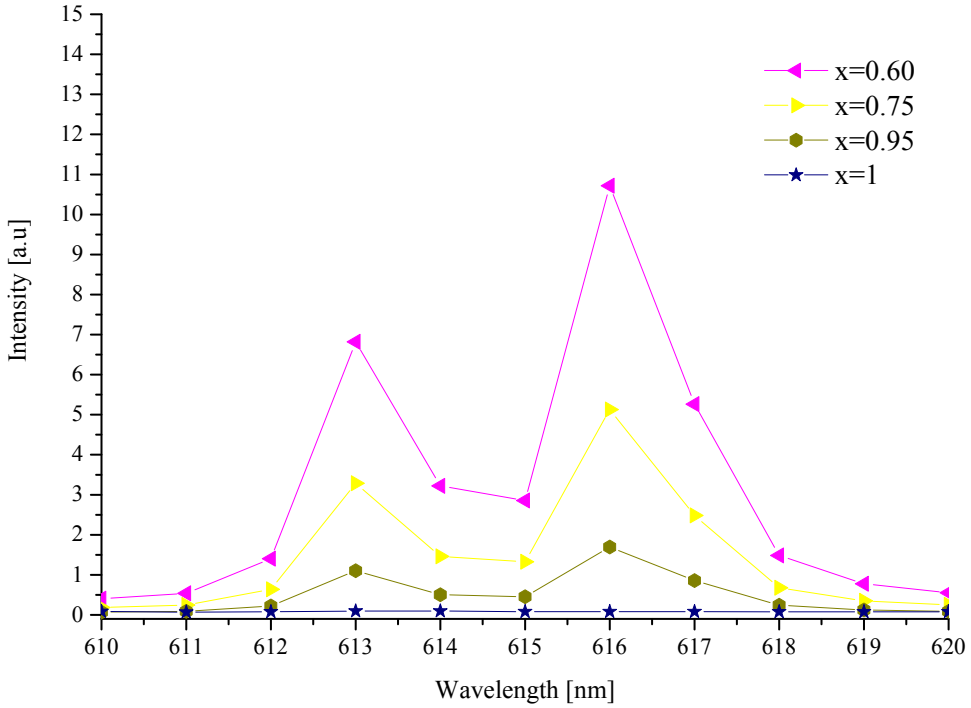

Figure 7.51: Emission spectra ranged from 610 nm to 620 nm of $LiEu_{(1-x)}Al_x(WO_4)(MoO_4)$ excited at 465 nm (x=0.60 to 1)

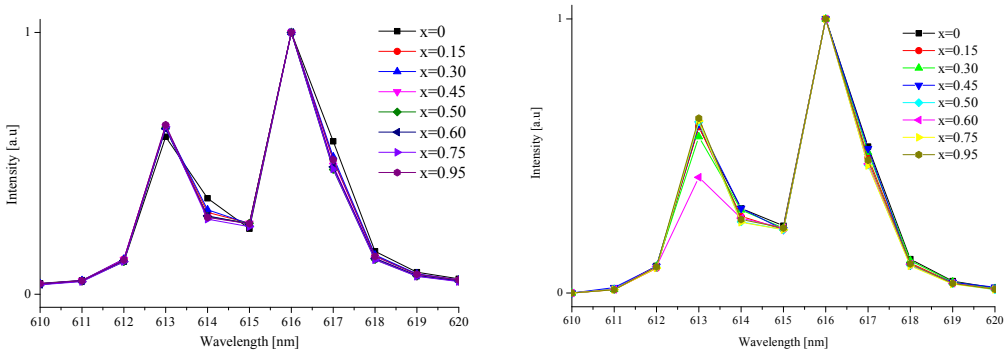

(a) (b)

Figure 7.52: Normalized emission spectra of $LiEu_{(1-x)}Al_x(WO_4)(MoO_4)$ excited at (a) 395 nm and (b) 465 nm

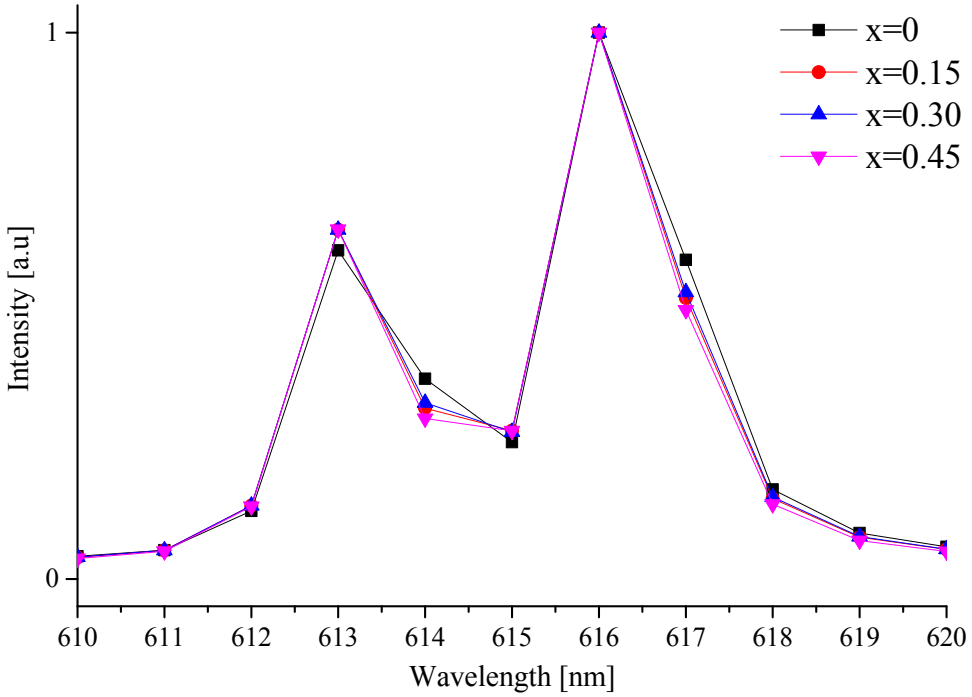

Figure 7.53: Normalized emission spectra of $LiEu_{(1-x)}Al_x(WO_4)(MoO_4)$ excited at 395 nm (x = 0 to 0.45)

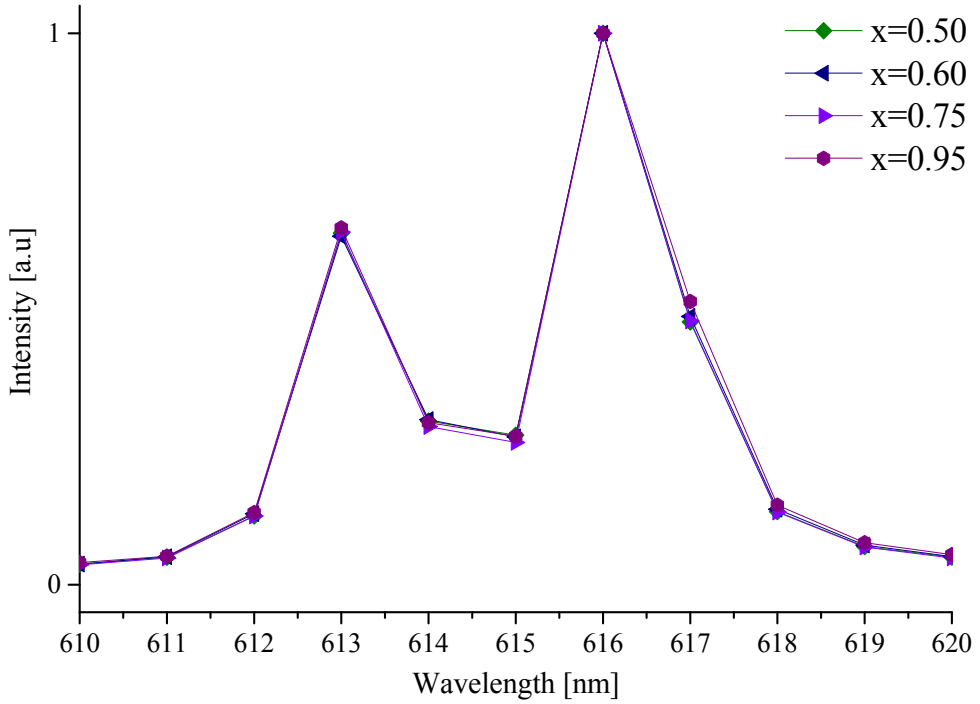

Figure 7.54: Normalized emission spectra of $LiEu_{(1-x)}Al_x(WO_4)(MoO_4)$ excited at 395 nm (x = 0.50 to 0.95)

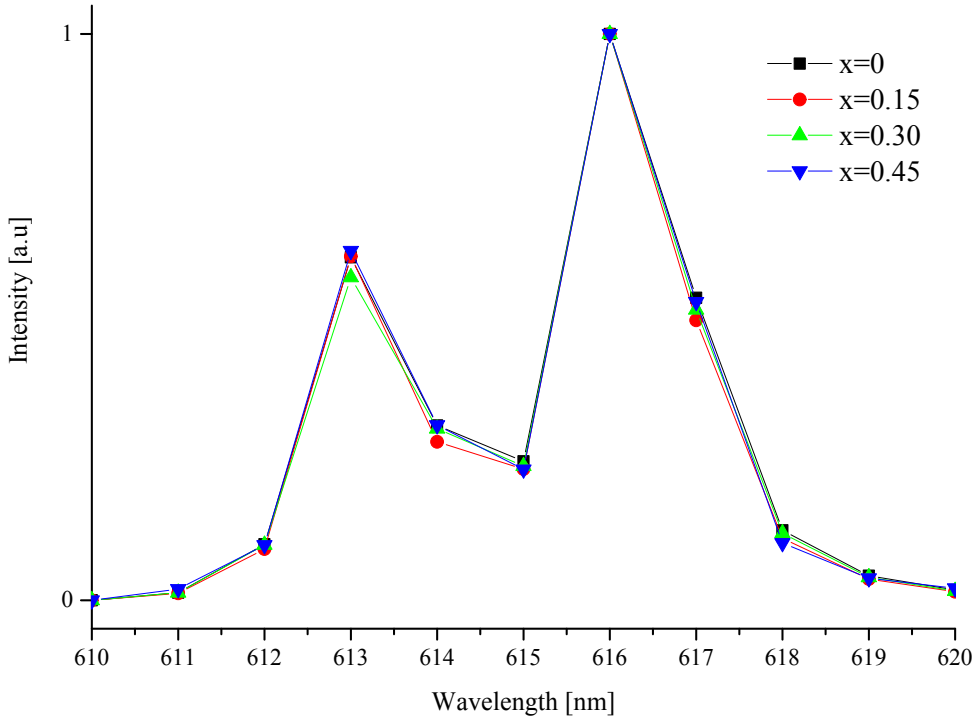

Figure 7.55: Normalized emission spectra of $LiEu_{(1-x)}Al_x(WO_4)(MoO_4)$ excited at 465 nm (x = 0 to 0.45)

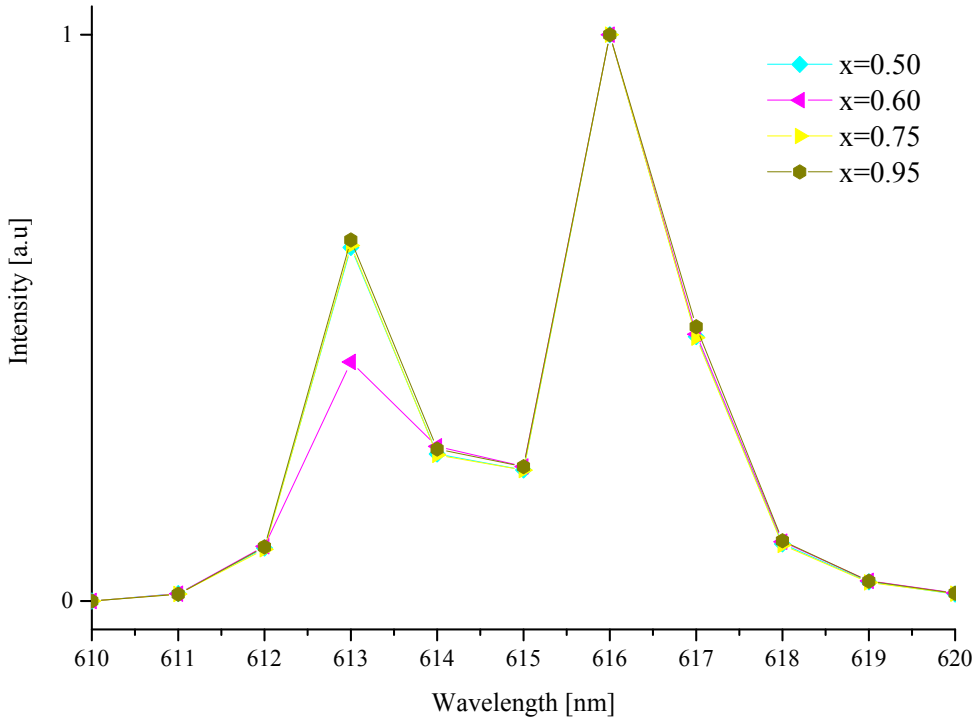

Figure 7.56: Normalized emission spectra of $LiEu_{(1-x)}Al_x(WO_4)(MoO_4)$ excited at 465 nm (x = 0.50 to 0.95)

Figure 7.57 (a) and (b) reveal that the overall trends of the luminous efficacies when excited at either 395 nm or 465 nm gradually reduce until the concentration of Al^{3+} cations reaches 50%. This decrease coincides with the decrease observed in the line-widths of the two main emission peaks, and indicates there was quenching taking place. As the concentration of the Al^{3+} cations increases to x=0.60 the luminous efficacy increases. Again this is where the distances between the Eu^{3+} cations are increasing so that the emission quenching mechanisms are reduced between them. Above x=0.60 there is less Eu^{3+} cations present and the luminous efficacies decrease as expected.

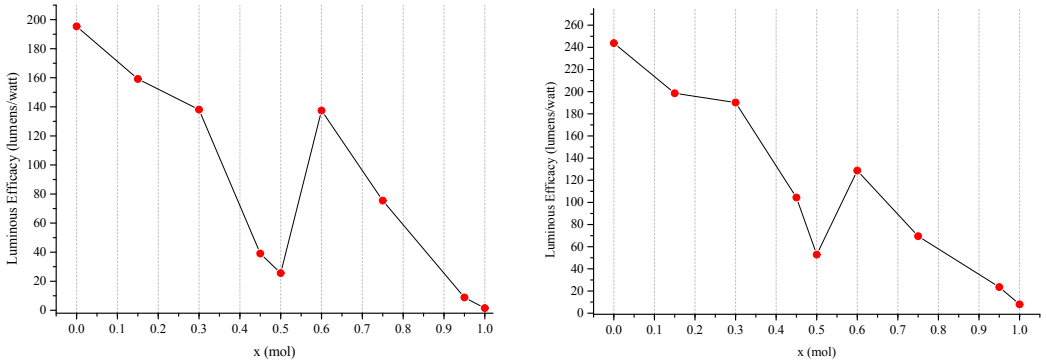

(a) (b)

Figure 7.57: Luminous efficacies of $LiEu_{(1-x)}Al_x(WO_4)(MoO_4)$ excited at (a) 395 nm and (b) 465 nm

All colour coordinates and colour temperature of the $LiEu_{(1-x)}Al_x(WO_4)(MoO_4)$ phosphors are listed in Table 7.10 with the data plotted in Figure 7.58 and Figure 7.59. The table and figures show that there was only a small change of colour coordinates and colour temperature as a function of increasing Al^{3+} cation concentration. No systematic trends in the CIE coordinates are apparent.

Table 7.10: CIE Colour coordinates of $LiEu_{(1-x)}Al_x(WO_4)(MoO_4)$

No.	Al^{3+} Concentration (mol)	Exc 395 nm			Exc 465 nm		
		Coordinates		Colour temp	Coordinates		Colour temp
		x	y		x	y	
1	0	0.6722	0.3276	867 K	0.6719	0.3279	869 K
2	0.15	0.6719	0.3278	869 K	0.6717	0.3280	870 K
3	0.30	0.6718	0.3279	870 K	0.6716	0.3282	871 K
4	0.45	0.6717	0.3281	871 K	0.6714	0.3284	873 K
5	0.50	0.6720	0.3276	870 K	0.6712	0.3294	880 K
6	0.60	0.6719	0.3278	869 K	0.6713	0.3284	874 K
7	0.75	0.6718	0.3280	870 K	0.6712	0.3286	874 K
8	0.95	0.6722	0.3276	867 K	0.6703	0.3295	881 K
9	1				N/A		

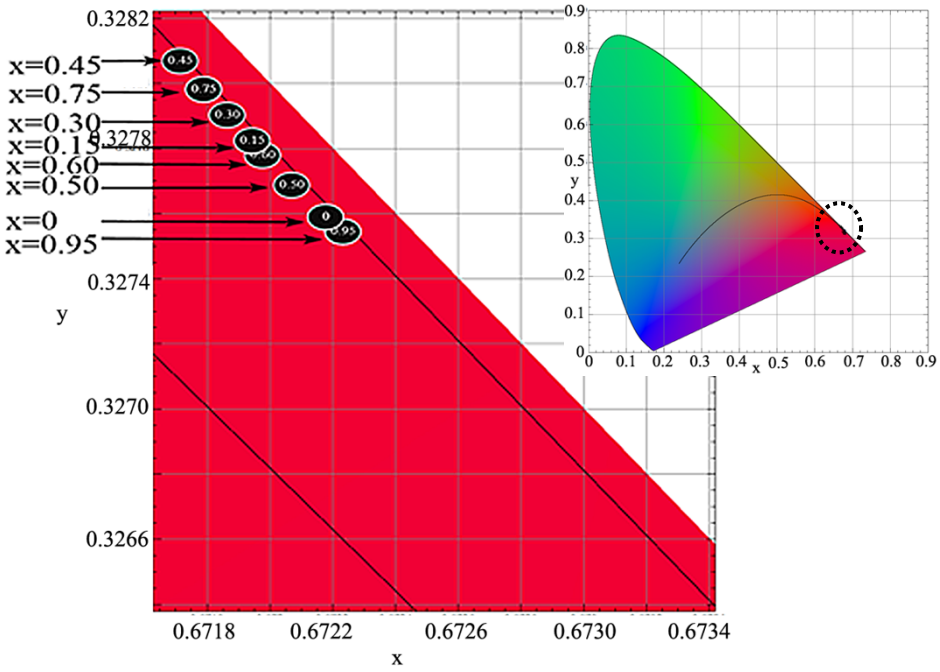

Figure 7.58: CIE diagram for $LiEu_{(1-x)}Al_x(WO_4)(MoO_4)$ excited at 395nm

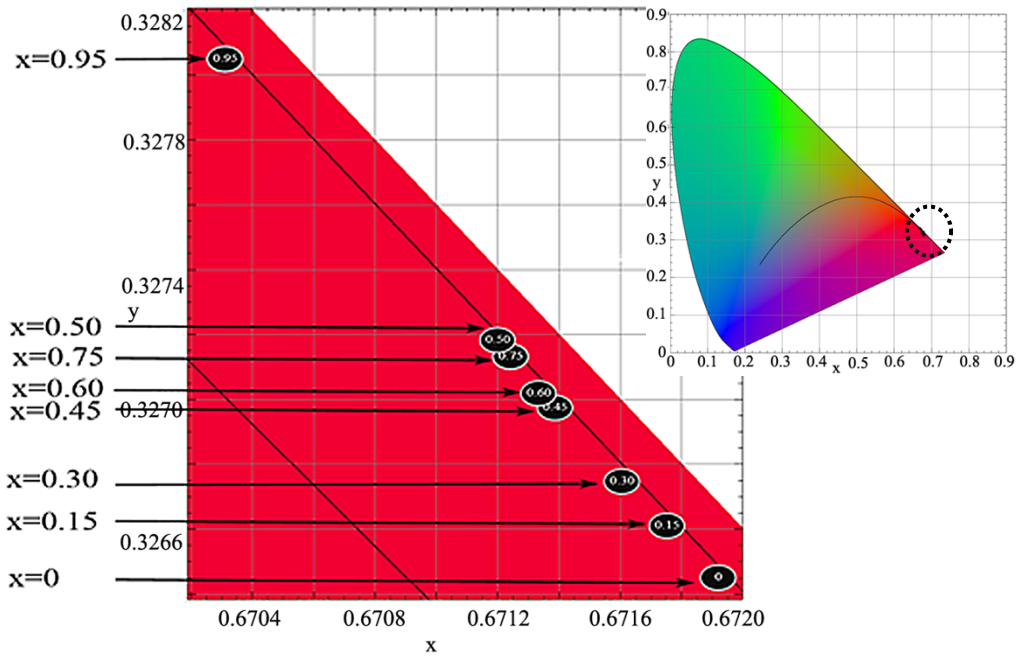

Figure 7.59: CIE diagram for $LiEu_{(1-x)}Al_x(WO_4)(MoO_4)$ excited at 465nm

7.4 SEM images of $LiAl(WO_4)_2$, $LiAl(MoO_4)_2$ and $LiAl(MoO_4)(WO_4)$

Figure 7.60 shows the $LiAl(WO_4)_2$ particles that exhibit angular rod-type shapes. The particles also tend to adhere between each other and agglomerate into a rounded mass. Similar anisotropic shapes are also seen in $LiAl(MoO_4)_2$ in Figure 7.61 and Figure 7.62 but with less adherence compared to Figure 7.60. Interestingly the particle shapes of $LiAl(MoO_4)(WO_4)$ were found to be more spherical and isotropic than the previous two images of $LiAl(WO_4)_2$ and $LiAl(MoO_4)_2$. Initially the image was doubted due to a mistake in selecting samples to be analysed in the SEM. However, a different sample of $LiAl(MoO_4)(WO_4)$ from a different batch was then selected with it still providing the same spherical particle images (see Figure 7.63 and Figure 7.64). The result of the Energy-dispersive X-ray spectroscopy (EDS), as can be observed in Figure 7.65, confirms that the particles correctly belong to $LiAl(MoO_4)(WO_4)$.

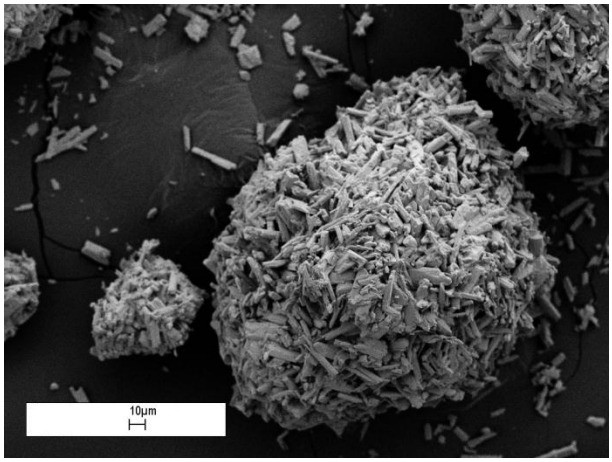

Figure 7.60: SEM image of $LiAl(WO_4)_2$ (with 1kx magnification)

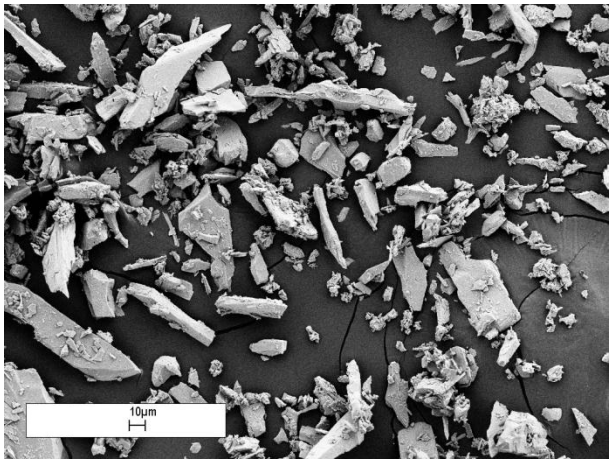

Figure 7.61: SEM image of $LiAl(MoO_4)_2$ (with 1kx magnification)

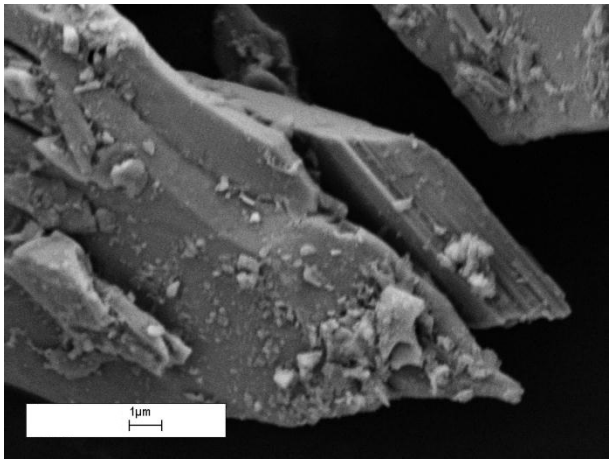

Figure 7.62: SEM image of $LiAl(MoO_4)_2$ (with 20kx magnification)

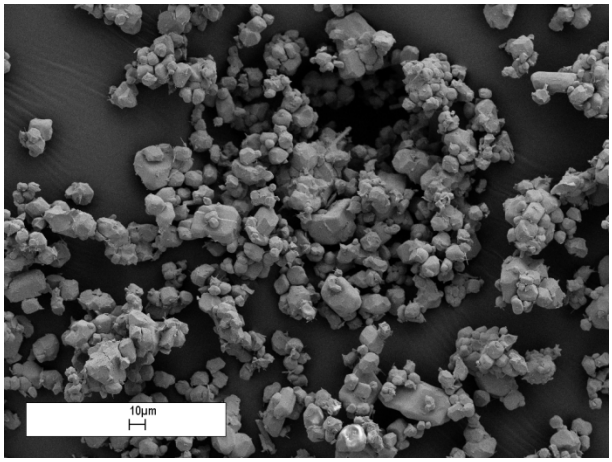

Figure 7.63: SEM image of of $LiAl(WO_4)(MoO_4)$ (with 1kx magnification)

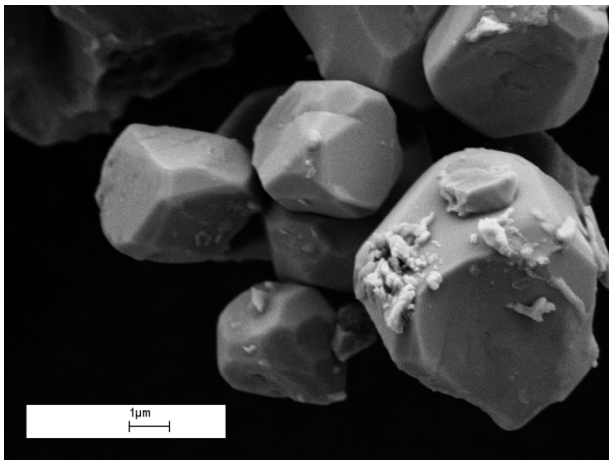

Figure 7.64: SEM image of of $LiAl(WO_4)(MoO_4)$ (with 25kx magnification)

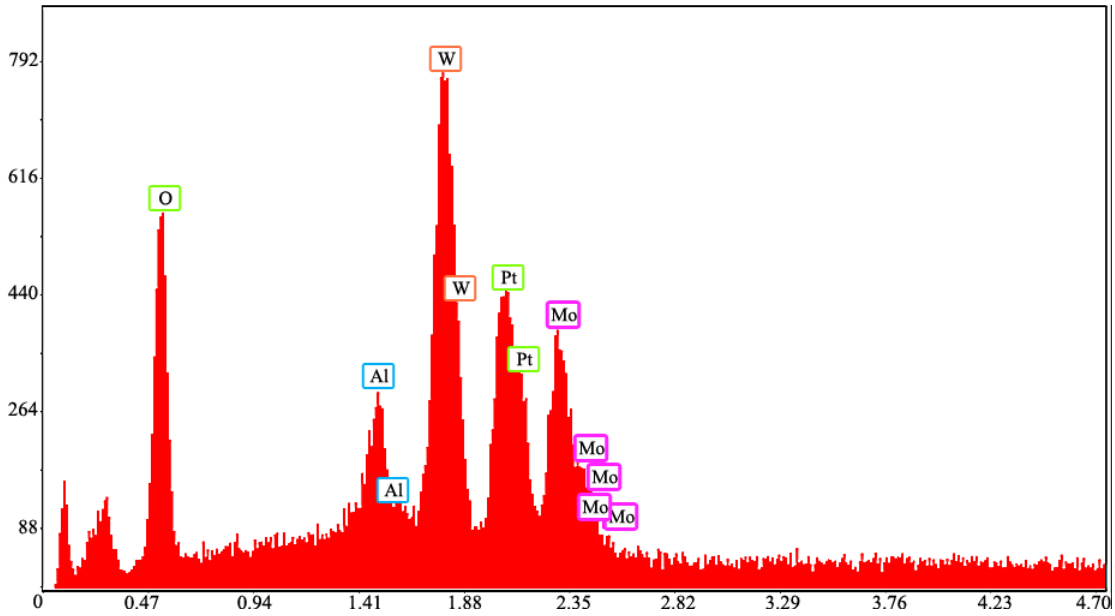

Figure 7.65: EDS results of the sample identifying each of the atomic components of Li, Al, W, Mo and O from $LiAl(WO_4)(MoO_4)$

7.5 Changes of Charge-Transfer-Bands in all Phosphors

In addition to measuring the emission spectra and their luminous efficacies, we also made measurements on the excitation spectra on all samples of $LiEu_{1-x}C_x(MoO_4)_{2-y}(WO_4)_y$, [C=$Y^{3+}$ and Gd^{3+}]. Examples of the overlaid excitation spectra of the samples are shown in Figure 7.66 to Figure 7.69, whereas the rest of the excitation spectra from other samples can be found in Appendix B. It can be observed from the figures (and in the appendices) that the concentrations of Eu^{3+} had an effect on the wide charge transfer (CT) bands at 250 nm to 350 nm. However we had no sufficient evidence yet to identify the specific reason behind the changes due to time constraints. It would be very interesting if this research can be expanded further in investigating the correlation between the CT bands of Eu^{3+} on each of the sample of molybdates / tungstates phosphors.

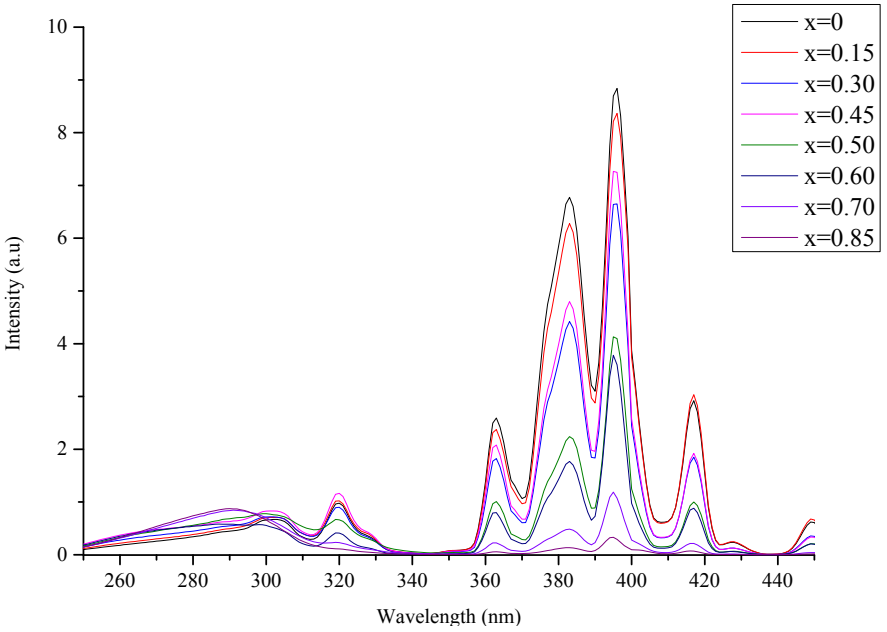

Figure 7.66: Excitation spectra of $LiEu_{(1-x)}Y(WO_4)_2$ excited at 616 nm

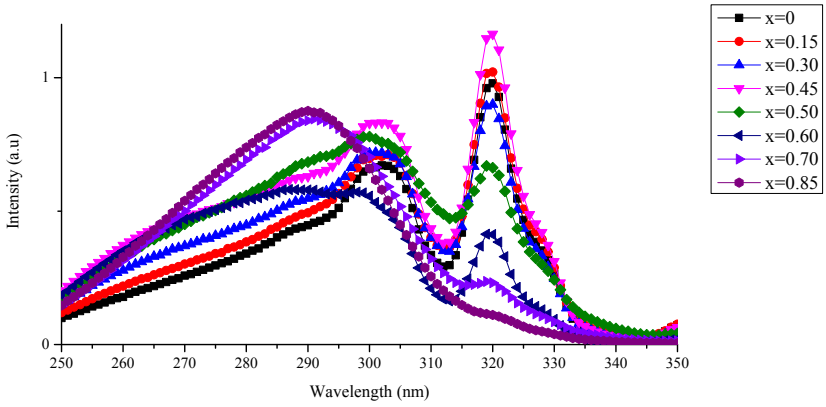

Figure 7.67: Close-up excitation spectra (250 – 350 nm) of $LiEu_{(1-x)}Y(WO_4)_2$ excited at 616 nm

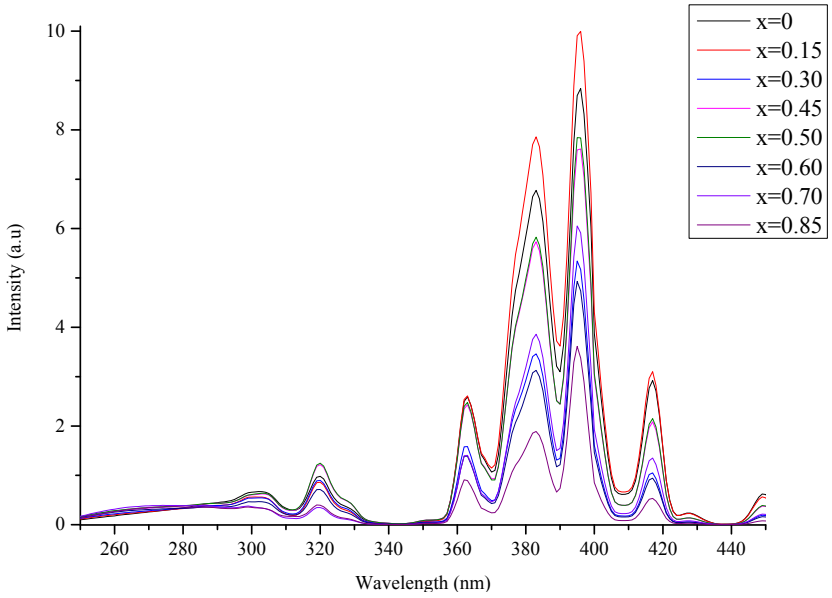

Figure 7.68: Excitation spectra of $LiEu_{(1-x)}Gd(WO_4)_2$ excited at 616 nm

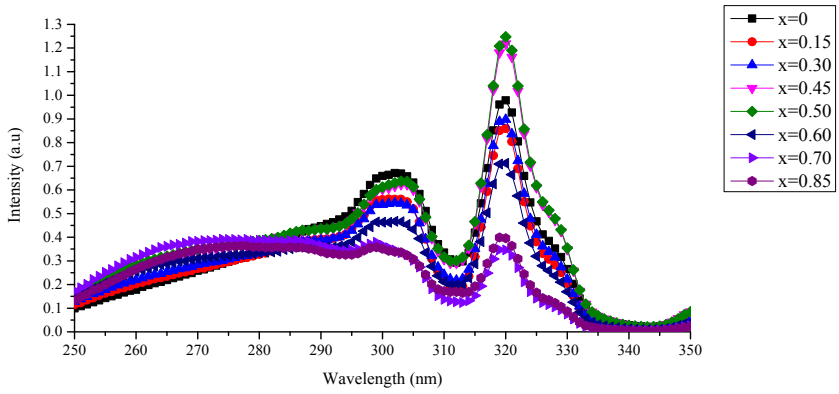

Figure 7.69: Close-up excitation spectra (250 – 350 nm) of $LiEu_{(1-x)}Gd(WO_4)_2$ excited at 616 nm

7.6 Conclusions

There are a number of interesting conclusions that can be made from this chapter:

1) All three compounds change their phase as the amount of Al^{3+} cations increases when substituting for the Eu^{3+} activators. Only $LiAl(MO_4)(WO_4)$ can be fully refined to a triclinic structure while $LiAl(MO_4)_2$ can be partially fitted. However, the structural details of $LiAl(WO_4)_2$ are unknown.
2) Although Al^{3+} is very small, it does appear to replace and occupy the sites that would have been occupied by Eu^{3+} cations. Excess Al^{3+} cations tend to form secondary phases as their concentration increases. The colour coordinates of all the phosphors do not shift much as the concentration of Al^{3+} cations increases.
3) Luminescence efficacies are at the optimum level when 50% of aluminium (III) is substituted in the tungstate compound and interestingly, 60% of aluminium (III) still provides tungstate and tungstate-molybdate compounds with a good emission intensity. This finding is very important (although some details of the crystal structures are unexplained) and proves that these red phosphors can be produced with much less cost by using less expensive Europium (III) and replacing around half of the Eu^{3+} cations with Al^{3+}.

7.7 References

1. Stone R, Silver J (September 2011) An Investigation Into Novel Red Emitting Phosphors and Their Applications. Dissertation, Brunel University.

2. Klevtsov P, Klevtsova R (1977) Polymorphism of the double molybdates and tungstates of mono-and trivalent metals with the composition M $R_3(EO_4)_2$. *Journal of Structural Chemistry*, 18(3), 339-355.

3. Soloveva L, Borisov S (1970) Crystal structure of $LiAl(MoO_4)_2$. *Soviet Physics Crystallography*, USSR, 15(3), 493.

Chapter 8

Conclusions and Future Works

Two approaches were taken herein in optimizing the use of europium in red phosphors:-

The first approach was by applying coating layers on the moisture sensitive phosphor; $CaS:Eu^{2+}$, whereas the second was aimed at modifying existing red phosphor compositions by substituting Eu^{3+} cations with lower cost cations.

To improve the life of moisture sensitive $CaS:Eu^{2+}$, 10 nm and 40 nm thickness coatings were applied by ALD to the phosphor particles. Although there were still photoluminescence degradation occurring at high humidity and high temperature, the rate of the degradation was shown to have slowed down. From what was observed on the uniformity of the coating layers on the particles, it certainly appears that further research to improve the uniformity of the coating layer would be worthwhile to prolong the life of this phosphor. A better quality coating technique would surely protect the sulfide particles from reacting with the atmospheric water and carbon dioxide. Nevertheless it is still worth noting that Al_2O_3 coated $CaS:Eu^{2+}$ (or any sulfide based phosphors) could be used as colour conversion materials for generating red light from blue LEDs if the environmental conditions experienced by the latter are not too severe on the coated phosphors.

With respect to the modification of existing phosphors, yttrium, gadolinium and aluminium have been used as potential cations to be embedded in the phosphor system. There were mixed conclusions that can be summarized from the different cations deployed in the phosphors. First of all, luminous efficacies of the phosphor system; $LiEu_{1-x}C_x(MoO_4)_{2-y}(WO_4)_y$, [$C$=$Al^{3+}$, Y^{3+} and Gd^{3+} while y = 0, 1 and 2] can generally be enhanced (or can be maintained for some samples) when the amount of the substituted cations reaches about 45 to 60 mol

% regardless of whatever is happening to the crystal structures. The luminous efficacy was also found to be very high especially for $LiEu_{0.5}Al_{0.5}(WO_4)_2$ recorded at 253.74 lm/W when excited at 465 nm.

Based on the work on yttrium in Chapter 5, although it can be concluded that the enhancement of the photoluminescence was due to the optimum distance of Eu^{3+} to Eu^{3+} inside the phosphor crystals, we also had an initial thought that the efficacy enhancements were closely related to the specific lattice volumes of the crystal structure. However further research on analysing the correlative relationship between the two needs to be expanded as we could not find conclusive evidence from the experiments on Gd^{3+} and Al^{3+} reported in the Chapters 6 and 7. Colour coordinates also did not shift much as Eu^{3+} was being replaced by other cations.

Among all 3 compounds (tungstates, molybdates and tungstate-molybdates), tungstate phosphors were the most difficult but interesting to analyse. For tungstates based phosphors, apart from our observation that the crystal structure on yttrium-tungstate and aluminium-tungstate changed to unknown phases (although surprisingly this did not happen to gadolinium-tungstate), the consistency of the luminous efficacies was also difficult to predict. Indeed the highest luminous efficacy came from the unknown crystal structure of the aluminium-tungstate compound as mentioned above. These findings have proven that these red phosphors are undergoing a quenching effect at 100 mol% of Eu^{3+} in the compound. The results found herein should be studied further in exploring the relationship between the crystal structure of the phosphor compounds and luminous efficacies produced by the respective phosphors.

It has been shown in this thesis that these phosphors can therefore be produced with less cost by replacing about half of the Eu^{3+} cations with the cations studied herein. This approach could therefore help relevant industries to become less dependent on Eu^{3+} by applying the findings from this thesis and thus be more cost efficient in their production.

Appendix A

The first consideration was rejected as the refined cell parameters of $Y_{0.15}$ to $Y_{0.50}$ are not consistent from one another. Although the R_{wp}s are slightly improved than the single-phase refinements but with more variables included in the refinement on the 2-phase analysis therefore such an improvement was worthless and consequently discarded. This rejection is also in line with what is observed in Figure 5.6 because there are no changes observed as Y^{3+} concentration increases from 0 to 50%.

The only difference between the second and the third considerations is on $Y_{0.85}$. The 2-phase refinement on Y0.85 produces R_{wp} 13.53 whereas single-phase refinement on the same sample results with R_{wp} 13.68. The 2-phase refinement demonstrates just a little improvement R_{wp} but with more parameters included in refining the peaks, this means the improvement is not likely acceptable and once again can be rejected.

Table A1: Lattice parameters of tetragonal I41/a:2 and monoclinic P12/n1 refined on $LiEu_{(x-1)}Y_xW_2O_8$

Y^{3+} (mol)	Tetragonal I41/a:2				Monoclinic P12/n1						R_{wp}
	a (Å)	c (Å)	Vol ($Å^3$)	%	a (Å)	b (Å)	c (Å)	β (°)	Vol ($Å^3$)	%	
0	5.20508(5)	11.3043(2)	306.265(7)	100			N/A				10.81
0.15	5.2005(1)	11.2593(3)	304.51(2)	100			N/A				16.71
0.30	5.19172(9)	11.2421(3)	303.02(1)	100			N/A				15.30
0.45	5.18318(7)	11.2183(2)	301.38(1)	100			N/A				14.74
0.50	5.1812(1)	11.2140(4)	301.04(2)	100			N/A				16.87
0.55	5.17865(9)	11.2070(3)	300.55(1)	65(1)	10.0474(6)	5.8092(3)	5.0106(3)	94.522(4)	291.55(3)	35(1)	13.72
0.70	5.1778(2)	11.2057(7)	300.42(3)	12(1)	10.0293(2)	5.8043(1)	5.0055(1)	94.400(1)	290.52(1)	88(1)	13.33
0.85	5.191(3)	11.09(1)	298.7(5)	1(7)	10.0128(2)	5.80064(7)	5.00417(8)	94.3114(9)	289.823(7)	99(7)	13.53
1.0		N/A			9.9899(1)	5.79480(6)	5.00271(5)	94.1986(7)	288.827(5)	100	12.57

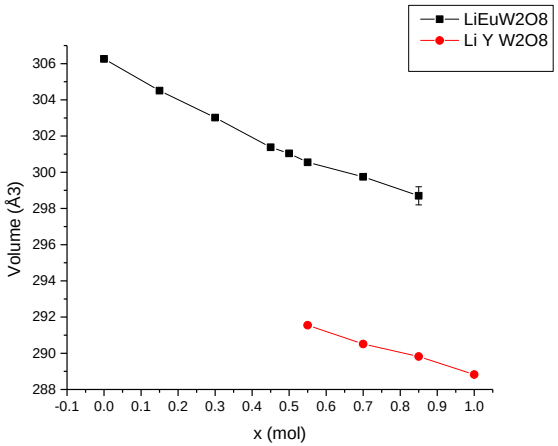

Figure A1: Cell volumes of tetragonal $LiEuW_2O_8$ and monoclinic $LiYW_2O_8$

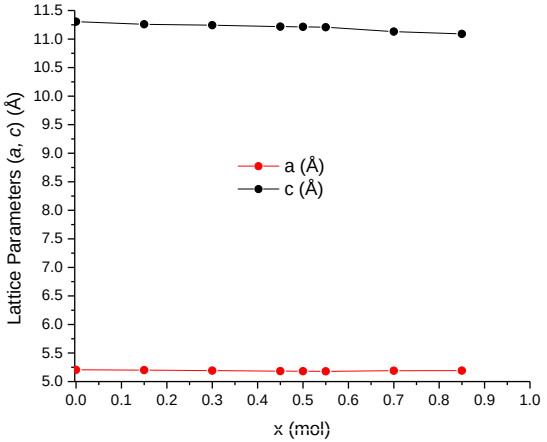

Figure A2: Lattice parameters of tetragonal

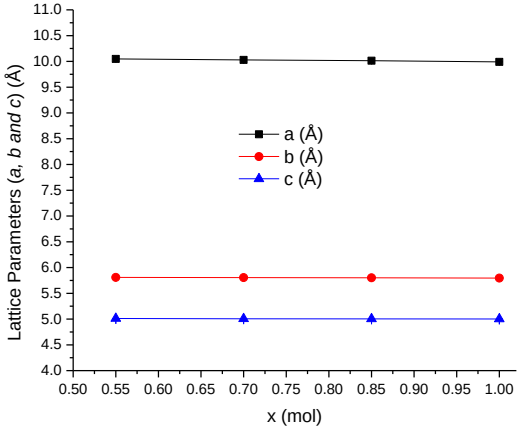

Figure A3: Lattice parameters of monoclinic $LiYW_2O_8$

Table A2: Lattice parameters of tetragonal I41/a:2 and monoclinic P12/n1 refined on $LiEu_{(x-1)}Y_xW_2O_8$

Y^{3+} (mol)	Tetragonal I41/a:2				Monoclinic P12/n1						R_{wp}
	a (Å)	c (Å)	Vol ($Å^3$)	%	a (Å)	b (Å)	c (Å)	β (°)	Vol ($Å^3$)	%	
0	5.20508(5)	11.3043(2)	306.265(7)	100			N/A				10.81
0.15	5.2005(1)	11.2593(3)	304.51(2)	100			N/A				16.71
0.30	5.19172(9)	11.2421(3)	303.02(1)	100			N/A				15.30
0.45	5.18318(7)	11.2183(2)	301.38(1)	100			N/A				14.74
0.50	5.1812(1)	11.2140(4)	301.04(2)	100			N/A				16.87
0.55	5.17865(9)	11.2070(3)	300.55(1)	65(1)	10.0474(6)	5.8092(3)	5.0106(3)	94.522(4)	291.55(3)	35(1)	13.72
0.70	5.1778(2)	11.2057(7)	300.42(3)	12(1)	10.0293(2)	5.8043(1)	5.0055(1)	94.400(1)	290.52(1)	88(1)	13.33
0.85		N/A			10.0128(2)	5.80065(7)	5.00420(8)	94.3111(9)	289.825(8)	100	13.68
1.0		N/A			9.9899(1)	5.79480(6)	5.00271(5)	94.1986(7)	288.827(5)	100	12.57

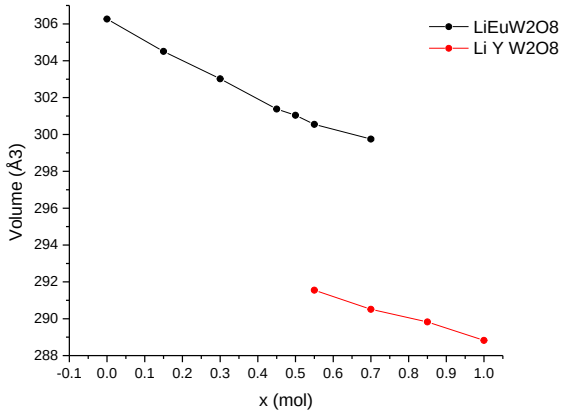

Figure A4: Cell volumes of tetragonal $LiEuW_2O_8$ and monoclinic $LiYW_2O_8$

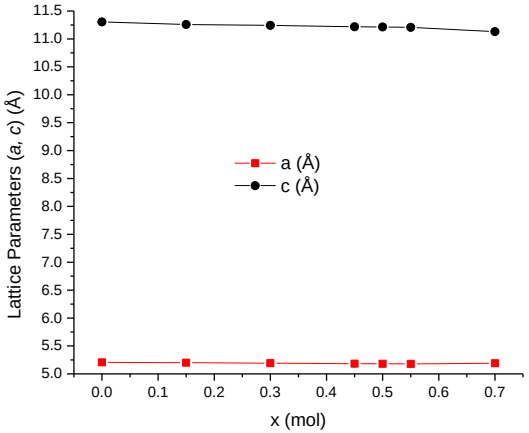

Figure A5: Lattice parameters of tetragonal

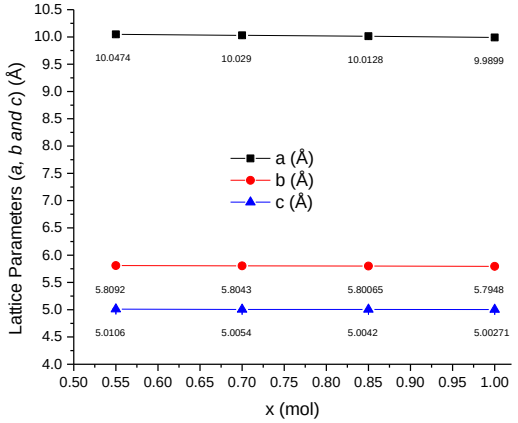

Figure A6: Lattice parameters of monoclinic $LiYW_2O_8$

Appendix B

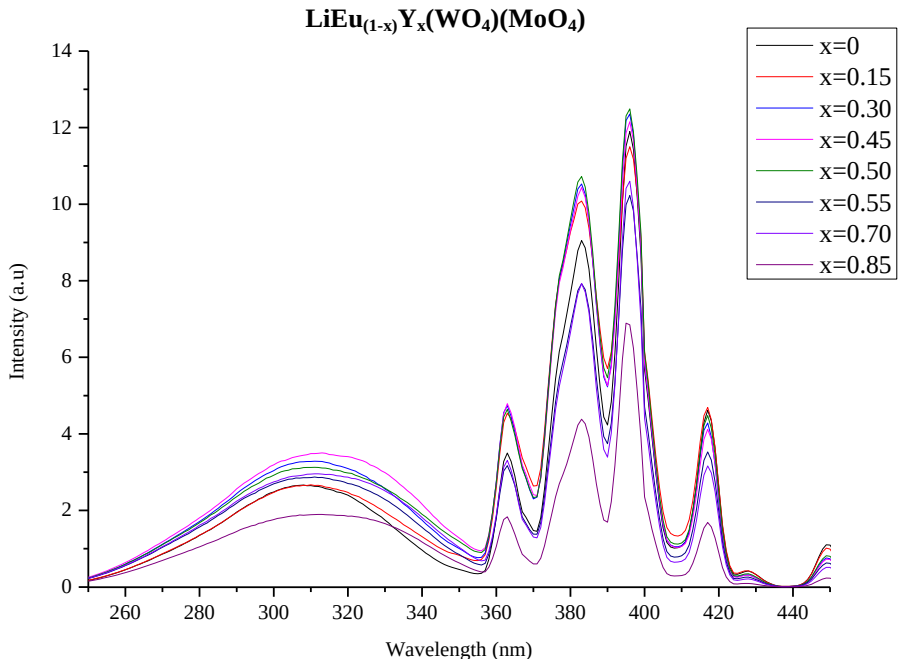

Excitation spectra of $LiEu_{(1-x)}Y_x(WO_4)(MoO_4)$ excited at 616 nm

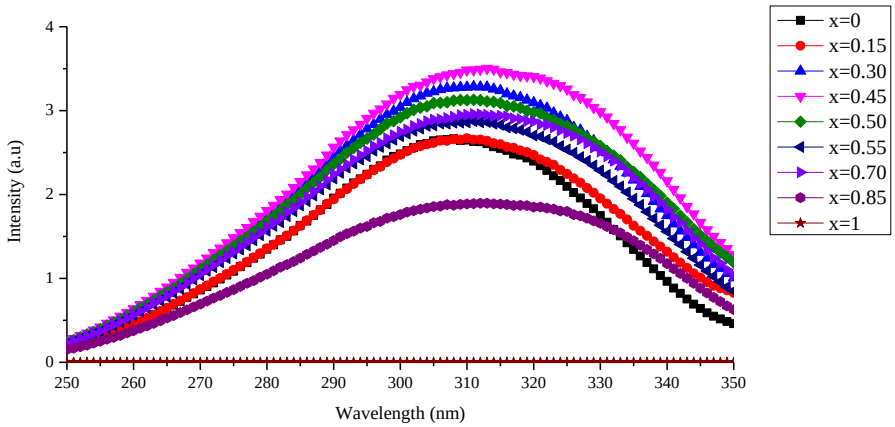

Close-up excitation spectra (250 – 350 nm) of $LiEu_{(1-x)}Y_x(WO_4)(MoO_4)$ excited at 616 nm

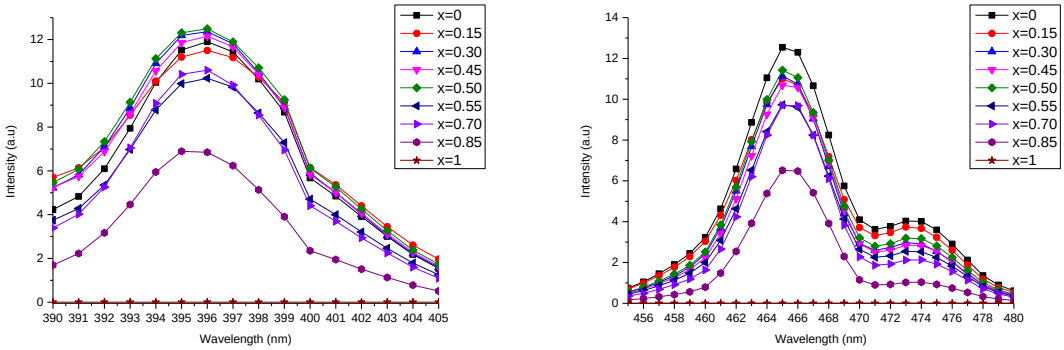

(a) (b)

Close-up excitation spectra at (a) 390 – 405 nm and (b) 455-480 nm of $LiEu_{(1-x)}Y_x(WO_4)(MoO_4)$ excited at 616 nm

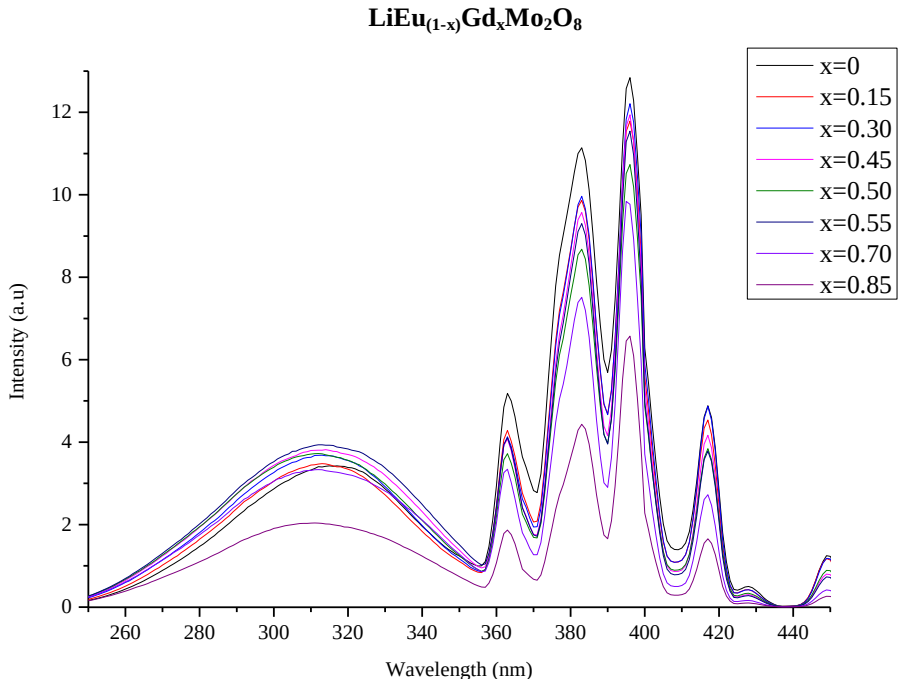

Excitation spectra of $LiEu_{(1-x)}Gd_xMo_2O_8$ excited at 616 nm

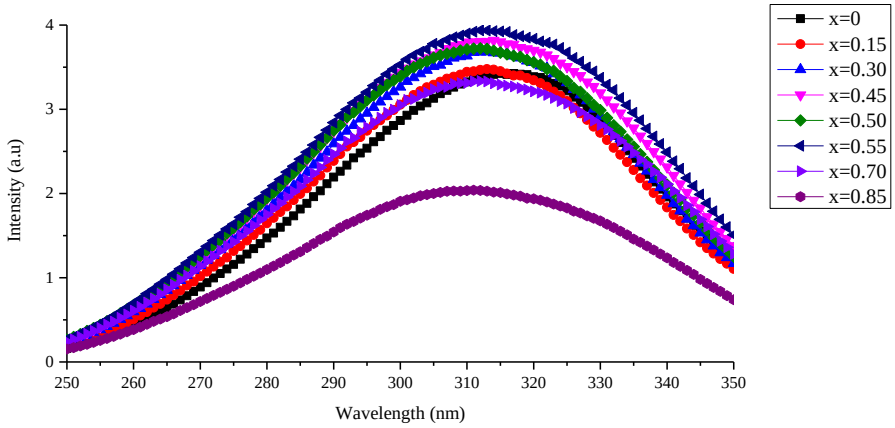

Close-up excitation spectra (250 – 350 nm) of $LiEu_{(1-x)}Gd_xMo_2O_8$ excited at 616 nm

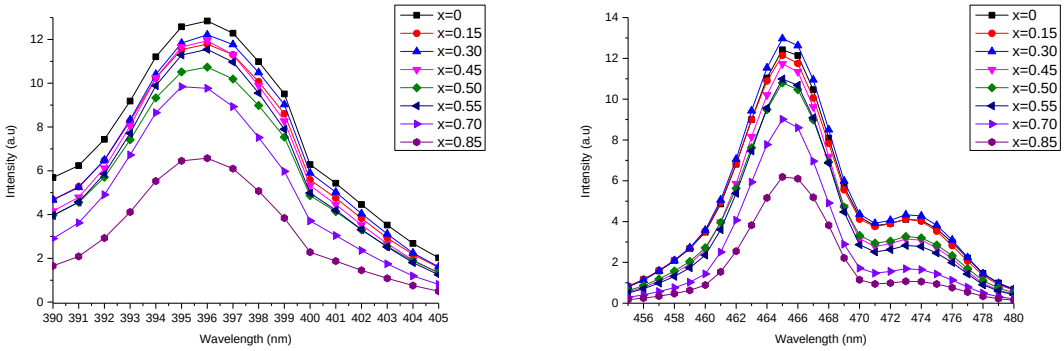

(a) (b)

Close-up excitation spectra at (a) 390 – 405 nm and (b) 455-480 nm of $LiEu_{(1-x)}Gd_xMo_2O_8$ excited at 616 nm

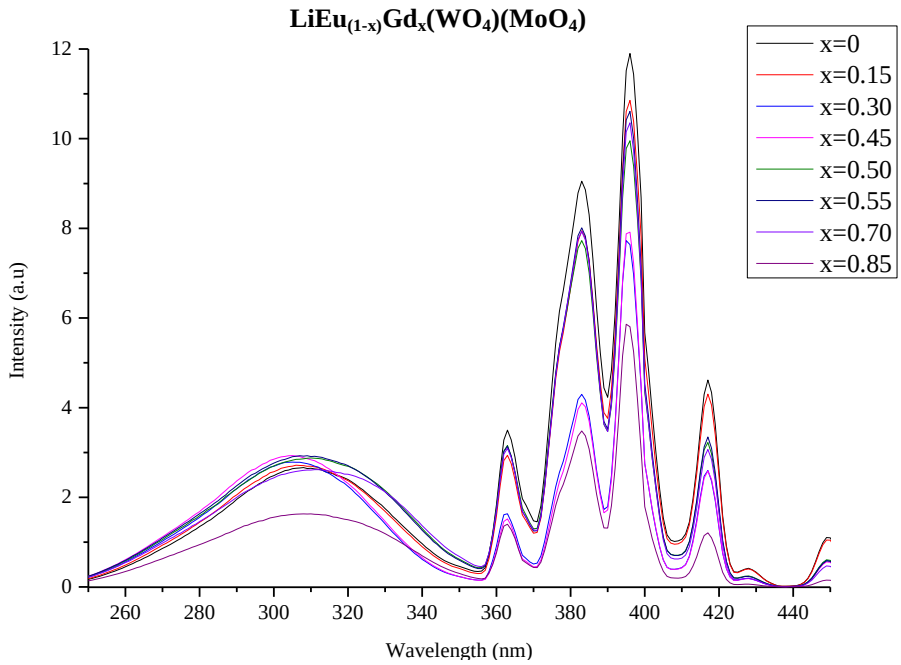

Excitation spectra of $LiEu_{(1-x)}Gd_x(WO_4)(MoO_4)$ excited at 616 nm

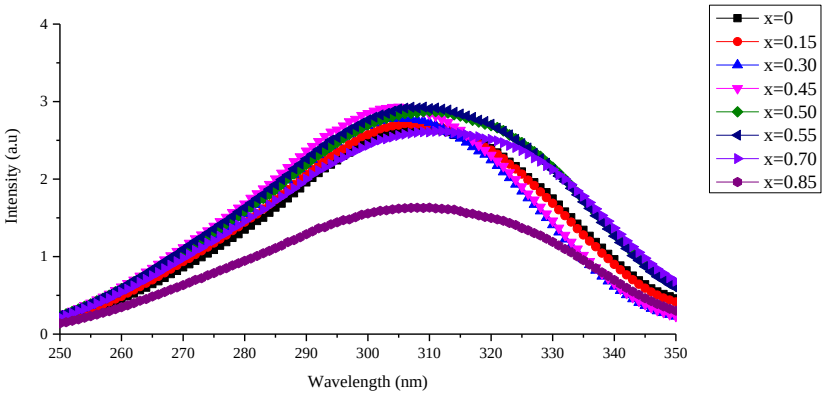

Close-up excitation spectra (250 – 350 nm) of $LiEu_{(1-x)}Gd_x(WO_4)(MoO_4)$ excited at 616 nm

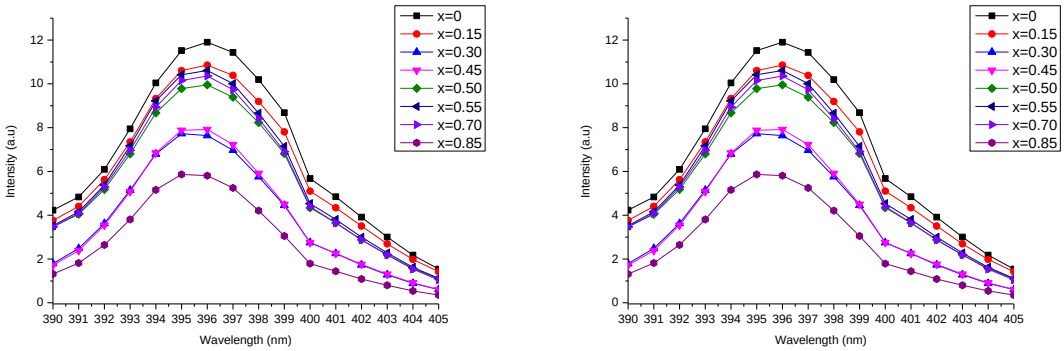

(a) (b)

Close-up excitation spectra at (a) 390 – 405 nm and (b) 455-480 nm of $LiEu_{(1-x)}Gd_x(WO_4)(MoO_4)$ excited at 616 nm